Università degli Studi di Cagliari

PHD DEGREE

INNOVATION SCIENCES AND TECHNOLOGIES

Cycle XXXIII

TITLE OF THE PHD THESIS

Analysis of multi-phase systems

relevant to bioengineering and materials science

Scientific Disciplinary Sector(s)

ING-IND/24

PhD Student: Gabriele Traversari

Supervisor Prof. Alberto Cincotti

Final exam. Academic Year 2019 – 2020
Thesis defence: April 2021 Session

INDEX

PAPERS……...…….. V

CONGRESSES, SEMINARS AND CONFERENCES…..…….. V

ABSTRACT…….. VI

Chapter 1. Introduction……. 1

1.1. Long-term preservation of hMSCs from UCB…… 2

1.1.1. Mesenchymal Stem Cells form Umbilical Cord Blood……. 2

1.1.2. Cryopreservation…… 4

1.1.3. Air-drying at room temperature and atmospheric pressure…… 8

1.2. Mechanical processing of powders by Ball Milling (BM)……..……. 10

References of the Chapter 1……..... 13

Chapter 2. Long-term preservation of hMSCs from UCB…… 18

2.1. Modelling the Osmotic Behaviour of Human Mesenchymal Stem Cells…… 18

2.1.1. Introduction…… 18

2.1.2. Model Equations…… 20

2.1.2.1. Dynamics…….. 21

2.1.2.2. Equilibrium with impermeant solutes……... 26

2.1.3. Results and discussion……... 28

2.1.3.1. Regression analysis……... 28

2.1.3.2. Model validation……... 32

2.1.3.3. Equilibrium conditions with impermeant solute……... 33

2.1.4. Conclusions and future work…… 37

Notation of the Subchapter 2.1……...…….. 38

References of the Subchapter 2.1…….. 40

2.2. Insights into the model of non-perfect osmometer cells for cryopreservation:
a parametric sweep analysis…… 42

2.2.1. Introduction……... 42

2.2.2. Model Equations……... 42

2.2.2.1. Dynamics……. 42

2.2.2.2. Equilibrium with impermeant solutes……. 45

2.2.2.3. Model Parameters…… 47

2.2.3. Results and discussion……. 48

2.2.3.1. Osmotic cycle with impermeant sucrose
in the absence of permeant DMSO…… 48

2.2.3.2. Osmotic cycle with permeant DMSO
in the absence of impermeant sucrose……... 57
2.2.4. Concluding remarks…… 61
Notation of the Subchapter 2.2…….. 63
2.3. hMSCs from UCB in contact with DMSO for cryopreservation:
experiments and modelling of osmotic injury and cytotoxicity……... 64
2.3.1. Introduction……. 64
2.3.2. Experimental Section…….. 67
2.3.2.1. Experimental setup and operating conditions…… 67
2.3.2.2. Cell count……... 68
2.3.2.3. Cell viability…….. 68
2.3.3. Modeling Section……... 70
2.3.4. Results and discussion……..….. 74
2.3.5. Conclusions…… 80
Notation of the Subchapter 2.3……. 81
References of the Subchapter 2.3……. 82
2.4. A compartmental model for the Air-Drying process of hMSCs in a desiccator unit……. 84
2.4.1. Introduction…… 84
2.4.2. Model Equations…… 86
2.4.2.1. Air-drying apparatus: system set-up……. 88
2.4.2.2. Material balance equations…… 90
2.4.2.3. Liquid phase in a single petri dish: liquid water…… 90
2.4.2.4. Liquid phase in a single petri dish: dissolved trehalose…… 91
2.4.2.5. Gas phase in a single petri dish: water vapor…… 91
2.4.2.6. Gas phase in the chamber of the desiccator unit: water vapor…….. 91
2.4.2.7. Adsorbent solid phase: water vapor adsorbed in silica gel…… 92
2.4.2.8. Intracellular liquid phase: water in cytoplasm…… 92
2.4.3. Mass transport: diffusion fluxes…….. 92
2.4.3.1. Evaporation in the Petri dish…….. 93
2.4.3.2. Adsorption in the silica gel……. 94
2.4.3.3. Leakage from a single petri dish
to the chamber of the desiccator unit…….. 95
2.4.3.4. Cell osmosis…… 95
2.4.4. Crystal formation: Population Balance Equation (PBE)……. 95
2.4.4.1. Nucleation rate…… 96
2.4.4.2. Crystal growth rate……. 96
2.4.4.3. Numerical solution of (PBE): the method of moments…….. 97

2.4.4.4. Quadrature Method of Moments……. 98
2.4.5. Results and discussion…….. 99
2.4.5.1. Parametric sensitivity analysis: Base case……... 100
2.4.5.2. Parametric sensitivity analysis: glass formation…….. 109
2.4.5.2.1. Case 1. Increasing the evaporative surface area……. 109
2.4.5.2.2. Case 2. Increasing the cross-sectional area surface for the leakage from the Petri dish…….. 110
2.4.5.2.3. Case 3. Reducing the sample height (volume)…… 111
2.4.5.2.4. Case 4. Reducing the trehalose osmolality……. 112
2.4.5.3. Parametric sensitivity analysis: crystal formation……... 114
2.4.5.3.1. Case 5. Reducing the evaporative surface area…….. 114
2.4.5.3.2. Case 6. Decreasing the cross-sectional area surface for the leakage from the Petri dish…….. 121
2.4.5.3.3. Case 7. Increasing sample volume…….. 123
2.4.5.3.4. Case 8. Increasing the trehalose osmolality…… 123
2.4.6. Conclusions…….. 124
2.4.A1. Appendix – Thermodynamic parameters……. 126
2.4.A1.1. Solid-liquid equilibria……. 126
2.4.A1.2. Vapor-liquid equilibrium…… 127
2.4.A1.2.1. Vapor pressure of pure water……. 127
2.4.A1.2.2. The coefficient of activity for water in the binary liquid system water + trehalose……..... 128
2.4.A1.3. Vapor-solid equilibrium……. 128
2.4.A1.4. Glass transition curve……. 129
2.4.A2. Appendix – Material transport parameters……. 130
2.4.A2.1. Diffusivity of water in the liquid phase……. 130
2.4.A2.2. Diffusivity of water in the gas phase……. 130
2.4.A2.3. Diffusional layer in the gas phase……. 131
2.4.A2.4. Diffusional layer in the liquid phase……. 131
2.4.A2.5. Properties of the adsorbent phase (silica gel)…… 131
2.4.A3. Appendix – System variables……. 131
2.4.A3.1. Volumes and constant values……. 131
2.4.A3.2. Initial Conditions…… 132
2.4.A3.3. Sample: liquid phase…….. 132
2.4.A3.4. Sample: cells and crystal sugar…….. 133
2.4.A3.5. Petri gas phase…… 133
2.4.A3.6. Chamber gas phase……. 133

2.4.A3.7. Solid phase: adsorbent…… 133
Notation of the Subchapter 2.4…… 135
References of the Subchapter 2.4…… 138
Chapter 3. Mechanical processing of powders by Ball Milling…… 140
3.1. Milling dynamics and propagation of mechanically activated self-sustaining reactions…….. 140
3.1.1. Introduction…….. 140
3.1.2. Numerical methods…….. 141
3.1.3. Results and discussion……. 144
3.1.4. Conclusions…….. 150
References of the Subchapter 3.1…… 152
3.2. A mapping approach to pattern formation in the early stages of mechanical alloying……. 154
3.2.1. Introduction…….. 154
3.2.2. Methodologies…….. 154
3.2.3. Results and discussion…….. 155
3.2.4. Conclusions……... 158
References of the Subchapter 3.2……. 159
3.3. Coupling of mixing and reaction in mechanochemical transformations…… 160
3.3.1. Introduction……... 160
3.3.2. Mechanical processing by ball milling…….. 162
3.3.3. Interface area changes during impacts……... 165
3.3.4. Chemical changes during impacts…….. 170
3.3.5. Reaction kinetics in binary systems…… 172
3.3.6. Reaction kinetics in ternary systems……... 181
3.3.7. Discussion……... 183
3.3.8. Conclusions……. 188
Notation of the Subchapter 3.3…….. 189
References of the Subchapter 3.3……... 190
Chapter 4. Conclusions and future works…….. 192

PAPERS

1 Casula, E., **Traversari**, **G.,** Fadda, S., Klymenko, O.V., Kontoravdi, C., Cincotti, A., (2019). Modelling the Osmotic Behaviour of Human Mesenchymal Stem Cells, *Biochemical Engineering Journal*, 151, ID 107296. https://doi.org/10.1016/j.bej.2019.107296

2 Pia, G., **Traversari**, **G.,** Cincotti, A., Delogu, F., (2019). A mapping approach to pattern formation in the early stages of mechanical alloying, *Philosophical Magazine Letters*, 99(5), pp. 192-198. https://doi.org/10.1080/09500839.2019.1653503

3 Cincotti, A., **Traversari**, **G.,** Pia, G., Delogu, F., (2020). Milling dynamics and propagation of mechanically activated self-sustaining reactions, *Advances in Materials Science and Engineering*, 2020, ID 8032985. https://doi.org/10.1155/2020/8032985

4 **Traversari**, **G.,** Cincotti, A., (2020). Insights into the model of non-perfect osmometer cells for cryopreservation: a parametric sweep analysis, in press *Cryobiology*, https://doi.org/10.1016/j.cryobiol.2020.11.013

5 **Traversari**, **G.,** Porcheddu A., Pia, G., Delogu, F., Cincotti, A., (2020). Coupling of mixing and reaction in mechanochemical transformations, Physics. Phys. Chem. Chem. Phys., 23, pp. 229-245. https://doi.org/10.1039/D0CP05647B

6 **Traversari**, **G.,** Cincotti, A., (2021). hMSCs from UCB in contact with DMSO for cryopreservation: experiments and modelling of osmotic injury and cytotoxicity, to be submitted *Chemical Engineering Journal*.

7 **Traversari**, **G.,** Cincotti, A., (2021). A compartmental model for the Air-Drying process of hMSCs in a desiccator unit, under preparation.

CONGRESSES, SEMINARS AND CONFERENCES

1. **Traversari, G.,** Cincotti, A., "Contact with DMSO for cryopreservation of hMSCs from UCB: experiments and modeling on the osmotic and cytotoxic effects", PBM 2018, 6th Population Balance Modelling Conference, 7-9 May 2018, Ghent, Belgium.
2. **Traversari, G.,** Cincotti, A., "Modelling the osmotic behaviour of human mesenchymal stem cells", Symposium meeting "Extreme Cryo 2020. Survival of the Frozen: An Avalanche of Ideas in Cool Biomedical Research", 31st Jan-1st Feb 2020, University of Alberta, Edmonton (CANADA).

ABSTRACT

In this thesis the focus is on the analysis of two multiphase systems related to biomedical engineering and materials science. First the long-term preservation of human Mesenchymal Stem Cells (hMSCs) from Umbilical Cord Blood (UCB) is addressed from the experimental as well as theoretical perspectives, then the modeling of mechanical processing of powders by Ball Milling (BM) is investigated.

The first topic is related to the field of tissue engineering or regenerative medicine, where the ability of stem cells to differentiate into specialized cell lineages for the replacement of damaged or non-functional tissues or organs is exploited. In this specific research field, preservation is a core technology to bring cell-based products to market, as they have to be supplied on demand. The principal preservation method consists of freezing the bio-specimens to cryogenic temperature in order to take advantage of the preservative power of the cold, typically using liquid nitrogen at -196 °C. Indeed, compared to the other preservation methods currently available like maintaining the bio samples in continuous culture, cryopreservation has the benefits of affording long shelf lives, genetic stability, reduced microbial contamination risks, and cost effectiveness. The other side of the coin is that cryopreserved biological material can be damaged by the cryopreservation process itself, and the process needs to be optimized through mathematical modeling, since a huge number of operating conditions is involved. To this aim, in this work first the non-perfect osmometer behavior of the precious hMSCs from UCB is analyzed by developing a novel mathematical model where cell mechanics and membrane surface area regulation are coupled to osmosis. Comparisons with data are provided to fit adjustable parameters and model validation. Then, based on this novel theoretical approach the addition and removal phases of a permeant Cryo-Protectant Agent (CPA) like Dimethyl Sulfoxide (DMSO) during a cryopreservation protocol is studied: the possibility to account for both the cytotoxic effect and osmotic injury (i.e. expansion lysis) is successfully verified by comparisons to experimental measurements in contrast with the classic approach found in the literature, where the two phenomena are analyzed separately. Finally, in the framework of the activities of a funded H2020 research project, a mathematical model is proposed to guide and support the development of a long-term preservation of hMSCs through air-drying at room temperature and atmospheric pressure, in alternative to cryo-preservation. In fact, the latter one presents its own problems, like a relatively high maintenance costs for the continuous liquid nitrogen supply and a serious environmental impact, due to the industrial production of liquid nitrogen which leaves a massive carbon footprint.

Regarding the second topic investigated in this work, BM is an easy and versatile method to activate and drive a variety of chemical transformations. Traditionally, it has been used in powder mineralurgy and metallurgy to blend particulate solids, decrease their particle size, refine their microstructure and enhance their chemical reactivity. More recently, it has been applied to the synthesis of fine chemicals and the fabrication of functional materials, determining a significant progress in the preparation of pharmaceuticals, crystalline polymorphs, metal-organic frameworks and deep-eutectic solvents. In this work it is shown that,

once the milling dynamics has been relatively clarified, so that the frequency and energy of impacts are known, the coupling with a relatively simple stochastic model can provide significant insight into the mechanochemical kinetics. More specifically the hypothesis is that macroscopic kinetics can be related to local processes occurring on the microscopic scale based on a few assumptions concerning the volume of powder effectively processed during individual impacts and the stirring of powders during BM. Therefore, in this work first the propagation of mechanically activated self-sustaining reactions during the mechanical processing of powder in ball mills is investigated. By using a numerical model to reconstruct the dynamics of a single ball and powder particles inside a BM reactor, it is shown that the propagation is significantly affected by reaction rate in individual particles, other factors being less influential, and a strong coupling between the dynamics of powder particles and the reaction propagation is observed. Then the refinement of the lamellar structure in composite Ag-Cu particles during the early stages of mechanical processing is addressed: a statistical description of the kinetics of processes activated by ball milling coupled with the mathematical description of advection cycles induced by plastic deformation is developed to model system behavior. Finally, a kinetic model that, taking into account the intrinsic statistical nature of the mechanical processing of powders by ball milling, combines a phenomenological description of the rheological behavior of molecular solids with the chemistry of interface reactions is developed. The ultimate goal is to find alternative synthetic routes to fine chemicals and pharmaceuticals like mechanochemistry.

Chapter 1. Introduction

To design and control the complex processes of modern technology involving multi-phase systems, the use of a conceptual representation of the chemical-physical process is mandatory. In fact, given the considerable complexity of the real system, any developed model generally provides a faithful representation of only a few characteristic properties of the process at hand. As a matter of fact, the first model proposed is often simple but unrealistic. However, by analyzing the main defects, a new model can be built, which corrects the deficiencies of the previous one but possibly remaining still quite simple to manipulate. Therefore, several models are generally developed before finding one that satisfactorily represents those particular characteristics of the process that one has chosen to consider.

These models consist of a more or less complex system of mathematical equations that link together the variables of the process under examination based on first principles of conservation (matter, energy and momentum), statistical balances (population balances) or empirical. Although mathematical models allow a more complete description of a given system than other models, sometimes the complexity of their solution has been a limitation. However, nowadays, thanks to the remarkable technological progress of the computational capacity and the processing speed of modern personal computers, the numerical resolution of the systems of equations even of the most complex mathematical models is no longer a limitation.

The general strategy for the analysis of complex processes follows a well-defined path, consisting of the following steps:

- Formulation of the problem and definition of the objectives and evaluation criteria;
- Preliminary analysis and classification of the process to be divided into sub-systems (elements);
- Preliminary definition of the relationships between the various sub-systems;
- Analysis of variables and relationships to obtain a system of equations as simple and consistent as possible;
- Mathematical simulation: writing of the relationships between variables and parameters;
- Check on the goodness of representation of the real process by the model through direct comparison with appropriate experimental results;
- Application of the model: interpretation and understanding of modeling results.

One of the main premises of this strategy is that the entire process can be divided into different subsystems (elements) and that the mathematical relationships existing between these, once assembled together, can simulate the entire process. These subsystems do not necessarily have to correspond to a real subdivision of the process. In fact, the reason for this subdivision is linked to the complexity of the process, often difficult to understand and adequately describe as a whole. Instead, through an appropriate manipulation of these

subsystems, an attempt is made to obtain a reasonably reliable representation of the entire process, based on simple and well-known principles (or experimental evidence) applied to the various elements.
Following this general approach, in this thesis work the focus is on the analysis of two multiphase systems related to biomedical engineering and materials science: long-term preservation of hMSCs from UCB reported in Chapter 2 and mechanical processing of powders by Ball Milling (BM) described in Chapter 3.

1.1 Long-term preservation of hMSCs from UCB

The recent development of cell-based therapies has increased the need of available living cells on demand. Tissue engineering, gene therapy, and cellular implantation all rely on the ability to store and transport cells and tissues in order to be clinically successful [1]. hMSCs from UCB addressed in this thesis are no exception.

1.1.1 Mesenchymal Stem Cells form Umbilical Cord Blood

The ability to readily expand in culture while maintaining a self-renewing phenotype has made hMSCs a promising candidate for many cell-based therapies [2]. This cell line has an enormous therapeutic potential for regeneration and replacement of degenerated tissues: it can promote angiogenesis, regeneration, remodeling, immune cell activation or suppression, and cellular recruitment [2]. In particular, the adipogenic, chondrogenic and osteogenic differentiation of this specific cell lineage has been investigated by many authors, as well as the in vitro differentiation into cardiomyocytes, endothelial cells, and neuronal cells [3-4]. Figure 1.1 shows the multipotency of mesenchymal stem cells.

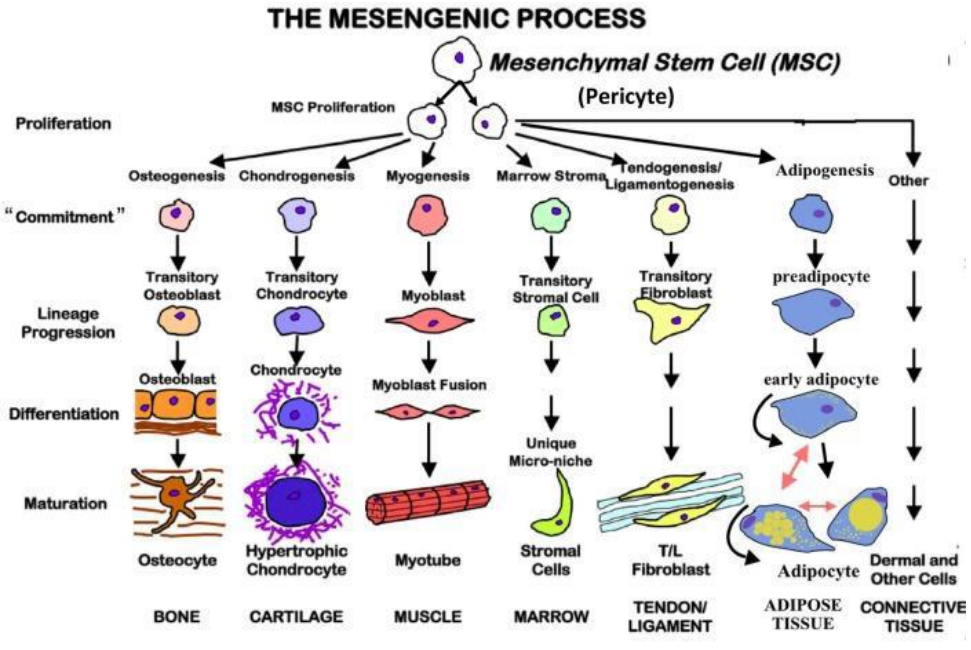

Figure 1.1: MSCs multipotency (from [2]).

In mammals, two main lines of stem cells can be distinguished [5]: embryonic stem cells (formed several days inside an egg after its fertilization), and non-embryonic stem cells (also known as adult stem cells, collected from other sources). These latter ones are further divided in hematopoietic cells (that differentiate into blood cells) and MSCs. Clearly, adult hMSCs do not raise ethical and legislative issues so that their use takes advantage of an increased likelihood for authority approval and public acceptance. They are typically derived from bone marrow [6]. However, due to the invasive nature of bone marrow aspiration, the identification of other sources has nowadays become a priority. In Figure 1.2 the main sources for collection of MSCs are shown.

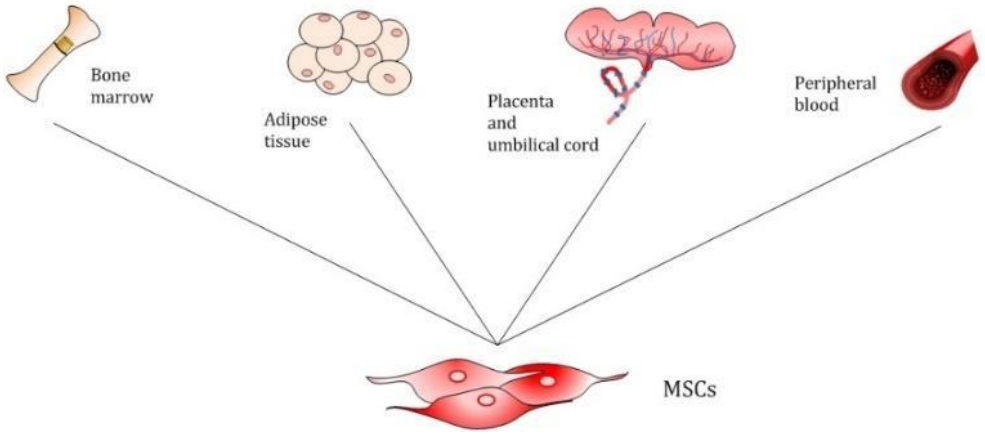

Figure 1.2: Main sources of MSCs (from [7]).

In particular fetal sources as UCB show an improved proliferation and differentiation potential, and longer life span due to the young age, if compared with adult sources such as bone marrow. This is because, proliferation and differentiation capability of stem cells decrease with age of the donor [8]. Furthermore, as donor age increases the availability of MSCs is reduced, as reported in Figure 1.3 [2].

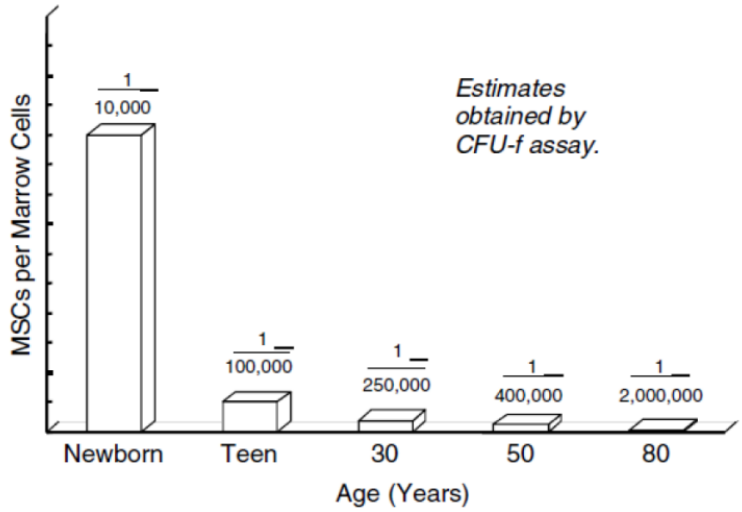

Figure 1.3: Dependence of number of MSCs from BM on total number of marrow cells with donor age (from [2]).

According to [9], several protocols for the cryopreservation of hMSCs are currently used, mainly derived from those developed and optimized for blood cells, with a huge range of CPA concentrations (typically DMSO), cooling and warming rates as well as equilibration times and temperatures. So far, no optimized cryo-preservation protocol has been developed for this cell lineage, since the corresponding osmotic behavior has not been investigated extensively.

1.1.2 Cryopreservation

Nowadays cryopreservation has achieved reasonable success in establishing protocols for preservation of cells and represents the principal technique for long-term preservation of biological material. Compared with other methods currently available to store cells and tissues, freezing to cryogenic temperatures has the benefits of affording long shelf lives, genetic stability, a limited risk of contamination during storage, and improved cost effectiveness [1]. Unfortunately, cryopreserved cells are damaged by the process itself [9]. Damage could result in a loss of viable or functional cells up to 50 % [11,12]. While such loss is acceptable for some cell lineages for research application, it becomes unacceptable in clinical practices, especially those involving hMSC from UCB, whose collection and isolation is known to be difficult [8]. In principle, cell expansion/proliferation may solve the problem, but an increased number of passages would inexorably make these cells lose their inherent features [13]. In addition, it would raise production costs and require approval from regulatory bodies. This pushes biopharmaceutical companies to develop optimized cryopreservation processes with reduced loss of viable cells.

Typically, cryo-preservation consists of three different steps (Figure 1.4): cooling to sub-zero temperatures with permeant or non-permeant CPAs, storage, thawing and return to physiological environment. Any of these steps can potentially lead to cell damage due to the physical and chemical phenomena involved such as cell shrinkage or swelling (i.e. excessive osmotic excursions), CPA cytotoxicity, intracellular ice or glass formation and disappearance [14].

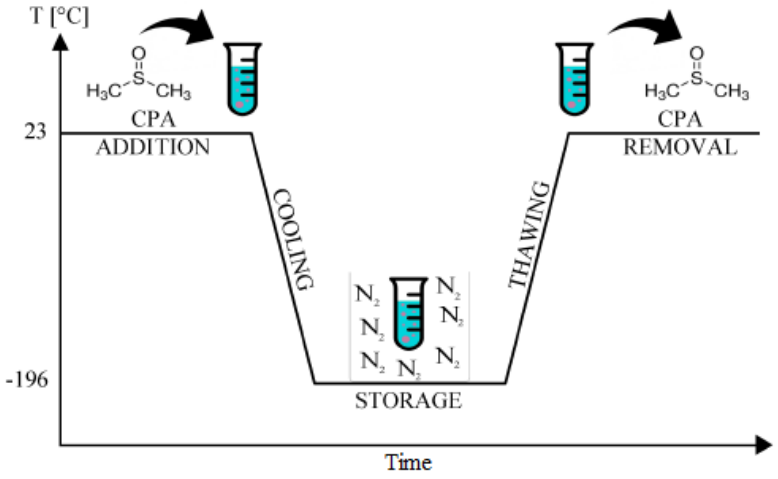

Figure 1.4: Stages of the cryopreservation process.

CPAs like DMSO are chemicals added to the medium containing cells to prevent damages from ice formation. These substances depress the freezing point of pure water and increase the viscosity of the solution. This means protection by reducing the occurrence of ice formation both thermodynamically and kinetically. The protecting action varies among different cell lineages according to the specific membrane permeability shown by a cell type to CPA [9]. However, despite their names CPAs may also cause injuries to cells due to cytotoxic effects and osmotic stresses. In particular, the last ones are related to the cell volume excursions due to water flux, taking place during CPA addition and removal which may result in a damaged cellular membrane [9].

Cooling and warming rates are also considered important factors, and cell fate after cryopreservation greatly depends on them [15]. During cooling, ice is first formed in the extracellular solution, as schematically depicted in Figure 1.5.

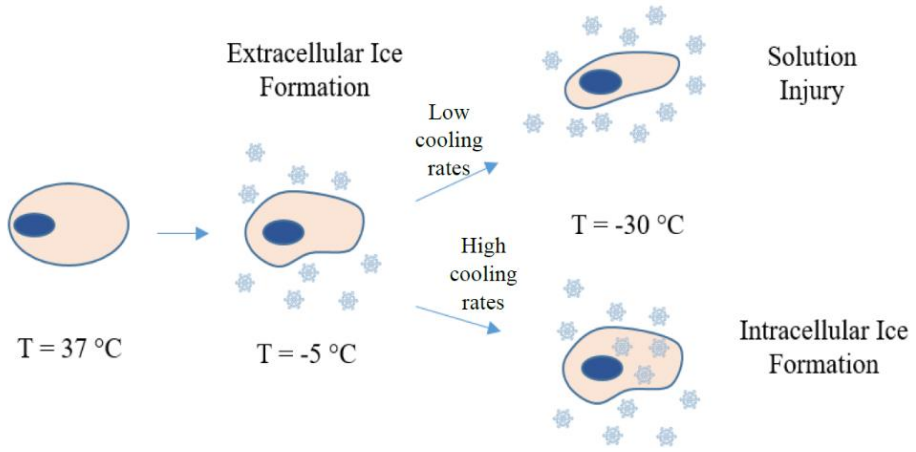

Figure 1.5: Two-factor Hypothesis by Mazur. Low cooling rates allow osmosis to take place reducing the intracellular water content. High cooling rates enhance intracellular ice formation hindering water efflux.

One of the unusual properties of water is a very strong solute rejection during ice crystal formation through nucleation and growth [16]: thus, extracellular osmolality increases due to water sequestration, and cells dehydrate (shrink) at a rate that depends on membrane permeability to water. This water efflux leads to an increased intracellular concentration of solutes, up to the osmotic equilibrium with the extracellular solution.

The intra- and extracellular concentrations of solutes continue to increase as temperature is lowered during the cooling phase and external ice formation proceeds. This goes on until the residual water in the intracellular liquid solution eventually solidifies as crystal ice or glass [16]. In any case, before reaching low temperatures, cells are exposed to relatively high, lethal concentration of electrolytes. This affects lipid-protein complexes, denatures macromolecules, decreases the size of unfrozen channels, and induces irreversible membrane fusion. These dangerous phenomena are collectively referred to solution injury in the cryopreservation field. Solution injury along with the lethal intracellular ice formation represent the two-factor hypothesis proposed by Mazur that mainly influence cells fate after cryopreservation, acting at low

and high cooling rates [14]. Indeed, by increasing the cooling rate, solution injury decreases since a limited osmosis may occur. However, more water is retained inside the cells, thus favoring intracellular ice formation (IIF), that damages cells and leads to their death.

Thus, an optimal cooling rate may be hypothesized as the best compromise between the solution effect and intracellular ice formation, as shown in Figure 1.6. This optimal cooling rate should vary from a cell lineage to another in principle, depending on the osmotic behavior of the cells under investigation, mainly on water permeability.

Thus, it is apparent that cryopreservation is a complex process where several physico-chemical and biological phenomena (namely osmosis, cytotoxicity, ice/glass formation and disappearance) occur in an interrelated manner depending on the operating conditions and system sizes and geometries.

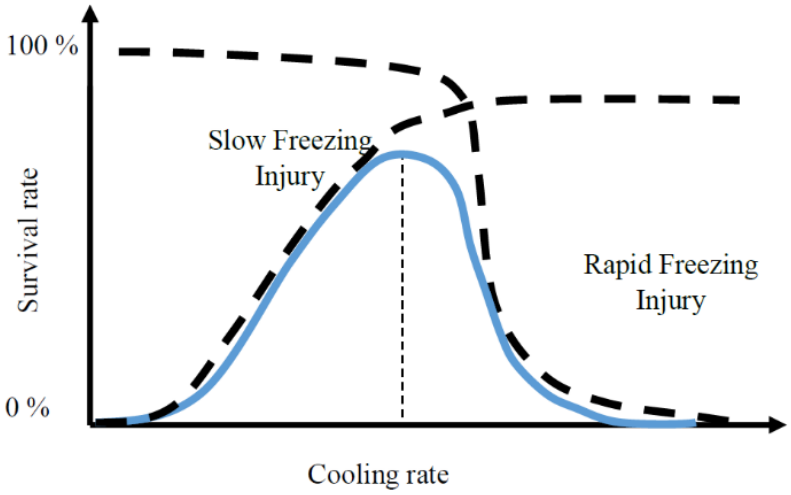

Figure 1.6: Optimal cooling rate (adapted from [17]).

To optimize a cryopreservation protocol in order to guarantee the highest percentage of cells survival, an experimental campaign aimed to determine the best cooling and warming rates as well as the strategy to add and remove CPAs (i.e. by choosing type, concentration, one-step or step-wise equilibration, duration and temperature) needs to be performed for every cell lineage with its specific osmotic behavior. However, the number of experimental variables and parameters is prohibitively large to permit a rigorous optimization [1]. On the other hand, best practices may be defined through mathematical modelling and numerical simulations [1]. At least, this allows to identify the most influential factors and reduce the experimental efforts, provided that the adopted mathematical model is valid and capable to describe the behavior of the system.

For this reason, Chapter 2 of this thesis work starts by developing a novel mathematical model for the description of the osmotic behavior during the cryopreservation of hMSCs from UCB. In cryopreservation the two-parameter formalism of perfect osmometer behavior is typically adopted and preferred due to its simplicity: according to this theoretical approach cell volume osmotic excursions are described as due only to the passive trans-membrane transport of water and permeant solutes such as CPAs; intracellular solutes, responsible of the isotonic osmolality, are assumed to be impermeant. Unfortunately, the application of the

two-parameter model fails to capture the osmotic response of hMSCs whenever a swelling phase is involved. To overcome this limitation, in this thesis the imperfect osmometer behavior of hMSCs is successfully modelled by improving the two-parameter formalism through the coupling of osmosis with cell mechanics and cell membrane Surface Area Regulation (SAR): now the transmembrane permeation of solutes (ions/salt) during the swelling phase through the temporary opening of mechanosensitive channels is allowed. This way cells can reach an equilibrium volume different from the initial isotonic one, when isotonic conditions are re-established after contact with impermeant or permeant solutes, such as sucrose or DMSO, respectively. The sequential best-fit procedure adopted to adjust model parameters is reported along with model validation through full predictions of system behavior.

Although this new model (called the SAR model) was conceived as a conservative development of the two-parameter formalism to avoid over-parameterization, a complex picture of the system emerges. To describe this, Chapter 2 of the thesis continues by reporting the insights into the description capability of non-perfect osmometer cells by means of the novel model. To this aim, first an appropriate non-dimensional version of the model equations is derived. Then, a parametric sweep analysis is performed and discussed to highlight the features of the SAR model in comparison with the two-parameter formalism: the conditions by which the first reduces to the second are identified. Only equilibrium equations with impermeant sucrose may be analytically derived from the model: their validity is here extended much more than originally assumed. When permeant DMSO comes into play, the temporary opening of mechanosensitive channels is difficult to predict and prevents the derivation of the equilibrium equations: in this case, a numerical integration of system dynamics up to steady state is required to determine the cell volume at equilibrium. It is concluded that cell volume at equilibrium depends on the position of the temporal window of mechanosensitive channels opening, which, in general, is a complex function of model parameters and operating conditions.

Later in Chapter 2, a combined analysis of osmotic injury and cytotoxic effect when hMSCs are contacted with DMSO is carried out from the experimental and theoretical perspectives. Experimentally, by means of a Coulter counter and flow-cytometer, a decrease of cell count and viability is measured when DMSO concentration, temperature and contact time increase. To interpret the data a novel mathematical model is developed and proposed, where the cell population is divided between viable and non-viable cells, and expansion lysis and cytotoxicity are described as two different reaction kinetics. This way, the need to set in advance the cell Osmotic Tolerance Limits (OTLs), as traditionally done in cryopreservation literature, is avoided. In particular, osmotic injury is described on the basis of the SAR model, by assuming that viable and non-viable cells burst during swelling when membrane tension increases above a critical value. On the other hand, the simultaneous cytotoxic effect of DMSO is described as a reaction kinetics from viable to non-viable cells. Comparisons to experimental data are provided by first performing a non-linear regression analysis (to evaluate unknown model parameters), then by predicting system behavior at operating conditions different from those used during the best-fit procedure, for model validation. It is found that the cytotoxic effect of DMSO to hMSCs is mild in comparison with other cell lineages, while expansion lysis is a very fast phenomenon for these cells. Thus, it is concluded that DMSO may be safely added in one step

without the need to design a complex step-wise procedure, provided that temperature is kept low during the operation and that contact time is strictly limited to the one necessary for osmotic equilibration. On the other hand, osmotic injury during the removal phase is extremely dangerous for cells and can be limited only by carefully avoiding excessive temporal increase of membrane stretching, i.e. by adopting a properly designed multi-step strategy, with cells suspended in a sequential series of washing solutions characterized by a decreased osmotic tonicity.

1.1.3 Air-drying at room temperature and atmospheric pressure

In the final section of Chapter 2, the identification of a valid alternative to cryo-storage for the long-term preservation of hMSCs is addressed. In fact, cryopreservation, although effective, presents several problems. These include high maintenance costs [18], need for specialized storage facilities, continuous LN supply, energy-dependency, safety concerns, and risk of pathogen transmission, all serious issues in clinical practice [19]. Besides these intrinsic problems, the industrial production of LN has a serious environmental impact too, leaving a massive carbon footprint. Hence, nowadays alternative options for cells storage are sought. These are typically based on water subtraction techniques from cell interior to induce reversible block of macromolecular interactions, allowing effective cells storage at non-cryogenic temperatures.

For instance, in the research project Drynet (GA No 734434 – Marie Skłodowska - Curie Actions, Research and Innovation Staff Exchange RISE, Call: H2020-MSCA-RISE-2015) the possibility to mimic mother nature where anhydrobiosis occurs for several vegetal and animal phyla is explored. In particular, anhydrobiosis allows seeds and small invertebrates like tardigrades survive long time spans (decades/centuries) in the absence of water [20], particularly thanks to the induced synthesis of sugars, as sucrose or trehalose which are called lyo-protectants for this reason. Thus, the research project Drynet aims to develop a cost-effective, ice-free process for long-term preservation of human cells and gametes, by checking the possibility to successfully store the cells by means of air-drying with trehalose at atmospheric pressure and room temperature. In the framework of the activities of the Drynet project, the development of a deterministic, mathematical model useful to guide and support the experiments on human cells air-drying is assigned to the research partner Università degli Studi di Cagliari. The results of this activity are shown and discussed in this thesis.

First an intense bibliographic search was carried out on mathematical modelling addressing the drying of animal cells. It was found that only the mathematical modelling of the freeze-drying process for non-living biomaterials (i.e. food) has been the subject of numerous studies, while living cells have never been accounted for by computational investigations, i.e. no modeling study focusing on preserving the viability of animal cells subjected to drying was found.

On the other hand, the role of sugar glass formation to effectively preserve living cells has been the topic of numerous experimental papers. A part from the speculations on the molecular mechanisms responsible of sugar glass capability to stabilize dried cells, a number of experimental works on drying protocols of animal

cells were proposed in the literature so far. Unfortunately, these protocols are significantly different in terms of operating conditions, geometries, cell lines and final result in terms of cell viability/functionality. For instance, the protocol developed by Zhang in 2010 [21] is based on the use of the freeze-drying process applied to a system containing hMSCs and trehalose. The viability of the cells after 12 hours from rehydration was reported as variable from 40% to 70%. On the other hand, in the freeze-drying protocol developed by Zhang in 2017 [22] applied to mouse fibroblasts with trehalose, cell viability was found virtually zero after 1 hour from rehydration. Gordon et al. [23] proposed an air-drying protocol for hMSCs with a mixture of trehalose and glycerol as lyoprotectants capable to reach a cell viability as high as 90% after 7 days from re-hydration. These extremely conflicting results in terms of viability reported in the literature are probably due to the adoption of different operating conditions and non-optimized system sizes and geometries. In this uncertainty and extreme variability of protocols and results, the orientation of a mathematical modelling activity is a difficult task. Nevertheless, even if this fragmentary and sometimes contradictory literature on the subject was found, a major conclusion may be safely taken: evaporation rate needs to be controlled in the air-drying process of living cells. In fact, from one side a sufficient but not excessive level of cell dehydration needs to be reached as pointed out by [24]. From the other side, an excessive evaporation rate has to be avoided during the air-drying process since it easily leads to the formation of a thin glassy film on top of the evaporating liquid surface, thus basically stopping cell dehydration before reaching the desired level [25,26]. This explains why the Japanese partner of the Drynet project, who is in charge of carrying out the experiments in a special lab desiccator unit with silica gel as water trap, uses to cover the liquid cell suspension to be dried with a lid not securely close [27,28]. However, it is easy to predict that by doing so the possibility to favor crystal formation of trehalose instead of sugar glass increases as evaporation rate decreases, depending on system sizes, geometries and operating conditions.

Therefore, in this work a general mathematical model capable to describe the air-drying process at room temperature and atmospheric pressure of hMSCs with trehalose sugar is developed. By referring to the desiccator unit of the Japanese partner of the Drynet project, the sequence of all the physico-chemical phenomena potentially involved in the process are accounted for in a compartmental model. More specifically, evaporation, cell osmosis, crystal or glass formation of trehalose sugar, water diffusion across the lid of the unsealed container of the cell suspension, and water adsorption onto porous medium are mathematically described by measuring the corresponding driving forces on the water+trehalose extended phase diagram and the other thermodynamic equilibria involved.

Given the absence of valuable data and the uncertainties related to the values assigned to model parameters, system sizes and geometries as well as operating conditions, the results of a parametric sensitivity analysis are shown in this work, starting from a base case. Generally speaking, a dynamic competition between evaporation and crystallization results from the simulations of the process. In fact, water evaporation can easily increase the trehalose concentration in the liquid phase so that solution viscosity rapidly increases leading to glass formation, with the desired desiccation level for an effective long-term preservation of the

suspended cells. However, an over-extended process duration results thus making the air-drying of cells economically unprofitable. On the other hand, if evaporation slows down too much, trehalose crystals instead of glass are formed, and the lyo-stability guaranteed by the sugar glass, is lost while an insufficient cell dehydration is achieved. This way an effective long-term preservation cannot be obtained, even if the duration of the process is reduced. The parametric sensitivity analysis performed in this work highlights the effect of system sizes and geometries on the competition between evaporation and crystallization rates, pointing out the crucial role played by diffusivity and its composition dependence in the liquid sample. It is concluded that, by varying system sizes and geometries as well as the operating conditions, the evaporation rate need to be optimized in order to reach an acceptable final cell viability (by favoring glass formation with a large cell dehydration) while reducing the duration of the air-drying process.

1.2 Mechanical processing of powders by Ball Milling (BM)

The mechanical processing of powders by ball milling (BM) is an easy and versatile method to activate and drive a variety of chemical transformations [29-30]. Traditionally, it has been used in powder mineralurgy and metallurgy to blend particulate solids, decrease their particle size, refine their microstructure and enhance their chemical reactivity [30-34]. Recently, it has been applied successfully to the synthesis of fine chemicals and the fabrication of functional materials. The renewed interest in the mechanical activation methods has determined a significant progress in the preparation of fine chemicals and pharmaceuticals [35-42], crystalline polymorphs [43-49], metal-organic frameworks and deep-eutectic solvents [50]. At present, mechanically activated reactions represent one of the areas of scientific investigation in organic and materials chemistry attracting more interest worldwide.

The interest in BM is partly justified by the simple working principles of ball mills and their scalability from lab to industrial scale. A ball mill is a mechanical device that includes a reactor that contains balls and materials to be processed. The reactor itself, or parts of it, undergo a periodic motion able to induce impacts between the balls and between the balls and the reactor walls [30-34,51]. During each impact, a small amount of powder is trapped between the milling tools and mechanically loaded at relatively high strain rates. Deformation processes of variable intensity and duration occur at the contact points between the trapped powder particles, generating intense mechanical stresses [52-53]. The mechanical stresses make the powder particles undergo compression and shearing [53], eventually resulting in severe mechanical deformation [29,32-33,54-55]. In turn, the solid phases can be effectively mixed on the microscopic scale, with formation of extended interfaces and enhancement of chemical reactivity [29,32-33,54-55].

The nature of the processed powders determines the nature and extent of the processes activated by impacts. In the case of powder mixtures of elemental metals, chemical effects are associated with microstructural refinement. In particular, forced mixing on the atomic scale can drive the mechanical alloying of the metals

[30-34]. Similarly, the effective mixing of chemicals on the molecular scale can give rise to physical and chemical changes in the case of inorganic and organic mixtures [56-58].

Physical and chemical changes depend on several factors. Among them, the powder charge inside the reactor, the number and size of milling balls, the frequency and energy of impacts, the processing temperature and the atmosphere inside the reactor [34]. Although processing parameters have not yet systematically investigated [30,59-62], it is the powder charge, number and size of balls, and frequency and energy of impacts that mostly affect the kinetics of mechanically activated reactions [63-80].

The fundamental knowledge concerning the way mechanochemical reactions take place on the microscopic scale is quite limited. This is mostly due to the lack of appropriate experimental methods to collect reliable kinetic data and of models to give the necessary interpretation.

In this regard, methodologies allowing real-time *in situ* monitoring based on X-ray diffraction [81-82], Raman spectroscopy [83-84] and their combination [85], promise to lead mechanochemistry to a decisive progress [34,86-91]. To this aim, a clear description of the milling dynamics inside the milling reactor is needed.

Generally speaking, in this work it is shown that, once the milling dynamics has been relatively clarified, so that the frequency and energy of impacts are known, a relatively simple stochastic model can provide significant insight into the mechanochemical kinetics [92-93]. Specifically, it is shown that macroscopic kinetics can be related to local processes occurring on the microscopic scale based on a few assumptions concerning the volume of powder effectively processed during individual impacts and the stirring of powders during BM.

Thus, Chapter 3 starts focusing on the propagation of mechanically activated self-sustaining reactions during the mechanical processing of powder in ball mills. A numerical model is used to reconstruct the dynamics of a single ball and powder particles inside the BM reactor under operational conditions. Taking advantage of the analytical description of the reactor swing, the equations of motion of ball and powder particles are solved numerically. The discrete element method is used to describe contacts between particles, ball and reactor walls. Reaction is ignited in an individual particle randomly selected among those compressed during an impact between ball and reactor. A simple kinetic law and a set of rules involving degree of chemical conversion and distance between particles are used to obtain a phenomenological description of the reaction propagation. It is shown that the propagation is significantly affected by reaction rate in individual particles, other factors being less influential. A strong coupling between the dynamics of powder particles and the reaction propagation is observed.

Then, Chapter 3 continues by addressing the refinement of the lamellar structure in composite Ag-Cu particles during the early stages of mechanical processing. In particular, the statistical description of the kinetics of processes activated by ball milling is combined with the mathematical description of advection cycles induced by plastic deformation. It is shown that the model curve satisfactorily best fits the experimental data obtained by suitably designed experiments.

Finally, the coupling of mixing and reaction in mechanochemical transformations is addressed at the end of Chapter 3. Driven by the promise of alternative synthetic routes to fine chemicals and pharmaceuticals, mechanochemistry is going through a period of intense growth. Mechanical forces are successfully utilized to activate chemical reactions involving an ever-growing variety of inorganic and organic substances with the aim of developing solvent-less processes to be used in the greener chemical industry of tomorrow. Down this path, the proper understanding of the relationships between processing variables, macroscopic transformation kinetics and microscopic chemistry represents one of the fundamental challenges to face. In this work, a kinetic model is developed by taking into account the intrinsic statistical nature of the mechanical processing of powders by ball milling and combining a phenomenological description of the rheological behavior of molecular solids with the chemistry of interface reactions. Specifically, discrete mixing maps are used to account for the co-deformation of molecular solids and the consequent increase of the interface area between initially segregated reactants. It is assumed that chemical reaction only occurs, with a certain probability, when reactants come into contact due to relocations induced by shearing. No diffusion is allowed. The systematic variation of the amount of powder involved in individual impacts, the composition of powder mixtures and the reaction probability at the interface provide a complete overview of the kinetic scenario. In particular, the different kinetic curves that can be originated from interface reaction are presented, pointing out how statistical, mixing and chemical factors affect the mechanochemical kinetics. Eventually, it is suggested how experimental findings can be used to gain information on the underlying mechanochemistry based on the outcomes of our kinetic modelling.

References of the Chapter 1

1. Fowler, A., Toner, M., (2005). Cryo-injury and biopreservation, in *Cell Injury: Mechanisms, Responses, and Repair*, Lee, R.C., Despa, F., Hamann, K.J., Editors, pp. 119-135. ISBN: 978-1-573-31617-0
2. Caplan, A., (2009). Why are MSCs therapeutic? New data: new insight. *J Pathol*, 217, pp. 318-324. https://doi.org/10.1002/path.2469
3. Hass, R., Kasper, C., Böhm, S., Jacobs, R., (2011). Different populations and sources of human mesenchymal stem cells (MSC): a comparison of adult and neonatal tissue-derived MSC, *Cell Commun Signal*, 9(12), pp. 1-14. https://doi.org/10.1186/1478-811X-9-12
4. Dimarino, A.M., Caplan, A.I., Bonfield, T.L., (2013). Mesenchymal stem cells in tissue repair, *Front Immunol*, 4, pp. 1-9. https://doi.org/10.3389/fimmu.2013.00201
5. Mafi, R., Hindocha, S., Mafi, P., Griffin, M., Khan, W.S., (2011). Sources of adult mesenchymal stem cells applicable for musculoskeletal applications - a systematic review of the literature. *Open Orthop J*, 5 Suppl 2, pp. 242-248. https://doi.org/10.2174/1874325001105010242
6. Friedenstein, A.J., Gorskaja, U.F., Kulagina, N.N., (1976). Fibroblast precursors in normal and irradiated mouse hematopoietic organs. *Exp Hematol*, 4(5), pp. 267-274. PMID: 976387.
7. Jossen, V., Pörtner, R., Kaiser, S.C., Kraume, M., Eibl, D., Eibl, R., (2014). Mass Production of Mesenchymal Stem Cells — Impact of Bioreactor Design and Flow Conditions on Proliferation and Differentiation, in *Cells and Biomaterials in Regenerative Medicine*, pp. 119-174. https://doi.org/10.5772/59385
8. Bieback, K., Kern, S., Klüter, H., Eichler, H., (2004). Critical parameters for the isolation of mesenchymal stem cells from umbilical cord blood, *Stem Cells*, 22, pp. 625-634. https://doi.org/10.1634/stemcells.22-4-625
9. Marquez-Curtis, L.A., Janowska-Wieczorek, A., McGann, L.E., Elliott, J.A.W., (2015). Mesenchymal stromal cells derived from various tissues: Biological, clinical and cryopreservation aspects. *Cryobiology*, 71(2), pp. 181-197. https://doi.org/10.1016/j.cryobiol.2015.07.003
10. Mazur, P., (2004). Principles of cryobiology. In: Fuller, B., Lane, N., Benson, E.E. (eds.) *Life in Frozen State*. CRC Press, London. ISBN-13 : 978-0415247009
11. Malpique, R., Ehrhart, F., Katsen-Globa, A., Zimmermann, H., Alves, P.M., (2009). Cryopreservation of adherent cells: strategies to improve cell viability and function after thawing. *Tissue Eng Part C Methods*, 15(3): pp. 373-386. https://doi.org/10.1089/ten.tec.2008.0410
12. Naaldijk, Y., Staude, M., Fedorova, V., Stolzing, A., (2012). Effect of different freezing rates during cryopreservation of rat mesenchymal stem cells using combinations of hydroxyethyl starch and dimethylsulfoxide. *BMC Biotechnol*, 12(49). https://doi.org/10.1186/1472-6750-12-49
13. Lee, M.W., Choi, J., Yang, M.S., Moon, Y.J., Park, J.S., Kim, H.C., Kim, Y.J., (2004). Mesenchymal stem cells from cryopreserved human umbilical cord blood. *Biochem Biophys Res Commun*, 320(1), pp. 273-278. https://doi.org/10.1016/j.bbrc.2004.04.206
14. Mazur, P., Leibo, S.P., Chu, E.H.Y., (1972). A two-factor hypothesis of freezing injury: Evidence from chinese-hamster tissue-culture cells, *Exp Cell Res*, 71, pp. 345-355. https://doi.org/10.1016/0014-4827(72)90303-5
15. Pegg, D.E., (2015). Principles of cryopreservation. *Methods Mol Biol*, 1257, pp. 3-19. https://doi.org/10.1007/978-1-4939-2193-5_1
16. Fowler, A., Toner, M., (2005). Cryo-injury and biopreservation, in *Cell Injury: Mechanisms, Responses, and Repair*, R.C. Lee, F. Despa, and K.J. Hamann, Editors., pp. 119-135.
17. Karlsson, J.O., Toner, M., (1996). Long-term storage of tissues by cryopreservation: critical issues, *Biomaterials*, 17, pp. 243-256. https://doi.org/10.1016/0142-9612(96)85562-1
18. Shevde, L.A., Riker, A.I., (2009). Current concepts in biobanking: Development and implementation of a tissue repository. *Front Biosci* (Schol Ed) 1, pp. 188-193. https://doi.org/10.2741/s18
19. Fountain, D., Ralston, M., Higins, N., Gorlin, J.B., Uhl, L., Wheeler, C., Antin, J.H., Churchill, W.H., Benjamin, R.J., (1997). Liquid nitrogen freezers: a potential source of microbial contamination o hematopoietic stem cell components. *Transfusion*, 37, pp. 585-591. https://doi.org/10.1046/j.1537-2995.1997.37697335152.x

20. Hand, S.C., Menze, M.A., Toner, M., Boswell, L., Moore, D., (2011). LEA proteins during water stress: Not just for plants anymore. *Annu Rev Physiol*, 73, pp. 115-134. https://doi.org/10.1146/annurev-physiol-012110-142203
21. Zhang, S., Qian, H., Wang, Z., Fan, J., Zhou, Q., Chen, G., Li, R., Fu, S., Sun, J., (2010). Preliminary study on the freeze-drying of human bone marrow-derived mesenchymal stem cells, *J Zhejiang Univ-Sci B (Biomed & Biotechnol)*, 11(11), pp. 889-894. https://doi.org/10.1631/jzus.B1000184
22. Zhang, M., Oldenhof, H., Sydykov, B., Bigalk, J., Sieme, H., Wolkers, W.F., (2017). Freeze-drying of mammalian cells using trehalose: preservation of DNA integrity, *Sci Rep*, 7, ID 6198. https://doi.org/10.1038/s41598-017-06542-z
23. Gordon, S.L., Oppenheimer, S.R., Mackay, A.M., Brunnabend, J., Puhlev, I., Levine, F., (2001). Recovery of Human Mesenchymal Stem Cells Following Dehydration and Rehydration, *Cryobiology*, 43(2), pp. 182-187. https://doi.org/10.1006/cryo.2001.2361
24. Aksan, A., Toner, M., (2004). Isothermal Desiccation and Vitrification Kinetics of Trehalose−Dextran Solutions. *Langmuir*, 20(13), pp. 5521-5529. https://doi.org/10.1021/la0355186
25. Aksan, A., Irimia, D., He, X., Toner, M., (2006). Desiccation kinetics of biopreservation solutions in microchannels. *J Appl Phys*, 99(6), ID 2181280. https://doi.org/10.1063/1.2181280
26. He, X., Fowler, A., Menze, M., Hand, S., Toner, M., (2008). Desiccation Kinetics and Biothermodynamics of Glass Forming Trehalose Solutions in Thin Films. *Ann Biomed Eng*, 36, ID 1428. https://doi.org/10.1007/s10439-008-9518-8
27. Watanabe, K., Imanishi, S., Akiduki, G., Cornette, R., Okuda, T. (2016). Air-dried cells from the anhydrobiotic insect, Polypedilum vanderplanki, can survive long term preservation at room temperature and retain proliferation potential after rehydration, *Cryobiology*, 73, pp. 93-98. https://doi.org/10.1016/j.cryobiol.2016.05.006
28. Kikuta, S., Watanabe, S.J., Sato, R., Gusev, O., Nesmelov, A., Sogame, Y., Cornette, R., Kikawada, T., (2017). Towards water-free biobanks: long-term dry-preservation at room temperature of desiccation-sensitive enzyme luciferase in air-dried insect cells. *Sci Rep*, 7, ID 6540. https://doi.org/10.1038/s41598-017-06945-y
29. James, S.L., Adams, C.J., Bolm, C., Braga, D., Collier, P., Friscic, T., Grepioni, F., Harris, K.D.M., Hyett, G., Jones, W., Krebs, A., Mack, J., Maini, L. Orpen, A.G., Parkin, I.P., Shearouse, W.C., Steed, J.W., Waddell, D.C., (2012). Mechanochemistry: opportunities for new and cleaner synthesis, *Chem Soc Rev*, 41, pp. 413- 447. https://doi.org/10.1039/C1CS15171A
30. Hernàndez, J.G., Bolm, C., (2017). Altering Product Selectivity by Mechanochemistry, *J Org Chem*, 82, pp. 4007-4019. https://doi.org/10.1021/acs.joc.6b02887
31. Sopicka-Lizer, M., editor. (2010). *High-Energy Ball Milling. Mechanochemical Processing of Nanopowders*, Cambridge (UK), Woodhead Publishing. ISBN 978-1-84569-531-6
32. Delogu, F., Mulas G., editors. (2010). *Experimental and Theoretical Studies in Modern Mechanochemistry*. Kerala (India), Transworld Research Network. ISBN: 978-81-7895-454-7
33. Baláž, P., Achimovičová, M., Baláž, M., Billik, P., Cherkezova-Zheleva, Z., Criado, J.M., Delogu, F., Dutková, E., Gaffet, E., Gotor, F.J., Kumar, R., Mitov, I., Rojac, T., Senna, M., Streletskiikl A., Wieczorek-Ciurowa, K., (2013). Hallmarks of mechanochemistry: from nanoparticles to technology. *Chem Soc Rev*, 42, pp. 7571-7637. https://doi.org/10.1039/C3CS35468G
34. Suryanarayana, C., (2001). Mechanical alloying and milling, *Prog Mater Sci*, 46, pp. 1-184. https://doi.org/10.1016/S0079-6425(99)00010-9
35. Braga, D., Maini, L., Grepioni, F., (2013). Mechanochemical preparation of co-crystals, *Chem Soc Rev*, 42, pp. 7638-7648. https://doi.org/10.1039/C3CS60014A
36. Friščić, T., Jones, W., (2009). Recent Advances in Understanding the Mechanism of Co-crystal Formation via Grinding, *Cryst Growth Des*, 9, pp. 1621-1637. https://doi.org/10.1021/cg800764n
37. Aakeröy, C., (2015). Is there any point in making co-crystals?, *Acta Crystallogr Sect. B*, 71, pp. 387-391. https://doi.org/10.1107/S2052520615010872
38. Halasz, I., Puskaric, A., Kimber, S.A.J., Beldon, P.J., Belenguer, A.M., Adams, F., Honkimaki, V., Dinnebier, R.E., Patel, B., Jones, W., Strukil, V., Friščić, T., (2013). Real-Time In Situ Powder X-ray Diffraction Monitoring of Mechanochemical Synthesis of Pharmaceutical Cocrystals, *Angew Chem Int Ed*, 52, pp. 11538-11541. https://doi.org/10.1002/anie.201305928

39. Corpinot, M.K., Stratford, S.A., Arhangelskis, M., Anka-Lufford, J., Halasz, I., Judas, N., Jones, W., Bucar, D.-K., (2016). On the predictability of supramolecular interactions in molecular cocrystals - the view from the bench, *Cryst Eng Comm*, 18, pp. 5434-5439. https://doi.org/10.1039/C6CE00293E
40. Dhumal, R.S., Kelly, A.L., York, P., Coates, P.D., Paradkar, A., (2010). Cocrystalization and simultaneous agglomeration using hot melt extrusion, *Pharm Res*, 27, pp. 2725-2733. https://doi.org/10.1007/s11095-010-0273-9
41. Medina, C., Daurio, D., Nagapudi, K., Alvarez-Nunez, F., (2010). Manufacture of pharmaceutical co-crystals using twin screw extrusion: a solvent-less and scalable process, *J Pharm Sci*, 99, pp. 1693-1696. https://doi.org/10.1002/jps.21942
42. Daurio, D., Nagapudi, K., Li, L., Quan, P., Nunez, F.A., (2014). Application of twin screw extrusion to the manufacture of cocrystals: scale-up of AMG 517-sorbic acid cocrystal production, *Faraday Discuss*, 170, pp. 235-249. https://doi.org/10.1039/C3FD00153A
43. Aitipamula, S., Chow, P., Tan, R.B.H., (2014). Polymorphism in cocrystals: a review and assessment of its significance, *Cryst Eng Comm*, 16, pp. 3451-3465. https://doi.org/10.1039/C3CE42008F
44. Losev, E., Boldyreva, E., (2014). The role of a liquid in "dry" co-grinding: a case study of the effect of water on mechanochemical synthesis in a "L-serine–oxalic acid" system, *Cryst Eng Comm*, 16, pp. 3857-3866. https://doi.org/10.1039/C3CE42321B
45. Fischer, F., Scholz, G., Benemann, S., Rademann, K., Emmerling, F., (2014). Evaluation of the formation pathways of cocrystal polymorphs in liquid-assisted syntheses, *Cryst Eng Comm*, 16, pp. 8272-8278. https://doi.org/10.1039/C4CE00472H
46. Belenguer, A.M., Lampronti, G.I., Cruz-Cabeza, A.J., Hunter, C.A., Sanders, J.K.M., (2016). Solvation and surface effects on polymorph stabilities at the nanoscale, *Chem Sci*, 7, pp. 6617-6627. https://doi.org/10.1039/C6SC03457H
47. Trask, A.V., Shan, N., Motherwell, W.D.S., Jones, W., Feng, S., Tan, R.B.H., Carpenter, K.J., (2005). Selective polymorph transformation *via* solvent-drop grinding, *Chem Commun*, pp. 880-882. https://doi.org/10.1039/B416980H
48. Hasa, D., Miniussi, E., Jones, W., (2016). Mechanochemical Synthesis of Multicomponent Crystals: One Liquid for One Polymorph? A Myth to Dispel, *Cryst Growth Des*, 16, pp. 4582-4588. https://doi.org/10.1021/acs.cgd.6b00682
49. Fischer, F., Heidrich, A., Greiser, S., Benemann, S., Rademann, K., Emmerling, F., (2016). Polymorphism of Mechanochemically Synthesized Cocrystals: A Case Study, *Cryst Growth Des*, 16, pp. 1701-1707. https://doi.org/10.1021/acs.cgd.5b01776
50. Crawford, D.E., Miskimmin, C.K.G., Albadarin, A.B., Walker, G., James, S.L., (2017). Organic synthesis by Twin Screw Extrusion (TSE): continuous, scalable and solvent-free, *Green Chem*, 19, pp. 1507-1514. https://doi.org/10.1039/C6GC03413F
51. Balaz, P., (2008). *Mechanochemistry in Nanoscience and Minerals Engineering*, Springer-Verlag Berlin Heidelberg, Berlin. ISBN 978-3-540-74855-7
52. Martin, C., Bouvard, D., Shima, S., (2003). Study of particle rearrangement during powder compaction by the Discrete Element Method, *J Mech Phys Solids*, 51, pp. 667-693. https://doi.org/10.1016/S0022-5096(02)00101-1
53. Delogu, F., (2008). A combined experimental and numerical approach to the kinetics of mechanically induced phase transformations, *Acta Mater*, 56, pp. 905–9012. https://doi.org/10.1016/j.actamat.2007.10.041
54. Stolle, A., Szuppa, T., Leonhardt, S.E.S., Ondruschka, B., (2011). Ball milling in organic synthesis: solutions and challenges, Chem. Soc. Rev., 40, pp. 2317-2329. https://doi.org/10.1039/C0CS00195C
55. Wang, G.-W., (2013). Mechanochemical organic synthesis, *Chem Soc Rev*, 42, pp. 7668-7700. https://doi.org/10.1039/C3CS35526H
56. Stolle, A., Ranu, B., (Eds.), (2015). *Ball Milling Towards Green Synthesis: Applications, Projects, Challenges*; RSC Green Chemistry Series, Cambridge (UK). PDF eISBN: 978-1-78262-198-0
57. *Mechanochemistry: From Functional Solids to Single Molecules*. Faraday Discuss. 170, RSC, Cambridge (UK), 2014. ISBN: 978-1-78262-170-6
58. Margetic, D., Strukil, V., (2016). *Mechanochemical Organic Synthesis*, Elsevier, New York. https://doi.org/10.1016/C2014-0-01621-8
59. Soni, P.R., (1998). *Mechanical alloying: fundamentals and applications*, Cambridge International Science Publishing, Cambridge (UK). ISBN 1 898326568

60. Lu, L., Lai, M.O., (1998). *Mechanical alloying*, Springer, Boston (MA), 1998. ISBN-10 0792380665
61. Chattopadhyay, P.P., Manna, I., Talapatra, S., Pabi, S.K., (2001). A mathematical analysis of milling mechanics in a planetary ball mill, *Mater Chem Phys*, 68, pp. 85-94. https://doi.org/10.1016/S0254-0584(00)00289-3
62. Venkataraman, S.K., Narayanan, K.S., (1998). Energetics of collision between grinding media in ball mills and mechanochemical effects, *Powder Technol.*, 96, pp. 190-201. https://doi.org/10.1016/S0032-5910(97)03368-8
63. Butyagin, P.Y., (1989). *Active states in mechanochemical reactions*, Harwood Academic Publishers, London. ISBN: 9783718649877
64. Burgio, N., Iasonna, A., Magini, M., Martelli, S., Padella, F., (1991). Mechanical alloying of the Fe–Zr system. Correlation between input energy and end products, Nuovo Cim. D, 13, pp. 459-476. https://doi.org/10.1007/BF02452130
65. Gaffet, E., Yousfi, L., (1995). Crystal to non-equilibrium phase transition induced by ball-milling, *Mater Sci Forum*, 90, pp. 51-58. https://doi.org/10.4028/www.scientific.net/MSF.88-90.51
66. Abdellaoui, M., Gaffet, E., (1995). The physics of mechanical alloying in a planetary ball mill: mathematical treatment, *Acta Metall Mater*, 43, pp. 1087-1098. https://doi.org/10.1016/0956-7151(95)92625-7
67. Le Brun, P., Froyen, L., Delaey, L., (1993). The modelling of the mechanical alloying process in a planetary ball mill: comparison between theory and in-situ observations, *Mater Sci Eng A*, 161, pp. 75-82. https://doi.org/10.1016/0921-5093(93)90477-V
68. Magini, M., Iasonna, A., Padella, F., (1996). Ball milling: an experimental support to the energy transfer evaluated by the collision model, *Scripta Mater*, 34, pp. 13-19. https://doi.org/10.1016/1359-6462(95)00465-3
69. Y., Chen, M., Bibole, R., Le Hazif, G., Martin, (1993). Ball-milling-induced amorphization in Ni_xZr_y compounds: a parametric study, *Phys Rev B*, 48, pp. 14-21. https://doi.org/10.1103/physrevb.48.14
70. Pochet, P., Tominez, E., Chaffron, L., Martin, G., (1995). Order-disorder transformation in Fe-Al under ball milling, *Phys Rev B*, 52, pp. 4006-4016. https://doi.org/10.1103/PhysRevB.52.4006
71. Mio, H., Kano, J., Saito, F., Kaneko, K., (2002). Effects of rotational direction and rotation-to-revolution speed ratio in planetary ball milling, *Mater Sci Eng A*, 332, pp. 75-80. https://doi.org/10.1016/S0921-5093(01)01718-X
72. Mio, H., Kano, J., Saito, F., Kaneko, K., (2004). Optimum revolution and rotational directions and their speeds in planetary ball milling, *Int J Miner Process*, 74, pp. S85-S92. https://doi.org/10.1016/j.minpro.2004.07.002
73. Feng, Y.T., Han, K., Owen, D.R.J., (2004). Discrete element simulation of the dynamics of high energy planetary ball milling processes, *Mater Sci Eng A*, 375-377, pp. 815-819. https://doi.org/10.1016/j.msea.2003.10.162
74. Kakuk, G., Zsoldos, I., Csanády, A., Oldal, I., (2009). Contributions to the modelling of the milling process in a planetary ball mill, *Rev Adv Mater Sci*, 22, pp. 21-38. http://www.ipme.ru/e-journals/RAMS/no_12209/kakuk.pdf
75. Jiang, X., Trunov, M.A., Schoenitz, M., Dave, R.N., Dreizin, E.L., (2009). Mechanical alloying and reactive milling in a high energy planetary mill, *J Alloys Compd*, 478, pp. 246-251. https://doi.org/10.1016/j.jallcom.2008.12.021
76. Huang, H., Pan, J., McCormick, P.G., (1997). On the dynamics of mechanical milling in a vibratory mill, *Mater Sci Eng A*, 232, pp. 55-62. https://doi.org/10.1016/S0921-5093(97)00084-1
77. Cocco, G., Delogu, F., Monagheddu, M., Mulas, G., Schiffini, L., (2000). Impact characteristics and mechanical alloying processes by ball milling: experimental evaluation and modelling outcomes, *Int J Non-E*, 11(3), pp. 235-269.
78. Streletskii, A.N., Courtney, T.H., (2000). Kinetic, chemical and mechanical factors affecting mechanical alloying of Ni-bcc transition metal mixtures, *Mater Sci Eng A*, 282, pp. 213-222. https://doi.org/10.1016/S0921-5093(99)00766-2
79. Cocco, G., Delogu, F., Schiffini, L., (2000). Toward a quantitative understanding of the mechanical alloying process, *J Mater Synth Proc*, 8, pp. 167-180. https://doi.org/10.1023/A:1011308025376
80. Delogu, F., Schiffini, L., Cocco, G., (2001). The invariant laws of the amorphization processes by mechanical alloying, *Philos Mag A*, 81, pp. 1917-1937. https://doi.org/10.1080/01418610010019107

81. Friščić, T., Halasz, I., Beldon, P.A., Belenguer, A.M., Adams, F., Kimber, S.A.J., Honkimäki, V., Dinnebier, R.E., (2013). Real-time and in situ monitoring of mechanochemical milling reactions, *Nat Chem*, 5, pp. 66-73. https://doi.org/10.1038/nchem.1505
82. Halasz, I., Friščić, T., Kimber, S.A.J., Užarević, K., Puškarić, A., Mottillo, C., Julien, P., Štrukil, V., Honkimäki, V., Dinnebier R.E., (2014). Quantitative in situ and real-time monitoring of mechanochemical reactions, *Faraday Discuss*, 170, pp. 203-221. https://doi.org/10.1039/C4FD00013G
83. Juribašić, M., Užarević, K., Gracin, D., Curić, M., (2014). Mechanochemical C-H bond activation: rapid and regioselective double cyclopalladation monitored by in situ Raman spectroscopy, *Chem Commun*, 50, pp. 10287-10290. https://doi.org/10.1039/C4CC04423A
84. Gracin, D., Strukil, V., Friščić, T., Halasz, I., Užarević, K., (2014). Laboratory Real-Time and In Situ Monitoring of Mechanochemical Milling Reactions by Raman Spectroscopy, *Angew Chem Int Ed*, 53, pp. 6193-6197. https://doi.org/10.1002/anie.201402334
85. Batzdorf, L., Fischer, F., Wilke, M., Wenzel, K.J., Emmerling, F., (2015). Direct In Situ Investigation of Milling Reactions Using Combined X-ray Diffraction and Raman Spectroscopy, *Angew Chem Int Ed*, 54, pp. 1799-1802. https://doi.org/10.1002/anie.201409834
86. Boldyrev, V.V., (1990). Mechanochemistry and mechanical activation of solids, *Russian Chem Bull*, 39, pp. 2029-2044. https://doi.org/10.1016/0167-2738(93)90157-X
87. Gilman, J.J., (1996). Mechanochemistry, *Science*, 274, pp. 65-68. https://doi.org/10.1126/science.274.5284.65
88. Gutman, E.M., (1998). *Mechanochemistry of Materials*, Cambridge International Science Publishing, Cambridge. https://doi.org/10.1039/9781782623885
89. Heinicke, G., (1984). *Tribochemistry*, Akademie Verlag, Berlin.
90. Delogu, F., Mulas, G., (2010). *Experimental and Theoretical Studies in Modern Mechanochemistry*, Transworld Research Network, Kerala. ISBN-10 : 8178954540
91. Butyagin, P. Y., (1971). Kinetics and Nature of Mechanochemical Reactions, *Usp. Khim.*, 40(11), pp. 1935-1959. https://doi.org/10.1070/RC1971v040n11ABEH001982
92. Napolitano, E., Mulas, G., Enzo, S., Delogu, F., (2000). Kinetics of mechanically induced anatase-to-rutile phase transformation under inelastic impact conditions, *Acta Mater*, 58, pp. 3798-3804. https://doi.org/10.1016/j.actamat.2010.03.024
93. Delogu, F., Cocco, G., (2000), Relating single-impact events to macrokinetic features in mechanical alloying processes, *J Mater Synth Process*, 8, pp. 271-277. https://doi.org/10.1023/A:1011382008963

Chapter 2. Long-term preservation of hMSCs from UCB

2.1 Modelling the Osmotic Behaviour of Human Mesenchymal Stem Cells

2.1.1 Introduction

Human Mesenchymal Stem Cells (hMSCs) are considered a promising candidate for the regeneration and replacement of degenerated tissues [1]: adipogenic, chondrogenic and osteogenic differentiation is well acknowledged in the literature and has been investigated by many groups, as well as *in vitro* differentiation into cardiomyocytes, endothelial cells, and neuronal cells [2,3]. hMSCs are primarily collected by means of bone marrow aspiration, which is a painful and invasive procedure. For this reason, other sources such as Umbilical Cord Blood (UCB) need to be identified. Moreover, since proliferation and differentiation capabilities decrease with the age of donors [4], hMSCs from UCB show an improved proliferation and differentiation potential, and longer life span when compared to hMSCs from bone marrow of adults. On the other hand, isolation and collection of hMSCs from UCB has been reported to be difficult [4-7], and with uncertain results [8]. Thus, the preservation of these cells must guarantee the highest level of cell viability and functionality to enable effective tissue regeneration.

Currently, the most widely used method is cryopreservation which consists in maintaining cells at very low sub-zero temperatures (about -196 °C). The methodology involves several physico-chemical phenomena taking place during the osmotic equilibration with a cryo-protectant agent (CPA) and its removal, as well as the cooling and thawing phases: cell osmotic response to the contact with CPAs and their cytotoxicity, intracellular ice or glass formation and disappearance. These phenomena are strictly interrelated and depend on the working conditions. Physicochemical changes in cells often lead to a decrease in their viability and functionality [9-10]. In this context, the optimization of operating conditions is crucial. However, the number of experimental variables and parameters is too large to permit any systematic exploration of experimental processing conditions. Rather, beneficial clues to best practices in cryopreservation can be obtained by numerical simulation [10], which allows the identification of most influential factors and a drastic reduction of experimental efforts provided the validity of the model can be ascertained in the range of conditions of interest.

Our recent experimental investigations of the osmotic behavior of hMSCs from UCB [6-7] revealed that these cells do not behave as perfect osmometers. Experimental findings indicate that positive cell volume excursions are limited during both the shrink-swell process following DMSO addition, and the restoration of isotonic conditions after the contact with hypertonic solutions of impermeant solutes (here called osmotic cycle with sucrose). On the other hand, when restoring the isotonic conditions following DMSO addition (here called osmotic cycle with DMSO), cell volume attains a final, equilibrium value that is different from the initial,

isotonic one, depending on system temperature. Actually, this limited recovery of the initial isotonic volume of the cells varies not only with temperature but also with solutes concentrations and the number of osmotic cycles, since hysteretic phenomena were also observed.

In the field of cryopreservation, the two-parameter [11] or the Kedem and Katchalsky formalisms [12] are the two models typically adopted to interpret the osmotic behavior of cells. They share the same basic assumption: the content of intracellular solutes responsible of the isotonic osmolality remains constant with time, since they are assumed to be impermeant through cell membrane (i.e. implying perfect osmometer behavior). Water and permeant CPAs are merely described through passive diffusion transport mechanisms through cell membrane between ideal liquid solutions, albeit in the Kedem and Katchalsky formalism coupled diffusion is taken into account by the reflection coefficient, whereas it is independent in the two-parameter model. As a consequence, even though they differ in the dynamics followed to establish osmotic equilibrium between intra- and extracellular compartments, the two approaches share the same driving forces of material transport, and, consequently, the same equilibrium points. The locus of equilibrium cell volume is represented by the Boyle Van't Hoff plot. Accordingly, at isotonic conditions cells necessarily return to isotonic osmolality and to their original isotonic volume regardless of the osmotic path and volume excursion followed previously. It is worth noting that the two-parameter formalism is typically preferred to that of Kedem and Katchalsky due to its simplicity and the high selectivity of aquaporins, which exclude co-transport of water and CPA through the same channels.

Therefore, it is not surprising that iterative re-fitting of data is necessary to follow the osmotic response of hMSCs from UCB when the two-parameter model is adopted [6-7]. This means that estimates of model parameters vary depending on conditions while they are supposed to remain unchanged. This certainly greatly diminishes the model's predictive capability and the significance of inferred parameter values. This in turn leads to unrealistic model artefacts, most notably to an apparent increase of the inactive volume fraction (i.e. the volume of organelles, proteins and other macromolecules that remains constant regardless of osmotic conditions; see below) depending on system temperature as well as solutes concentration, and number of osmotic cycles [6-7].

Besides, removing the assumption of ideal, dilute solutions thus following the approach developed by Elliott and co-workers [13-14], would not solve the problem: with the thermodynamics of non-ideal solutions embedded into the two-parameter formalism, cells would keep returning to isotonic osmolality and to their original isotonic volume when isotonic conditions are re-established after an osmotic cycle with sucrose or DMSO, albeit not in a completely linear fashion in the Boyle Van't Hoff plot. Similarly, by accounting for the concentration dependence of the cell permeability to cryoprotectant and water in the framework of the two-parameter model, only the kinetics followed in the osmotic excursion would be affected.

According to the biophysics and physiology literature, a much more complex picture than the one usually considered in cryopreservation studies with the two-parameter model emerges for the control of cell volume and shape [15-19]: in principle, the combined effect of mechanics (hydrostatics, active membrane contractility, membrane and cortical tension, cytoskeleton and its adhesion to membrane), electrical and chemical potentials

(Gibbs-Donnan equilibrium, water and ion flows through passive and active channels) should all be taken into account to explain the osmotic response of a cell population, and the regulation of its surface area with membrane folds and blebs by means of exo- and endocytosis.

In particular, the pump-leak concept (i.e. an active influx of ions balanced, to preserve electro-neutrality, by a passive leak in the opposite direction) is well recognized as playing a role in the Regulatory Volume Decrease/Increase (RVD/I) following osmotic shocks, in combination with the folding/unfolding of cell membrane [15-18]. The choice to address the trans-membrane exchange of electro-neutral chemical species as ions/salt was made on purpose in order to avoid the description of the coupling between electro-magnetic field and mass diffusion used in the well-known pump and leak physiological model (PLM) [20-21]. On the other hand, the PLM involves active mechanisms such as ion pumps which consume energy. For this reason, these mechanisms are considered only for long-term regulation of cell volume but are typically neglected in cryopreservation where only relatively short-term responses are taken into account.

An increasing number of theoretical and experimental articles describe the cell SAR through variations of membrane tension and its relaxation mechanisms: microvilli and caveolae act as membrane reservoirs or sinks capable of quickly accommodating sudden mechanical stresses by exchanging part of the lipid bilayer with the main membrane in order to maintain tension homeostasis [22-25]. On the other hand, only a limited number of studies linking ion channels and cell osmotic regulation with cell mechanics are found in the literature [17,23].

Unfortunately, a quantitative understanding of the whole picture is still lacking, and a general model embedding all the phenomena described above is not yet available. On the other hand, a comprehensive mechanistic model may prove to be overparameterized, which may preclude its validation and a reliable determination of its parameter values. Moreover, when considered in the framework of the whole cryopreservation process, such a model would describe only the osmotic behavior of the cells while the cytotoxicity and ice/glass formation would still be left out. A further addition of these aspects to the model would likely render it intractable.

On the basis of these considerations, in this work the imperfect osmometer behavior of hMSCs is modelled and discussed as a conservative development of the two-parameter formalism: the idea is to minimize the increase in complexity compared with the widely adopted theoretical approach in cryopreservation to reasonably interpret the peculiar osmotic behavior of hMSCs. The novel model proposed here couples osmosis with cell mechanics and cell membrane SAR. The adopted fitting procedure is reported along with a validation of model's predictive power as well as an analysis of osmotic equilibrium conditions when contacting cells with impermeant solutes.

2.1.2 Model Equations

The failure of the two-parameter model to interpret the osmosis of hMSCs [6-7] prompted us to develop a new, improved model. In particular, the apparent increase in the inactive volume fraction needed to successfully fit the swelling phase of the osmotic cycle with impermeant sucrose using the two-parameter model, means that

less cytosol (water and solutes) is exchanged with the environment to reach osmotic equilibrium at isotonic condition, resulting in a lower cell volume than the isotonic one. This lowering of exchangeable cytosol may be obtained only through its intracellular redistribution, by sequestration to form the so-called inactive (to osmosis) volume ($V_{\mathrm{Cytosol}} \rightarrow V_{\mathrm{B}}$), or extrusion to the surrounding environment ($V_{\mathrm{Cytosol}} \rightarrow \mathrm{Exterior}$). In the latter case, along with water, intracellular osmolytes, traditionally considered impermeant in the two-parameter model, can also exit the cell.

The first scenario was originally proposed in the 1930s for red blood cells by Ponder [28-30]. However, it seems unlikely that the inactive cell volume may increase by about 300%, according to the data measured by the authors for hMSCs [6-7], and it may be ruled out.

Conversely, the exchange of water and intracellular osmolytes is the basis of the pump-leak concept for ions. However, this approach involves active mechanisms such as ion pumps which consume energy. As such, they are considered only for long-term regulation of cell volume through RVD and RVI, but are typically neglected in cryopreservation, where only relatively short-term responses are taken into account. On the other hand, a passive diffusion mechanism coupling mechanics with osmosis recently appeared in the literature to model the exchange of ions/salt between intra- and extracellular compartments [17-19]. It was suggested that the presence of mechanosensitive (MS) ion channels triggered by osmotic excursions of cell volume may be responsible for the short-term response involved in cryopreservation. Expanding on this work, we propose an improvement to the two-parameter formalism by augmenting it with a model for SAR of the cellular membrane, describing the transient behavior due to osmosis and cell mechanics, thus mimicking homeostasis via endo- and exo-cytosis.

2.1.2.1 Dynamics

Referring to Figure 2.1.1, the typical salt-water sack model is adopted for a spherical cell, i.e., a volume of ideal, aqueous solution representing the cytoplasm is surrounded with a semipermeable phospholipid bilayer membrane, which regulates the exchange of water and solutes between the intra- and extracellular compartments.

These exchanges may lead to variations in the total cell volume through changes in the volumes of intracellular water, V_{W}, and solutes, V_{Ions} and V_{CPA}:

$$V_{\mathrm{Cell}} = V_{\mathrm{B}} + V_{\mathrm{Ions}} + V_{\mathrm{W}} + V_{\mathrm{CPA}}. \quad (1)$$

A part of the total cell volume, V_{B}, corresponding to the nucleus, organelles, proteins, and other macromolecules, is supposed to be unaffected by the osmotic variations. The combined volume of organelles and macromolecules is denoted as $V_{\mathrm{B}} = \upsilon_{\mathrm{B}} V_{\mathrm{Cell}}^{0}$, where V_{Cell}^{0} is the initial isotonic cell volume, and υ_{B} is the inactive volume fraction under isotonic conditions that remains constant and is considered a characteristic feature of the cell lineage.

In the model proposed herein, water exchange is determined by coupling osmosis with cell mechanics, so that a counter-gradient of hydrostatic pressure always opposes the osmotic pressure difference during any shrinkage as well as swelling phases [17-19].

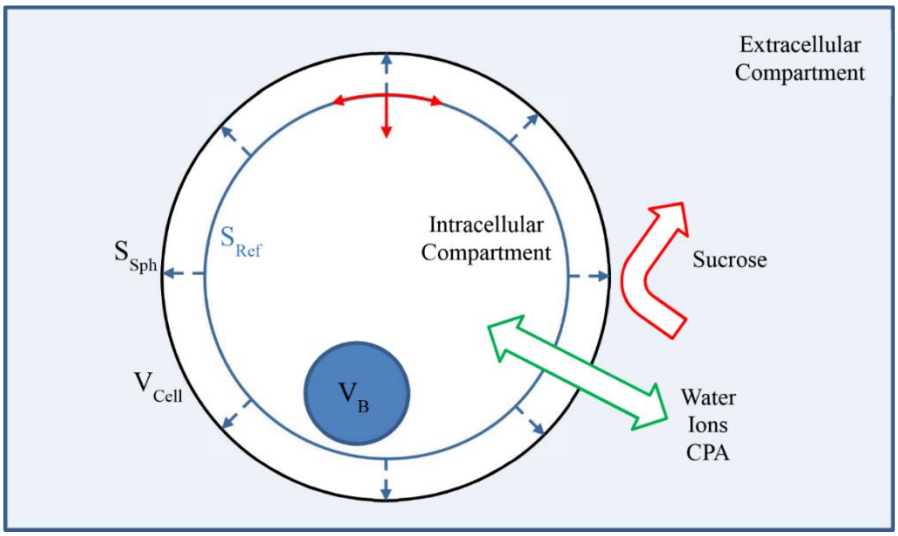

Figure 2.1.1: Schematic representation of a cell according to the "saltwater sack" model.

Water exchange can then be described by passive diffusion or down-hill transport along the gradient of a combined potential $\Phi = P - \Pi$. Thus, the volume of water contained in a cell may vary with time according to the following equation and initial isotonic condition:

$$\frac{dV_W}{dt} = -L_P\, S_{Sph}(\Delta P - \Delta\Pi), \qquad V_W(0) = V_W^0 = V_{Cell}^0 - V_{Ions}^0 - V_B \qquad @ \quad t = 0, \tag{2}$$

where $\Delta P = P^{INT} - P^{EXT}$ is the hydrostatic driving force (see below), and $\Delta\Pi = \Pi^{INT} - \Pi^{EXT}$ is the classical osmotic driving force of the two-parameter model, with the osmotic pressure proportional to solutes concentration expressed in terms of osmolalities according to the Van't Hoff equation: $\Pi = RTM$ (all symbols are defined in the Notation section).

In particular, as external sucrose is considered to be impermeant, intra- and extracellular solutes osmolalities are determined as $M^{INT} = (M_{Ions}^{INT} + M_{CPA}^{INT})$ and $M^{EXT} = (M_{Ions}^{EXT} + M_{Sucrose}^{EXT} + M_{CPA}^{EXT})$ correspondingly. The components of M^{INT} are time-dependent, and are defined using molar volumes $\tilde{v}$, and dissociation constant φ for salt/ions ($M_{Ions}^{INT} = \frac{\varphi}{\tilde{v}_{Ions}} \frac{V_{Ions}}{V_W}$ and $M_{CPA}^{INT} = \frac{1}{\tilde{v}_{CPA}} \frac{V_{CPA}}{V_W}$). External osmolalities are assumed to be constant with time because the volume of the extracellular solution is significantly greater than the cumulative cytoplasm volume of the suspended cells ($\frac{V_{cells}}{V_{External}} \cong 10^{-4}$). According to Equation 2, the rate of water exchange is proportional to water permeability L_P, which follows an Arrhenius-type dependence on temperature $L_P = L_P^{\infty} exp\left(-\frac{E_{a,W}}{RT}\right)$, and to the varying surface area of the spherical cell volume $S_{Sph} = 4\pi\left(\frac{3V_{Cell}}{4\pi}\right)^{\frac{2}{3}}$.

The passive diffusion of permeant CPA through cell membrane surface area S_{Sph} is described by

$$\frac{dV_{CPA}}{dt} = \tilde{v}_{CPA}\, P_{CPA} S_{Sph}\left(M_{CPA}^{EXT} - M_{CPA}^{INT}\right), \qquad V_{CPA}(0) = V_{CPA}^0 \quad @ \quad t = 0, \tag{3}$$

where the same kind of temperature dependence is adopted for CPA permeability: $P_{CPA} = P_{CPA}^{\infty} exp\left(-\frac{E_{a,CPA}}{RT}\right)$.

With the exception of the hydrostatic driving force ΔP appearing in Equation 2, the two equations reported above represent the two-parameter formalism, with water osmosis driven by the gradient of total solutes

osmolalities between the two facing compartments, whereas the independent permeation of CPA is caused only by the gradient of this solute. It is worth noting that, the very standard version of the two-parameter model is with S_{Sph} fixed to its initial value, even if it may be left free to vary as formerly noted by Kleinhans [11]. Moreover, the assumption of ideal, dilute solutions already made in the original two-parameter model by Kleinhans [11] could be removed by following the thermodynamics approach developed by Elliott and co-workers [13-14]. But this is out of the scope of this paper, where a different deviation from the classic two-parameter model is proposed.

The instantaneous mechanical response ΔP to osmotic shock $\Delta \Pi$ is determined by in-plane tension of the cell membrane, schematically depicted in Figure 2.1.1 by red curved arrows. In particular, during swelling in hypotonic conditions, as water enters the cell, its membrane surface area must increase to accommodate the new volume. This growth is sustained by membrane reservoirs activated through a temporary increase of cell membrane tension. Thus, the stretching of the cell membrane produces a force pushing inward (see the straight red arrow pointing towards the center of the spherical cell in Figure 2.1.1). According to the Laplace's law, this increase in membrane tension, $\Delta\sigma$, is mechanically equilibrated by hydrostatic pressure so that:

$$\Delta P = P^{\mathrm{INT}} - P^{\mathrm{EXT}} = \frac{2\,h\,\Delta\sigma}{r}, \tag{4}$$

where h is the combined thickness of the membrane and cytoskeletal cortex, and r is the cell radius. Considering the cortex and the membrane as a single layer [17], h is assumed constant for simplicity, while the cell radius varies with time as $r = \left(\frac{3V_{\mathrm{Cell}}}{4\pi}\right)^{\frac{1}{3}}$.

During swelling, P^{INT} temporarily exceeds P^{EXT}, resulting in a net force pointing outward (see the straight blue arrow in Figure 2.1.1) which opposes the continuation of water influx by pushing water out of cell.

The variation of cell membrane tension is determined by the deviation of the actual tension σ from the resting tension σ_{R} of the cell membrane:

$$\Delta\sigma = \sigma - \sigma_{\mathrm{R}}. \tag{5}$$

Recent studies have established the key role of the membrane tension in the regulation of cell motility and morphology, but the mechanism of tension sensation and the precise relationship between the membrane tension and the cell mechanical properties are still unknown [31]. Different models have been proposed to describe the influence of tension on cell membrane surface area [22-25,27]. In this work, an elastic cortex model [17] is adopted to describe its mechanical behavior, according to which:

$$\sigma = \frac{K}{2}\left(\frac{S_{\mathrm{Sph}}}{S_{\mathrm{Ref}}} - 1\right), \tag{6}$$

with K representing the elastic modulus of the cell membrane. Thus a linear stress-strain dependence is adopted, with strain being measured as deviation of S_{Sph} from a reference value S_{Ref}.

Under steady state conditions (regardless of whether this was preceded by a shrinkage or swelling in response to external stimuli), from a mechanical perspective, the cell is assumed to be in a resting state, characterized by the minimum surface-to-volume ratio corresponding to a spherical shape with the membrane surface area S_{Sph}, and a membrane resting tension $\sigma_{\mathrm{R}} > 0$. The latter quantity is regarded as a characteristic feature of a

given cellular lineage. Under steady state conditions, according to Equation 5, $\Delta\sigma = 0$ so that the hydrostatic pressure difference in Equation 4 gives $\Delta P = 0$. This implies that the inward force shown in Figure 2.1.1 resulting from the membrane tension, in resting condition is mechanically equilibrated by the reaction of the cytoskeleton, while S_{Ref} in Equation 5 attains a specific value ($S_{\mathrm{Ref}} = S_{\mathrm{Sph}}\left(1 + \frac{2\sigma_{\mathrm{R}}}{K}\right)^{-1}$). Thus, the reference value S_{Ref} for measuring the strain of the membrane is lower than S_{Sph}, as depicted in Figure 2.1.1: S_{Ref} represents the membrane surface area in a totally relaxed state (when $\sigma = 0$ and, correspondingly, $S_{\mathrm{Sph}} = S_{\mathrm{Ref}}$). The variation of the plasma membrane tension affects also the cell SAR [32]. When the cell volume changes, the cell membrane responds by trying to recover homeostasis. The main hypothesis of SAR is that whenever the membrane tension increases, some extra lipid bilayer is recruited from accessible endomembrane reserves to recover the resting tension value. On the contrary, when the tension drops below its resting value the membrane becomes slack so that part of it needs to be removed into reserves to recover the resting tension (Figure 2.1.2).

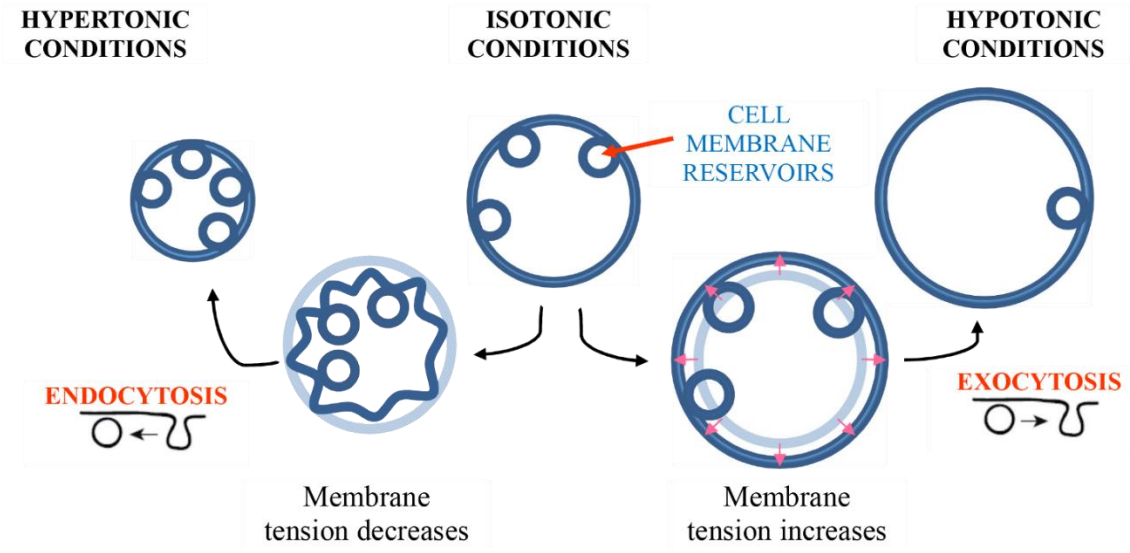

Figure 2.1.2: Schematic representation of cell membrane SAR: endocytosis under hypertonic conditions and exocytosis under hypotonic conditions.

This way an equilibrium condition for surface area membrane can be always re-established. The nature of these reserves is not yet clear [33]. Minor increases in the membrane tension could be buffered by undulations of the membrane such as filopodia, microvilli, membrane ruffles [33-34] that flatten with increasing tension, while more dramatic tension increases involve the disassembly of caveolae [34]. Other mechanisms by which the membrane tension is maintained are blebs, when internal tension is higher than external one, and vacuole-like dilatations, in the opposite case. In addition to the readily available plasma membrane buffers, cells can modulate their membrane tension using endomembranes by exo- and endo-cytosis [34].

On the basis of these considerations, the temporal variation of the cell membrane reference surface area is assumed here to vary proportionally to the force ($S_{\mathrm{Ref}} \cdot \Delta\sigma$) exerted on it

$$\frac{dS_{\mathrm{Ref}}}{dt} = k_{\mathrm{S}}\,\Delta\sigma\,S_{\mathrm{Ref}}, \qquad S_{\mathrm{Ref}}(0) = S_{\mathrm{Ref}}^{0} = \frac{S_{\mathrm{Sph}}^{0}}{1+\frac{2\,\sigma_{\mathrm{R}}}{K}} \quad @ \quad t = 0, \tag{7}$$

with k_{S} representing a proportionality constant. The initial value of S_{Ref} corresponds to the resting conditions of initial isotonic cells. Alternatively, Equation 7 may be seen as the rate of membrane area generation, which is equivalent to the flux of lipid bilayer between the cell membrane and membrane reservoirs and is proportional to the driving force $\Delta\sigma$.

Equations 6-7 represent the essential novelty of this work, allowing us to couple osmosis with SAR through cell mechanics, thus describing dynamic excursions of the cell membrane tension as being dependent on two different kinetics: a trigger by osmotic shocks, that is a rapid departure from resting tension the rate of which is proportional to water permeability L_{P}, followed by a relatively slow relaxation governed by k_{S}. Therefore, during swelling the momentary increase of the cell membrane tension can activate the opening of mechanosensitive ion channels distributed over the membrane surface area as depicted in Figure 2.1.3, while at resting condition or during shrinkage these channels remain closed [17].

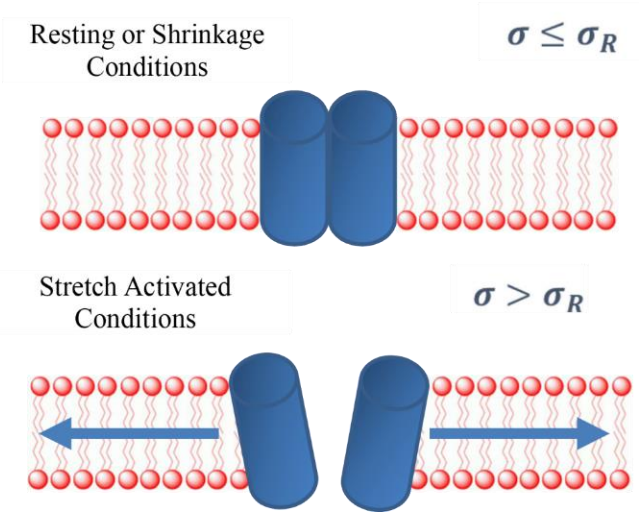

Figure 2.1.3: Schematic representation of activation mechanism for the mechanosensitive channels.

Accordingly, ions/salt may permeate the cell membrane as per the following equation describing their passive diffusion through the cell membrane surface area S_{Sph}:

$$\frac{dV_{\mathrm{Ions}}}{dt} = P_{\mathrm{Ions}} S_{\mathrm{Sph}} \left(M_{\mathrm{Ions}}^{\mathrm{EXT}} - M_{\mathrm{Ions}}^{\mathrm{INT}}\right), \qquad V_{\mathrm{Ions}}(0) = V_{\mathrm{Ions}}^{0} = \frac{\left(V_{\mathrm{Cell}}^{0} - V_{\mathrm{B}}\right)}{1+\frac{\varphi}{\bar{v}_{\mathrm{Ions}} M_{\mathrm{Ions}}^{\mathrm{INT},0}}} \quad @ \quad t = 0, \tag{8}$$

where the independent permeation of salt/ions is governed only by the gradient of that solute (as it was for CPA in Equation 2), and the corresponding on/off permeability following an Arrhenius-type temperature dependence when the mechanosensitive channels are open and being zero when they are closed:

$$P_{\mathrm{Ions}} = \begin{cases} 0 & \sigma \leq \sigma_{\mathrm{R}} \\ P_{\mathrm{Ions}}^{\infty} exp\left(-\frac{E_{\mathrm{a,Ions}}}{RT}\right) & \sigma > \sigma_{\mathrm{R}} \end{cases}. \tag{9}$$

The initial condition in Equation (8) deserves a comment. It is well-known that initial, isotonic intracellular osmolality is due not only to ions but also to other non-ionic solutes dispersed in the cytoplasm (and not accounted for by the inactive volume). However, in the proposed model the initial, intracellular isotonic osmolality is attributed to ions exclusively, so that its exchange is proportional to the gradient across cell membrane with the ions (PBS) dissolved in the external solution. Besides, if this assumption was removed, external ions could be exchanged based on the gradient of any extracellular solute like sucrose or CPA, as modelled for water in Equation 2. But this possibility is intentionally left out in the proposed model.

2.1.2.2 Equilibrium with impermeant solutes

The magnitude of the cell volume when osmotic equilibrium is reached can be determined by solving Equations 2-8 at steady state. To this aim, the analysis of proposed model benefits from making a distinction between the phases when cells are in contact with a solution containing or not the solute during an osmotic cycle with impermeant sucrose: first isotonic cells are contacted with hypertonic solutions of sucrose added to isotonic PBS until equilibrium is reached (this is called phase I, and cells shrink); then cells return to isotonic PBS until a new equilibrium point is reached (this is called phase II, and cells swell). This single osmotic cycle with impermeant sucrose corresponds to the experimental RUNS 1-3 (phase I) followed by RUNS 4-6 (phase II) whose operating conditions are detailed in Table 2.1.1.

Table 2.1.1: Experimental runs under transient conditions.

Initial Condition	RUN	$M_{Sucrose}^{EXT}$ $\left[\frac{mOsm}{L}\right]$	M_{CPA}^{EXT} $\left[\frac{mOsm}{L}\right]$	T [K]
Isotonic cells in contact with sucrose – phase I (3 temperatures)	1	300	0	290
	2	300	0	300
	3	300	0	310
Returning to isotonic conditions after contact with sucrose – phase II (3 temperatures)	4	0	0	290
	5	0	0	300
	6	0	0	310
Isotonic cells in contact with DMSO – phase I (3 temperatures)	7	0	1700	290
	8	0	1700	300
	9	0	1700	310
Returning to isotonic conditions after contact with DMSO - phase II (3 temperatures)	10	0	0	290
	11	0	0	300
	12	0	0	310
Isotonic cells in contact with DMSO – phase I (2 concentrations)	13	0	700	300
	14	0	1200	300
Isotonic cells in contact with sucrose, followed by restoring of isotonic conditions – phase I and phase II, repeated (2 cycles)	15	300	0	300
		0	0	300

These experimental runs were performed by the authors [6-7]. The case of two consecutive osmotic cycles with impermeant sucrose corresponds to the experimental RUN 15 reported in Table 2.1.1 as well.

For the case of isotonic cells in contact with a hypertonic solution of sucrose (phase I), the classic Boyle Van't Hoff equation

$$\frac{V_{\mathrm{Cell}}^{\mathrm{I}}}{V_{\mathrm{Cell}}^{0}} = \upsilon_{\mathrm{B}} + \frac{(1-\upsilon_{\mathrm{B}})}{1+\mu}\left(\frac{M^{0}}{M^{\mathrm{I}}} + \mu\right), \tag{10}$$

ensuing from the two-parameter model is derived also from the proposed model, since no ion exchange takes place during shrinkage when membrane tension is always lower than the resting value and MS channels remain closed. In Equation 10, isotonic osmolality is reported as $M^{0} = M_{\mathrm{Ions}}^{\mathrm{INT},0}$, while the osmolality of the external hypertonic solution is represented by $M^{\mathrm{I}} = M^{\mathrm{EXT,\,I}} = M_{\mathrm{Ions}}^{\mathrm{EXT,I}} + M_{\mathrm{Sucrose}}^{\mathrm{EXT,I}}$. For the sake of completeness, in Equation 10 the contribution of solutes to the initial cell volume at isotonic condition is taken into account by the term $\mu \cdot \frac{(1-\upsilon_{\mathrm{B}})}{1+\mu}$. Here $\mu = \frac{\widetilde{\upsilon}_{\mathrm{Ions}}\, M^{0}}{\varphi}$ represents the ration between ions and water intracellular volumes at isotonic conditions: it is a very small number which could be safely neglected. The first term in Equation 10 is clearly the contribution of the inactive volume, while the term $\frac{(1-\upsilon_{\mathrm{B}})}{1+\mu} \cdot \frac{M^{0}}{M^{\mathrm{I}}}$ represents the contribution of the intracellular water.

A linear dependence between the cell volume at equilibrium and the inverse of the external osmolality allows the inactive volume fraction, υ_B, to be determined through a simple linear regression. It is worth noting that, the Boyle Van't Hoff equation (as derived from the two-parameter model at steady state) does not depend on temperature, and predicts a perfect osmometer behavior with $\frac{V_{\mathrm{Cell}}^{\mathrm{I}}}{V_{\mathrm{Cell}}^{0}} = 1$ when isotonic condition $\frac{M^{0}}{M^{\mathrm{II}}} = 1$ are re-established (phase II of the osmotic cycle with sucrose, where $M^{\mathrm{II}} = M^{\mathrm{EXT,II}} = M_{\mathrm{Ions}}^{\mathrm{EXT,II}}$).

In the new model, on the other hand, the swelling in phase II causes the membrane to stretch and reach tensions above σ_{R} which leads to MS channels opening and causing a leakage of ions from the cells. Assuming that the relaxation time of membrane tension is larger than the characteristic time of ion and water permeations (i.e. k_{S} low, with L_{P} and P_{Ions} high) and ΔP is negligible with respect to $\Delta\pi$ in Equation 2, at osmotic equilibrium the following equation holds:

$$\frac{V_{\mathrm{Cell}}^{\mathrm{II}}}{V_{\mathrm{Cell}}^{0}} = \upsilon_{\mathrm{B}} + \frac{(1-\upsilon_{\mathrm{B}})}{1+\mu}\left(\frac{M^{0}}{M^{\mathrm{II}}} + \mu\right)\left(\frac{\mu+\lambda\frac{M^{0}}{M^{\mathrm{I}}}}{\mu+\lambda\frac{M^{0}}{M^{\mathrm{II}}}}\right), \tag{11}$$

with $\lambda = \frac{P_{\mathrm{Ions}}}{R\,T\,L_{\mathrm{P}}}$. The contributions of inactive, water and ionic volume fractions is readily recognized. In particular, the last bracketed term on the right-hand side of Equation 11 represents the deviation from the Boyle Van't Hoff equation (compare with Equation 10). It clearly depends on λ, the ratio between ion and water permeabilities: when $\lambda = 0$, Equation 11 is equal to the Boyle Van't Hoff equation since no leakage of ions actually takes place, and the new model reduces to the two-parameter model at equilibrium; however, as λ increases, the linear profile of the cell volume vs the reciprocal of external osmolality is lost, and a progressively lower cell volume is reached. Moreover, the permeabilities of water and ions can change differently with temperature ($E_{\mathrm{a,W}} \neq E_{\mathrm{a,Ions}}$). As a consequence, Equation 11 predicts a partial recovery of the isotonic cell volume that depends on system temperature.

The single osmotic cycle with sucrose represented by Equations 10 and 11 for the shrinking (I) and swelling (II) phases respectively, can be generalized to a series of n (≥2) osmotic cycles to obtain

$$\frac{V_{\mathrm{Cell}}^{\mathrm{I(n)}}}{V_{\mathrm{Cell}}^{0}} = \upsilon_{\mathrm{B}} + \frac{(1-\upsilon_{\mathrm{B}})}{1+\mu}\left(\frac{M^{0}}{M^{\mathrm{I(n)}}} + \mu\right)\prod_{\mathrm{i}=2}^{\mathrm{n}} \alpha^{(\mathrm{i}-1)}, \tag{12}$$

$$\frac{V_{\mathrm{Cell}}^{\mathrm{II(n)}}}{V_{\mathrm{Cell}}^{0}} = \upsilon_{\mathrm{B}} + \frac{(1-\upsilon_{\mathrm{B}})}{1+\mu}\left(\frac{M^{0}}{M^{\mathrm{II(n)}}} + \mu\right)\prod_{\mathrm{i}=1}^{\mathrm{n}} \alpha^{(\mathrm{i})}, \tag{13}$$

where $\alpha^{(\mathrm{i})} = \left(\frac{\mu+\lambda^{(\mathrm{i})}\frac{M^{0}}{M^{\mathrm{I(i)}}}}{\mu+\lambda^{(\mathrm{i})}\frac{M^{0}}{M^{\mathrm{II(i)}}}}\right)$ and $\lambda^{(\mathrm{i})} = \frac{P_{\mathrm{Ions}}\left(T^{(\mathrm{i})}\right)}{R\,T^{(\mathrm{i})}\,L_{\mathrm{P}}\left(T^{(\mathrm{i})}\right)}$. The contributions of the inactive, water and ion volume fractions is easily recognized as above, and the deviation from the Boyle Van't Hoff Equation 10 is conveniently grouped in the last product term on the right-hand side. In particular, the shrinking phase I of the second cycle (represented by Equation 12 with n=2) is still characterized by a linear profile of equilibrium cell volume $\frac{V_{Cell}^{\mathrm{I(2)}}}{V_{\mathrm{Cell}}^{0}}$ vs the reciprocal of external osmolality $\frac{M^{0}}{M^{\mathrm{I(2)}}}$. Actually, this linearity is preserved for every shrinking phase I in a series of n osmotic cycles, while is never obtained for any swelling phase II.

2.1.3 Results and discussion

This section first addresses the fitting of experimental data to estimate the parameters of the model proposed to interpret the osmotic behavior shown by hMSCs from UCB. This was measured by the authors under equilibrium and transient conditions, when contacting the cells at different temperatures with hypertonic solutions of sucrose or DMSO added to isotonic PBS [6-7] and then returning them to isotonic conditions. The operating conditions of the dynamic runs used in this section are detailed in Table 2.1.1. Then, model validation is performed by checking model capabilities to fully predict the system behavior in experimental runs not used for regression. Finally, the equilibrium conditions with an impermeant solute predicted by the proposed model are analyzed and discussed to gain a deeper insight into the osmotic effect of temperature, external osmolality and number of cycles. gPROMS ModelBuilder software v4.0 is used to solve numerically the model as well as to perform the regression analyses.

2.1.3.1 Regression analysis

The proposed model represented by Equations 1-8 contains several parameters (namely, the inactive volume fraction, rate constant of SAR, temperature dependent permeabilities of water, ions and CPA), whose values need to be determined through regression. To improve reliability, instead of adjusting all of the model parameters simultaneously, in this work a sequential best-fitting procedure is adopted. It follows a series of steps characterized by a progressive increase of model complexity: first, determine only υ_{B} from equilibrium runs in hypertonic solutions with sucrose at different osmolalities, but at constant temperature; then, keeping υ_{B} constant at the value just estimated, determine L_{P}, P_{Ions}, and k_{S} from the dynamic runs of the osmotic cycle with sucrose at constant osmolality, but at three different temperatures (see runs 1-6 in Table 2.1.1); finally,

keeping all the previous parameters constant, determine P_{CPA} from the dynamic runs of the osmotic cycle with DMSO at constant osmolality, but three different temperatures (i.e., runs 7-12 in Table 2.1.1).

The operating conditions of the equilibrium runs used in the first step for determining υ_{B} are not reported here and may be found in [6]. Figure 2.1.4 shows the Boyle Van't Hoff plot obtained when contacting isotonic hMSCs with hypertonic solutions of sucrose. As pointed out in the modelling section, in this case the proposed model represented by Equation 10 reduces to the classical linear profile of the Boyle Van't Hoff plot. An acceptable correlation is obtained for the linear regression (R^2 = 0.99), and the inactive volume fraction υ_{B} results equal to 0.2. This value is reported in Table 2.1.2 along with all the other parameters.

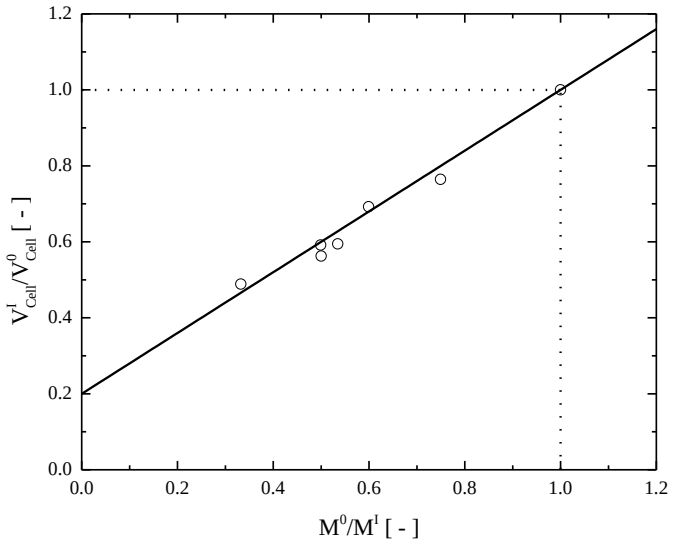

Figure 2.1.4: Boyle van't Hoff plot for hMSCs from UCB in hypertonic range (contact with sucrose at 300 K). $M^0 = M_{\mathrm{Ions}}^{\mathrm{INT},0}$, $M^{\mathrm{I}} = M^{\mathrm{EXT,\,I}} = M_{\mathrm{Ions}}^{\mathrm{EXT,I}} + M_{\mathrm{Sucrose}}^{\mathrm{EXT,I}}$. Data measured by the authors [6].

Table 2.1.2: Model parameters

Parameter	Value	Unit	Reference
$E_{\mathrm{a,CPA}}$	72570	[J mol^{-1}]	This work
$E_{\mathrm{a,Ions}}$	22150	[J mol^{-1}]	This work
$E_{\mathrm{a,W}}$	50000	[J mol^{-1}]	This work
h	0.5	[µm]	[17]
K	33000	[Pa]	[35]
k_{S}	$3.7\cdot10^{-6}$	[Pa^{-1} s^{-1}]	This work
L_{P}^{∞}	64.2	[µm Pa^{-1} s^{-1}]	This work
$P_{\mathrm{CPA}}^{\infty}$	$1.268\cdot10^{12}$	[µm s^{-1}]	This work
$P_{\mathrm{Ions}}^{\infty}$	$4.47\cdot10^{-3}$	[µm L s^{-1} mOsm^{-1}]	This work
R	8.314472	[J mol^{-1} K^{-1}]	[36]
V_{Cell}^{0}	1800	[µm^3]	[7]
σ_{R}	826	[Pa]	[25]
υ_{B}	0.2	[-]	This work
$\tilde{v}_{\mathrm{CPA}}$	$7.1\cdot10^{-5}$	[m^3 mol^{-1}]	[36]
$\tilde{v}_{\mathrm{Ions}}$	$2.7\cdot10^{-5}$	[m^3 mol^{-1}]	[36]
φ	2	[-]	[37]

To reduce their number in the regression analysis some are taken from the literature. This is the case for the resting tension σ_R, membrane thickness h, and elastic modulus K, the values of which are not available for the specific cells under investigation but may be found for similar lineages.

In particular, the resting tension reported in Table 2.1.2 is obtained from the value of $\sigma_R \cdot h = 413$ pN/μm reported for fibroblasts by [25] and the membrane thickness $h = 0.5$ μm for generic eukaryotic cells is taken from [17]. The elastic modulus K shown in Table 2.1.2 is for hMSCs from bone marrow, as provided by [35]. Since the hypertonic solutions of sucrose and DMSO used for the experimental runs described in Table 2.1.1 are based on isotonic PBS, NaCl is the salt taken as representative of the ions exchanged between the intra- and extracellular compartments. Accordingly, the values of $\tilde{v}_{Ions}$ and φ reported in Table 2.1.2 are the molar volume and dissociation constants of sodium chloride, respectively. The comparison between model fitting and experimental data measured under transient conditions for the osmotic cycle with impermeant sucrose at three different system temperatures is reported in Figure 2.1.5.

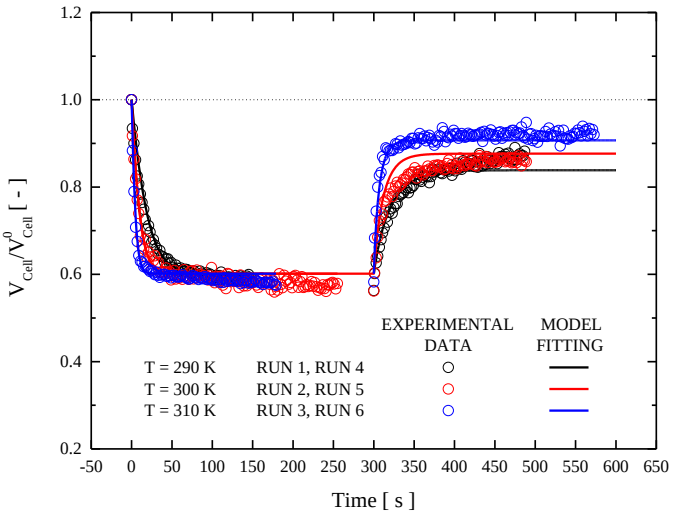

Figure 2.1.5: Comparisons between model fitting and experimental data under transient conditions for an osmotic cycle with sucrose. Data measured by the authors [6-7].

Here the cell volume normalized to its isotonic value ($V^0_{Cell} \approx 1800$ μm^3) is shown as a function of time: the exposure of cells to the hypertonic solution invariably induces shrinkage followed by swelling when isotonic conditions are restored. The higher the temperature, the higher the rate of volume variation during both the shrinking and swelling phases. Therefore, the higher the temperature, the faster the new equilibrium volume is reached by the cells. However, although the new equilibrium condition is independent of the temperature in the shrinking phase, it varies for the swelling phase, at the end of the osmotic cycle. Moreover, only a partial recovery of the initial isotonic volume is attained in the swelling phase: the deviation from the initial isotonic volume is more pronounced at low temperatures and decreases when the temperature increases. The model reproduces well all of the features of the osmotic behavior experimentally observed for hMSCs, providing reliable estimates of the temperature-dependent water and ions permeabilities (L_P and P_{Ions}), and SAR constant rate (k_S) for this cell lineage, as reported in Table 2.1.2. The fidelity of the novel model is certainly more than

acceptable if compared to the two-parameter model that would simulate a complete recovery of the initial isotonic volume regardless of the temperature. The values obtained for water permeability fall into the relatively broad range of values reported in the literature for different cell lineages [7]. On the other hand, from Table 2.1.2 an ions permeability equal to $6.91 \cdot 10^{-6}$ mol s^{-1} m^{-2} can be calculated at 300 K and isotonic osmolality: this value is slightly higher than the range 10^{-7}-10^{-6} mol s^{-1} m^{-2} reported in the literature for Na^{+} [17]. Besides, from the value found for k_S shown in Table 2.1.2, a characteristic time of about 330 seconds may be derived for cell membrane SAR at 300 K and isotonic osmolality. This time for membrane relaxation is much longer than the characteristic times corresponding to ions and water permeation (44 and 0.02 s, respectively). Moreover, from the values adopted for σ_R and h reported in Table 2.1.2, a characteristic ΔP equal to 10^2 Pa may be calculated from Laplace Equation (4) at initial cell radius. This hydrostatic pressure difference is much lower than the characteristic osmotic pressure difference $\Delta \Pi = RT\ \Delta M$ equal to 7.5×10^5 Pa calculated at 300 K and isotonic osmolality difference. These justify the assumption made when deriving Equations 10-13. The comparison between model fitting and experimental data measured under transient conditions for the osmotic cycle with permeant DMSO at three different temperatures is reported in Figure 2.1.6.

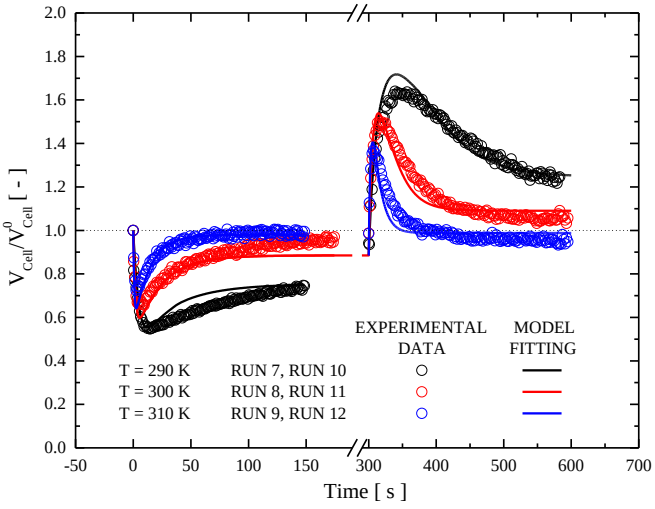

Figure 2.1.6: Comparisons between model fitting and experimental data under transient conditions for an osmotic cycle with DMSO. Data measured by the authors [6-7].

In this case, the temporal profile of the normalized cell volume is characterized by the classical shrink-swell dynamics observed during the exposure to a hypertonic solution, followed by a swell-shrink excursion when isotonic conditions are restored. This is well-known behavior due to the relatively high water permeability in comparison with DMSO. In this case also, the higher the temperature the higher the rate of volume variation, and the faster the new equilibrium condition is reached by the cells. However, unlike in the previous case shown in Figure 2.1.5, the new equilibrium condition always depends on the temperature during both the exposure to a hypertonic solution and after restoring isotonic conditions. The model reproduces well all the details of the osmotic behavior experimentally observed for hMSCs, providing reliable estimates for this cell

lineage of the temperature dependent DMSO permeability (P_{CPA}) reported in Table 2.1.2. The obtained values for CPA permeability fall into the relatively broad range of values reported in the literature for different cell lineages as discussed in [7]. As in the above case, the fidelity of the novel model is certainly more than acceptable if compared with the two-parameter model that predicts, regardless of the temperature, a volume excursion beyond the initial isotonic volume at the end of exposure to a hypertonic solution, and its complete recovery when isotonic conditions are restored [7,37-38]. It is worth noting that the deviation from the perfect osmometer behavior predicted by the two-parameter model is more pronounced at low temperatures and reduces when the temperature increases.

2.1.3.2 Model validation

Finally, the predictive capability of the proposed model is validated using test data from experimental runs performed under transient conditions when contacting cells with hypertonic solutions of DMSO of two different osmolalities but at constant temperature (see Figure 2.1.7), and data from two consecutive osmotic cycles with sucrose at constant osmolality and temperature (see Figure 2.1.8).

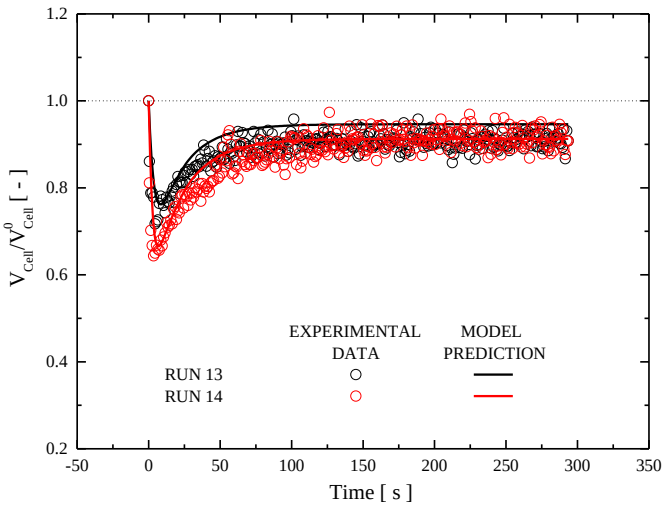

Figure 2.1.7: Comparisons between model predictions and experimental data under transient conditions for DMSO addition. Data measured by the authors [6].

In particular, the predicted effect of changing the external osmolality in the shrink-swell dynamics during DMSO addition is shown in Figure 2.1.7: when the concentration of the permeant solute is increased, a lower and anticipated minimum is reached during the cell volume excursion, as expected, and eventually a lower osmotic equilibrium value is attained. The prediction is sufficiently accurate considering the precision of experimental data. This is particularly true for run 14 where the external osmolality of DMSO is closer to the one used for the regression analysis, as expected. Note that, with the two-parameter model reproducing a perfect osmometer behavior, an equilibrium volume larger than the initial isotonic one would result due to DMSO addition, and the higher the external osmolality the higher the equilibrium cell volume [37].

In addition, the proposed model is capable of predicting with acceptable accuracy the progressive decrease of the equilibrium cell volume after each osmotic cycle with sucrose, as shown in Figure 2.1.8. This is particularly true for the first cycle which resembles the operating conditions used during the regression analysis, as expected. However, the prediction may be considered acceptable even for the second cycle (model accuracy is within 6% even for the second cycle): in this case, the perfect osmometer behavior would predict a complete recovery of the initial, isotonic volume at the end of every cycle.

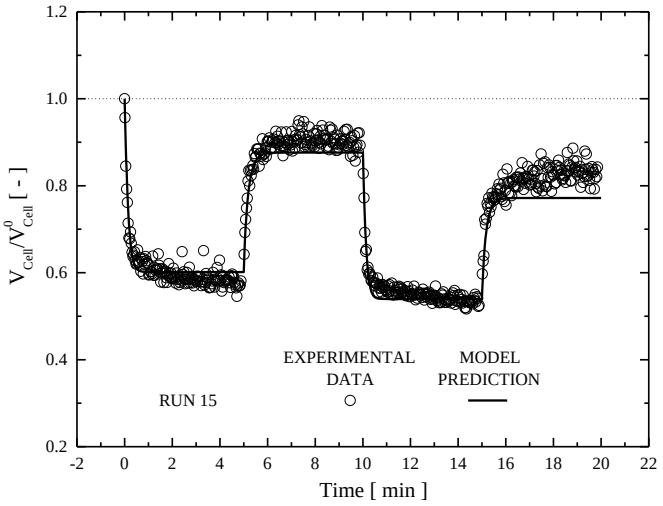

Figure 2.1.8: Comparisons between model predictions and experimental data under transient conditions for two consecutive osmotic cycles with sucrose. Data measured by the authors [7].

2.1.3.3 Equilibrium conditions with impermeant solute

The equilibrium conditions obtained from the proposed model for an osmotic cycle with impermeant sucrose are reported in Figure 2.1.9.

Specifically, the black line corresponds to Equation 10 and it shows, for initially isotonic cells, the equilibrium volume in the shrinkage phase I as a function of the reciprocal external osmolality. It can be seen that increasing the external osmolality of sucrose leads to more extensive shrinkage of the cell volume regardless of the temperature, and the obtained linear profile is characteristic of the BVH plot. Thus, for an external sucrose osmolality of 300 $\frac{mOsm}{L}$ the equilibrium cell volume equal to 60% of the initial isotonic one is attained, independently of the system temperature.

The temperature only affects the time required to reach the equilibrium point. Starting from this, the red, blue and purple curves correspond to Equation 11 and represent, at three different temperatures, the equilibrium volume during the following swelling phase II in the osmotic cycle with sucrose. For the sake of comparison, the three temperatures considered here and the sucrose osmolality of 300 $\frac{mOsm}{L}$ are exactly the same as those used for the experimental runs reported in Table 2.1.1 and Figure 2.1.5. Clearly, in the swelling phase II the temperature level affects not only the dynamics of the process, but also the final equilibrium point, which always results in a partial recovery of the initial isotonic volume when the isotonic osmolality is restored.

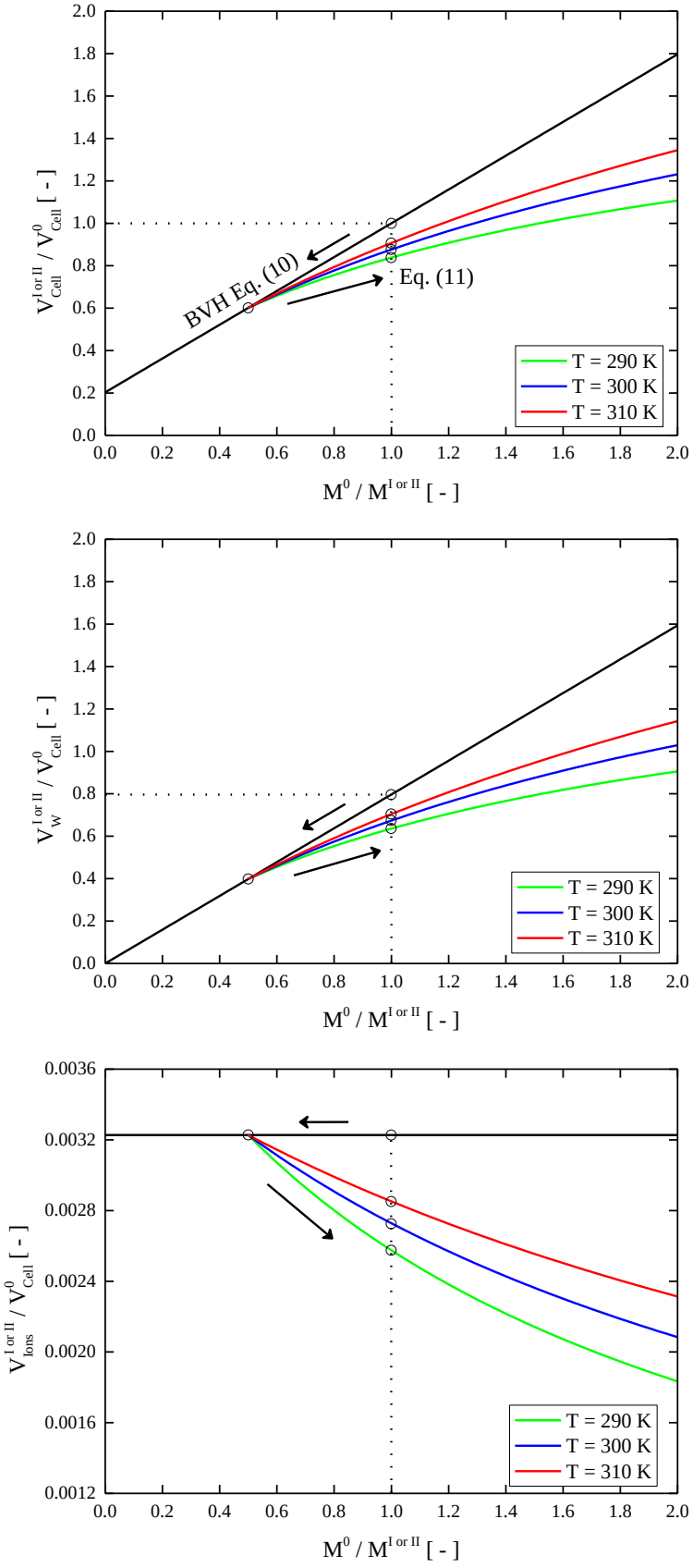

Figure 2.1.9: Equilibrium conditions for an osmotic cycle with impermeant sucrose: effect of temperature in terms of cell volume (a), with water (b) and ions (c) contributions. $M^{0} = M_{\mathrm{Ions}}^{\mathrm{INT},0}$, $M^{\mathrm{I}} = M^{\mathrm{EXT,\,I}} = M_{\mathrm{Ions}}^{\mathrm{EXT,I}} + M_{\mathrm{Sucrose}}^{\mathrm{EXT,I}}$, $M^{\mathrm{II}} = M^{\mathrm{EXT,\,II}} = M_{\mathrm{Ions}}^{\mathrm{EXT,II}}$.

This partial recovery is more pronounced at lower temperatures: the deviation of the proposed model from the perfect osmometer simulated by the two-parameter model increases at lower temperatures.

To rationalize this system behavior, Figures 2.1.9b-9c show the water and ions volumic contributions corresponding to the cell volume in Figure 2.1.9a. It is clear that during the shrinkage phase I of the osmotic cycle only intracellular water exits the cell, while the ion content remains constant at the initial, isotonic value. In this case, the proposed model reduces to the two-parameter model since during shrinkage the membrane tension diminishes and mechanosensitive ion channels do not open. On the contrary, during the following swelling phase II, ions leak out of the cell since ion channels are now open because of an increased membrane tension. According to Table 2.1.2, the temperature dependences of ions and water permeabilities are different: the relatively higher activation energy for the permeation of water with respect to that for ions leads to a lower value of λ in Equation 11 as the temperature increases. Therefore, the progressive tendency of the proposed model towards the perfect osmometer behavior (i.e. a complete recovery of the initial isotonic volume when restoring isotonic conditions) is due to the water permeability being proportionally higher than the permeability of ions as the temperature increases: equilibrium conditions are reached exclusively due to water, which permeates much faster in comparison with ions at higher temperatures.

Figure 2.1.10 shows the effect of the external osmolality at constant temperature on the equilibrium conditions for the osmotic cycle with impermeant sucrose in terms of cell volume (see Figure 2.1.10a) as well as the corresponding water and ions contributions (see Figures 10b-10c).

In this case, Equations 10 and 11 for the shrinkage and the following swelling phases, respectively, are plotted by varying the concentration of sucrose in the hypertonic solution during the contact with cells, before restoring the isotonic conditions. Partial recovery is always obtained, with ions leaking out of the cells only during the swelling phase. This leakage is larger for higher values of the external osmolality of sucrose, and, correspondingly, the partial recovery of the initial isotonic cell volume is more pronounced. This time, λ does not change since the temperature is constant. Now water and ions permeate at a constant rate in the three cases examined, and their variation cannot be deemed responsible for this behavior. This effect is due to a larger excursion of the cell volume when increased sucrose osmolality is adopted for the shrinkage phase of the osmotic cycle: the larger the shrinkage the larger the swelling excursion to recover isotonic conditions, and the larger the resulting leakage of intracellular ions.

Finally, Figure 2.1.11 shows the cell volume variations during the two consecutive cycles with sucrose at the operating conditions of run 15 in Table 2.1.1 (the corresponding temporal variation is reported in Figure 2.1.8). Figure 2.1.11 is the graphical representation of Equations 12-13. Starting from cells at isotonic conditions, the sequence of shrinkage and swelling phases during the two cycles is represented by the black and red lines, respectively. In particular, in this plot the shrinkage phases are represented by the straight black lines pointing towards the common intercept which corresponds to the inactive volume fraction v_B, while the swelling phases are represented by the red curves. The progressive decrease of the equilibrium cell volume after each osmotic cycle with sucrose is evident. It occurs due to continuous leakage of ions taking place during every swelling phase, when mechanosensitive channels open due to membrane stretching.

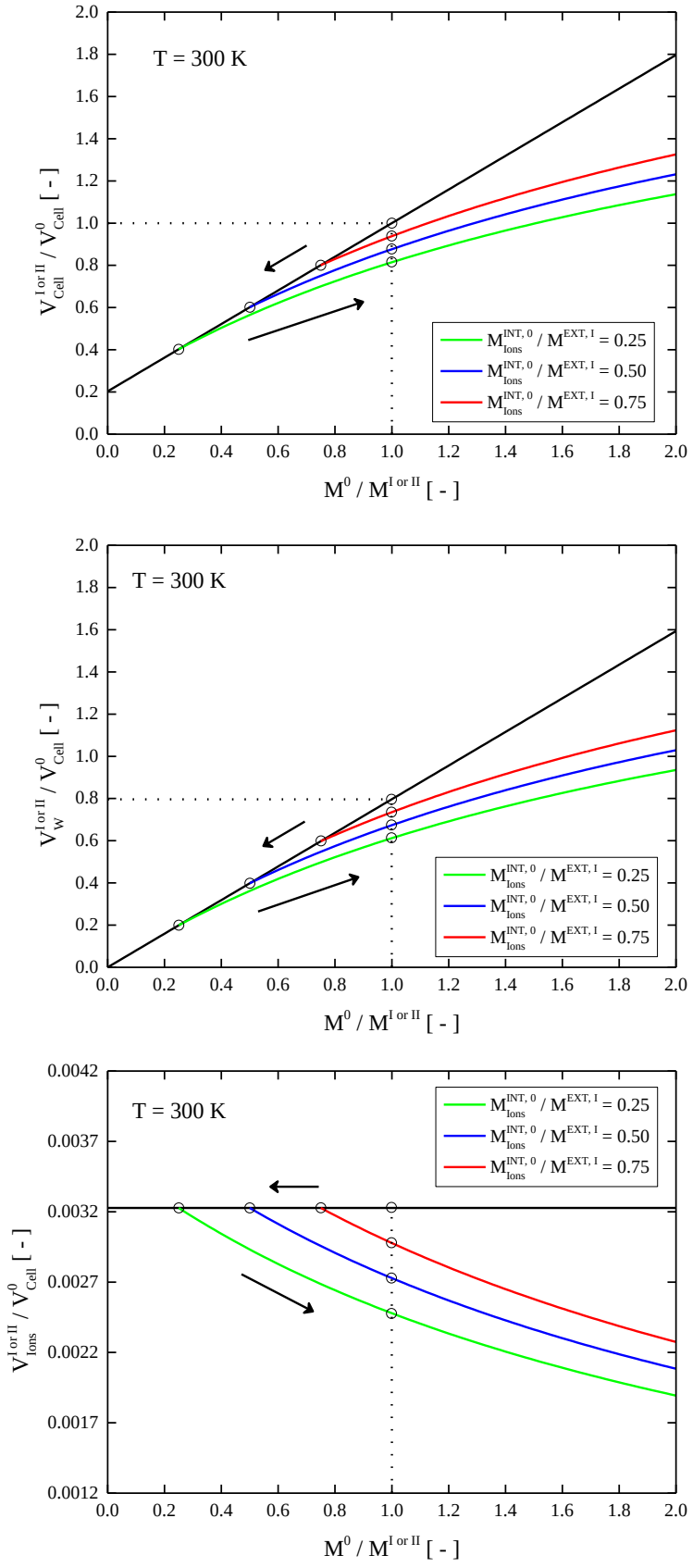

Figure 2.1.10: Equilibrium conditions for an osmotic cycle with impermeant sucrose: effect of external osmolality in terms of cell volume (a), with water (b) and ions (c) contributions. $M^{0} = M_{\text{Ions}}^{\text{INT,0}}$, $M^{\text{I}} = M^{\text{EXT, I}} = M_{\text{Ions}}^{\text{EXT,I}} + M_{\text{Sucrose}}^{\text{EXT,I}}$, $M^{\text{II}} = M^{\text{EXT, II}} = M_{\text{Ions}}^{\text{EXT,II}}$.

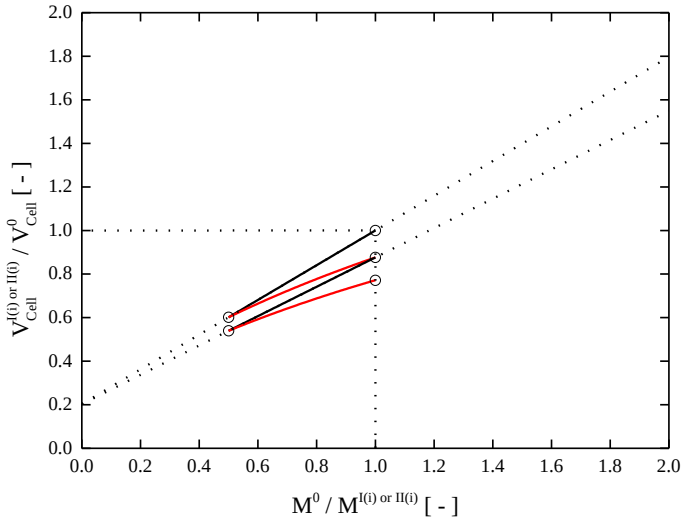

Figure 2.1.11: Equilibrium conditions for two consecutive osmotic cycles with impermeant sucrose. $M^{0} = M_{\text{Ions}}^{\text{INT},0}$, $M^{\text{I(i)}} = M^{\text{EXT, I(i)}} = M_{\text{Ions}}^{\text{EXT,I(i)}} + M_{\text{Sucrose}}^{\text{EXT,I(i)}}$, $M^{\text{II(i)}} = M^{\text{EXT, II(i)}} = M_{\text{Ions}}^{\text{EXT,II(i)}}$.

2.1.4 Conclusions and future work

In this work, a novel mathematical model capable of describing the peculiar osmotic behavior of human Mesenchymal Stem Cells from Umbilical Cord Blood is proposed for the optimization of the cryopreservation protocol. These cells show a non-perfect osmometer response to osmotic shocks, which cannot be described by the simple two-parameter formalism typically adopted in cryopreservation studies. The new model couples osmosis with cell mechanics and cell membrane surface area regulation which allows trans-membrane permeation of solutes during the swelling phase through temporary opening of mechanosensitive ion channels in the cell membrane. Thus, cells can reach an equilibrium volume different from the initial isotonic one, when isotonic conditions are re-established after contact with impermeant or permeant solutes. The model, trained through data fitting for parameter estimation and validated through prediction of a test set of experimental runs, shows acceptable agreement with measured data.

Further validations need to be addressed given that the model predicts an elastic expansion of the cell membrane surface area (up to 30%) larger than what is reported in the literature for different cell lineages. For comparison, membrane expansion by 2-4 % has been reported for protoplasts [32,39], while excessive elastic membrane expansion could lead to cell lysis and may therefore be unrealistic. The dependence of the rate of membrane area variation upon tension can be revised in the future when experimental evidence and relevant measurements become available. A relevant experiment would be to analyze the elastic response of this cell lineage through indentation or pulling tethers in order to check if the relatively large membrane area expansion is realistic, and estimate the values of more specific elastic parameters (i.e. elastic modulus and resting tension). Moreover, the hypothesis of the coexistence of different sources of membrane reservoirs should be investigated. Indeed, a practically instantaneous release of more accessible membrane reservoirs, i.e. unfolding of the membrane, could be considered as an elastic expansion of the cell surface. On the contrary, the release from endomembranes is considerably more sluggish in its contribution to an increase in the cell surface area.

Finally, additional investigation should be performed to analyze the behavior of mechanosensitive ion channels in this specific cell lineage. The minimum opening tension could be measured through patch clamp analysis and atomic force microscopy, and the variation of the amount of intracellular ionic solutes could be investigated by fluorescence analysis to validate the simplifications made in this work.

Notation of the Subchapter 2.1

$E_{\mathrm{a,CPA}}$	activation energy for CPA permeation
$E_{\mathrm{a,Ions}}$	activation energy for ions/salt permeation
$E_{\mathrm{a,W}}$	activation energy for water permeation
h	membrane + cortex thickness
K	elastic modulus of cell membrane
k_{S}	rate of variation of reference surface of cell
L_{P}	water permeability
L_{P}^{∞}	pre-exponential factor for water permeation
M^{EXT}	extracellular osmolality
M^{INT}	intracellular osmolality
M^{I}	extracellular osmolality during phase I
M^{II}	extracellular osmolality during phase II
$M_{\mathrm{CPA}}^{\mathrm{EXT}}$	extracellular CPA osmolality
$M_{\mathrm{Ions}}^{\mathrm{EXT}}$	extracellular ions/salt osmolality
$M_{\mathrm{Sucrose}}^{\mathrm{EXT}}$	extracellular sucrose osmolality
$M_{\mathrm{CPA}}^{\mathrm{INT}}$	intracellular CPA osmolality
$M_{\mathrm{Ions}}^{\mathrm{INT}}$	intracellular ions/salt osmolality
$M_{\mathrm{Ions}}^{\mathrm{INT,0}}$	initial intracellular ions/salt osmolality
P_{CPA}	CPA permeability
P_{Ions}	Ions/salt permeability
$P_{\mathrm{CPA}}^{\infty}$	pre-exponential factor for CPA permeation
$P_{\mathrm{Ions}}^{\infty}$	pre-exponential factor for ions/salt permeation
r	cell radius
R	universal gas constant
S_{Ref}	reference area for cell membrane
S_{Sph}	cell membrane area
S_{Ref}^{0}	initial, reference area for cell membrane
S_{Sph}^{0}	initial, isotonic cell membrane area
t	Time
T	absolute temperature
V_{B}	inactive cell volume
V_{Cell}	cell volume
V_{CPA}	intracellular CPA volume
V_{Ions}	intracellular ions/salt volume
V_{W}	intracellular water volume
V_{Cell}^{0}	initial, isotonic cell volume
V_{W}^{0}	initial, isotonic intracellular water volume
V_{Ions}^{0}	initial, isotonic intracellular Ions/salt volume
V_{Cell}^{I}	cell volume at equilibrium after phase I
V_{Cell}^{II}	cell volume at equilibrium after phase II
V_{Ions}^{I}	ions/salt intracellular volume at equilibrium after phase I
V_{Ions}^{II}	ions/salt intracellular volume at equilibrium after phase II
$V_{\mathrm{Ions}}^{\mathrm{II,0}}$	ions/salt intracellular volume at the beginning of phase II

V_{W}^{I}	water intracellular volume at equilibrium after phase I
V_{W}^{II}	water intracellular volume at equilibrium after phase II
$V_{\mathrm{W}}^{\mathrm{II},0}$	water intracellular volume at the beginning of phase II
ΔP	hydraulic pressure gradient
$\Delta \Pi$	osmotic pressure gradient
$\Delta \sigma$	variation of membrane tension
λ	non-dimensional parameter appearing in Equations 11-13, A8-A9
μ	non-dimensional parameter appearing in Equations 10-13, A6-A9
v_{B}	inactive cell volume fraction
$\tilde{v}_{\mathrm{CPA}}$	molar volume of CPA
$\tilde{v}_{\mathrm{Ions}}$	molar volume of ions/salt
Π^{EXT}	extracellular osmotic pressure
Π^{INT}	intracellular osmotic pressure
σ	membrane tension
σ_{R}	membrane resting tension
φ	dissociation constant for salt in water

References of the Subchapter 2.1

1. Caplan, A., (2009). Why are MSCs therapeutic? New data: new insight. *J Pathol*, 217, pp. 318-324. https://doi.org/10.1002/path.2469
2. Hass, R., Kasper, C., Böhm, S., Jacobs, R., (2011). Different populations and sources of human mesenchymal stem cells (MSC): a comparison of adult and neonatal tissue-derived MSC, *Cell Commun Signaling* 9:12, pp. 1-14. https://doi.org/10.1186/1478-811X-9-12
3. Dimarino, A.M., Caplan, A.I., Bonfield, T.L., (2013). Mesenchymal stem cells in tissue repair, *Front Immunol*, 4, pp. 1-9. https://doi.org/10.3389/fimmu.2013.00201
4. Bieback, K., Kern, S., Klüter, H., Eichler, H., (2004). Critical parameters for the isolation of mesenchymal stem cells from umbilical cord blood, *Stem Cells*, 22, pp. 625-634. https://doi.org/10.1634/stemcells.22-4-625
5. Wexler, S.A., Donaldson, C., Denning-Kendall, P., Rice C., Bradley B., Hows J.M., (2003). Adult bone marrow is a rich source of human mesenchymal 'stem' cells but umbilical cord and mobilized adult blood are not, *Br J Haematol*, 121, pp. 368-374. https://doi.org/10.1046/j.1365-2141.2003.04284.x
6. Casula, E., Asuni, G.P., Sogos, V., Cincotti, A., (2015). hMSCs from UCB: isolation, characterization and determination of osmotic properties for optimal cryopreservation, *Chem Eng Trans*, 43, pp. 265-270. https://doi.org/10.3303/CET1543045
7. Casula, E., Asuni, G.P., Sogos, V., Fadda, S., Delogu, F., Cincotti, A., (2017). Osmotic behaviour of human mesenchymal stem cells: Implications for cryopreservation, *Plos One*, 12, ID e0184180. https://doi.org/10.1371/journal.pone.0184180
8. Parekkadan, B., Sethu, P., van Poll, D., Yarmush, M.L., Toner, M., (2007). Osmotic selection of human mesenchymal stem/progenitor cells from umbilical cord blood, *Tissue Eng*, 13, pp. 2465-2474. https://doi.org/10.1089/ten.2007.0054
9. Mazur, P., Leibo, S.P., Chu, E.H.Y., (1972). A two-factor hypothesis of freezing injury: Evidence from chinese-hamster tissue-culture cells, *Exp Cell Res*, 71, pp. 345-355. https://doi.org/10.1016/0014-4827(72)90303-5
10. Karlsson, J.O., Toner, M., (1996). Long-term storage of tissues by cryopreservation: critical issues, *Biomaterials*, 17, pp. 243-256. https://doi.org/10.1016/0142-9612(96)85562-1
11. Kleinhans, F.W., (1998). Membrane permeability modeling: Kedem-Katchalsky vs a two-parameter formalism, *Cryobiology*, 37, pp. 271-289. https://doi.org/10.1006/cryo.1998.2135
12. Kedem, O., Katchalsky, A., (1958). A thermodynamic analysis of the permeability of biological membranes to non-electrolytes, *Biochim Biophys Acta*, 27, pp. 229-246. https://doi.org/10.1016/0006-3002(58)90330-5
13. Prickett, R.C., Elliott, J.A.W., Hakda, S., McGann, L.E., (2008). A non-ideal replacement for the Boyle van't Hoff equation, *Cryobiology*, 57, pp. 130-136. https://doi.org/10.1016/j.cryobiol.2008.07.002.
14. Ross-Rodriguez, L.U., Elliott, J.A.W., McGann, L.E., (2012). Non-ideal solution thermodynamics of cytoplasm, *Biopreserv Biobank*, 10, pp. 462-471. https://doi.org/10.1089/bio.2012.0027
15. Lang, F., Busch, G.L., Ritter, M, Völkl, H., Waldegger, S., Gulbins, E., Häussinger, D., (1998). Functional significance of cell volume regulatory mechanisms, *Physiol Rev*, 78, pp. 247-306. https://doi.org/10.1152/physrev.1998.78.1.247
16. Hoffmann, E.K., Lambert, I.H., Pedersen, S.F., (2009). Physiology of cell volume regulation in vertebrates, *Physiol Rev*, 89, pp. 193-277. https://doi.org/10.1152/physrev.00037.2007
17. Jiang, H.Y., Sun, S.X., (2013). Cellular pressure and volume regulation and implications for cell mechanics, *Biophys J*, 105, pp. 609-619. https://doi.org/10.1016/j.bpj.2013.06.021
18. Sachs, F., Sivaselvan, M.V., (2015). Cell volume control in three dimensions: water movement without solute movement, *J Gen Physiol*, 145, pp. 373-380. https://doi.org/10.1085/jgp.201411297
19. Tao, J., Sun, S.X., (2015). Active biochemical regulation of cell volume and a simple model of cell tension response, *Biophys J*, 109, pp. 1541-1550. https://doi.org/10.1016/j.bpj.2015.08.025
20. Keener, J., Sneyd, J., (2009). Mathematical Physiology I: Cellular Physiology, in S.S. Antman, J.E. Marsden, L. Sirovich (Eds), Interdisciplinary. Applied Mathematics series, Ed. Springer-Verlag, New York. https://doi.org/10.1007/978-0-387-79388-7
21. Kay, A.R., Blaustein, M.P., (2019). Evolution of our understanding of cell volume regulation by the pump-leak mechanism, *J Gen Physiol*, 51, pp. 407-416, https://doi.org/10.1085/jgp.201812274.

22. Rauch, C., Farge, E., (2000). Endocytosis switch controlled by transmembrane osmotic response and phospholipid number asymmetry, *Biophys J*, 78, pp. 3036-3047. https://doi.org/10.1016/S0006-3495(00)76842-1
23. Morris, C.E., Wang, J.A., Markin, V.S., (2003). The invagination of excess surface area by shrinking neurons, *Biophys J*, 85, pp. 223-235. https://doi.org/10.1016/S0006-3495(03)74468-3
24. Sens, P., Turner, M.S., (2006). Budded membrane microdomains as tension regulators, *Phys Rev E*, 73, ID 031918. https://doi.org/10.1103/PhysRevE.73.031918
25. Tinevez, J.Y., Schulze, U., Salbreux, G., Roensch, J., Joanny, J.F., Paluch, E., (2009). Role of cortical tension in bleb growth, *PNAS*, 106, pp. 18581-18586. https://doi.org/10.1073/pnas.0903353106
26. Sinha, B., Koster, D., Ruez, R., Gonnord, P., Bastiani, M., Abankwa, D., Stan, R.V., Butler-Browne, G., Vedie, B., Johannes, L., Morone, N., Parton, R.G., Raposo, G., Sens, P., Lamaze, C., Nassoy, P., (2011). Cells respond to mechanical stress by rapid disassembly of caveolae, *Cell*, 144, pp. 402-413. https://doi.org/10.1016/j.cell.2010.12.031
27. Pietruch, A., Bruckner, B.R., Janshoff, A., (2013). Membrane tension homeostasis of epithelial cells through surface area regulation in response to osmotic stress, *Biochim Biophys Acta*, 1833, pp. 712-732. https://doi.org/10.1016/j.bbamcr.2012.11.006
28. Macleod, J., Ponder, E., (1933). The measurement of red cell volume: IV. Alterations in cell volume in hypotonic plasma, *J Physiol*, 77, pp. 181-188. https://doi.org/10.1113/jphysiol.1934.sp003209
29. Macleod, J., Ponder, E., (1936). Solvent water in the mammalian erythrocyte, *J Physiol*, 86, pp. 147-152. https://doi.org/10.1113/jphysiol.1936.sp003349
30. Ponder, E., (1935). The measurement of red-cell volume. Conductivity measurements, *J Physiol*, 85, pp. 439-49. https://doi.org/10.1113/jphysiol.1935.sp003330
31. Diz-Munoz, A., Fletcher, D.A., Weiner, O.D., (2013). Use the force: membrane tension as an organizer of cell shape and motility, *Trends Cell Biol*, 23, pp. 47-53. https://doi.org/10.1016/j.tcb.2012.09.006
32. Morris, C.E., Homann, U., (2001). Cell surface area regulation and membrane tension, *J Memb Biol*, 179, pp. 79-102. https://doi.org/10.1007/s002320010040
33. Titushkin, I., Cho, M., (2006). Distinct membrane mechanical properties of human mesenchymal stem cells determined using laser optical tweezers, *Biophys J*, 90, pp. 2582-2591. https://doi.org/10.1529/biophysj.105.073775
34. Gauthier, N.C., Masters, T.A., Sheetz, M.P., (2012). Mechanical feedback between membrane tension and dynamics, *Trends Cell Biol*, 22, pp. 527-535. https://doi.org/10.1016/j.tcb.2012.07.005
35. Yourek, G., Hussain, M.A., Mao, J.J., (2007). Cytoskeletal changes of mesenchymal stem cells during differentiation. *Asaio J*, 53, pp. 219-228. https://doi.org/10.1097/MAT.0b013e31802deb2d
36. Perry, R.H., Green, D.W., Maloney, J.O. (1997). *Perry's chemical engineers' handbook*. 7th ed. McGraw-Hill chemical engineering series, New York. ISBN 0-07-049841-5
37. Fadda, S., Cincotti, A., Cao, G., (2011). Rationalizing the equilibration and cooling stages of cryopreservation: the effect of cell size distribution, *Aiche J*, 57, pp. 1075-1095. https://doi.org/10.1002/aic.12320
38. Fadda, S., Cincotti, A., Cao, G., (2010). The effect of cell size distribution during the cooling stage of cryopreservation without CPA, *Aiche J*, 56, pp. 2173-2185. https://doi.org/10.1002/aic.12137
39. Wolfe, J., Dowgert, M.F., Steponkus, P.L., (1986). Mechanical Study of the Deformation and Rupture of the Plasma-Membranes of Protoplasts during Osmotic Expansions, *J Memb Biol*, 93, pp. 63-74. https://doi.org/10.1007/BF01871019

2.2 Insights into the model of non-perfect osmometer cells for cryopreservation: a parametric sweep analysis

2.2.1 Introduction

The SAR model described in the Subchapter 2.1 was conceived as a conservative development of the two-parameter formalism explicitly to avoid over-parameterization: the simplifying assumption of ideal liquid solutions is maintained, but the description of transport mechanisms is enriched by accounting for three additional phenomena (namely ion/salt conditional permeation, membrane surface area regulation, and counter-gradient of hydrostatic pressure to osmosis), thus introducing five additional parameters (i.e. membrane resting tension, thickness and elastic modulus, ion/salt permeability, and membrane relaxation rate constant). Nonetheless, a complex picture of the system results as it will be shown in this work: depending on the relative values of the model parameters and operating conditions, when isotonic conditions are re-established after any osmotic excursion where the cell membrane is stretched, cell volume at equilibrium depends on the position of the temporal window of mechano-sensitive channels opening.

In this work, first an appropriate non-dimensional version of the equations for the SAR model is derived, in order to minimize the number of model parameters. Then, a parametric sweep analysis is discussed to highlight model features in comparison with the two-parameter model, that basically represents a special case of the SAR model. Regarding this, the conditions in terms of the values of the adjustable parameters by which the SAR model reduces to the two-parameter model are identified. Besides, only equilibrium equations after an osmotic cycle with impermeant sucrose may be analytically derived for the SAR model, albeit without the advantageous linearity of the Boyle Van't Hoff equation. It is shown that, the validity of these equilibrium conditions with respect to the values of the adjustable parameters may be generalized and extended much more than originally assumed. On the contrary, when a permeant CPA comes into play the difficulty to predict the temporary opening of MS channels prevents the derivation of the corresponding equilibrium equations: in this case, a numerical integration of system dynamics (prolonged until steady state is eventually reached) is required to determine cell volume at equilibrium.

2.2.2 Model Equations

2.2.2.1 Dynamics

Starting from the model equations in dimensional form reported in the Subchapter 2.1, in this work the corresponding non-dimensional equations are derived by defining a reference, constant value to scale all the variables. The resulting equations in non-dimensional form are collectively reported in Tables 2.2.1-2, with Ordinary Differential Equations (ODEs) conveniently separated by auxiliary Algebraic Equations (AEs). It is

worth noting that the non-dimensional time ($\tau = \frac{t}{t^*}$) is defined with respect to a reference value based on water permeability and depends on temperature $\left(t^* = \frac{\left(\frac{3}{4\pi} V_{\text{Cell}}^0\right)^{\frac{1}{3}}}{3\, L_{\text{P}}(T)\, R\, T\ \ \text{M}^0} \right)$.

Table 2.2.1: Ordinary Differential Equations (OEDs) of the SAR model in non-dimensional form.

Equation	Initial Condition	Number
$\frac{d\zeta_{\text{W}}}{d\tau} = -\Phi_{\text{Sph}}(\Delta\text{p} - \Delta\omega)$	$\zeta_{\text{W}}(0) = \zeta_{\text{W}}^0 = \left(\frac{1-\upsilon_{\text{B}}}{1+\mu_{\text{Ions}}}\right) \quad @ \quad \tau = 0$	(1)
$\frac{d\zeta_{\text{CPA}}}{d\tau} = -\lambda_{\text{CPA}}\ \Phi_{\text{Sph}}\ \Delta\omega_{\text{CPA}}$	$\zeta_{\text{CPA}}(0) = \zeta_{\text{CPA}}^0 = 0 \quad @ \quad \tau = 0$	(2)
$\frac{d\zeta_{\text{Ions}}}{d\tau} = -\lambda_{\text{Ions}}\ \Phi_{\text{Sph}}\ \Delta\omega_{\text{Ions}}$	$\zeta_{\text{Ions}}(0) = \zeta_{\text{Ions}}^0 = \mu_{\text{Ions}}\left(\frac{1-\upsilon_{\text{B}}}{1+\mu_{\text{Ions}}}\right) \quad @ \quad \tau = 0$	(3)
$\frac{d\Phi_{\text{Ref}}}{d\tau} = \lambda_{\text{S}}\ \Phi_{\text{Ref}}\ \Delta\Omega$	$\Phi_{\text{Ref}}(0) = \Phi_{\text{Ref}}^0 = \left(\frac{1}{1+\frac{\Omega_{\text{R}}}{K'}}\right) \quad @ \quad \tau = 0$	(4)

Table 2.2.2: Auxiliary Algebraic Equations (AEs) of the SAR model in non-dimensional form.

Equation	Number
$\zeta_{\text{Cell}} = \upsilon_{\text{B}} + \zeta_{\text{Ions}} + \zeta_{\text{W}} + \zeta_{\text{CPA}}$	(5)
$\Delta\text{p} = \text{p}^{\text{INT}} - \text{p}^{\text{EXT}} = \frac{\beta\ \Delta\Omega}{(\zeta_{\text{Cell}})^{\frac{1}{3}}}$	(6)
$\Delta\Omega = \ \Omega - \Omega_{\text{R}}$	(7)
$\Omega = K'\left(\frac{\Phi_{\text{Sph}}}{\Phi_{\text{Ref}}} - 1\right)$	(8)
$\Phi_{\text{Sph}} = (\zeta_{\text{Cell}})^{\frac{2}{3}}$	(9)
$\Delta\omega = \omega^{\text{INT}} - \omega^{\text{EXT}}$	(10)
$\omega^{\text{INT}} = \omega_{\text{Ions}}^{\text{INT}} + \omega_{\text{CPA}}^{\text{INT}}$	(11)
$\omega_{\text{Ions}}^{\text{INT}} = \frac{\zeta_{\text{Ions}}}{\mu_{\text{Ions}}\ \zeta_{\text{W}}}$	(12)
$\omega_{\text{CPA}}^{\text{INT}} = \frac{\zeta_{\text{CPA}}}{\mu_{\text{CPA}}\ \zeta_{\text{W}}}$	(13)
$\omega^{\text{EXT}} = (\omega_{\text{Ions}}^{\text{EXT}} + \omega_{\text{Sucrose}}^{\text{EXT}} + \omega_{\text{CPA}}^{\text{EXT}})$	(14)
$\Delta\omega_{\text{CPA}} = \omega_{\text{CPA}}^{\text{INT}} - \omega_{\text{CPA}}^{\text{EXT}}$	(15)
$\Delta\omega_{\text{Ions}} = \omega_{\text{Ions}}^{\text{INT}} - \omega_{\text{Ions}}^{\text{EXT}}$	(16)
$\lambda_{\text{Ions}} = \begin{cases} 0 & \Delta\Omega \le 0 \\ \lambda_{\text{Ions}} & \Delta\Omega > 0 \end{cases}$	(17)

As a consequence, in this work system temperature is assumed constant during any simulation. Moreover, in the adopted non-dimensionalization each dimensional variable or parameter uniquely corresponds to a non-dimensional one. Thus, from here on every variable or parameter is called with its generic name without specifying to refer to dimensional or the non-dimensional one, unless necessary.

In contrast with the classic two-parameter model, the SAR model allows the trans-membrane exchange of the solutes responsible of the initial isotonic osmolality, identified as ions as schematically depicted in Figure 2.2.1. Here the inactive (v_B), water (ζ_W), CPA (ζ_{CPA}) and ion (ζ_{Ions}) volume fractions contribute to form the cell volume (ζ_{Cell}), as defined by Equation 5 in Table 2.2.2.

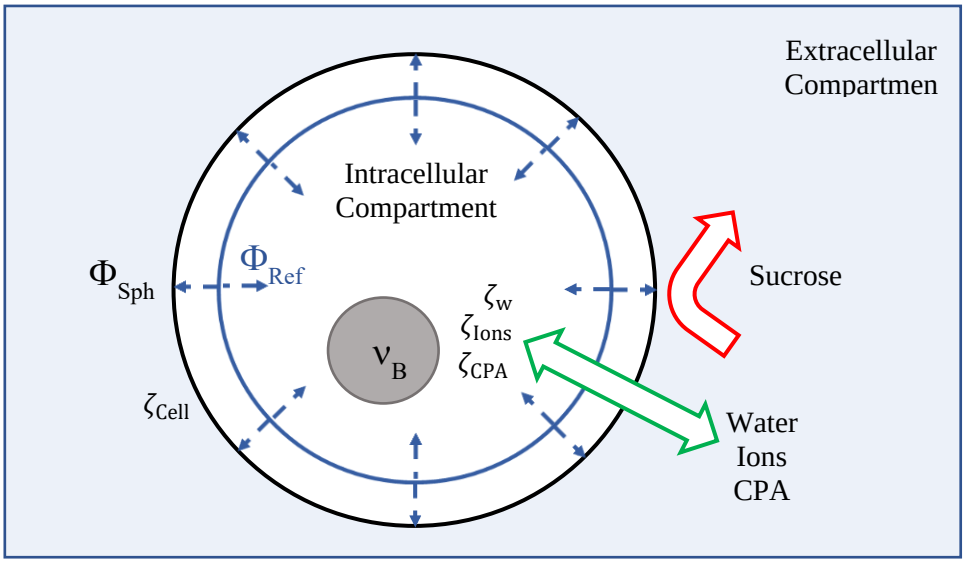

Figure 2.2.1: Schematic representation of a cell according to the SAR model.

Except for the inactive volume and any impermeant solutes like sucrose, in the SAR model water and CPA as well as ion may be exchanged between intra- and extracellular compartments as expressed by Equations 1-3 in Table 2.2.1, respectively. Here the non-dimensional kinetic parameters like ion and CPA permeability (λ_{Ions} and λ_{CPA}) are defined with respect to water permeability (L_P). In particular, a conditional ion exchange represented by Equation 3 is considered as expressed by Equation 17, depending on the opening of MS channels. These are assumed to be distributed all over the cell membrane, the spherical surface area (Φ_{Sph}) of which varies in time as cells shrink or swell (see Equation 9); MS channels open when the cell membrane is mechanically stretched above its resting tension (i.e. $\Omega > \Omega_R$ or $\Delta\Omega > 0$). This stretching of the cell membrane surface area (Φ_{Sph}) is measured by the surface strain from its reference value (Φ_{Ref}) as defined by Equations 7-8, and is only temporary: membrane relaxation through the exchange of surface area with membrane reservoirs is able to bring cell back to the resting condition by following Equation 4, where the non-dimensional kinetic parameter (λ_S) is also defined with respect to water permeability (L_P).

Basically, in the SAR model a cell under isotonic conditions is seen as an inflatable balloon whose surface Φ_{Sph} is initially stretched from Φ_{Ref} at a resting tension Ω_R representing homeostatic condition, as expressed

by the initial condition of Equation 4. In response to an osmotic gradient $\Delta\omega$ between intra- and extracellular compartments expressed by Equations 10-16, the cell inflates or deflates (through the exchange of water, CPA, and ions) by changing its spherical volume ζ_{Cell} and its membrane surface area Φ_{Sph}. As a consequence, the ratio $\frac{\Phi_{\mathrm{Sph}}}{\Phi_{\mathrm{Ref}}}$ varies from its value at resting condition $(1+\frac{\Omega_{\mathrm{R}}}{K'})$ in a proportional fashion with cell membrane tension Ω, i.e. an elastic response from a mechanical perspective, with K' representing the non-dimensional elastic modulus defined in Equation 8. This variation has two consequences: according to the Laplace law (i.e. Equation 6) a counter-gradient of hydrostatic pressure $\Delta\mathrm{p}$ always opposing the osmotic driving force $\Delta\omega$ in the water exchange rate emerges (note the opposite signs of the two driving forces in Equation 1), while MS channels open allowing ion exchange (inward or outward depending on their gradient) if the membrane is stretched, i.e. if $\Omega > \Omega_{\mathrm{R}}$ or $\left(\frac{\Phi_{\mathrm{Sph}}}{\Phi_{\mathrm{Ref}}}\right) > \left(1+\frac{\Omega_{\mathrm{R}}}{K'}\right)$. On the other hand, the variation of membrane tension with respect to the resting condition is only temporary due to membrane relaxation governed by Equation 4: it eventually vanishes through the exchange of surface area with membrane reservoirs, which brings the membrane tension back to its resting value in order to maintain cell homeostasis.

The exchange rates reported in Table 2.2.1 are all determined as proportional to the product of a flux represented by a driving force and the corresponding cross-sectional area, with non-dimensional ions and CPA permeability ($\lambda_{\mathrm{Ions}}, \lambda_{\mathrm{CPA}}$) as well as λ_{S} being the constants of proportionality. For water, CPA and ion exchange rates the cross-sectional area is represented by the spherical cell membrane area Φ_{Sph} in Equations 1-3, while in the membrane generation/relaxation rate expressed by Equation 4 Φ_{Ref} is multiplied with the driving force $\Delta\Omega$ for the exchange flux of lipid bilayer with membrane reservoirs.

The two-parameter model in non-dimensional form consists of a subset of the equations reported in Tables 2.2.1-2 for the SAR model, namely Equation 1 (with $\Delta\mathrm{p} = 0$) and Equation 2 for the ODE system shown in Table 2.2.1 where the content of intracellular ions is kept constant at its initial value (i.e. initial condition of Equation 3), along with Equations 5, 9-15 for the auxiliary AEs system reported in Table 2.2.2. Basically, with respect to the two-parameter formalism the SAR model introduces three additional phenomena (ion permeation, membrane surface area regulation, and counter-gradient of hydrostatic pressure to osmosis) along with five adjustable non-dimensional parameters (cell membrane resting tension Ω_{R}, thickness β and elastic modulus K', ion/salt permeability λ_{Ions}, and membrane relaxation rate constant λ_{S}). Since in the SAR model ion permeation depends on the opening of MS channels whose duration is governed by the rate of membrane relaxation which, in turn, is triggered by osmosis, a much more complex picture than in the two-parameter model is depicted, where all phenomena are strictly interrelated and affect each other.

2.2.2.2 Equilibrium with impermeant solutes

Cell volume ζ_{Cell} at osmotic equilibrium can be determined by solving model equations in Tables 2.2.1-2 at steady state. If a permeant CPA is absent, in the osmotic cycle with impermeant sucrose steady state is reached when the driving forces appearing in Equations 1, 3 and 4 for the exchange rate of water, ions and membrane reference surface are equal to zero. Assuming $\Delta\mathrm{p} \ll \Delta\omega$ and λ_{S} is small (so that membrane relaxation is

relatively slow and MS channels remain open during swelling), it was possible to derive the equations reported in Table 2.2.3 for the cell volume at equilibrium.

More specifically, in Equations 18-19 the equilibrium value of cell volume after an osmotic cycle with impermeant sucrose in the absence of CPA and with $\omega^{\mathrm{EXT,\,II}} \leq \omega^{\mathrm{EXT,\,I}}$ is reported: during phase I, cells first shrink due to the contact with hypertonic solutions of sucrose and ions ($\omega^{\mathrm{EXT,\,I}} = \omega_{\mathrm{Sucrose}}^{\mathrm{EXT,\,I}} + \omega_{\mathrm{Ions}}^{\mathrm{EXT,\,I}}$), then swell back when removing sucrose in phase II by contacting with relatively hypotonic solutions made only of ions, without sucrose ($\omega^{\mathrm{EXT,\,II}} = \omega_{\mathrm{Ions}}^{\mathrm{EXT,\,II}}$).

It is worth noting that a complete mechanical relaxation of membrane tension is assumed to be reached at the end of phase I, before phase II starts.

Table 2.2.3: Equilibrium conditions of the SAR model in non-dimensional form after an osmotic cycle with impermeant sucrose in the absence of CPA with $\omega^{\mathrm{EXT,\,II}} \leq \omega^{\mathrm{EXT,\,I}}$: phase I, contact with hypertonic solutions of sucrose and ions ($\omega^{\mathrm{EXT,\,I}} = \omega_{\mathrm{Sucrose}}^{\mathrm{EXT,\,I}} + \omega_{\mathrm{Ions}}^{\mathrm{EXT,\,I}}$); phase II, removing sucrose ($\omega^{\mathrm{EXT,\,II}} = \omega_{\mathrm{Ions}}^{\mathrm{EXT,\,II}}$).

Equation	Number
$\zeta_{\mathrm{Cell}}^{\mathrm{I}} = \underbrace{v_{\mathrm{B}}}_{\mathrm{Inactive}} + \underbrace{\left(\frac{1-v_{\mathrm{B}}}{1+\mu_{\mathrm{Ions}}}\right)\left(\frac{1}{\omega^{\mathrm{EXT,\,I}}}\right)}_{\mathrm{Water}} + \underbrace{\mu_{\mathrm{Ions}}\left(\frac{1-v_{\mathrm{B}}}{1+\mu_{\mathrm{Ions}}}\right)}_{\mathrm{Ions}}$	(18)
$\zeta_{\mathrm{Cell}}^{\mathrm{II}} = \underbrace{v_{\mathrm{B}}}_{\mathrm{Inactive}} + \underbrace{\left(\frac{1-v_{\mathrm{B}}}{1+\mu_{\mathrm{Ions}}}\right)\left(\frac{1}{\omega^{\mathrm{EXT,\,II}}}\right)\left(\frac{\mu_{\mathrm{Ions}}+\frac{\lambda_{\mathrm{Ions}}}{\omega^{\mathrm{EXT,\,I}}}}{\mu_{\mathrm{Ions}}+\frac{\lambda_{\mathrm{Ions}}}{\omega^{\mathrm{EXT,\,II}}}}\right)}_{\mathrm{Water}} + \underbrace{\mu_{\mathrm{Ions}}\left(\frac{1-v_{\mathrm{B}}}{1+\mu_{\mathrm{Ions}}}\right)\left(\frac{\mu_{\mathrm{Ions}}+\frac{\lambda_{\mathrm{Ions}}}{\omega^{\mathrm{EXT,\,I}}}}{\mu_{\mathrm{Ions}}+\frac{\lambda_{\mathrm{Ions}}}{\omega^{\mathrm{EXT,\,II}}}}\right)}_{\mathrm{Ions}}$	(19)

In Table 2.2.3 the contributions of water and ions to cell volume are highlighted. Note that $\mu_{\mathrm{Ions}} = \frac{\widetilde{v}_{\mathrm{Ions}}\, M^0}{\varphi}$ represents the ratio between the intracellular ion and water volumes at isotonic conditions: it is a very small number which is typically neglected in the two-parameter model.

During phase I, isotonic cells shrink, no ion exchange takes place since membrane tension is always lower than the resting value and MS channels remain closed. Thus, the classic Boyle Van't Hoff equation (i.e. Equation 18) resulting from the two-parameter model is derived also from the SAR model: a linear dependence between the cell volume at equilibrium ($\zeta_{\mathrm{Cell}}^{\mathrm{I}}$) and the inverse of the external osmolality ($\frac{1}{\omega^{\mathrm{EXT,\,I}}}$) allows the inactive volume fraction, v_B, to be determined through a simple linear regression. Besides, this Boyle Van't Hoff equation does not depend on temperature, and predicts a perfect osmometer behavior, that is $\zeta_{\mathrm{Cell}}^{\mathrm{II}} = 1$ when the isotonic conditions are re-established in phase II by setting $\omega^{\mathrm{EXT,\,II}} = 1$.

On the contrary, during the swelling in phase II in the SAR model cell membrane is stretched and reaches tensions above Ω_{R} which leads to MS channels opening and leakage of intracellular ions: now the cell volume at equilibrium is given by Equation 19. More specifically, the deviation from the Boyle Van't Hoff equation

is represented by the term $\left(\frac{\mu_{\mathrm{Ions}}+\frac{\lambda_{\mathrm{Ions}}}{\omega^{\mathrm{EXT,\,I}}}}{\mu_{\mathrm{Ions}}+\frac{\lambda_{\mathrm{Ions}}}{\omega^{\mathrm{EXT,\,II}}}}\right)$ (cf. with Equation 18), and it clearly depends on λ_{Ions}: now the linear profile of cell volume ($\zeta_{\mathrm{Cell}}^{\mathrm{II}}$) vs the reciprocal of external osmolality ($\frac{1}{\omega^{\mathrm{EXT,\,II}}}$) is lost, that is a non-perfect osmometer behavior results. It should be noted that, Equation 19 reduces to the Boyle Van't Hoff equation when $\lambda_{\mathrm{Ions}} = 0$: in such a case no leakage of ions may actually take place since ion permeability is zero, and the new model reduces to the two-parameter model at equilibrium. Moreover, since $\lambda_{\mathrm{Ions}}(\mathrm{T})$ shows an Arrhenius-like dependence, Equation 19 predicts a partial recovery of the isotonic cell volume that depends on system temperature.

2.2.2.3 Model Parameters

The corresponding values of the model parameters in non-dimensional form at room temperature are reported in Table 2.2.4.

Table 2.2.4: Model parameters in non-dimensional form (base case) determined at a system temperature of 298 K, based on the parameter values reported in Table 2.1.2.

Parameter	Expression	Value
β	$\frac{2\,h}{\left(\frac{3}{4\pi}V_{\mathrm{Cell}}^{0}\right)^{\frac{1}{3}}}$	$1.32\cdot10^{-1}$
λ_{CPA}	$\frac{\tilde{v}_{\mathrm{CPA}}\,P_{\mathrm{CPA}}(T)}{L_{\mathrm{P}}(T)\,R\,T}$	$6.26\cdot10^{-2}$
λ_{Ions}	$\frac{P_{\mathrm{Ions}}(T)}{L_{\mathrm{P}}(T)\,R\,T}$	$2.14\cdot10^{-3}$
λ_{S}	$\frac{k_{\mathrm{S}}\left(\frac{3}{4\pi}V_{\mathrm{Cell}}^{0}\right)^{\frac{1}{3}}}{3\,L_{\mathrm{P}}(T)}$	$8.42\cdot10^{1}$
μ_{CPA}	$\tilde{v}_{\mathrm{CPA}}\,M^{0}$	$2.13\cdot10^{-2}$
μ_{Ions}	$\frac{\tilde{v}_{\mathrm{Ions}}\,M^{0}}{\varphi}$	$4.05\cdot10^{-3}$
K'	$\frac{K}{2\,R\,T\,M^{0}}$	$2.22\cdot10^{-2}$
v_{B}	$\frac{V_{\mathrm{B}}}{V_{\mathrm{Cell}}^{0}}$	0.2
Ω_{R}	$\frac{\sigma_{\mathrm{R}}}{R\,T\,M^{0}}$	$1.11\cdot10^{-3}$

This represents the base case of the *one factor at time* parametric sweep analysis performed in this work, where every non-dimensional parameter is varied individually except for μ_{CPA}, μ_{Ions} and v_{B} that are kept constant. At first glance, based on the values of the kinetic parameters (cf. λ_{S}, λ_{CPA}, and λ_{Ions}) shown in Table 2.2.1, in the base case membrane relaxation should be the fastest phenomenon with respect to water permeation, while ion exchange should represent the slowest one.

2.2.3 Results and discussion

To the best of our knowledge, the SAR model is the first and only mathematical model available in the literature of cryopreservation addressing the behavior of non-perfect osmometer cells that do not return back to their initial volume when isotonic conditions are re-established after an osmotic excursion. In this work, a parametric sweep analysis is used to discuss model features in comparison with the two-parameter model. For the sake of clarity, this analysis is carried out by simulating the osmotic cycle with impermeant sucrose in the absence of permeant DMSO and vice versa.

2.2.3.1 Osmotic cycle with impermeant sucrose in the absence of permeant DMSO

The case of cells put in contact with sucrose is examined first. More specifically, isotonic cells are suspended in a hypertonic solution of sucrose added to isotonic ions (like PBS) in the shrinking phase I (i.e. $\omega_{\mathrm{Sucrose}}^{\mathrm{EXT,I}} = 1$, $\omega_{\mathrm{Ions}}^{\mathrm{EXT,I}} = 1$), before returning back to isotonic conditions when removing sucrose in the swelling phase II (i.e. $\omega_{\mathrm{Sucrose}}^{\mathrm{EXT,II}} = 0$, $\omega_{\mathrm{Ions}}^{\mathrm{EXT,II}} = 1$). The duration of phases I and II is the same and is kept constant equal to 10 in non-dimensional time τ, i.e. about ten times longer than the characteristic time of water permeation. This choice is to ensure that the trans-membrane exchange of water and solutes may reach equilibrium as well as membrane relaxation may be completed within any single phase composing the osmotic cycle, at least in the base case of the parametric sweep analysis.

For the base case value of model parameters given in Table 2.2.4, the resulting temporal profiles of cell volume (ζ_{Cell}) with its water (ζ_{W}) and ion (ζ_{Ions}) contributions are reported in Figure 2.2.2 (top panels).

Here the numerical solution of the SAR model (black lines) is compared with that of the two-parameter model (red lines) as obtained through the COMSOL Multiphysics® software run with a numerical tolerance of 10^{-6}. During phase I, cells shrink due to water exit and no difference in cell volume and its composition between the two models is shown, with a content of intracellular ions (ζ_{Ions}) remaining constant in time for both models. For the SAR model the temporal profiles of osmotic ($\Delta\omega$) and hydraulic pressure ($\Delta\mathrm{p}$) gradients along with the ratio $\frac{\Phi_{\mathrm{Sph}}}{\Phi_{\mathrm{Ref}}}$ are also shown in Figure 2.2.2 (bottom panels). The osmotic driving force between the intra- and extracellular compartments ($\Delta\omega$) starts from a negative value and progressively increases as water exits the cell until vanishing at the end of phase I, when the osmotic equilibrium is reached. On the other hand, the hydraulic pressure counter-gradient ($\Delta\mathrm{p}$) first decreases (starting from zero and becoming negative counteracting water exit), then reverses the direction and starts increasing (remaining negative to keep on to counteract water exit), thus showing a minimum before vanishing at the end of phase I.

This behavior is due to membrane relaxation represented by the temporal profile of the ratio $\frac{\Phi_{\mathrm{Sph}}}{\Phi_{\mathrm{Ref}}}$ reported in Figure 2.2.2: an initial decrease of Φ_{Sph} triggered by water exosmosis with membrane tension becoming slack (see Equations 7-8), followed by a returning back to its resting condition as Φ_{Ref} catches up with Φ_{Sph} according to Equation 4 by removing excess membrane into membrane reservoirs.

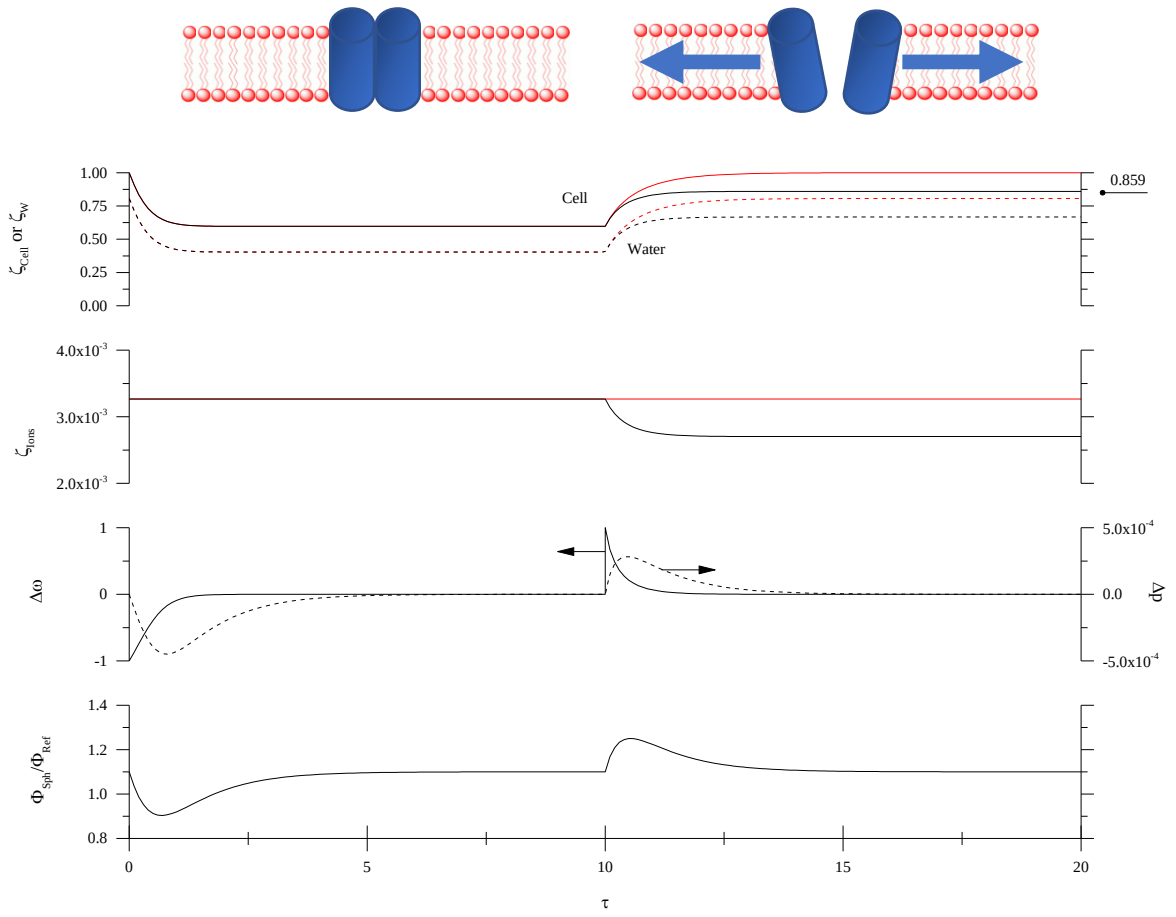

Figure 2.2.2: Osmotic cycle with impermeant sucrose in the absence of permeant CPA: comparisons between the results of the SAR model (black) and the two-parameter model (red) using the parameter values reported in Table 2.2.4 (base case).

Accordingly, during the shrinking phase I MS channels remain closed and ions are not exchanged; the two-parameter and the SAR models show the same profiles for ζ_{Cell}, ζ_W and ζ_{Ions} and their simulations cannot be distinguished. On the contrary, during phase II swelling occurs so that cell volume and water content increase as shown in Figure 2.2.2. Now, in the SAR model the cell membrane is stretched from the beginning of phase II but membrane relaxation is eventually completed once again as represented by the value of $\frac{\Phi_{Sph}}{\Phi_{Ref}}$: it promptly increases due to the increase of Φ_{Sph} triggered by osmosis, then reaches a maximum before returning back towards its initial value as Φ_{Ref} catches up with Φ_{Sph} through the recruitment of extra lipid bilayer from accessible membrane reservoirs. Accordingly, during the swelling phase II MS channels are always open and ions are exchanged in the SAR model, while they are impermeant in the two-parameter model. Now the simulations with the two models are different: since at the start of phase II the extracellular compartment is hypotonic with respect to cytoplasm (i.e. $\Delta\omega = \Delta\omega_{Ions} > 0$), ion content inside the cell decreases in the SAR model. For this reason the amount of water entering the cells before equilibrium is eventually reached is lower with respect to the two-parameter model, and a cell volume smaller than the initial isotonic one is finally attained (i.e. $\zeta_{Cell} = 0.859 \ @ \tau = 20$).

A closer look to Figure 2.2.2 reveals that in the SAR model the hydrostatic pressure gradient Δp ($\sim 10^{-4}$) may be safely neglected with respect to $\Delta\omega$ (~ 1) when determining the driving force of water exchange rate represented by Equation 1. Together with the MS channels remaining closed these are the reasons why the temporal profiles of cell volume (ζ_{Cell}), water and ion content (ζ_W and ζ_{Ions}) from the SAR and the two-parameter models cannot be distinguished in phase I, while their difference in phase II may be ascribed only to ion exchange. Moreover by looking at the temporal profiles of $\frac{\Phi_{Sph}}{\Phi_{Ref}}$, membrane relaxation is the slowest phenomenon among those accounted for in the SAR model both in phase I and II, even though its constant is about 100 times larger than water permeability (i.e. $\lambda_S \sim 10^2$ in Table 2.2.4). This behavior is due to Φ_{Ref} which, regardless of the specific value assigned to λ_S, always follows water osmosis with some delay and tries to keep up with the variations of Φ_{Sph}, both slowing down when approaching the steady state.

The equilibrium conditions given by Equations 18-19 are plotted in Figure 2.2.3 for the base case (bold lines).

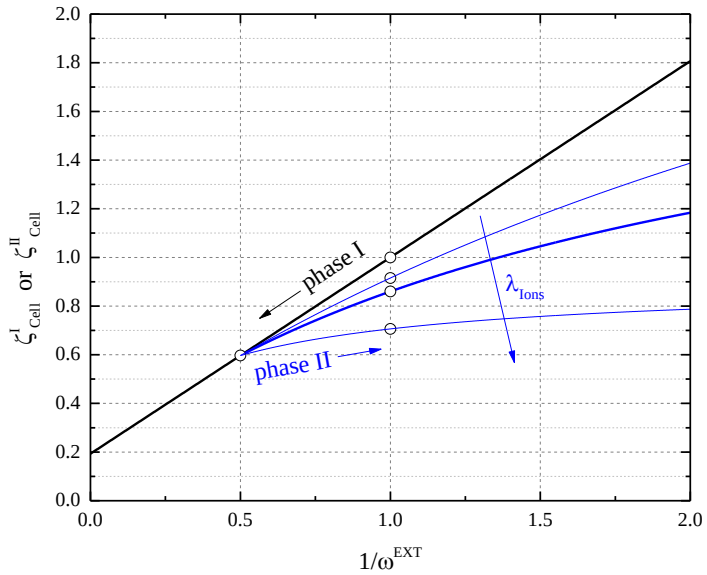

Figure 2.2.3: Equilibrium conditions (ζ^{I}_{Cell} and ζ^{II}_{Cell}) of the SAR model for the osmotic cycle with sucrose in the parametric sweep analysis: variation of ion permeability ($\lambda_{Ions} = 1.07 \cdot 10^{-3}$, $2.14 \cdot 10^{-3}$, $1.07 \cdot 10^{-2}$), with base case in bold lines. Circles represent the corresponding numerical integration of the dynamic SAR model (ζ_{Cell} @ $\tau = 10$ and ζ_{Cell} @ $\tau = 20$).

Here, a perfect agreement is shown with the values (circles) reached by ζ_{Cell} at the end of phase I and II taken from the corresponding dynamic simulation of the SAR model reported in Figure 2.2.2 (i.e. ζ_{Cell} @ $\tau = 10$ and ζ_{Cell} @ $\tau = 20$ for phase I and II, respectively). Actually, as shown in Figure 2.2.3 this agreement may be extended to the cases when ion permeability is varied with respect to its base case value in the parametric sweep analysis, by using a smaller ($1.07 \cdot 10^{-3}$) and larger ($1.07 \cdot 10^{-2}$) λ_{Ions} (not shown for the sake of brevity). The reason of this agreement is that the equilibrium equations were derived under the assumptions of a negligible hydrostatic pressure gradient and a relatively slow but complete membrane relaxation within every single phase of the osmotic cycle; as seen above, these are two conditions that result and are also met by dynamic simulations.

As clearly shown in Figure 2.2.3, only the swelling phase II is affected by the change of ion permeability, given that in the shrinking phase I membrane tension is slack, MS channels remain closed, and ions are not exchanged. More specifically, at the end of the osmotic cycle the recovery of the initial, isotonic cell volume in phase II is lower if λ_{Ions} increases, since a higher ion leakage from cells takes place during the swelling. Clearly when λ_{Ions} is equal to zero, the SAR model reduces to the two-parameter model and a perfect osmometer behavior is obtained, with a complete recovery of the isotonic volume at the end of the osmotic cycle. On the other hand, when increasing ion permeability, the recovery of the isotonic cell volume achieved during phase II is progressively hindered, and the cells remain shrunk at the volume reached at the end of phase I.

To proceed with the parametric sweep analysis, the variation of the membrane relaxation rate constant λ_S is now investigated. The case of an infinitely slow membrane relaxation (i.e. $\lambda_S = 0$) for the SAR model is considered in Figure 2.2.4, where the temporal profiles of the same variables reported in Figure 2.2.2 are shown.

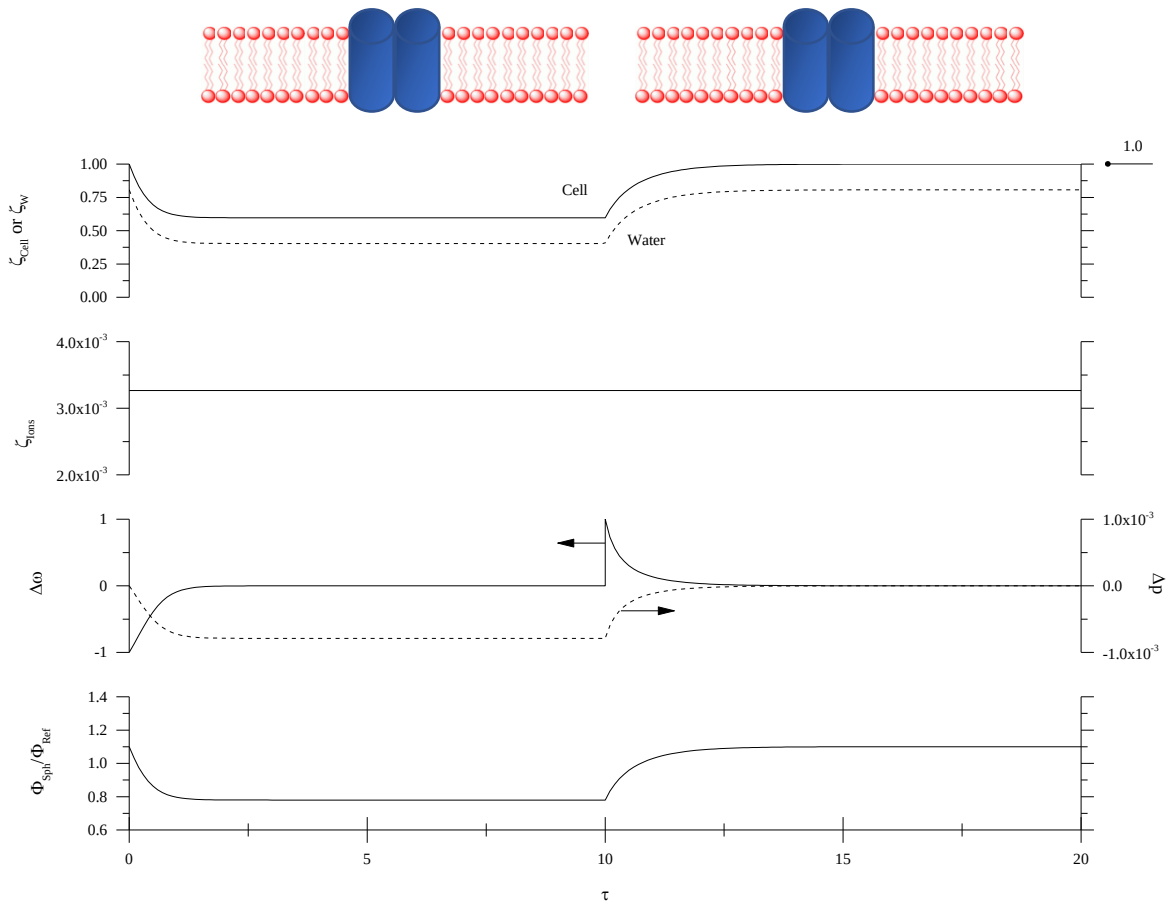

Figure 2.2.4: Osmotic cycle with impermeant sucrose in the absence of permeant CPA: results of the SAR model in the parameter sweep analysis with an infinitely slow membrane relaxation rate ($\lambda_S = 0$). The simulation of the two-parameter model is not reported because it does not change from Figure 2.2.2.

Now Φ_{Ref} does not change with time and remain constant at its initial value according to Equation 4, while Φ_{Sph} follows the osmotic shrinkage and swelling during phase I and II, respectively. For this reason, in Figure

2.2.4 the ratio $\frac{\Phi_{Sph}}{\Phi_{Ref}}$ is always smaller than its initial value, i.e. the cell membrane is always slack during the entire osmotic cycle and the initial resting condition is eventually reached only at the end of phase II. Thus, MS channels are always closed and no ion exchange takes place, i.e. a complete recovery of the isotonic cell volume is reached at the end of phase II ($\zeta_{Cell} = 1 \ @ \ \tau = 20$), just like in the two-parameter model. Actually, in this case not only the final value at equilibrium but the full temporal profiles of cell volume (ζ_{Cell}) with its water (ζ_W) and ion (ζ_{Ions}) contributions simulated by the two models are the same during the whole osmotic cycle. cycle investigated in this work: for instance, if the isotonic cells were contacted with a hypotonic instead. However, this equivalence between the two models is only apparent and depends on the specific osmotic of a hypertonic solution before returning to isotonic conditions (a simulation not shown for brevity), a stretched membrane with MS channels always open and the exchange of ions would be obtained in the SAR model even when $\lambda_S = 0$. This would lead to an equilibrium cell volume at the end of the osmotic cycle different from the initial, isotonic one in the SAR model, while a complete recovery would be simulated by the two-parameter model as always. Therefore when an infinitely slow membrane relaxation is considered the SAR model does not reduce to the two-parameter model.

The case of $\lambda_S = 8.42$ (i.e. about ten times smaller than its base case value) is reported in Figure 2.2.5 for the SAR model. In comparison with Figure 2.2.4, now ions are exchanged during phase II as it was for the base case shown in Figure 2.2.2: in particular, ion leakage starts when MS channels open since the membrane is stretched above its resting value, as highlighted by the vertical green line.

However, the opening time of the MS channels does not coincide with the start of phase II as it was in Figure 2.2.2, but is delayed in time depending on λ_S: the lower λ_S the later the opening of MS channels with respect to the beginning of phase II.

As a consequence, when gradually reducing the constant of membrane relaxation rate λ_S, a progressively shorter temporal window of MS channels opening during phase II is obtained so that no opening at all occurs when λ_S reaches its minimum value as shown in Figure 2.2.4.

This narrowing down of the temporal window for MS channels opening in phase II as λ_S decreases causes a smaller ion leakage from the cells which in turn leads to a larger water swelling, and a more complete recovery of the isotonic cell volume at the end of the osmotic cycle (cf. Figure 2.2.2 with Figure 2.2.5 and then Figure 2.2.4, where $\zeta_{Cell} \ @ \ \tau = 20$ changes from 0.859 to 0.908 and then 1, respectively).

Besides, in Figures 2.2.4-5 Δp ($\sim 10^{-3}$) is still negligible with respect to $\Delta\omega$ (~ 1) for the determination of the driving force of water exchange in Equation 1, whereas it is expected to increase much more when the membrane relaxation constant is reduced so significantly from the base case shown in Figure 2.2.2.

The low sensitivity of the SAR model to λ_S is highlighted in Figure 2.2.6, where the cell volume reached at the end of phase II when the dynamic simulation of the osmotic cycle is completed (i.e. $\zeta_{Cell} \ @ \ \tau = 20$) is reported in a semi-log plot to account for a wide variation of this parameter.

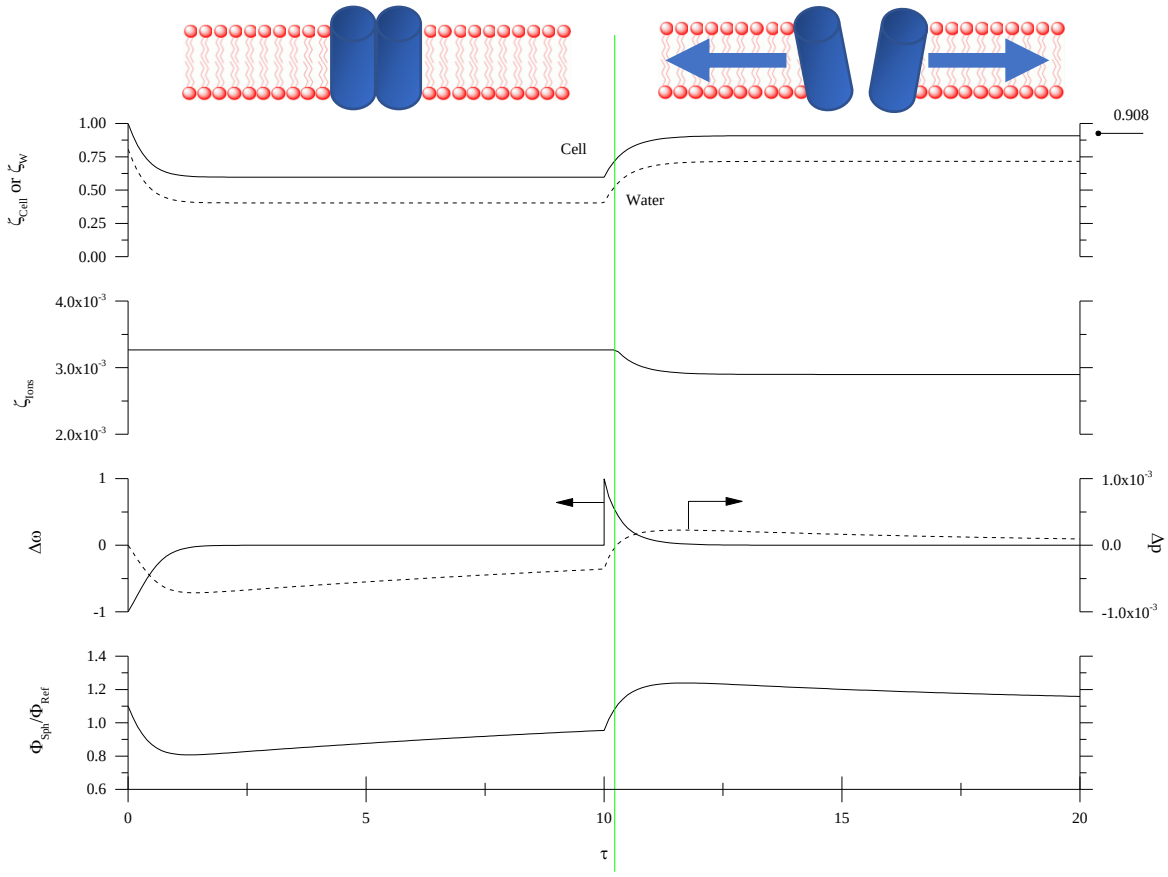

Figure 2.2.5: Osmotic cycle with impermeant sucrose in the absence of permeant CPA: results of the SAR model in the parameter sweep analysis with a membrane relaxation rate slower than in the base case ($\lambda_S = 8.42$). The vertical, green line represents the time of MS channels opening. The simulation of the two-parameter model is not reported because it does not change from Figure 2.2.2.

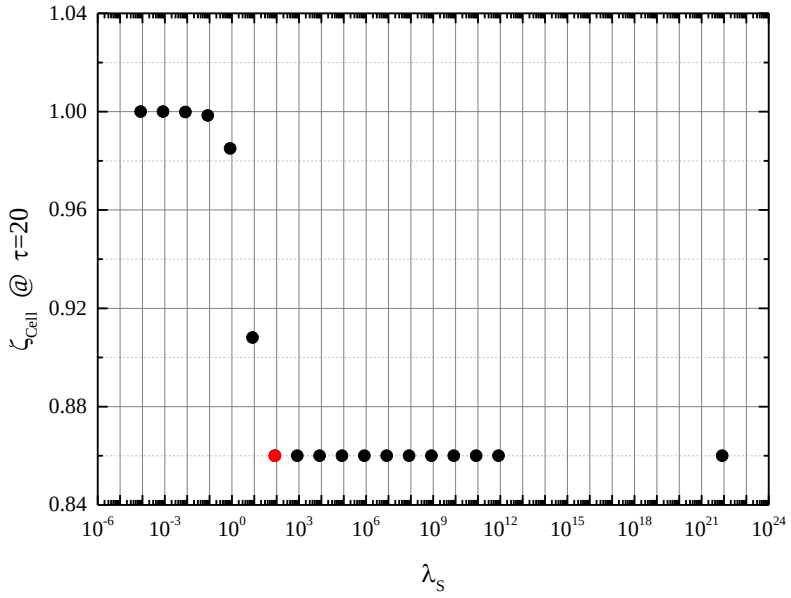

Figure 2.2.6: Osmotic cycle with impermeant sucrose in the absence of permeant CPA: results of the SAR model in terms of the cell volume at the end of phase II (ζ_{Cell} @ $\tau = 20$) for the sweep of parameter λ_S (total duration of osmotic cycle is 20, i.e. 10 for both phase I and II); base case in red.

It is shown that, starting from the base case (red symbol) an increase of 20 orders of magnitude for λ_S does not affect the cell volume attained at the end of phase II which remains constantly equal to 0.859, i.e. the same value given by the equilibrium condition plotted in Figure 2.2.3 for the base case.

On the other hand, when λ_S is decreased from its base case value the final cell volume increases until reaching a complete recovery of the initial, isotonic cell volume. This is caused by a too slow membrane relaxation rate with respect to the other phenomena taken into account in the SAR model: in this region of the parametric space the relaxation of cell membrane is not completed within the shrinking phase I when lowering λ_S below a critical value and keeping constant the duration of the phase. Thus, when the swelling phase II starts membrane is still slack as in Figure 2.2.5, and MS channels do not open and ion leakage does not begin until enough water has entered the expanding cell and membrane stretching may begin. The determination of this precise moment is not easy unless by the numerical integration of the full set of ODEs and AEs in Tables 2.2.1-2, and the equilibrium conditions given by Equations 18-19 are not valid in this region of the parametric space. On the contrary, when membrane relaxation is relatively fast the equilibrium Equations 18-19 are capable to predict the system behavior in a very wide range of λ_S as shown in Figure 2.2.6. Therefore, the validity of the derived equilibrium conditions may be extended not only to any value assigned to ion permeability λ_{Ions} but also to any value used for the constant of the membrane relaxation rate λ_S, provided that the phase duration is long enough that membrane relaxation is completed.

Besides, it is apparent that the two-parameter model represents the special subcase of the SAR model with an infinitely fast membrane relaxation, i.e. $\lambda_S = +\infty$. In fact, in such a limiting case Φ_{Ref} instantaneously follows the osmotic variations of Φ_{Sph}, so that the membrane is neither slack (in phase I) nor stretched (in phase II) but constantly kept at its resting tension, MS channels are always closed, and ions are never exchanged. Unfortunately, this cannot be shown through a numerical integration, since it is not possible to set an infinite value for λ_S. Moreover, regardless of the specific numerical algorithm adopted to solve the equations of the model, a limitation on the use of very large numbers always emerges from the need to respect a numerical tolerance, depending on the accuracy of the computing machine.

A very similar behavior shown by the SAR model when varying λ_S is obtained in the parametric sweep of the elastic modulus K' of cell membrane tension (not shown for the sake of brevity). In fact when reducing K' from its base case value a cell with a more elastic membrane is considered. This corresponds from one side to a reduced hydrostatic pressure difference Δp (becoming even more negligible with respect to the osmotic driving force $\Delta\omega$ in the water exchange rate), from the other to a slower membrane relaxation rate that is not completed within phase I. Therefore, when K' is gradually reduced the opening of MS channels during phase II is delayed and ion exchange begins progressively later than the start of phase II. Thus a reduced leakage of ions is obtained and the cell volume reached at the end of the osmotic cycle increases towards the complete recovery of the initial, isotonic cell volume. On the contrary, if K' increases above its base case value, membrane relaxation is fast enough to be concluded within phase I; now ion leakage starts at the very beginning of phase II, and cell volume at the end of any phase composing the osmotic cycle reaches the same values determined by the equilibrium conditions represented by Equations 18-19. Moreover, the hydrostatic pressure

difference remains negligible in comparison with the osmotic driving force. Therefore, the validity of the equilibrium Equations 18-19 for the osmotic cycle with impermeant sucrose in the absence of a permeant CPA may be extended to any value assigned to the elastic modulus K', provided that the phase duration is long enough that cell membrane relaxation is completed. Besides, it is apparent that the SAR model reduces to the two-parameter model when considering an infinitely large elastic modulus, i.e. $K' = +\infty$. In this case, an infinitively rigid membrane that is kept always at resting condition is obtained. Again, this result cannot be shown through a numerical integration of model equations since an infinite value for K' cannot be set nor can very large numbers be used at a pre-set numerical tolerance.

Proceeding further with the parametric sweep analysis, a negligible sensitivity of the SAR model is found with respect to the resting tension Ω_R: wide variations of this parameter are capable to affect very slightly only the hydrostatic pressure difference Δp that remains negligible in comparison to Δω anyway. For this reason, no further comments are reported in this work on this parameter, and the equilibrium conditions of Equations 18-19 are always valid. On the contrary, the effect of β is shown in Figure 2.2.7 where the cell volume reached at the end of phase II when the dynamic simulation of the osmotic cycle is completed (i.e. $\zeta_{\text{Cell}}\ @\ \tau = 20$) is reported in a semi-log plot to account for a wide variation of this parameter.

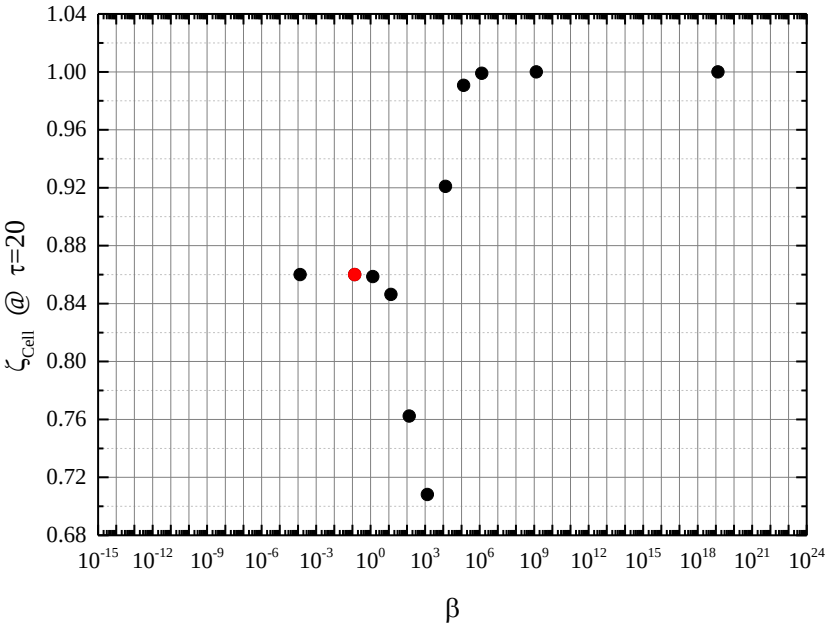

Figure 2.2.7: Osmotic cycle with impermeant sucrose in the absence of permeant CPA: results of the SAR model in terms of the cell volume at the end of phase II ($\zeta_{\text{Cell}}\ @\ \tau = 20$) for the sweep of parameter β (total duration of osmotic cycle is 20, i.e. 10 for both phase I and II); base case in red.

It is shown that by decreasing β from its base case value (red symbol) the numerical solution of the SAR model does not change and remains equal to 0.859, i.e. the same value given by the equilibrium conditions plotted in Figure 2.2.3. On the contrary, when this parameter increases the cell volume at the end of phase II shows a minimum, i.e. it first decreases then grows up to its maximum possible value in this simulation that corresponds to a complete recovery of the initial, isotonic cell volume. To understand this behavior, it is worth noting that

β represents the ratio between membrane thickness and isotonic cell radius. As such it greatly affects the hydrostatic pressure difference Δp determined through the Laplace law expressed by Equation 6.

This is shown in detail in Figure 2.2.8 where the results of the simulations with the SAR and the two-parameter models are compared for the case of a three orders of magnitude increase with respect to the base case value, i.e. $\beta = 1.32 \cdot 10^2$: during the shrinking phase I the exosmosis of water driven by the osmotic driving force $\Delta\omega$ (~1) is now visibly hindered by the counter-gradient of hydrostatic pressure Δp (~0.3), and a slower osmosis results (cf. Figures 2.2.2 and 2.2.8).

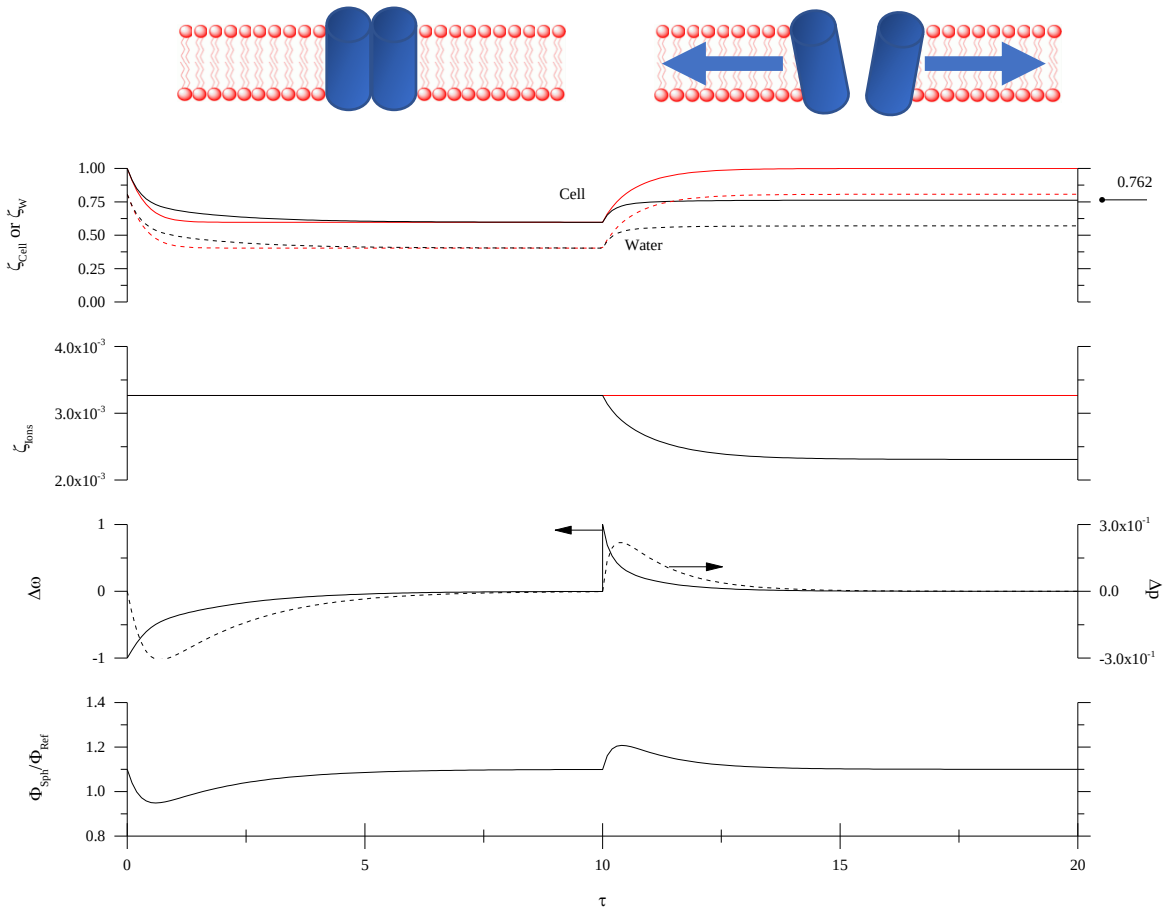

Figure 2.2.8: Osmotic cycle with impermeant sucrose in the absence of permeant CPA: comparisons between the results of the SAR model (black) and the two-parameter model (red) in the parameter sweep analysis with $\beta = 1.32 \cdot 10^2$, three orders of magnitude increase with respect to its base case value. The simulation of the two-parameter model is reported for convenience even though it does not change with respect to Figure 2.2.2.

Despite this a complete membrane relaxation is still achieved in phase I since the ratio $\frac{\Phi_{Sph}}{\Phi_{Ref}}$ returns to its initial value. Moreover, the SAR and the two-parameter models share the same extension of the shrinkage of cell volume and water content albeit following different dynamic paths, given that MS channels are closed and no ion-exchange takes place. On the contrary, during phase II the stretching of cell membrane begins immediately when the phase starts: MS channels promptly open and ion leakage may occur from the beginning of the phase.

In comparison with the base case reported in Figure 2.2.2, due to the large counter-gradient of hydrostatic pressure Δp that significantly limits the swelling of water driven by the osmotic driving force $\Delta\omega$, a more pronounced ion leakage is now obtained in phase II (cf. ζ_{Ions} @ $\tau = 20$). As a consequence, less water swells back during phase II and a smaller cell volume is eventually reached at the end of the osmotic cycle (i.e. $\zeta_{\mathrm{Cell}} = 0.762$ @ $\tau = 20$). If parameter β increases even further (i.e. $\beta = 1.32 \cdot 10^4$, five orders of magnitude larger than its base case value, not shown for the sake of brevity) the duration of phase I is not long enough for a complete membrane relaxation due to a very high counter-gradient of hydrostatic pressure Δp ($\sim$1.2): in this case osmosis and cell volume excursions are basically stopped during the entire osmotic cycle, and a limited ion leakage takes place in phase II.

Basically these results confirm that the validity of the equilibrium conditions represented by Equations 18-19 is strictly confined to a negligible counter-gradient of the hydrostatic pressure Δp with respect to the osmotic driving force $\Delta\omega$, as it was originally assumed during the derivation. However, it is worth noting that values of $\beta \geq 1$ are not really possible, given that membrane thickness is always smaller than cell radius. Thus, when limiting the results of the parametric sweep analysis to realistic values assigned to the model parameters, the derived equilibrium Equations 18-19 can be considered generally valid, and the hydrostatic pressure difference may be safely neglected to determine the driving force of water exchange in Equation 1. This conclusion represents a relevant simplification of the SAR model for future use but it is also a very reassuring result, given that a negligible hydrostatic pressure difference across the membrane of any animal cell is a reiterated assumption in the literature of cryopreservation, physiology and bio-physics addressing the modelling of cell osmosis and the control of cell volume and shape.

2.2.3.2 Osmotic cycle with permeant DMSO in the absence of impermeant sucrose

The case of cells in contact with permeant DMSO in the absence of sucrose is examined to highlight the effect of CPA permeability λ_{CPA}. More specifically, the investigated osmotic cycle consists of isotonic cells first suspended in a hypertonic solution of DMSO added to isotonic ions (like PBS) in phase I ($\omega_{\mathrm{CPA}}^{\mathrm{EXT,I}} = 5.67$, $\omega_{\mathrm{Ions}}^{\mathrm{EXT,I}} = 1$), followed by CPA removal in phase II by returning back to isotonic ions ($\omega_{\mathrm{CPA}}^{\mathrm{EXT,II}} = 0$, $\omega_{\mathrm{Ions}}^{\mathrm{EXT,II}} = 1$). For the base case parameter values given in Table 2.2.4, the resulting temporal profiles of cell volume with its water, ion and CPA contributions are reported in Figure 2.2.9 (top panels) for the two-parameter and the SAR models.

During phase I DMSO is loaded into cell cytoplasm (ζ_{CPA}) and the well-known shrink-swell dynamics followed by the cell volume (ζ_{Cell}) is obtained with both models: isotonic cells suspended in a hypertonic solution initially shrink by losing water and accumulating CPA to increase internal osmolality, until the external osmolality is first reached and then overcome when cells start swelling back, thus showing a minimum in volume excursion. The two-parameter and SAR models show the same temporal profiles exclusively up to a point indicated by the first green line shown in Figure 2.2.9, when stretching of cell membrane begins after the swelling has already started.

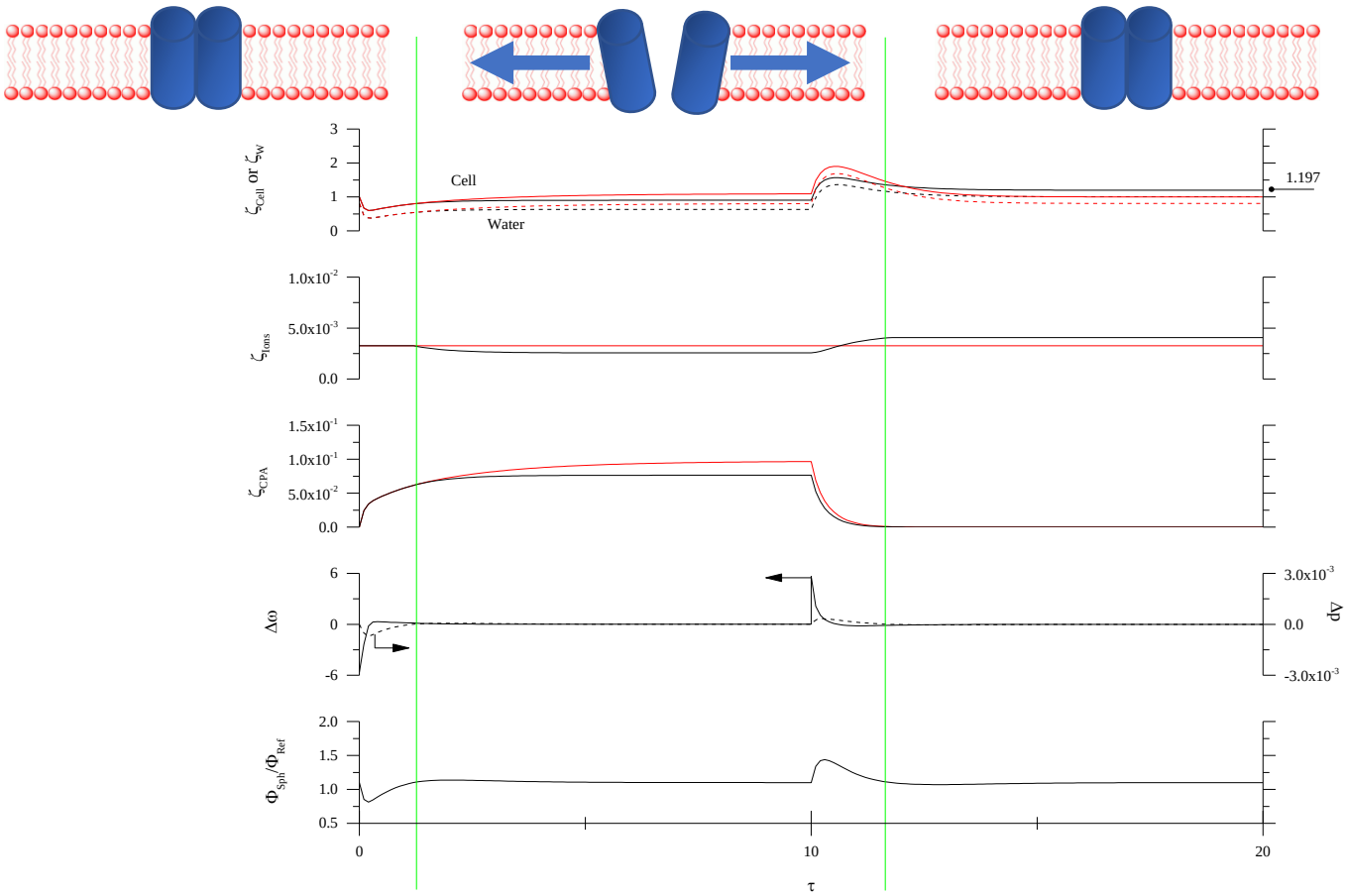

Figure 2.2.9: Osmotic cycle with permeant DMSO in the absence of impermeant sucrose: comparisons between the results of the SAR model (black) and the two-parameter model (red) using the parameter values reported in Table 2.2.4 (base case). The vertical, green lines indicate opening and closing of MS channels.

At this point, MS channels open and ion leakage from the now hypertonic cells begins in the SAR model, while a constant ion content inside the cells is simulated by the two-parameter model. As a consequence, in the two-parameter model the cell volume reached at the end of phase I is larger than both its initial, isotonic value (due to CPA addition to cytoplasm) and the corresponding cell volume simulated by the SAR model, where a simultaneous ion leakage took place.

Generally speaking, the cell volume reached at the end of phase I in the SAR model may result above, equal to, or below, the initial, isotonic cell volume: it depends on the extent of ion leakage during CPA addition which varies with the parameter values and operating conditions. In Figure 2.2.9, in particular, the cell volume reached at the end of phase I in the SAR model is lower than the initial, isotonic cell volume since a relatively extended ion leakage with respect to CPA addition is obtained with the adopted parameter values and operating conditions. As shown in the middle panel of Figure 2.2.9, the CPA quantity loaded into the cells at the end of phase I is larger in the two-parameter model than in the SAR model. Moreover, cell membrane relaxation in the SAR model is completed within the duration of phase I, and the hydrostatic pressure difference is always negligible with respect to the osmotic gradient, as shown in the bottom panels of Figure 2.2.9.

During phase II, when removing DMSO the well-known swell-shrink dynamics is simulated by the two models. The cells initially swell by accumulating water and releasing CPA to reduce the internal osmolality even if in the SAR model intracellular ions increase, driven by the negative $\Delta\omega_{\mathrm{Ions}}$ in Equation 16 resulting from the water uptake. This process continues until the external osmolality is first reached and then overcome so that cells shrink back, thus showing a maximum in volume excursion. In contrast with phase I, now the temporal profiles simulated by the two models are different for the whole duration of phase II: in the SAR model cells start to accumulate ions at the beginning of phase II when the membrane is promptly stretched and MS channels open, while a constant ion content is obtained with the two-parameter model. The ion exchange simulated by the SAR model continues until membrane relaxation is eventually reached as indicated by the second vertical green line shown in Figure 2.2.9. The late opening of MS channels with respect to the start of phase I is responsible of the different extent of the ion exchange in the SAR model between the two phases composing the osmotic cycle: more ions enter the cells in phase II than exit in phase I as clearly shown in Figure 2.2.9. As a consequence, at the end of the osmotic cycle the water content and cell volume are larger than their initial isotonic values in the SAR model (i.e. $\zeta_{\mathrm{Cell}} = 1.197 \,@\, \tau = 20$), while a complete recovery is obtained according to the two-parameter model.

The temporary opening of MS channels in the SAR model is represented by the temporal window contained between the two vertical green lines shown in Figure 2.2.9, whose position depends on the values of the model parameters as well as on the operating conditions (such as external osmolality and its composition, system temperature, and phase duration). Cell volume and its components reached at the end of the osmotic cycle depend on the position of this temporal window which cannot be determined easily for any possible run unless by a numerical integration of system dynamics represented by the entire set of ODEs and AEs of the SAR model. This is what prevents the derivation from the SAR model of the equilibrium conditions for the osmotic cycle with a permeant CPA. On the contrary, for the osmotic cycle with impermeant sucrose in the absence of CPA the position of this temporal window may be easily predicted: if phases I and II are sufficiently long, MS channels remain closed or open respectively, without any switching during the whole duration of any single phase, and the equilibrium conditions represented by Equations 18-19 in Table 2.2.3 can be derived.

To demonstrate the relevant role played by the position of the temporary opening of MS channels and the irregularities of the simulations with the SAR model, the osmotic cycle when the adopted CPA permeability λ_{CPA} is one order of magnitude smaller than its base case value is shown in Figure 2.2.10.

As expected, the system response is generally slower for both the two-parameter and the SAR models when compared with the base case (cf. Figures 2.2.9 and 2.2.10). In particular, the shrink-swell dynamics of phase I is still simulated by both models with a more pronounced initial cell shrinkage before swelling starts, as expected. Accordingly the opening of MS channels in the SAR model is delayed with respect to the base case. Despite this, a larger ion leakage is obtained (cf. $\zeta_{\mathrm{Ions}} \,@\, \tau = 10$ in Figures 2.2.9 and 2.2.10). This unexpected behavior is due to a faster ion exchange as determined by Equation 3: when a lower λ_{CPA} is used an increased driving force $\Delta\omega_{\mathrm{Ions}}$ results from the more pronounced initial shrinkage of cell volume and water exosmosis.

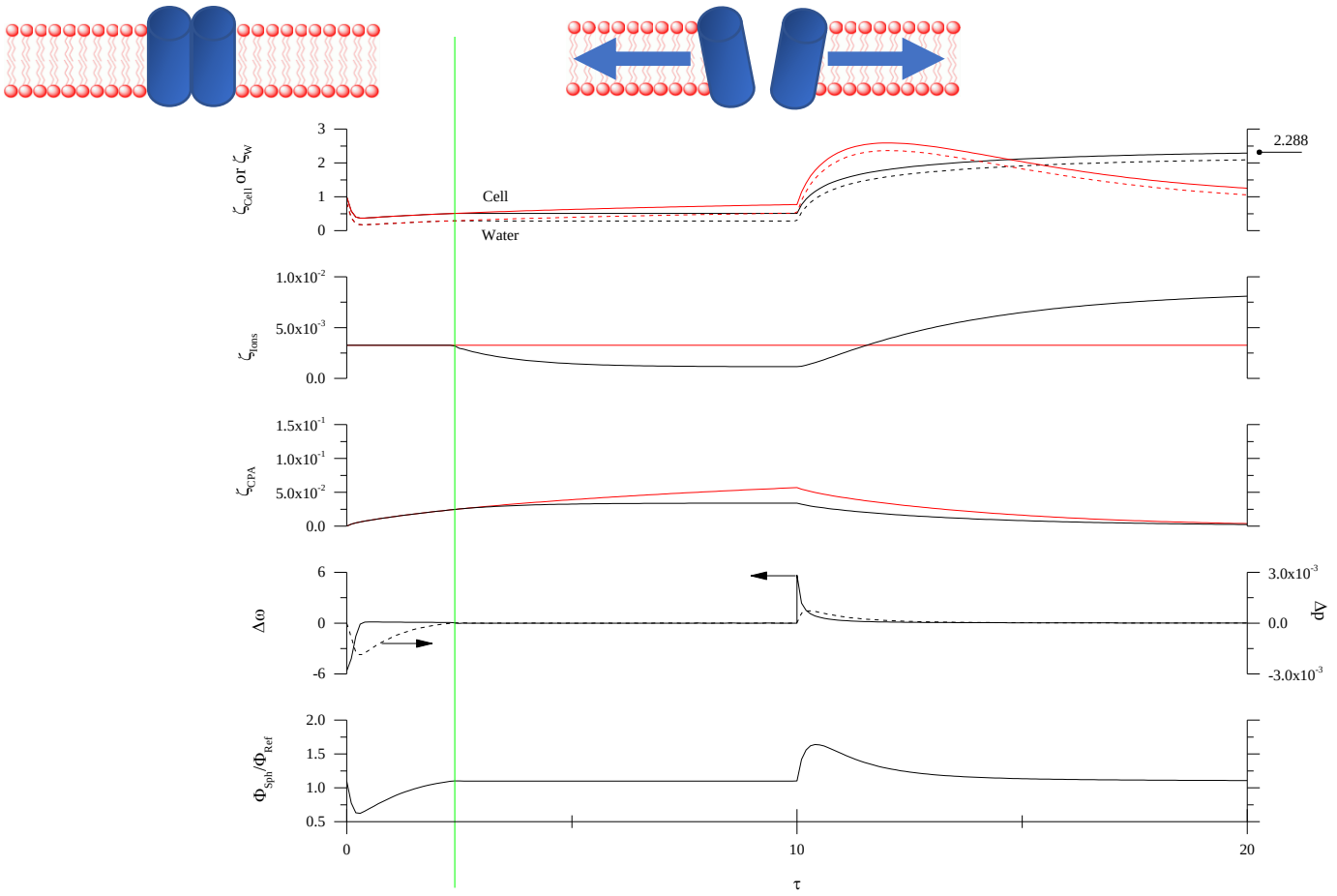

Figure 2.2.10: Osmotic cycle with permeant DMSO in the absence of impermeant sucrose: comparisons between the results of the SAR model (black) and the two-parameter model (red) in the parameter sweep analysis with $\lambda_{CPA} = 6.26 \cdot 10^{-3}$, one order of magnitude decrease with respect to its base case value. The vertical, green line indicate opening of MS channels.

Regarding this aspect it is worth noting that when further decreasing λ_{CPA} to critical values the case of an impermeant CPA is eventually simulated: if phase duration is maintained constant, the shrink-swell dynamics of phase I progressively disappears being replaced by only shrinkage. In such a limiting case, since no opening of MS channels occurs during phase I, the corresponding simulations with the SAR and the two-parameter models cannot be distinguished anymore for the whole phase I, and a constant ion content inside the cells is obtained with both models.

Therefore, in the SAR model the extent of ion leakage during phase I shows a maximum when λ_{CPA} is reduced starting from the base case value while keeping constant the duration of the phase; this corresponds to a minimum in water and CPA content (ζ_W, ζ_{CPA} @ $\tau = 10$) as well as in cell volume (ζ_{Cell} @ $\tau = 10$) lower than the initial, isotonic value. This is just an example of the complexity and irregularity of the system behavior simulated by the SAR model in comparison with the two-parameter formalism. This irregularity of the SAR model outcomes is due to the non-linear interconnection among all the different phenomena accounted for, and increases significantly when varying the operating conditions (such as external osmolality and its composition, system temperature, and phase duration) instead of keeping them constant as in this work.

Another example of the irregularity in the SAR model outcomes is obtained in the phase II shown in Figure 2.2.10: when CPA permeability is decreased with respect to its base case value, the characteristic swell-shrink dynamics of phase II is still simulated by the two-parameter model whereas it is lost in the SAR model. According to the latter one, only swelling occurs and MS channels are never closed. As a consequence, while in the two-parameter model cells return back to the initial isotonic volume at the end of the osmotic cycle with a complete CPA removal and a constant ion content, in the SAR model cell volume levels up to a larger value, with CPA totally removed but with an increased content of intracellular ions in comparison with the initial, isotonic conditions. This peculiar osmotic response is due to a critically slow CPA removal rate: when λ_{CPA} is reduced, during phase II CPA inside the cells is retained more than in the base case; even if water swelling has already started the cells remain hypertonic with respect to the suspending solution, the cell membrane remains stretched and MS channels open so that the extracellular ions continue to enter the cells until membrane relaxation is eventually completed.

To conclude the parametric sweep analysis, when CPA permeability is increased one order of magnitude with respect to its base case value, the system response is generally faster for both models (not shown for the sake of brevity): as expected, in the SAR model the opening and closing of MS channels are anticipated in phase I and II, respectively, with preservation of shrink-swell dynamics followed by the swell-shrink one.

It is worth noting that, the order of magnitude for the water and CPA exchange rates considered in this case are comparable (i.e. $\lambda_{\mathrm{CPA}} = 6.26 \cdot 10^{-1}$), while ion exchange is much slower ($\lambda_{\mathrm{Ions}} = 2.14 \cdot 10^{-3}$ in Table 2.2.4). As a consequence, during phase I and II only water and CPA are actually exchanged, with ion content remaining nearly constant even in the SAR model, regardless of the opening of MS channels. Accordingly, a limited cell volume excursion is obtained, and a very similar system response is simulated by the two-parameter and SAR models: in other words, when CPA permeability increases towards water permeability the SAR model reduces to the two-parameter model due to a negligible ion exchange.

2.2.4 Concluding remarks

In this work, the recently proposed SAR model is addressed in contrast with the classic two-parameter model to describe the non-perfect osmotic behavior of a cell suspension during cryopreservation. First, an appropriate non-dimensional version of the model equations is derived to identify the relevant non-dimensional parameters. Then, a parametric sweep analysis is performed and discussed to highlight the features of the proposed model. It is shown that the SAR model progressively reduces to the two-parameter formalism when a negligible ion/salt exchange between intra- and extracellular compartments takes place, i.e. when ion/salt permeability is reduced below a critical value or CPA permeability is increased above a critical one. For the same reason, the SAR model with a cell membrane characterized by zero elasticity or infinite constant of relaxation rate is equivalent to the two-parameter model, given that at these extreme conditions MS channels cannot open.

Generally speaking, in the SAR model cell volume and its composition at equilibrium are shown to depend on the position of the temporal window of MS channels opening, which is a complex function of model parameters and operating conditions: whereas at the end of any osmotic cycle a complete recovery of the initial, isotonic

cell volume always results from the two-parameter model, in general a larger or lower cell volume is obtained with the new model, depending on the exact opening and closing time of MS channels during the osmotic excursions. This is not the case when the osmotic cycle with an impermeant solute like sucrose is used, where MS channels are open only during phase II when cells are suspended back in an isotonic solution. For this reason, with the SAR model only equilibrium equations after contact with impermeant sucrose may be analytically derived, albeit without the advantageous linearity of the Boyle Van't Hoff equation. This paper demonstrates that the validity of these osmotic equilibrium equations with impermeant sucrose may be extended to any realistic set of model parameters, provided that enough time is allowed to the cell membrane for a complete relaxation. On the other hand, when a permeant CPA comes into play, a numerical integration of system dynamics, prolonged until steady state is eventually reached, is required to determine cell volume at equilibrium.

Finally, when determining the rate of water exchange a negligible hydrostatic pressure gradient across the cell membrane is obtained for any realistic set of the model parameter values. While representing a justification to simplify the dynamic version of the SAR model for future use, this confirms that animal cells are well-known to possess a very fragile membrane made only of a double layer of phospholipid molecules. Despite this simplification of the SAR model, this paper shows that the mechanics of the cell membrane coupled with surface area regulation may be considered responsible for ion/salt exchange and the control of cell volume during cryopreservation without resorting to the complex pump and leak physiological model.

Notation of the Subchapter 2.2

h	membrane thickness	[µm]
K	elastic modulus of the cell membrane	[Pa]
K'	non-dimensional elastic modulus of the cell membrane	[—]
k_S	constant of membrane relaxation rate	[Pa^{-1} s^{-1}]
L_P	water permeability	[µm Pa^{-1} s^{-1}]
M	osmolality	[mOsm L^{-1}]
p	non-dimensional hydrostatic pressure	[—]
P	hydrostatic pressure	[Pa]
P_{CPA}	CPA permeability	[µm s^{-1}]
P_{Ions}	ion permeability	[µm L s-1 mOsm-1]
r	radius of the spherical cell	[µm]
R	universal gas constant	[J mol-1 K-1]
S_{Ref}	membrane area of the cell used as reference to determine surface strain	[$µm^2$]
S_{Sph}	membrane area of the spherical cell	[$µm^2$]
t	time	[s]
T	absolute temperature	[K]
V_B	inactive volume	[$µm^3$]
V_{Cell}	cell volume	[$µm^3$]
V_{CPA}	intracellular CPA volume	[$µm^3$]
V_{Ions}	intracellular ion volume	[$µm^3$]
V_W	intracellular water volume	[$µm^3$]
β	non-dimensional cell membrane thickness	[—]
ζ_{Cell}	non-dimensional cell volume	[—]
ζ_{CPA}	intracellular CPA volume fraction	[—]
ζ_{Ions}	intracellular ion volume fraction	[—]
ζ_W	intracellular water volume fraction	[—]
λ_{CPA}	ratio between CPA and water permeabilities	[—]
λ_{Ions}	ratio between ion and water permeabilities	[—]
λ_S	ratio between the constant of membrane relaxation rate and water permeability	[—]
μ_{CPA}	ratio between CPA and water intracellular volumes at isotonic conditions	[—]
μ_{Ions}	ratio between ion and water intracellular volumes at isotonic conditions	[—]
Π	osmotic pressure	[Pa]
σ	membrane tension	[Pa]
σ_R	membrane resting tension	[Pa]
τ	non-dimensional time	[—]
υ_B	inactive volume fraction	[—]
$\tilde{\upsilon}_{CPA}$	molar volume of CPA	[m^3 mol^{-1}]
$\tilde{\upsilon}_{Ions}$	molar volume of ions	[m^3 mol^{-1}]
Φ_{Ref}	non-dimensional membrane area of the cell used as reference to determine surface strain	[—]
Φ_{Sph}	non-dimensional membrane area of the spherical cell	[—]
φ	dissociation constant for ions/salt in water	[Osm mol^{-1}]
ω	non-dimensional osmolality	[—]
Ω	non-dimensional membrane tension	[—]

Superscript

0	initial or isotonic condition
I	phase I (addition of permeant or impermeant solute) of the osmotic cycle
II	phase II (removal of permeant or impermeant solute) of the osmotic cycle
INT	intracellular
EXT	extracellular
*	reference value for non-dimensional variable

2.3 hMSCs from UCB in contact with DMSO for cryopreservation: experiments and modelling of osmotic injury and cytotoxicity

2.3.1 Introduction

Traditionally the problem of optimizing a cryopreservation process has been attacked by analyzing separately the different phenomena involved, both experimentally and theoretically [1-4]. In particular, during pre-freezing addition and post-thawing removal of CPAs cells may be damaged by excessive volume excursions driven by osmosis and CPA cytotoxicity. So far several possible mechanisms for osmotic injury have been hypothesized [5]: (i) mechanical rupture of the cell membrane in hypo-osmotic conditions, i.e. expansion lysis; (ii) cell membrane damage caused by frictional forces between exchanged water and membrane pores [6]; (iii) cell shrinkage in hyper-osmotic condition is resisted by cytoskeleton components, and the resultant interaction between shrunken cell membrane and cytoskeleton damages the cells [7]; (iv) cell shrinkage induces irreversible membrane fusion/change, so that the effective area of cell membrane is reduced and, when returned to isotonic condition, the cells lyse before their normal volume is recovered [8]; (v) hyperosmotic stress causes a net influx of non-permeating solutes so that, when cells are returned to iso-osmotic conditions, they swell beyond their normal isotonic volume and lyse [9-10]. These mechanisms suggest the existence of a safety range for osmotic excursions delimited by a minimum and a maximum cell volume where osmotic injury does not occur, i.e. the OTLs. The experimental determination of OTLs has been the subject of several experimental investigations in the cryopreservation literature, even if a mathematical model capable to describe osmotic injury is still lacking. Since the extent of cells shrinkage or swelling depends on membrane permeabilities to water and permeant solutes, OTLs varies from cell to cell lineage just like the cytotoxic effect of DMSO. This latter one, according to some experimental studies, is related to DMSO interaction with the phospholipid double layer composing the cell membrane, capable to reduce membrane thickness [11] or promote the formation of pores [12]. In fact these mechanisms are confirmed by molecular dynamics simulations which show that cell membrane response to cytotoxicity varies when increasing the concentration level of DMSO [13]: first, at relatively low DMSO concentrations (~ 2.5-7.5 mol%), only a decrease in membrane thickness takes place, while at intermediate concentrations (~ 10-20 mol%) a transient formation of water pores occurs, and finally, at higher concentrations (~ 25-100 mol%), the double-layer structure of cells membrane is completely destroyed. However, it is still not clear how DMSO interacts with the internal structures of the cells, which intracellular molecular mechanisms are involved and how they are related to the reduction of cells viability measured at a larger scale with the conventional techniques currently available. For these reasons, still today the term cytotoxic effect refers to a global, undefined damage to cells other than the excessive osmotic excursions experienced when contacted with a toxic CPA as measured, for instance, by cell membrane integrity or viability/functionality assays.

The contact of cells with CPAs has been investigated both experimentally and theoretically by following three different approaches basically: studying only the injury caused by excessive osmotic excursions [14-19],

focusing only on the cytotoxic effect [20-21], or examining the two phenomena together in a combined analysis [22-27]. In the first case, osmotic injury is analyzed alone by limiting or neglecting cytotoxicity with the specific aim of determining OTLs, i.e. by working at small CPAs concentrations, low temperatures, and short contact times or directly without using any cytotoxic CPA. This way, the OTLs of human spermatozoa [5], human oocytes [15-16], human red blood cells [17,19], and mouse embryonic stem cells [18] were experimentally determined. In the second approach, tissues instead of cells suspension are typically addressed: by assuming that osmotic shifts do not contribute to cell death due to protection of the matrix, cytotoxicity is analyzed alone and osmotic injury neglected [20]. This is the case of articular cartilage from pigs [20] or human dermal tissue [21] contacted with hypertonic solutions of DMSO at varying osmolalities, temperatures, and contact times. Overall, cell viability was found to decrease with longer exposure to DMSO at increasing concentrations and higher temperatures. A first-order reaction kinetics with respect to the residual number of viable cells was proposed in [20], with an Arrhenius-like dependence on system temperature of the reaction constant which was found to increase with DMSO osmolality. In the third approach the design of optimal CPA pre-freezing addition and post-thawing removal is typically addressed. This goal is sought by avoiding the osmotic injury while simultaneously limiting the cytotoxic effect, i.e. by adopting a multistep strategy for CPA addition/removal while working at low temperatures, CPA concentrations, and short contact times, respectively. This way the case of human $CD34^+$ stem cells from UCB with DMSO [22-23], human and murine oocytes, and adherent endothelial cells with DMSO, propylene, or ethylene glycol [24-27] were analyzed.

It is apparent that, in the papers referenced above where osmotic injury is investigated the accurate determination of constraints for the cell volume excursions (i.e. OTLs) is crucial. Actually, from the theoretical perspective this is mandatory, since a mathematical model capable to take into account osmotic injury (as for instance expansion lysis) has never been proposed so far. For this reason the problem of simulating osmotic injury has been circumvented by confining cell volume excursions within the safety range of pre-set OTLs where cell osmosis is described through the classic Kedem-Katchalsky [28] or two-parameter formalisms [29]. On the other hand, the way OTLs are experimentally determined raises a serious concern: usually, cells are first suspended in hypo- or hyper-tonic solutions, then osmotic injury is measured by checking membrane integrity or cells viability/functionality. The latter ones are evaluated through the analysis of fluorescent staining, sperm mobility, and hemolysis via spectrophotometry, flow cytometry or under a microscope [5,15-19]. To do so cells are necessarily suspended back to isotonic or nearly isotonic conditions, while in principle osmotic injury due to excessive cells shrinkage or swelling should be determined right after the contact with the non-isotonic solutions, in order to avoid misinterpreting the cause of damage. Therefore, the osmotic injury measured in these papers is actually due to a complete osmotic cycle, i.e. shrinkage followed by swelling or vice versa when contacting with hyper- or hypo-osmotic solutions, respectively. Besides it is worth noting that, in these papers lysis during swelling is generally found more lethal than excessive shrinkage [5,15,18-19,22] as originally pointed out by Lovelock [9], or osmotic injury after suspending the cells in hypertonic solutions is found especially damaging only when returning back to isotonic [5,17].

The same concern of misinterpretation on the true cause of damage to a cell suspension is raised by the way the cytotoxic effect is experimentally evaluated through cell membrane integrity or viability/functionality tests: these are typically performed again by re-suspending the cells into isotonic or nearly isotonic conditions after the contact with CPAs [20,21], when a lethal excessive swelling may take place, unless precautions to avoid it are specifically taken [27]. Therefore, it is apparent that the typical evaluation of the cytotoxic effect cannot be effectively separated by osmotic injury for a cell suspension.

For these reasons, in this work a combined analysis of osmotic injury and cytotoxic effect for hMSCs in contact with DMSO is investigated from the experimental and theoretical perspectives. In particular, cell count and viability are measured through a Coulter Counter and flow-cytometer respectively, when the cell population is abruptly suspended back to isosmotic conditions after contacting with hypertonic solutions of DMSO at varying osmolality, temperature and contact time. The measured decrease of cell count and viability are interpreted as the effects of osmotic injury and cytotoxicity, respectively. More specifically, the decrease of cell count is ascribed only to expansion lysis, i.e. cell bursting. Of course, cell burst may take place whenever an excessive swelling occurs during the contact with CPAs, but its occurrence is mostly expected when cells, after being contacted with CPA at high concentrations, are abruptly suspended back to isosmotic conditions for measurements. A novel mathematical model capable to account for the kinetics of expansion lysis as well as of cytotoxicity is developed to interpret data, without the need to set in advance the cell OTLs as traditionally done in cryopreservation literature. The new model is based on the Surface Area Regulation (SAR) model proposed in the Subchapter 2.1 [3] for the description of the peculiar osmotic behavior of hMSCs from UCB measured when contacted with DMSO at relatively low osmolalities, i.e. when osmotic injury and cytotoxicity did not occur. More specifically, in this work the coupling of osmosis with cell mechanics and membrane area regulation is adopted to describe the kinetics of expansion lysis due to excessive osmotic swelling: cells burst during swelling when membrane tension increases above a critical value, thus simulating the decrease of cell count measured by the Coulter Counter. The simultaneous cytotoxic effect of DMSO is described as a reaction kinetics from viable to non-viable cells to account for the decrease of cell viability measured by the flow-cytometer: in particular, a first-order reaction rate with respect to the number of viable cells is proposed, with the Arrhenius-like and power-law dependences of the reaction constant on system temperature and DMSO concentration, respectively.

Comparisons between experimental data and theoretical simulations are provided: first, a non-linear regression analysis is performed to evaluate unknown model parameters adjusted through a best-fitting procedure; then, the predictive capability of the proposed model is successfully tested by predicting system behavior measured at operating conditions different from those used during the best-fit procedure.

2.3.2 Experimental Section

2.3.2.1 Experimental setup and operating conditions

The hMSCs from UCB of three different donors were collected and isolated as described in [30]. The experimental runs carried out in this work consist in two sequential stages: the contact phase of the cells with DMSO, when the permeant CPA is loaded into the cytoplasm, followed by removal, when the CPA exit the cells. Both phases are carried out in a single step. The contact of hMSCs is performed by suspending about 10^6 cells in 1 ml of hypertonic solutions containing DMSO (Sigma-Aldrich) added to isotonic PBS at varying osmolality, temperature and duration as shown in Table 2.3.1.

Table 2.3.1: Operating conditions for the contact phase with DMSO. The subsequent removal phase is always performed by abruptly suspending the cells back into isotonic PBS (i.e. one step) at 27 °C for 15 min,

DMSO [vol.%]	Contact temperature [°C]	Contact time [min]		
0; 5; 10; 15; 20; 25; 30 [δ]	10	30	60	120
0; 5; 10; 15; 20; 25; 30 [δ]	22	30	60	120
0; 5; 10; 15; 20; 25; 30 [δ]	37 5	30	60	

[δ] 5; 10; 15; 20; 25; 30 vol.% of DMSO correspond to about 705; 1410; 2110; 2820; 3520; 4225 mOsm/L or 1.3; 2.5; 3.8; 5.1; 6.3; 7.6 mol.%

More specifically, system response at 7 DMSO concentrations (from 0 to 30 vol.%), 3 temperatures (from 5 to 37 °C) and 4 contact times (from 5 to 120 min) is investigated. It is worth noting that, the concentration range explored in this work is below 10 mol.% of DMSO, as reported in Table 2.3.1: according to [13] in our experimental runs not only the integrity of cell membrane is not damaged by the cytotoxic effect but also its permeability does not change since no transient formation of water pores is actually taking place at these DMSO concentration levels. The cases of the lowest temperature (i.e. 10 °C) combined with the shortest contact time (i.e. 5 min), as well as the highest temperature (i.e. 37 °C) with the longer contact time (i.e. 120 min) are skipped to avoid the negligible or excessive cell damage expected at these extreme conditions, respectively. A freezing-point-depression osmometer (Advanced Micro Osmometer Model 3300, Advanced Instruments, Norwood, MA) is used to measure solution osmolality. System temperature is controlled within a ± 0.2°C interval by circulating water-NaCl bath at 2% wt./vol as suggested by [31]. To this aim, isotonic cells were injected into a suitably manufactured beaker allowing perfect mixing and dispersion in the suspending solution.

The subsequent removal phase is performed by abruptly suspending the cells back into isotonic PBS (i.e. one step) at 27 °C for 15 min, after centrifugation at 400g for 5 minutes. Cell count and viability are measured by means of a Coulter Counter and a flow-cytometer respectively, only before the contact phase and at the end of the removal phase, in order to evaluate the combined effect of osmotic injury and cytotoxicity. Separate

experimental runs are performed for individual donors and repeated at least three times, before pooling and averaging data.

2.3.2.2 Cell count

Cell count is measured using a Coulter Counter Multisizer 4 (Beckman Coulter), initially calibrated using latex beads (diameter 10 μm, Beckman Coulter). Before each experiment, the instrument electrolyte solution is replaced by the appropriate hypertonic solution to avoid mismatch with the sample solution and consequent electrical conductivity gradients [32]. Coulter Counter's capability of measuring the number of cells of a relatively large population represents a significant advantage over micrographic analysis and direct microscopic inspection, which are necessarily restricted to small samples. In this regard, Coulter Counter's performances are comparable with those of cytofluorimeters [33]. However, since impedance measurements do not discriminate single cells by debris or cell agglomerates, a data treatment is required. To this aim, the dot plot measured by the Coulter Counter is adopted, as shown in Figure 2.3.1 where a representative case is reported.

Here individual points correspond to the amplitude and duration for any single event (i.e. voltage pulse with height and width) detected by the Coulter Counter during its passage through the sensing zone, i.e. cells, debris and agglomerates. In particular, the pulse amplitude is related to cell size, and, after calibration, can be expressed as cell diameter measured in μm. Debris and cell agglomerates are filtered out through gating as shown in Figure 2.3.1a, by considering only the events falling within the red rectangular representing single, intact cells, i.e. by assuming that debris and cell agglomerates are characterized by relatively small diameters and large width, respectively.

2.3.2.3 Cell viability

Cell viability is determined by a dual staining assay analyzed in a flow-cytometer (FACScan Becton Dickinson), in order to separate viable cells from apoptotic and necrotic ones. First, cells are washed with isotonic PBS at 27 °C, then, after centrifugation at 400g for 5 minutes, are re-suspended in 1X Binding Buffer at a concentration of 10^6 cells/ml. Later 100 μL of the resulting solution are transferred to a 5 mL culture tube, where 5 μL of Alexa Fluor® 488 annexin V and 5 μL of Propidium Iodide (PI) (Life Technologies) are added for staining. After incubation for 15 min at 27 °C, 400 μL of 1X Binding Buffer are added and the cells are finally analyzed in the flow-cytometer by examining a constant number of events (i.e. 10^4)

Data from flow-cytometer need to be treated as well. By means of the software Kaluza (Beckman Coulter), first debris and cell agglomerates are filtered out through an elliptical gating on the dot-plot of Forward Scatter (FSC) vs Side Scatter (SSC) measured by the flow-cytometer as shown in Figure 2.3.2a, where a representative case is reported. Here individual points correspond to FSC (i.e. size) and SSC (i.e. internal complexity) for any single event detected by the flow-cytometer. Then, on the selected population of cells, the dot plot of Annexin vs PI expressions is analyzed to differentiate viable cells from apoptotic and necrotic ones, as shown in Figure 2.3.2b where cells falling within four different quadrants are identified.

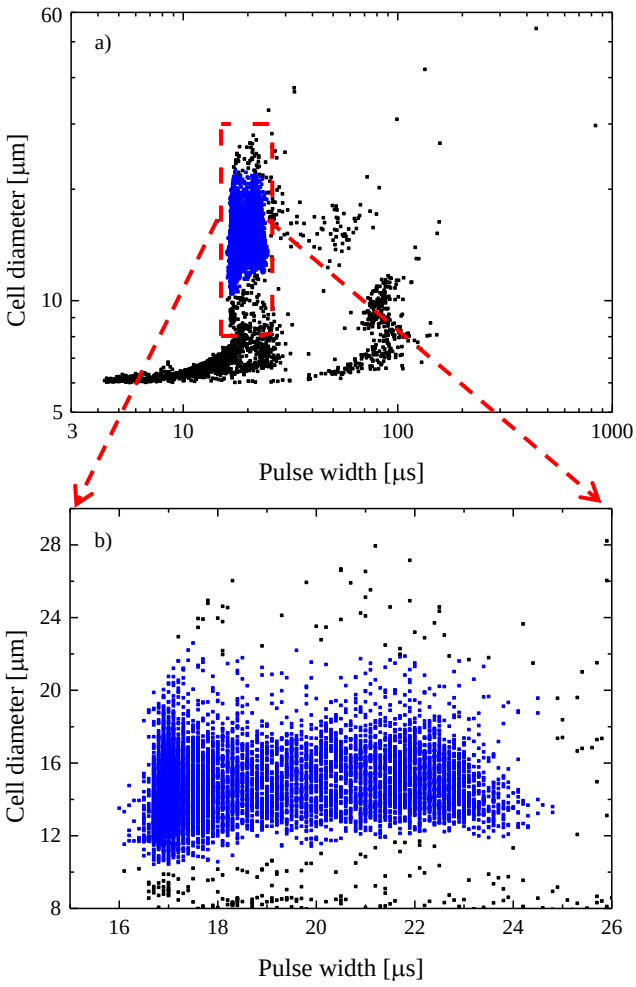

Figure 2.3.1: Data treatment for Coulter Counter measurements to isolate cells from debris and agglomerates: gating of a representative diameter vs pulse dot-plot (a); zoom of the gated region (b).

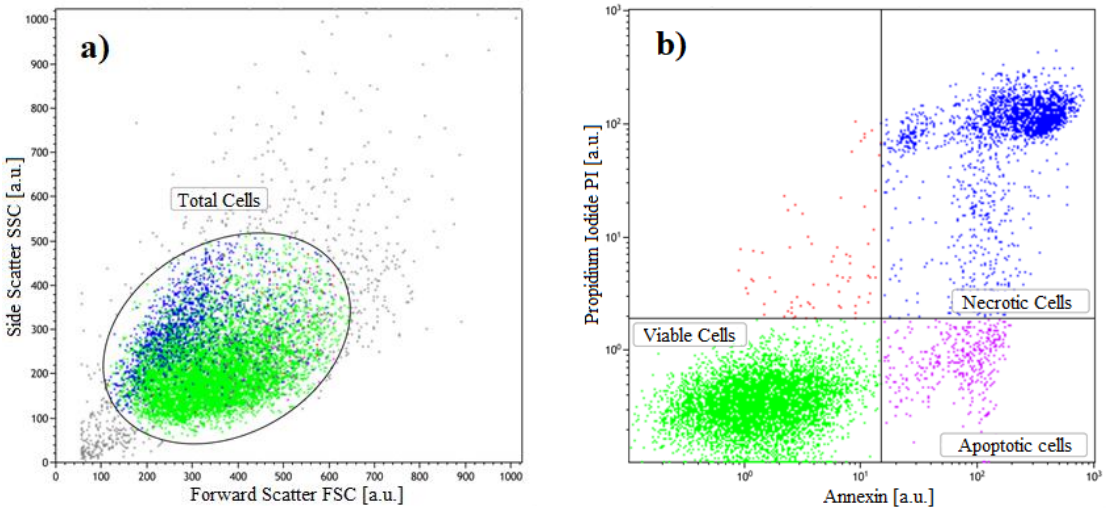

Figure 2.3.2: Data treatment for flow-cytometer by means of software Kaluza: dot plot of FSC vs SSC with elliptical gating to isolate cells from debris and agglomerates (a); dot plot of Annexin vs PI expressions to separate viable cells from apoptotic and necrotic ones.

In fact, apoptotic phenomena are characterized by morphological changes that appear in sequential fashion, including loss of asymmetry and attachment in plasma membrane, condensation of the cytoplasm and nucleus, and internucleosomal cleavage of DNA. Loss of plasma membrane is one of the earliest changes. In apoptotic cells, the Phospholipid phosphatidylSerine (PS) present in the membrane is translocated from the inner to the outer leaflet of the plasma membrane, thereby exposing PS to the external cellular environment. On the other hand, necrotic cells simply show a damaged membrane. Annexin is a 35-36 kDa Ca^{2+} dependent phospholipid-binding protein, that shows high affinity for PS. Since Annexin is a non-permeable protein, it binds to cells only when PS is exposed in the outer layer. Conjugating Annexin V with fluorochromes as FITC allows to detect early apoptotic cells through flow cytometric analysis. The loss of membrane integrity typical of necrotic processes is detected by a vital dye such as PI: viable cells with intact membranes exclude PI, whereas membranes of dead and damaged cells are permeable to PI, a DNA intercalant. Therefore on the basis of the dot plot for cells positive or negative to Annexin and PI shown in Figure 2.3.2b, cells may be divided according to three different conditions: viable cells (negative to both Annexin and PI staining); apoptotic cells (positive to Annexin but negative to PI staining); necrotic cells (positive to both Annexin and PI staining). The case of cells positive to PI but negative to Annexin staining is not taken into account, since a cell without membrane integrity cannot be negative to Annexin marker in principle. As apparent in Figure 2.3.2b, the number of these cells is negligible.

Viability is finally determined as the ratio between the number of viable cells and the total number of cells, both shown in Figure 2.3.2b. More specifically, the total number of cells in Figure 2.3.2b is obtained by summing up the viable, necrotic, and apoptotic cells and is equal to the number of cells resulting from the gating in Figure 2.3.2a. It is worth noting that, the total number of cells measured by the flow-cytometer is assumed to be proportional to the total number of cells measured by the Coulter Counter, since they are both determined after removal of debris and cell agglomerates. On the other hand, these two numbers do not coincide since they are independently measured by two different apparatuses working at two different conditions: the Coulter Counter measures the number of cells suspended in a pre-set volume of solution, while the flow-cytometer measures the distribution of viable, necrotic, and apoptotic cells within a pre-set number of cells.

2.3.3 Modeling Section

The proposed model quantitatively describes osmotic injury due to expansion lysis and cytotoxic effect as two simultaneous reactions taking place during CPA addition and removal. To this aim, the cell population is divided in two sub-populations, i.e. viable and non-viable cells, as expressed by the following equation:

$$N_{\mathrm{TOT}}(t) = N_{\mathrm{V}}(t) + N_{\mathrm{NV}}(t) \quad (1)$$

where N_i with $i = \mathrm{TOT}, \mathrm{V}, \mathrm{NV}$ represents the number of cells. It is apparent, that non-viable cells are the sum of the necrotic and apoptotic cells reported in Figure 2.3.2b.

The two populations of viable and non-viable cells (N_V and N_{NV}) vary with time according to the reaction scheme shown in Figure 2.3.3.

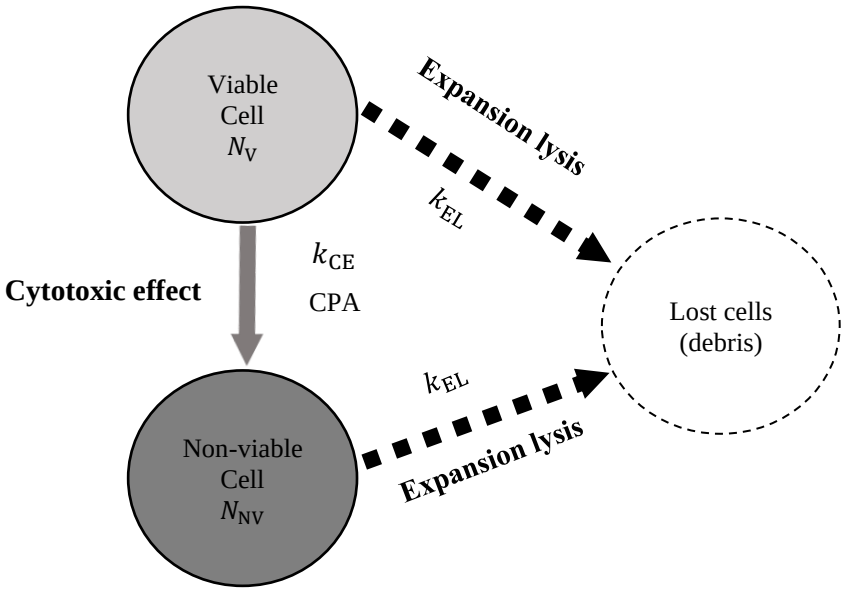

Figure 2.3.3: Schematic representation of cell system response to the addition/removal of a toxic CPA in the proposed model: cells are divided between viable and non-viable populations. Viable cells transform into non-viable ones following the reaction kinetics of cytotoxicity; both populations decrease in number due to osmotic injury following the reaction kinetics of expansion lysis, i.e. transforming into lost, undetected cells like debris.

In particular, when contacted with a toxic and permeant CPA like DMSO, viable cells are transformed in time to non-viable ones by following the reaction kinetics of the cytotoxic effect, thus mimicking the decrease of cell viability experimentally measured by flow-cytometry. For this reason, the number of viable and non-viable cells are expressed as a function of time (t) in Equation 1, with the first ones acting as the reactant which decreases in time being gradually transformed into the latter ones representing the reaction product. Clearly this transformation of a cell sub-population into the other cannot explain the temporal dependence of the total number of cells $N_{TOT}(t)$ appearing in Equation 1, which is exclusively due to the reaction representing expansion lysis shown in Figure 2.3.3 as well.

According to the reaction scheme, the role of the consumed reactant in the reaction representing osmotic injury is played by both viable and non-viable cells. In fact, even if membrane integrity of necrotic cells is actually lost (given that they are experimentally identified through the PI exclusion test), a simplifying assumption of the proposed model is that both sub-populations of cells (N_V and N_{NV}) share the same osmotic response. This is valid when cells are contacted with the permeant DMSO as well as during CPA removal, when cells are suspended back to isotonic PBS and an excessive swelling may take place leading to expansion lysis.

According to this picture, osmotic injury may occur equally in viable and non-viable cells which are transformed into lost, undetected cells like debris, thus mimicking the decrease of cell count experimentally measured by the Coulter Counter. Based on these assumptions, the following number balances in a closed reacting system may be written with the corresponding initial conditions:

$$\frac{dN_{\mathrm{V}}(t)}{dt} = -(k_{\mathrm{CE}} + k_{\mathrm{EL}})\, N_{\mathrm{V}}, \qquad N_{\mathrm{V}}(t) = N_{\mathrm{V}}^{0} = N_{\mathrm{TOT}}^{0}\, R_{\mathrm{V}}^{0}, \qquad @ \quad t = 0 \tag{2}$$

$$\frac{dN_{\mathrm{NV}}(t)}{dt} = k_{\mathrm{CE}}\, N_{\mathrm{V}} - k_{\mathrm{EL}}\, N_{\mathrm{NV}}, \qquad N_{\mathrm{NV}}(t) = N_{\mathrm{NV}}^{0} = N_{\mathrm{TOT}}^{0}\left(1 - R_{\mathrm{V}}^{0}\right), \qquad @ \quad t = 0 \tag{3}$$

where for the kinetics of the reaction rates representing the cytotoxic effect and expansion lysis, namely $k_{\mathrm{CE}}\, N_{\mathrm{V}}$ and $k_{\mathrm{EL}}\, N_i$ with $i = \mathrm{V}, \mathrm{NV}$ respectively, a first-order dependence is assumed with respect to the corresponding number of cells acting as reactants. The initial conditions are defined on the basis of the viability ratio ($R_{\mathrm{V}}(t) = \frac{N_{\mathrm{V}}(t)}{N_{\mathrm{TOT}}(t)}$) evaluated at $t = 0$.

According to Equations 2-3, while non-viable cells are produced by cytotoxicity but consumed by expansion lysis, viable cells are always consumed by both reactions. Clearly, by summing up Equations 2 and 3 the balance on N_{TOT} is obtained:

$$\frac{dN_{\mathrm{TOT}}(t)}{dt} = -k_{\mathrm{EL}}\, \underbrace{(N_{\mathrm{V}} + N_{\mathrm{NV}})}_{N_{\mathrm{TOT}}}, \qquad N_{\mathrm{TOT}}(t) = N_{\mathrm{TOT}}^{0}, \qquad @ \quad t = 0 \tag{4}$$

which confirms that only expansion lysis is responsible for the decrease of the total number of cells.

In the kinetics of the cytotoxic reaction shown in Figure 2.3.3, CPA plays the role of a catalyst whose concentration affects the reaction rate but it is never consumed nor produced. Accordingly, for the reaction rate constant of cytotoxicity (k_{CE}) a generic power-law dependence is assumed with respect to the concentration of the toxic CPA along with the classis Arrhenius-like dependence from system temperature [20,24,27]:

$$k_{\mathrm{CE}} = k_{\mathrm{CE}}^{0} \exp\left(-\frac{E_{\mathrm{a,CE}}}{RT}\right) \left(M_{\mathrm{CPA}}^{\mathrm{INT}}\right)^{\alpha} \tag{5}$$

Here the order α is seen as a characteristic feature of the specific cell lineage-CPA system at hand and its value may be estimated only through the comparisons to experimental data, like the pre-exponential factor k_{CE}^{0} and the activation energy $E_{\mathrm{a,CE}}$. It is worth noting that $M_{\mathrm{CPA}}^{\mathrm{INT}}$ is the intracellular osmolality of the permeant CPA: as a consequence, it varies in time during CPA addition and removal, depending on the specific osmotic response of the cells under investigation. Assuming that both reaction order α and activation energy $E_{\mathrm{a,CE}}$ appearing in Equation 5 are positive, the cytotoxic effect is expected to increase with temperature and CPA concentration.

Regarding the reaction rate representing expansion lysis, it is obvious that the constant k_{EL} depends on the osmotic behavior of the specific cell lineage under investigation and its coupling with membrane mechanics. Unfortunately, if the Kedem-Katchalsky or two-parameter formalisms are adopted to describe cell osmosis, a definition of k_{EL} cannot be derived since no coupling with cell membrane mechanics is taken into account in these theoretical approaches. However, in this work we take advantage of the SAR model [3,34] whose equations are reported in the Subchapter 2.1.

In this work the reaction rate constant of expansion lysis during swelling is seen as a function of the cell membrane tension above its resting value, i.e. $k_{\mathrm{EL}}(\Delta\sigma)$ with $\Delta\sigma = (\sigma - \sigma_{\mathrm{R}})$. More specifically, expansion lysis is assumed to occur if a critically high membrane tension $\sigma_{Break} > \sigma_{\mathrm{R}}$ is achieved during the osmotic

swelling: when σ increases towards σ_{Break} (i.e. when $\Delta\sigma$ approaches $\Delta\sigma_{\mathrm{Break}} = \sigma_{\mathrm{Break}} - \sigma_{\mathrm{R}}$) the cells burst losing their identity and transforming into debris. From a mechanical perspective this means that cell behavior during osmotic swelling is similar to a classic brittle material in a tensile test: a linear, elastic response until the tensile strength is reached and breakage occurs. On the basis of these considerations, the transformation from viable and non-viable cells to debris via expansion lysis is expressed by defining the following rate constant

$$k_{\mathrm{EL}}(\Delta\sigma) = \begin{cases} \dfrac{d\Delta\sigma}{dt}\ \gamma(\Delta\sigma) & if\ \ \dfrac{d\Delta\sigma}{dt} > 0\ \ and\ \ \Delta\sigma > 0 \\ 0 & if\ \ \dfrac{d\Delta\sigma}{dt} \le 0\ \ or\ \ \Delta\sigma \le 0 \end{cases} \tag{6}$$

where the rate of membrane tension variation is calculated as the analytical derivative of Equation 6 (Subchapter 2.1) of the SAR model giving

$$\frac{d\Delta\sigma}{dt} = \left(\sigma + \frac{K}{2}\right)\left(\frac{2}{3\,V_{\mathrm{Cell}}}\frac{dV_{\mathrm{Cell}}}{dt} - k_{\mathrm{S}}\,\Delta\sigma\right) \tag{7}$$

while the so-called transition function $\gamma(\Delta\sigma)$ is calculated as

$$\gamma(\Delta\sigma) = \frac{K_{\mathrm{W}}(\Delta\sigma)^{K_{\mathrm{W}}-1}}{(\sigma_{\mathrm{Break}} - \sigma_{\mathrm{R}})^{K_{\mathrm{W}}}} \tag{8}$$

Basically, this definition of k_{EL} introduces two additional model parameters, namely K_{W} and σ_{Break} appearing in Equation 8. In fact, K is the elastic modulus of cell membrane and k_{S} is the constant of membrane relaxation rate already present in the SAR model along with the resting tension σ_{R}. According to Equation 6, a conditional osmotic injury is hypothesized: expansion lysis occurs only if cell membrane is already stretched (i.e. during swelling) and its tension is increasing (i.e. $\Delta\sigma > 0$ and $\frac{d\Delta\sigma}{dt} > 0$). On the contrary, expansion lysis does not occur if cell membrane is at resting conditions or loose like during osmotic shrinkage (i.e. $\Delta\sigma \le 0$), or when an already stretched membrane is actually relaxing (i.e. $\frac{d\Delta\sigma}{dt} \le 0$ with $\Delta\sigma > 0$). Therefore, no osmotic damage due to excessive shrinkage is taken into account in this work.

It is worth noting that Equation 6 for k_{EL} does not come out of the blue but it is actually derived by following the same approach adopted by the authors [35-36] to model the mitotic rate in a growing cell population, as originally proposed by [37-38]. The approach is based on the assumption that expansion lysis does not take place exclusively when $\Delta\sigma_{\mathrm{Break}}$ is reached (i.e. deterministic event). On the contrary, this model constraint is relaxed in order to account for heterogeneity in the cell population during lysis (i.e. statistical event). To this aim the Weibull distribution characterized by two adjustable parameters, namely K_{W} and $\Delta\sigma_{\mathrm{Break}}$:,

$$f_{EL}(\Delta\sigma) = \frac{K_{\mathrm{W}}}{(\Delta\sigma_{\mathrm{Break}})^{K_{\mathrm{W}}}}(\Delta\sigma)^{K_{\mathrm{W}}-1} \tag{9}$$

is assumed to represent the probability density function for the expansion lysis event, from which the transition function $\gamma(\Delta\sigma)$ reported in Equation 8 is readily derived. Depending on the value of the so-called shape factor K_{W}, this function may show a monotonic decrease ($K_{\mathrm{W}} < 1$), or it may be characterized by a maximum ($K_{\mathrm{W}} > 1$), whose position is related to the specific value of the scale factor $\Delta\sigma_{\mathrm{Break}}$. By increasing the shape factor above 1, the Weibull distribution narrows around a maximum located at $\Delta\sigma_{\mathrm{Break}}$. In this case, the transition

function $\gamma(\Delta\sigma)$ increases monotonically towards infinitely large values. This means that the probability of expansion lysis occurrence $f_{\mathrm{EL}}(\Delta\sigma)$ is maximum if $\Delta\sigma$ is close to $\Delta\sigma_{\mathrm{Break}}$, but the rate of expansion lysis $\gamma(\Delta\sigma)$ accelerates considerably when membrane tension $\Delta\sigma$ overcomes $\Delta\sigma_{\mathrm{Break}}$: given that expansion lysis is modelled as a statistical event, if cells reach a membrane tension larger than $\Delta\sigma_{\mathrm{Break}}$ without lysing, the rate of expansion lysis increases so much that shortly after lysis will probably occur. The name of the variables is defined with units in the Notation section.

2.3.4 Results and discussion

The SAR model was developed to interpret the non-perfect osmotic behavior of hMSCs from UCB when contacted with permeant (DMSO) and impermeant (sucrose) solutes [3]. More specifically, with a maximum contact time of 5 min, equilibrium as well as dynamic runs were performed at varying temperatures (i.e. 17, 27, and 37 °C) and relatively small DMSO osmolalities (i.e. 1700 mOsm/L, which is equal to 12 vol.% or 3 mol.%). At these operating conditions negligible cytotoxic effect and expansion lysis were measured, i.e. the viability ratio R_{V} and cell count N_{TOT} determined by flow-cytometry and Coulter Counter, respectively, remained constantly equal to the corresponding initial value during every experimental run. Through a sequential best fit procedure, all the unknown parameters of the SAR model were determined [3] and the corresponding values are reported in Table 2.1.2 in the Subchapter 2.1.

In this work, the SAR model is used to describe the osmotic response of viable N_{V} and non-viable N_{NV} cells during experimental runs performed at relatively long contact times (up to 120 min) and large DMSO osmolalities (up to 4225 mOsm/L, which is equal to 30 vol.% or 7.6 mol.%), where expansion lysis as well as cytotoxicity take place. To do so, the equations of the SAR model reported in the Subchapter 2.1 are coupled with Equations 1-9. More specifically, the SAR model is used to simulate $M_{\mathrm{CPA}}^{\mathrm{INT}}(t)$, $\Delta\sigma(t)$, and $\frac{d\Delta\sigma}{dt}$ appearing in Equations 5-8 which are necessary to determine the kinetic constants k_{CE} and k_{EL} of the reaction rates representing the cytotoxic effect and expansion lysis, correspondingly. Basically, with respect to the osmotic parameters of the SAR model reported in Table 2..2, in the model proposed in this work 5 additional parameters are introduced to describe cytotoxicity and expansion lysis, namely: k_{CE}^{0}, $E_{\mathrm{a,CE}}$, and α (for the reaction rate of the cytotoxic effect), K_{W} and σ_{Break} (for the reaction rate of expansion lysis). The values of these 5 parameters are determined through a regression analysis by keeping constant the osmotic parameters of the SAR model reported in Table 2.3.2: only the data at contact times of 30 and 60 min among the experimental runs in Table 2.3.1 are best-fitted through the comparisons to model results. The data from the experimental runs at contact times of 5 and 120 min are used for model validation, by full prediction of system behavior.

In Figures 2.3.4-5 the comparisons between data and model results are shown, while the values of the adjustable parameters obtained from the regression analysis is reported in Table 2.3.3.

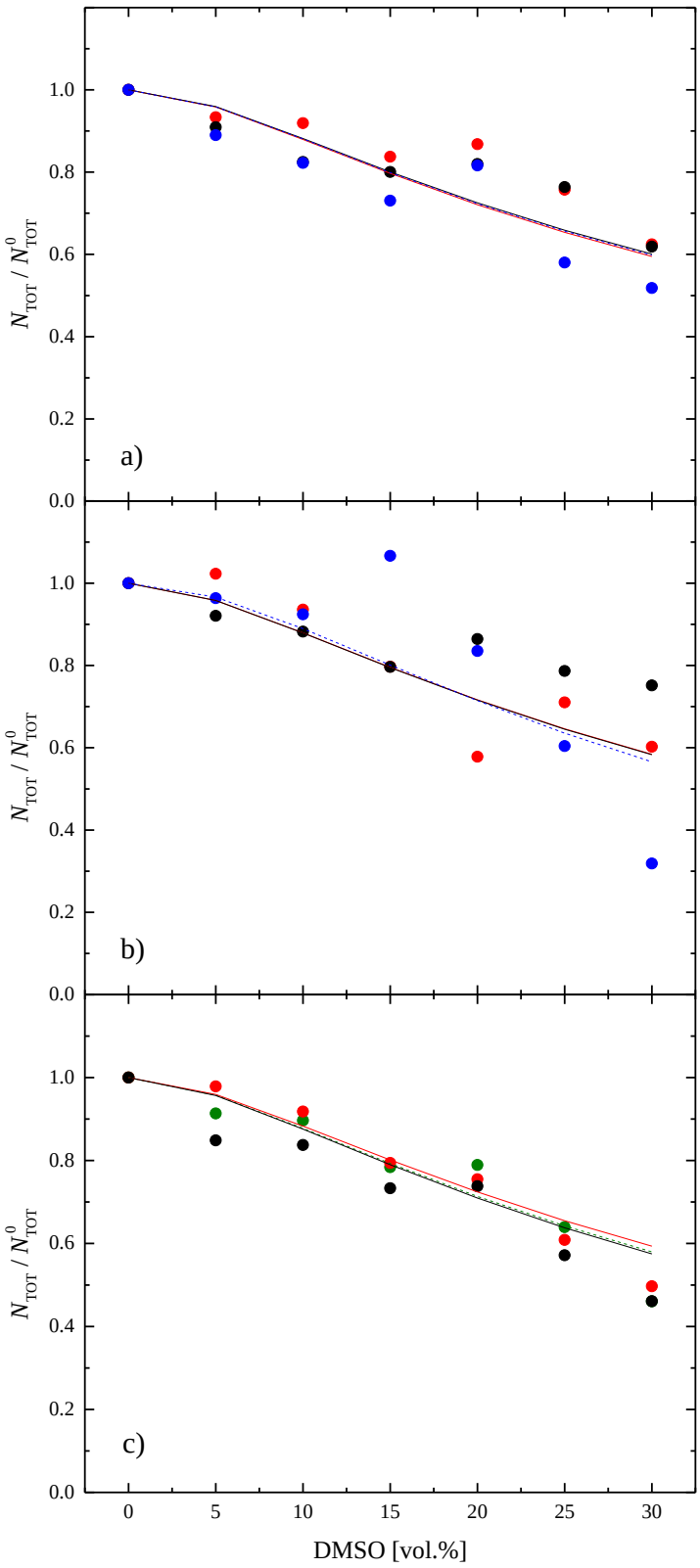

Figure 2.3.4: Normalized cell count measured by Coulter Counter at the end of the removal phase as a function of vol.% of DMSO used during the contact phase: varying the temperature during the contact phase a) 10 °C; b) 22 °C; c) 37 °C, and contact times 5 min, 30 min, 60 min, 120 min. Symbol represents measured data, solid line represents model fitting, dashed line represents model prediction.

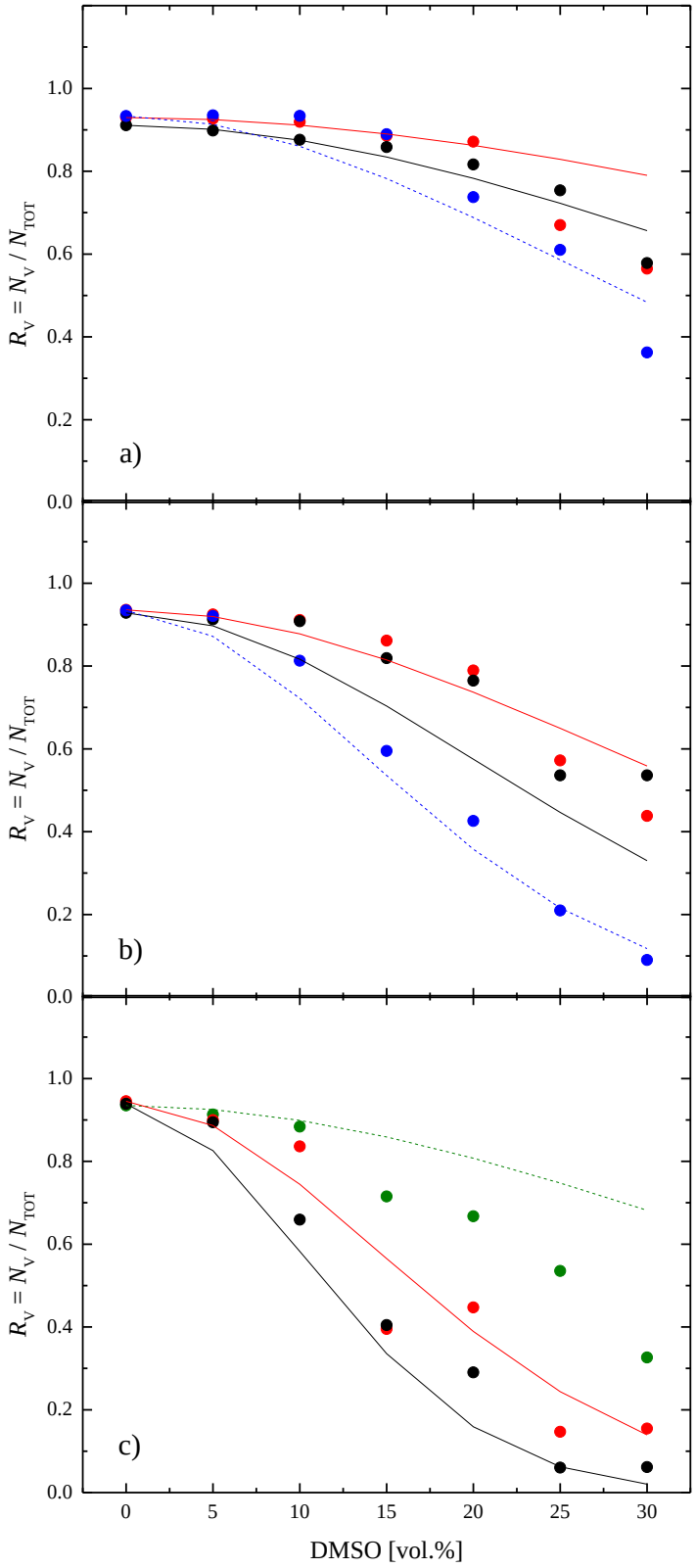

Figure 2.3.5: Viability ratio measured by flow-cytometer at the end of the removal phase as a function of vol.% of DMSO used during the contact phase: varying the temperature during the contact phase a) 10 °C; b) 22 °C; c) 37 °C, and contact times 5 min, 30 min, 60 min, 120 min. Symbol represents measured data, solid line represents model fitting, dashed line represents model prediction.

Table 2.3.3: Parameter values of the reaction rates representing the cytotoxic effect and expansion lysis.

Parameter	Value	Unit
$E_{a,CE}$	66110	[J mol^{-1}]
K_W	2.23	[-]
k_{CE}^0	20.214	[L^{α} s^{-1} mOsm$^{-\alpha}$]
α	1.9	[-]
σ_{Break}	11840	[Pa]

In particular, in Figure 2.3.4 the cell count (normalized with the corresponding initial value) measured by the Coulter Counter at the end of the removal phase is reported as a function of the vol.% of DMSO used during the contact phase, for every experimental run in Table 2.3.1. Analogously, in Figure 2.3.5 the viability ratio measured by the flow-cytometer at the end of the removal phase is shown as a function of vol.% of DMSO used during the contact phase.

For the sake of comparison, separated data are shown for the three temperature levels used during the contact phase, while the varying contact time is accounted for by using different colors, i.e. 5 min, 30 min, 60 min, and 120 min, for data (closed circle) as well as theoretical results (solid line for model fitting and dashed line for model prediction). Both data of cell count in Figure 2.3.4 and viability ratio in Figure 2.3.5 are clearly shown to decrease as DMSO concentration increases. However, whereas data of viability ratio in Figure 2.3.5 are shown to vary also with temperature and contact time in a consistent fashion, only scattered measurements of cell count are obtained at varying temperature and contact time as reported in Figure 2.3.4, especially at 10 and 22 °C. In fact, data of cell count from Coulter Counter are characterized by a much greater level of variability, i.e. less reproducibility (not shown for the sake of clarity), than the one of viability ratio from flow-cytometer. This is due to the completely different strategy used for the measurements by the two techniques: flow-cytometry analyzes a constant number of events, while Coulter Counter counts the number of events present in a fixed volume. Moreover, it is worth noting that a fraction of non-viable cells (about 10%) is always initially present in the sample since the data of viability ratio shown in Figure 2.3.5 always starts from a value lower than 1.

Overall, model fittings and predictions may be considered satisfactory, especially if compared to the other studies on the topic available in the literature where no prediction is provided and osmotic injury is neglected [20-24] or avoided by working within the range delimited by pre-set OTLs [27]. Interestingly, in these papers the initial cell viability is always equal to 1. Regarding the parameter values in Table 2.3.3, a slightly larger reaction order α in the kinetics representing the cytotoxic effect (Equation 5) is found in this work in comparison with those reported in the literature [24,27] for other cell lines and CPAs (i.e. 1.9 vs 1.6). However, a much lower k_{CE}^0 (i.e. ~ 20 s^{-1} vs 1.7·10^5 s^{-1}) with a comparable activation energy $E_{a,CE}$ (i.e. ~ 66 kJ mol^{-1} vs 56 kJ mol^{-1}) for the cytotoxic reaction are obtained in this work in comparison with the literature [27].

As a consequence, the comparisons with model results on cell count in Figure 2.3.4 are less satisfactory than those on viability in Figure 2.3.5. In particular, model fitting and predictions for cell count almost overlap showing a clear dependence on DMSO concentration, regardless of temperature and contact time. This dependence is apparently double linear: a slower decrease at DMSO vol.% lower than 5-10, with an increasing slope at higher concentration levels. On the contrary, cell viability in Figure 2.3.5 shows an inverted sigmoid function with respect to DMSO concentration, with a clear detrimental effect when increasing temperature and To better understand system behavior, the simulated temporal profiles of some key variables of the proposed model are shown in Figure 2.3.6 for the experimental run of a contact phase at 22 °C, 30 vol.% DMSO, and 30 min as contact time, taken as representative.

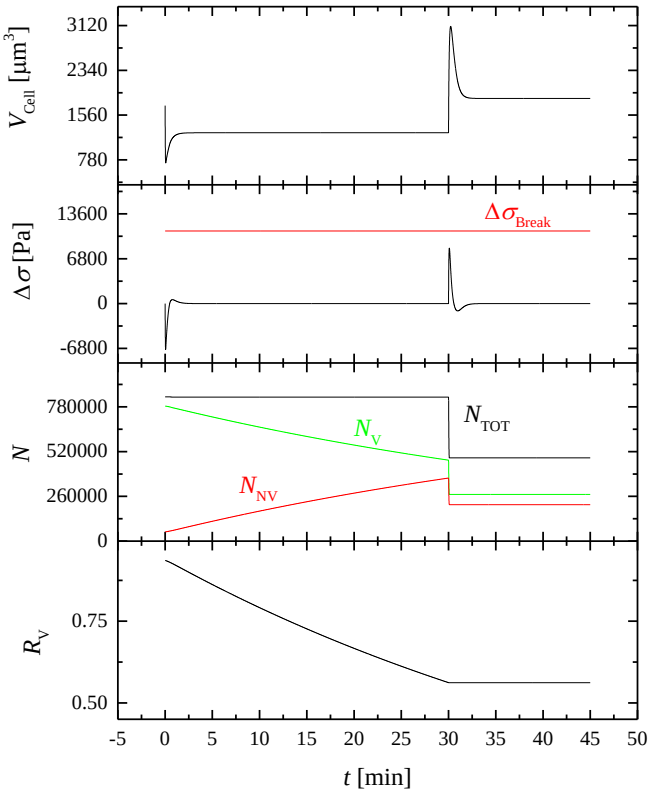

Figure 2.3.6: Temporal profiles of cell volume (V_{Cell}), cell membrane tension above resting condition ($\Delta\sigma$), total cell count (N_{TOT}), number of viable (N_{V}) and non-viable (N_{NV}) cells, and viability ratio ($R_{\mathrm{V}} = \frac{N_{\mathrm{V}}}{N_{\mathrm{TOT}}}$) for the experimental run of a contact phase at 22 °C, 30 vol.% DMSO, and 30 min as contact time.

In particular, the transient cell volume (V_{Cell}) is reported for this case along with the corresponding cell membrane tension above resting condition ($\Delta\sigma$), total cell count (N_{TOT}), number of viable (N_{V}) and non-viable (N_{NV}) cells, and viability ratio ($R_{\mathrm{V}} = \frac{N_{\mathrm{V}}}{N_{\mathrm{TOT}}}$). It is apparent that, during the contact phase (i.e. for $t < 30$ min) cells show the classic shrink-swell dynamics due to a membrane permeability to DMSO lower than that to water, followed by the swell-shrink dynamics during the removal phase.

The cytotoxic effect is strictly confined in the contact phase: this is demonstrated by the continuous decrease of the number of viable cells N_{V} transformed into the increasing non-viable cells N_{NV}, while N_{TOT} does not

vary significantly until the beginning of the removal phase at 30 min. As a consequence, the viability ratio R_V continuously declines in the first 30 min. Later, when the removal phase starts, cytotoxic effect stops, since intracellular concentration of DMSO diminishes, and expansion lysis occurs: this is demonstrated by the fall of N_{TOT} as well as N_V and N_{NV} while viability ratio remains constantly equal to the value reached at the end of the contact phase. Basically, cytotoxicity and expansion lysis are not simultaneous phenomena: the first one takes place only when the intracellular concentration of DMSO is large during the contact phase; on the other hand, expansion lysis occurs only during the osmotic swelling in the removal phase, when cell membrane is significantly stretched above resting condition as shown by the positive $\Delta\sigma$. Moreover, the rate of the cytotoxic effect is slower than osmosis which is concluded within 5 min, but is much slower than expansion lysis. To gain a deeper insight into the proposed model, it is worth noting that the positive $\Delta\sigma$ never actually reaches the $\Delta\sigma_{Break}$ when expansion lysis occurs during the swelling of the removal phase shown in Figure 2.3.6. Regarding this, according to Equations 8-9 the Weibull distribution $f_{EL}(\Delta\sigma)$ and transition function $\gamma(\Delta\sigma)$ corresponding to the values assigned to K_W and σ_{Break} in Table 2.3.3 are plotted in Figure 2.3.7.

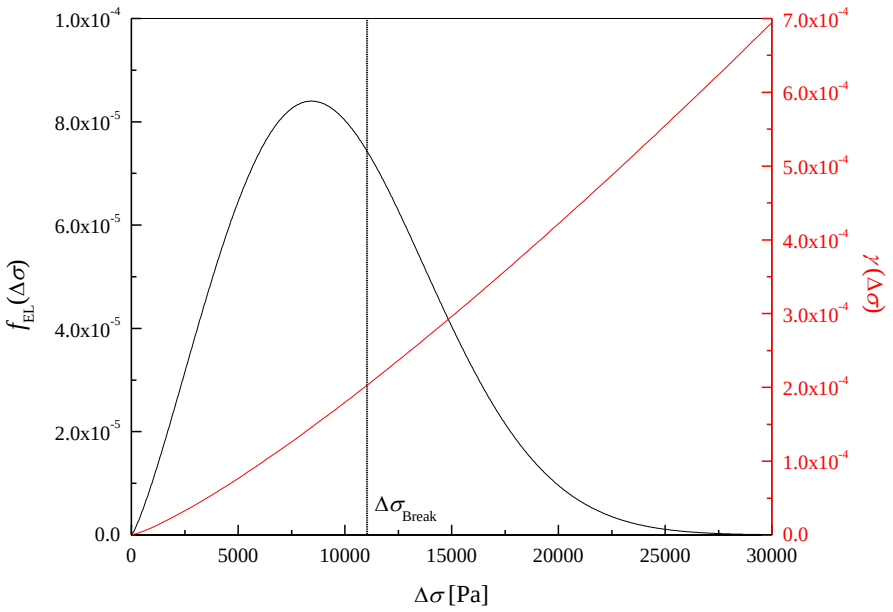

Figure 2.3.7: Weibull distribution $f_{EL}(\Delta\sigma)$ of Equation 9 and transition function $\gamma(\Delta\sigma)$ of Equation 8 corresponding to the parameter values of K_W and σ_{Break} determined for hMSCs as reported in Table 2.3.3.

Here it is shown that, in the simulations of the proposed model the Weibull distribution is log-normal (i.e. bell-shaped with asymmetry), with a single mode positioned at a $\Delta\sigma$ slightly smaller than $\Delta\sigma_{Break}$. This is due to a shape factor larger than 1 but not large enough for the coincidence of mode and median at $\Delta\sigma = \Delta\sigma_{Break}$. This means that the probability of expansion lysis occurrence is higher at $\Delta\sigma$ smaller than $\Delta\sigma_{Break}$ as clearly shown in Figure 2.3.6. Besides, the corresponding transition function $\gamma(\Delta\sigma)$ shown in Figure 2.3.7 does not increase that much. Therefore, membrane tension acceleration $(\frac{d\Delta\sigma}{dt})$ in Equation 6 plays a relevant role in the expansion

lysis of hMSCs: at the beginning of the osmotic swelling in removal phase a very rapid increase of membrane stretching occurs.

These results suggest that, generally speaking the cytotoxic effect of DMSO to hMSCs is lower than for other cells lineages, i.e. it is characterized by a slower reaction rate. Therefore, if DMSO addition to the cells is carried out at low temperatures and by strictly reducing the contact time to the one necessary for the osmotic equilibration, the cytotoxic effect of DMSO to hMSCs should be considerably limited. On the other hand, expansion lysis occurs only during the removal phase. This means that the contact between DMSO and hMSCs may be realized safely with a one-step strategy, i.e. by abruptly adding the whole DMSO into the extracellular solution in order to shorten the contact time. Vice versa, expansion lysis during the removal phase is a very fast phenomenon and can be limited only by carefully avoiding an excessive temporal increase of membrane stretching. To this aim the classic multi-step strategy may be adopted, by suspending the cells sequentially in a series of washing solutions characterized by a decreased osmotic tonicity.

2.3.5 Conclusions

In this work, a combined analysis of osmotic injury and cytotoxic effect when hMSCs from UCB are contacted with DMSO is carried out from the experimental and theoretical perspectives. A novel mathematical model is developed and proposed to interpret data, without the need to set in advance the cell Osmotic Tolerance Limits (OTLs), as traditionally done in cryopreservation literature. The model is based on the adoption of the SAR model recently proposed by the authors to describe the non-perfect osmotic behavior of hMSCs, where osmosis is coupled with cell mechanics and membrane area regulation. Comparisons between experimental data and theoretical simulations are provided, first by performing a non-linear regression analysis to evaluate unknown model parameters, then by checking its reliability to predict system behavior measured at operating conditions different from those used during the best-fit procedure.

It is found that the cytotoxic effect of DMSO onto hMSCs is only mild and confined to the contact phase, while expansion lysis is fast and takes place only during the swelling in the removal phase. Thus it is concluded that the cytotoxic effect may be limited considerably by adding DMSO in one step at low temperature and by strictly reducing the contact time to the one necessary for the osmotic equilibration. On the other hand, to limit the osmotic injury during the removal phase the excessive temporal increase of membrane stretching need to be carefully avoided by adopting a properly designed multi-step strategy.

Notation of the Subchapter 2.3

k_{CE}	Cytotoxic effect reaction rate	[s^{-1}]
k_{CE}^{0}	Cytotoxic effect reaction rate parameter	[L^{α} s^{-1} $mOsm^{-\alpha}$]
k_{EL}	Expansion lysis reaction rate	[s^{-1}]
E_{a}	Activation Energy	[J mol^{-1}]
$E_{\mathrm{a,CE}}$	Cytotoxic effect reaction activation energy	[J mol^{-1}]
f_{EL}	Expansion lysis Weibull distribution	[Pa^{-1}]
K	Young Modulus – Elastic Constant	[Pa]
K_{W}	Exponent of the Weibull distribution	[-]
k_{S}	SAR rate constant	[Pa^{-1} s^{-1}]
L_{P}	Water Permeability	[µm Pa^{-1} s^{-1}]
M	Osmolality	[mOsm L^{-1}]
N	Number	[-]
P_{CPA}	CPA Permeability	[µm s^{-1}]
P_{Ions}	Ions Permeability	[µm L s^{-1} $mOsm^{-1}$]
R	Universal Gas Constant	[J mol^{-1} K^{-1}]
R_{V}	Viability Ratio	[-]
T	Temperature	[K]
t	time	[s]
V_{Cell}	Mean Cell Volume	[$µm^3$]
α	Cytotoxic effect reaction rate parameter	[-]
γ	Transition function	[Pa^{-1}]
σ	Cell Membrane Tension	[Pa]

Superscripts

$^{\mathrm{INT}}$	referred to the intracellular solution
^{0}	referred to the initial time
$^{\infty}$	referred to infinite Temperature

Subscripts

$_{\mathrm{CPA}}$	referred to the CPA
$_{\mathrm{Ions}}$	referred to the Ions
$_{\mathrm{Break}}$	referred to the Critical Tension
$_{\mathrm{NV}}$	Non-Viable Cells
$_{\mathrm{R}}$	referred to the resting condition
$_{\mathrm{TOT}}$	Total Cells
$_{\mathrm{V}}$	Viable Cells
$_{\mathrm{W}}$	referred to the water

References of the Subchapter 2.3

1. Karlsson, J.O.M., Toner, M.: Cryopreservation. In: Lanza, R., Langer, R., Vacanti, J. (eds.) *Principles of Tissue Engineering*, 2nd edn. Academic press, San Diego (2000). eBook ISBN: 9780080539676
2. Fadda, S., Cincotti, A., Cao, G., (2010). The effect of cell size distribution during the cooling stage of cryopreservation without CPA, *AIChE J.*, 56, pp. 2173-2185. https://doi.org/10.1002/aic.12137
3. Casula, E., Traversari, G., Fadda, S., Klymenko, O.V., Kontoravdi, C., Cincotti, A., (2019). Modelling the Osmotic Behaviour of Human Mesenchymal Stem Cells, *Biochem Eng J*, ID 107296, https://doi.org/10.1016/j.bej.2019.107296
4. Benson, J.D., (2021) Mathematical Modeling and Optimization of Cryopreservation in Single Cells. In: Wolkers, W., Oldenhof, H., (eds), *Cryopreservation and Freeze-Drying Protocols. Methods in Molecular Biology*, vol 2180. Humana, New York, NY. https://doi.org/10.1007/978-1-0716-0783-1_4
5. Gao, D.Y., Liu, J., Liu, C., McGann, L.E., Watson, P.F., Kleinhans, F.W., Mazur, P., Critser, E.S., Critser, J.K., (1995). Andrology: Prevention of osmotic injury to human spermatozoa during addition and removal of glycerol. *Hum*, 10.5, pp. 1109-1122. https://doi.org/10.1093/oxfordjournals.humrep.a136103
6. Muldrew, K., McGann, L.E., (1994). The osmotic rupture hypothesis of intracellular freezing injury, *Biophys J*, 66, pp. 532-41. https://doi.org/10.1016/s0006-3495(94)80806-9
7. Meryman, H.T., (1970). The exceeding of a minimum tolerable cell volume in hypertonic suspension as a cause of freezing injury. In Wolstenholme, G.E.W., O'Connor, M., (eds), *The Frozen Cell*. CIBA Foundation Symposium. Churchill, London, pp. 51-67. https://doi.org/10.1002/9780470719732.ch4
8. Steponkus, P.A., Wiest, S.C., (1979) Freeze-thaw induced lesions in the plasma membrane. In Lyons, J.M., Graham, D., Raison, J.K., (eds), *Low Temperature Stress in Crop Plants: The Role of the Membrane*. Academic Press, New York, pp. 231-254.
9. Lovelock, J.E., (1953). The haemolysis of human red blood-cells by freezing and thawing. *Biochim Biophys Acta*, 10, pp. 414–426. https://doi.org/10.1016/0006-3002(53)90273-X
10. Mazur, P., Leibo, S.P., Chu, E.H.Y., (1972). A two-factor hypothesis of freezing injury: Evidence from Chinese hamster tissue-culture cells. *Exp Cell Res*, 71(2): pp. 345-355. https://doi.org/10.1016/0014-4827(72)90303-5
11. Hughes, Z.E., Mark A.E., Mancera R.L., (2012). Molecular dynamics simulations of the interactions of DMSO with DPPC and DOPC phospholipid membranes, *J Phys Chem B*, 116(39), pp. 11911-11923. https://doi.org/10.1021/jp3035538
12. Fernandez, M.L., Reigada, R., (2014). Effects of dimethyl sulfoxide on lipid membrane electroporation. *J Phys Chem B*, 118(31), pp. 9306-9312. https://doi.org/10.1021/jp503502s
13. Gurtovenko, A.A., Anwar, J., (2007). Modulating the structure and properties of cell membranes: the molecular mechanism of action of dimethyl sulfoxide. J *Phys Chem B*, 111(35), pp. 10453-10460. https://doi.org/10.1021/jp073113e
14. Bieback, K., Kern, S., Klüter, H., Eichler, H., (2004). Critical parameters for the isolation of mesenchymal stem cells from umbilical cord blood. *Stem Cells*, 22(4): pp. 625-634. https://doi.org/10.1634/stemcells.22-4-625
15. Newton, H., Pegg, D.E., Barrass, R., Gosden, R.G., (1999). Osmotically inactive volume, hydraulic conductivity, and permeability to dimethyl sulphoxide of human mature oocytes, *Reproduction*, 117(1), pp. 27-33. https://doi.org/10.1530/jrf.0.1170027
16. Mullen, S.F., Agca, Y., Broermann, D.C., Jenkins, C.L., Johnson, C.A., Critser, J.K. (2004). The effect of osmotic stress on the metaphase II spindle of human oocytes, and the relevance to cryopreservation, *Hum*, 19(5), pp. 1148–1154. https://doi.org/10.1093/humrep/deh201
17. Lusianti, R.E., Benson, J.D., Acker, J.P., Higgins, A.Z., (2013). Rapid removal of glycerol from frozen-thawed red blood cells, *Biotechnol Prog*, 29(3), pp. 609-620. https://doi.org/10.1002/btpr.1710
18. Kashuba, C.M., Benson, J.D., Critser, J.K., (2014). Rationally optimized cryopreservation of multiple mouse embryonic stem cell lines: I - Comparative fundamental cryobiology of multiple mouse embryonic stem cell lines and the implications for embryonic stem cell cryopreservation protocols, *Cryobiology*, 68, pp. 166-175. https://doi.org/10.1016/j.cryobiol.2013.12.007
19. Zhurova, M., Lusiantic, R.E., Higginsc, A.Z., Acker J.P., (2014). Osmotic tolerance limits of red blood cells from umbilical cord blood, *Cryobiology*, 69, pp. 48-54. https://doi.org/10.1016/j.cryobiol.2014.05.001

20. Elmoazzen, H.Y., Poovadan, A., Law, G.K., Elliott, J.A.W., McGann, L.E., Jomha, N.M., (2007). Dimethyl sulfoxide toxicity kinetics in intact articular cartilage. *Cell Tissue Bank*, 8, pp. 125–133. https://doi.org/10.1007/s10561-006-9023-y
21. Wang, X., Hua, T.C., Sun, D.W., Liu, B., Yang, G., Cao, Y., (2007). Cryopreservation of tissue-engineered dermal replacement in Me 2 SO: toxicity study and effects of concentration and cooling rates on cell viability. *Cryobiology* 55(1), pp. 60-65. https://doi.org/10.1016/j.cryobiol.2007.05.006
22. Hunt, C.J., Armitage, S.E., Pegg, D.E., (2003). Cryopreservation of umbilical cord blood: 1. osmotically inactive volume, hydraulic conductivity and permeability of CD34+ cells to dimethyl sulphoxide. *Cryobiology*, 46, pp. 61–75. https://doi.org/10.1016/S0011-2240(02)00180-3
23. Hunt, C.J., Armitage, S.E., Pegg, D.E., (2003). Cryopreservation of umbilical cord blood: 2. Tolerance of CD34+ cells to multimolar dimethyl sulphoxide and effect of cooling rate on recovery after freezing and thawing, *Cryobiology*, 46, pp. 76–87. https://doi.org/10.1016/S0011-2240(02)00181-5
24. Benson, J.D., Kearsley, A.J., Higgins, A.Z. (2012). Mathematical optimization of procedures for cryoprotectant equilibration using a toxicity cost function, *Cryobiology*. 64(3), pp. 144-151. https://doi.org/10.1016/j.cryobiol.2012.01.001
25. Karlsson, J.O.M., Szurek, E.A., Higgins, A.Z., Lee, S.R, Eroglu, A., (2014). Optimization of Cryoprotectant Loading into Murine and Human Oocytes, *Cryobiology*, 68, pp. 18-28. https://doi.org/10.1016/j.cryobiol.2013.11.002
26. Davidson, A.F., Benson, J.D., Higgins, A.Z., (2014). Mathematically optimized cryoprotectant equilibration procedures for cryopreservation of human oocytes, *Theor Biol Medical Model*, 11(13). https://doi.org/10.1186/1742-4682-11-13
27. Davidson, A.F., Glasscock, C., McClanahan, D.R., Benson, J.D., Higgins, A.Z., (2015) Toxicity Minimized Cryoprotectant Addition and Removal Procedures for Adherent Endothelial Cells, *PLoS ONE*, 10(11), ID e0142828. https://doi.org/10.1371/journal.pone.0142828
28. Kedem, O., Katchalsky, A., (1958). A thermodynamic analysis of the permeability of biological membranes to non-electrolytes, *Biochim Biophys Acta*, 27, pp. 229-246. https://doi.org/10.1016/0006-3002(58)90330-5
29. Kleinhans, F.W., (1998). Membrane permeability modeling: Kedem-Katchalsky vs a two-parameter formalism, *Cryobiology*, 37(4), pp. 271-289. https://doi.org/10.1006/cryo.1998.2135
30. Casula, E., Asuni, G.P., Sogos, V., Fadda, S., Delogu, F., Cincotti, A., (2017). Osmotic behaviour of human mesenchymal stem cells: Implications for cryopreservation, *PLoS ONE*, 12(9): e0184180. https://doi.org/10.1371/journal.pone.0184180
31. Lee, M.W., Choi, J., Yang, M.S., Moon, Y.J., Park, J.S., Kim, H.C., Kim, Y.J., (2004). Mesenchymal stem cells from cryopreserved human umbilical cord blood. *Biochem Biophys Res Commun*, 320(1), p. 273-278. https://doi.org/10.1016/j.bbrc.2004.04.206
32. Bryan, K., Engler, A., Gulati, A., Manalis, S.R., (2012). Continuous and Long-Term Volume Measurements with a Commercial Coulter Counter. *PLoS ONE*, 7(1), e29866. https://doi.org/10.1371/journal.pone.0029866
33. Acker, J.P., Pasch, J., Heschel, I., Rau, G., McGann, L.E., (1999). Comparison of Optical Measurement and Electrical Measurement Techniques for the Study of Osmotic Responses of Cells Suspensions. *Cryo Letters*, 20, pp. 315-324.
34. Traversari, G., Cincotti, A., (2020). Insights into the model of non-perfect osmometer cells for cryopreservation: a parametric sweep analysis, in press Cryobiology. https://doi.org/10.1016/j.cryobiol.2020.11.013
35. Fadda, S., Cincotti, A., Cao, G., (2012). A novel population balance model to investigate the kinetics of in vitro cell proliferation: Part I. Model development, *Biotechnol Bioeng*, 109(3), pp. 772-781. https://doi.org/10.1002/bit.24351
36. Fadda, S., Cincotti, A., Cao, G., (2012). A novel population balance model to investigate the kinetics of in vitro cell proliferation: Part II. Numerical solution, parameters' determination and model outcomes, *Biotechnol Bioeng*, 109(3), pp. 782-796. https://doi.org/10.1002/bit.24350
37. Koch, A., Schaecter, M., (1962). A model for statistics of the cell division process, *J Gen Microbiol*, 29, pp. 435–444. https://doi.org/10.1099/00221287-29-3-435
38. Hatzis, C., Srienc, F., Fredrickson, A.G., (1995). Multistaged corpuscolar models of microbial growth: Monte Carlo simulations, *Biosystems* 36, pp. 19–35. https://doi.org/10.1016/0303-2647(95)01524-O

2.4 A compartmental model for the Air-Drying process of hMSCs in a desiccator unit

2.4.1 Introduction

Progress in personalized/regenerative medicine, drug testing, and disease modelling, prompted by the latest achievements in differentiated cells reprogramming (like induced pluripotent stem cells, iPSCs, direct reprogramming), resulted in massive increase in stored cell lines under Liquid Nitrogen (LN) at -196 °C [1-3]. However, cryostorage, although effective, presents several problems. These include high maintenance costs [4], need for specialized storage facilities, continuous LN supply, energy-dependency, safety concerns, and risk of pathogen transmission, all serious issues in clinical practice [5]. Besides these intrinsic problems, the industrial production of LN has a serious environmental impact too, leaving a massive carbon footprint. Hence, nowadays alternative options for cells storage are sought. These are typically based on water subtraction techniques to induce reversible block of macromolecular interactions, allowing effective cells storage at non-cryogenic temperatures.

For instance, in the research project Drynet (GA No 734434 – Marie Skłodowska - Curie Actions, Research and Innovation Staff Exchange RISE, Call: H2020-MSCA-RISE-2015) the possibility to mimic mother nature where anhydrobiosis occurs for several vegetal and animal phyla is explored. In particular, anhydrobiosis allows seeds and small invertebrates like tardigrades survive long time spans (decades/centuries) in the absence of water [6], particularly thanks to the induced synthesis of sugars, as sucrose or trehalose. Thus, the research project Drynet aims to develop a cost-effective, ice-free process for long-term preservation of human cells and gametes, by checking the possibility to successfully dehydrate the cells by means of air-drying with trehalose at atmospheric pressure and room temperature. In the framework of the activities of the Drynet project, the development of a deterministic, mathematical model useful to guide and support the experiments of air-drying of human cells is assigned to the research partner Università degli Studi di Cagliari. The results of this activity are shown and discussed in this work.

First an intense bibliographic search was carried out on mathematical modelling addressing the drying of animal cells. It was found that only the mathematical modelling of the freeze-drying process for non-living biomaterials (i.e. food) has been the subject of numerous studies, while living cells have never been accounted for by computational investigations, i.e. no modeling study focused on preserving the viability of animal cells subjected to drying was found. On the other hand, the role of sugar glass formation to effectively preserve living cells has been the topic of numerous experimental papers. For instance, the water replacement hypothesis was formulated in [7]: according to this speculation, sugar glass should be capable to stabilize cell membranes in the dry state, most likely by hydrogen bonding to polar head-groups of lipids in membranes. This interaction should result in maintenance of cell membrane in a physical state similar to that seen in the presence of water, thus avoiding the mechanical collapse of the membrane in a dehydrated cell. An alternative viewpoint has been also hypothesized, where the interaction of trehalose with water instead of with cell membrane is considered

responsible of the preservation capability [8]. According to this conjecture, trehalose in water should be capable to form glass at relatively high temperature, and this glass formation should be in itself sufficient to stabilize dry biomaterials. On the contrary, in principle the formation of dihydrate trehalose crystals subtracts water from the residual liquid phase, and this should help cells dehydration as pointed out by other authors [9,10,11]. Regarding this, crystal formation following water evaporation at room temperature is typically considered a slow phenomenon for the binary system trehalose + water [9]: even if favored from a thermodynamic viewpoint [10] the formation of trehalose crystals is kinetically hindered so that glass is easily obtained. For this reason, in the papers addressing the long-term preservation of biological material an extended phase diagram reporting the glass transition curve in addition to the solubility of the crystals is usually referred to when discussing the choice of operating conditions to design the experimental runs.

Even if this fragmentary and sometimes contradictory literature on the subject was found, a major conclusion may be safely taken: evaporation rate needs to be controlled in the air-drying process of living cells. In fact, from one side a sufficient but not excessive level of cell dehydration needs to be reached as pointed out by [12]. In particular, the capacity of mammalian cells to survive dehydration down to a certain water content (~ 50-60 % of original water volume) without significant loss of viability was assessed, even if it was noted that these cells die upon removal of 10-15% additional water. From the other side, an excessive evaporation rate has to be avoided during the air-drying process since it easily leads to the formation of a thin glassy film on top of the evaporating liquid surface, thus basically stopping cell dehydration before reaching the desired level [13,14]. This explains why the Japanese partner of the Drynet project, who is in charge of carrying out the experiments in a special lab desiccator unit with silica gel as water trap, uses to cover the container of the liquid cell suspension to be dried with a lid not securely close [15,16]. However, it is easy to predict that by doing so the possibility to favor crystal formation instead of glass increases as evaporation rate decreases, depending on system sizes, geometries and operating conditions.

Therefore, in this work a mathematical model capable to describe the air-drying process at room temperature and atmospheric pressure of hMSCs with trehalose sugar is developed. By referring to the desiccator unit of the Japanese partner of the Drynet project, the sequence of all the physico-chemical phenomena potentially involved in the process are accounted for in a compartmental model. More specifically, evaporation, cell osmosis, crystal or glass formation of trehalose sugar, water diffusion across the lid of the unsealed petri dishes, and water adsorption onto porous medium are mathematically described by measuring the corresponding driving forces on the water+trehalose extended phase diagram and the other thermodynamic equilibria involved. Regarding this, a bibliographic search aimed to determine the thermodynamic equilibria and the transport parameters was also performed, and the complete phase diagram of the investigated water+trehalose system was reconstructed. This activity consists in the determination of the various equilibria of liquid, solid and vapor phases, including solubility curves, the liquid-vapor equilibrium curve and that relating to the formation of an amorphous glass phase. In the literature conflicting data concerning this phase diagram are reported, first because the water+trehalose system has generally been the subject of a limited number of studies, but also because the solid phase of trehalose has several thermodynamically stable forms whose formation

depends on operating conditions and the thermodynamic path followed to obtain that specific phase. In spite of these uncertainties, a state diagram was decided for the water + trehalose system and the various liquid, solid and vapor equilibria used to determine the driving forces of the phenomena considered in the developed model. In this regard it was also necessary to identify the water vapor adsorption isotherms on silica gel.
Given the absence of valuable data and the uncertainties related to the values assigned to model parameters, system sizes and geometries as well as the operating conditions, the results of a parametric sensitivity analysis are shown in this work, starting from a base case. Generally speaking, a dynamic competition between evaporation and crystallization results from the simulations of the process. In fact, water evaporation can easily increase the trehalose concentration in the liquid phase so that solution viscosity rapidly increases leading to glass formation, with the desired desiccation level for an effective long-term preservation of the suspended cells. However, an over-extended process duration results thus making the air-drying of cells economically unprofitable. On the other hand, if evaporation slows down too much, trehalose crystals instead of glass are formed, and the lyo-stability guaranteed by the sugar glass is lost while an insufficient cell dehydration is achieved. This way an effective long-term preservation cannot be obtained, even if the duration of the process is reduced. The parametric sensitivity analysis performed in this work highlights the effect of system sizes and geometries on the competition between evaporation and crystallization rates, pointing out the crucial role played by diffusivity and its composition dependence in the liquid sample. It is concluded that, by varying system sizes and geometries as well as the operating conditions, the evaporation rate need to be optimized in order to reach an acceptable final cell viability (by favoring glass formation with a large cell dehydration) while reducing the duration of the air-drying process.

2.4.2 Model Equations

In this section the equations of the proposed model are reported. In order to reduce the mathematical and numerical complexity, the different phases present in the system are described by means of a compartmental modelling approach, i.e. a series of perfectly mixed compartments in communication among each other, kept at constant system temperature and pressure.
The air-drying process is assumed to take place inside a specific desiccator unit, i.e. a closed system containing a certain amount of silica gel and a given number of Petri dishes where cells are suspended in a liquid solution with a lyo-protectant (trehalose sugar): basically the air-drying process consists in the water transfer from the liquid samples in the Petri dishes and the cells suspended therein to the adsorbing silica gel, passing through the space left by the lid covering the unsealed Petri dishes (hereon called leakage transport since it originates from the unsealed leaking petri dishes).
During the process water vapor accumulates into the volume of the petri dishes due to the resistance opposed by the leakage transport to the water transfer through the space between the lid and the unsealed petri dish. The adsorption onto silica gel of water vapor coming from the petri dishes keeps the Relative Humidity (RH) in the chamber of the desiccator unit at low levels, thus enhancing the leakage transport. As a consequence, water is removed via evaporation from the liquid phase of the sample and the cells suspended therein contained

in the petri dishes, determining an increase of trehalose concentration and a raise of the osmotic tonicity (i.e. osmolality) in the liquid phase. This has two consequences: from one hand, the cells in suspension shrink due to exosmosis of water, from the other trehalose crystals precipitates if the solubility of the sugar in the liquid phase is exceeded. However, if the evaporation rate is relatively faster than crystal formation, the glass transition composition may be eventually reached, and glass of the residual liquid solution is formed instead of trehalose crystals.

In summary, the air-drying of hMSCs in the apparatus investigated in this work involves the occurrence at 25 °C and atmospheric pressure of a series of different physico-chemical phenomena such as evaporation, leakage from petri to chamber, adsorption, crystal formation or glass transition, and cell osmosis. To better describe these phenomena, the system behavior is followed by referring to Figure 2.4.1, where the extended phase diagram of the binary system (water + trehalose) is shown and the relevant driving forces of the competing phenomena in the process (i.e. evaporation and crystallization) are indicated.

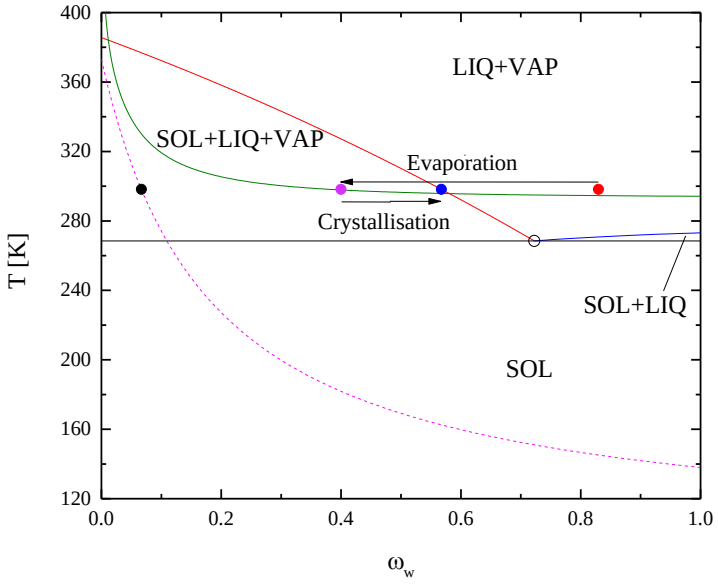

Figure 2.4.1: Extended phase diagram of the water+trehalose binary system

In particular, the initial composition of the liquid phase inside the petri dish at 25 °C is represented by the red point shown in Figure 2.4.1. Water evaporation causes an increase in trehalose concentration corresponding to a shift to the left of the composition of the residual liquid phase. The driving force of evaporation is represented in Figure 2.4.1 as the difference in concentration between the red and violet points. The latter one is positioned at 25 °C in the vapor-liquid equilibrium line (corresponding to a low water partial pressure in the overhead gaseous phase) superimposed on the phase diagram of the binary system. Of course, an extended water evaporation may lead the composition of the residual liquid phase beyond the solubility limit (red curve in Figure 2.4.1) into the tri-phasic zone (SOL+LIQ+VAP) thus triggering crystal formation, whose driving force is super-saturation, i.e. the difference of current concentration with respect to the solubility one represented by the blue point in Figure 2.4.1. It is apparent that, once inside the tri-phasic zone, a dynamic competition between the evaporation and crystallization rates may result, with the two phenomena pushing the composition

of the liquid phase in opposite directions: the first one tries to increase the concentration of the dissolved trehalose (i.e. moving the red point towards the left in Figure 2.4.1), whereas the second works on reducing the distance from the solid-liquid equilibrium curve represented by the blue point (i.e. moving the red point towards the right in Figure 2.4.1), once the solubility limit has been overcome. If evaporation is relatively faster than crystal formation, the composition of the residual liquid phase eventually reaches the glass transition curve (represented by the black point in Figure 2.4.1). At this large trehalose concentration water evaporation is hindered from a kinetics perspective, since diffusivity in the liquid phase decreases to critical values. On the other hand, also crystal formation rate is lowered in favor of glass transition, due to a critically high solution viscosity.

2.4.2.1 Air-drying apparatus: system set-up

The system setup consists of a desiccator unit with an internal chamber containing 20 unsealed petri dishes covered by lids on a shelf and silica gel adsorbent at the bottom, as schematically depicted in Figure 2.4.2. The liquid sample in any petri dish contains the cells in suspension. The liquid sample is enclosed by a silicone insulator (drawn in red in Figure 2.4.2) in order to fix its position: during evaporation the liquid sample maintains a cylindrical volume, i.e. height decreases with a constant surface area of evaporation. The population of cells in suspension is assumed to be singles sized, i.e. the population is composed by a number of cells sharing the same volume. Some relevant system sizes and geometries are also reported in Figure 2.4.2 in scale.

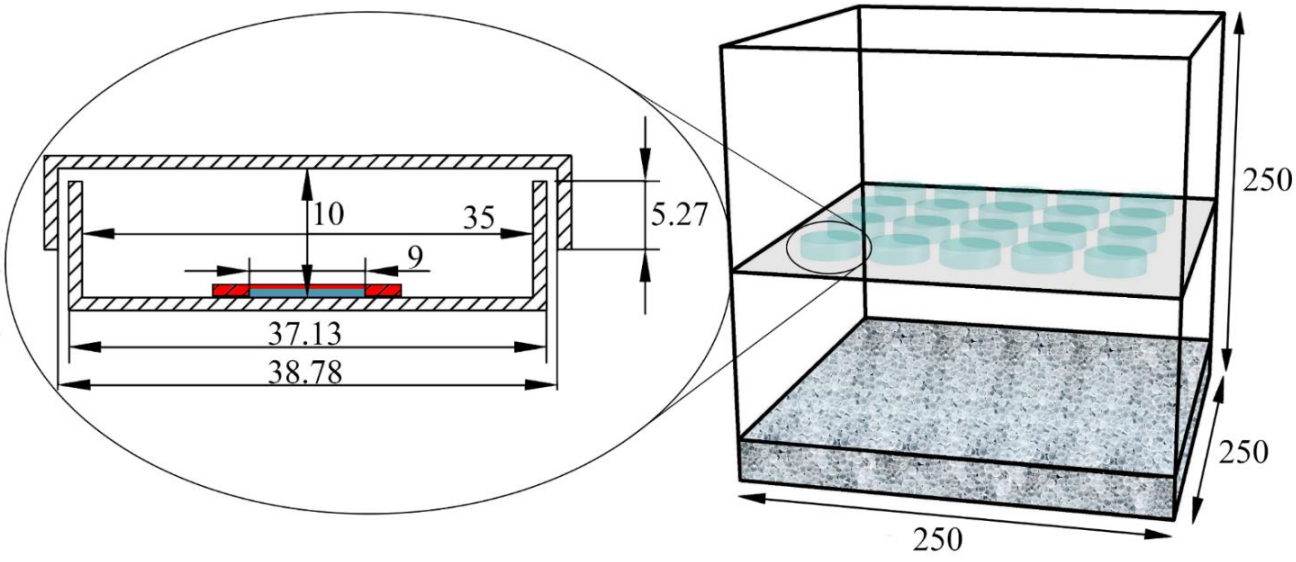

Figure 2.4.2: Schematic representation of the system: a desiccator unit with 20 unsealed Petri dishes and silica gel. The section of a single Petri dish taken as representative is zoomed on the left showing the silicone insulator (red) containing the liquid sample where cells are suspended with trehalose (blue). The reported sizes are given in mm.

On the contrary, in Figure 2.4.3 a schematic not in scale representation of the phenomena accounted for by the proposed model is given to highlight the transfer of water from the liquid sample containing the shrinking cells inside any single Petri dish towards the adsorbing silica gel. Only osmosis between the suspended cells and the liquid phase is not represented.

Inside any petri dish both liquid and gas phases are present, exchanging water via evaporation: water content increases in the vapor phase and decreases in the liquid phase, thus concentrating the dissolved trehalose.

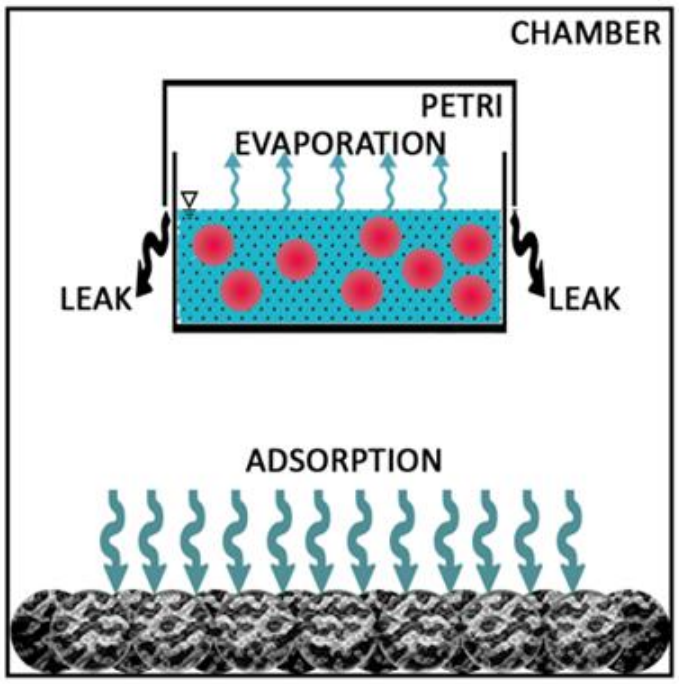

Figure 2.4.3: Schematic representation of water transport inside the desiccator unit (not in scale): only one petri dish is shown, taken as representative.

On the contrary, trehalose crystal formation reduces the amount of dissolved sugar, while the cells suspended in the liquid phase exchange water via osmosis in response to the variations of trehalose concentration: when the concentration of dissolved trehalose increases, cells shrink due to water exosmosis, while swelling occurs if trehalose content is reduced.

In the gas phase of the Petri dish, water vapor is exchanged with the chamber of the desiccator unit: driven by the gradient in vapor concentration between the two compartments, a passive transport (leakage) through the opening of the unsealed petri takes place.

This way, water vapor coming from the petri dishes through the leakage is eventually trapped by the adsorbent silica gel placed at the bottom of the chamber. The adsorbing porous medium helps to maintain RH low in the chamber, thus sustaining a continuous flow of water until a complete dehydration of the sample and the cells in suspension is reached.

Regarding crystal formation in a concentrated liquid sample, trehalose dihydrate is the most stable form at 25 °C according to thermodynamics. The reaction scheme and stoichiometry to form solid dihydrate trehalose starting from the parent liquid component is shown in the following Equation 1,

$$2H_2O^{(L)} + TRE^{(L)} \leftrightarrow (TRE \cdot 2H_2O)^{(S)} \quad (1)$$

where water sequestration from the liquid sample to form the crystal is apparent. In this work crystal formation is modelled following the Classical Nucleation Theory (CNT), by describing nucleation from a supersaturated liquid solution followed by crystal growth. Nucleation consists of the birth of a new small crystal when the aggregation of solute molecules reaches a thermodynamically stable structure. Then, crystal growth follows as driven mainly by a diffusive process which subtracts solute molecules from the liquid solution to increase the size of crystal.

In the sequel, model equations are described in sections 2.2-2.4: first the material balances of the different phases in the compartmental model are written down in section 2.2, by describing the involved physico-chemical phenomena; then, the diffusion fluxes of water transport between the different compartments/phases composing the system are defined in section 2.3., by taking into account the equilibrium equations at the contact surfaces between different phases. For the sake of brevity, the thermodynamics and transport parameters used in the model simulations are described respectively in the appendices A1 and A2, while, a series of system variables linked to the independent variables are reported in the appendix A3.

2.4.2.2 Material balance equations

According to Figure 2.4.3, in the air-drying process the volume of the liquid sample containing the cells in suspension is progressively reduced through evaporation and crystal formation or glass transition until a complete consumption may be eventually reached. For this reason, the material balances in the different compartments/phases are not given in terms of species concentration but are referred to their absolute content. Thus, in the following equations n_W^L and n_{TRE}^L represent the mole number of water and dissolved trehalose present in the liquid phase contained into any single petri dish, respectively; n_W^{PG} and n_W^{CG} represent the mole number of water present in the Gas phases inside any single Petri dish (PG) and in the entire desiccator Chamber (CG); n_W^{ADS} stands for the mole number of water adsorbed in the whole silica gel (ADS) put inside the desiccator unit; V_W^{CELL} is the volume of water contained in a single cell. A Notation section is provided, where all symbols are reported with units.

2.4.2.3 Liquid phase in a single petri dish: liquid water

In the adopted compartmental model, the material balance of water in the liquid phase contained in a single petri dish is determined by evaporation, osmosis and crystal formation of dihydrate trehalose, as expressed in the following equation

$$\frac{dn_W^L}{dt} = \underbrace{-S^L J_{EVAP}}_{evaporation} \underbrace{+N^{CELL} S^{CELL} J_{OSM}}_{osmosis} \underbrace{-2R_{CRYSTAL}}_{crystallisation} \quad (2)$$

$$@\ t = 0, \qquad n_W^L = n_W^{0,L}$$

In particular, evaporation rate is modelled as a diffusive flux J_{EVAP} multiplied to the corresponding cross-sectional surface S^L, i.e. the contact surface of the liquid and gas phases inside a single petri dish (evaporative

surface). Analogously, the osmotic flow of water is given by the product of the osmotic flux J_{OSM} from a single cell and the total surface of cells $N^{CELL}\,S^{CELL}$, where N^{CELL} represents the total number of cells suspended in the liquid phase and S^{CELL} the surface area of a single cell membrane. While evaporative flow is always a negative term in Equation 2 (i.e. $J_{EVAP} \geq 0$), water transferred via osmosis between liquid phase and cytoplasm may be a positive or negative term (i.e. $J_{OSM} \gtreqless 0$) when cells shrink or swell, respectively, depending on the osmolality gradient between intra- and extracellular compartments. Finally, liquid water is always consumed by crystallization of dihydrate trehalose (i.e. $R_{CRYSTAL} \geq 0$) following the stoichiometry shown in Equation 1.

2.4.2.4 Liquid phase in a single petri dish: dissolved trehalose

The material balance of dissolved trehalose in the liquid phase contained in a single petri dish is affected only by crystal formation of dihydrate trehalose following the reaction stoichiometry of Equation 1:

$$\frac{dn_{TRE}^{L}}{dt} = \underbrace{-R_{CRYSTAL}}_{crystallisation} \qquad (3)$$

$$@\ t = 0, \qquad n_{TRE}^{L} = n_{TRE}^{0,L}$$

2.4.2.5 Gas phase in a single petri dish: water vapor

The material balance of water in the gas phase contained in a single petri dish is determined by evaporation from the liquid phase and leakage to the desiccator chamber through the space of the unsealed lid (see Figure 2.4.3)

$$\frac{dn_{W}^{PG}}{dt} = \underbrace{S^{L}J_{EVAP}}_{evaporation}\ \underbrace{-S^{LEAK}J_{LEAK}}_{leakage} \qquad (4)$$

$$@\ t = 0, \qquad n_{W}^{PG} = n_{W}^{0,PG}$$

where water flows are modelled as a flux multiplied to the corresponding cross-sectional surface. Thus, S^{LEAK} is the surface of the annular surface area between external wall of the petri dish and the lid shown in Figure 2.4.2. In Equation 4 evaporation rate is always a positive term for the gas phase inside the petri dish (i.e. $J_{EVAP} \geq 0$), while the leakage rate to the desiccator chamber is negative (i.e. $J_{LEAK} \geq 0$)

2.4.2.6 Gas phase in the chamber of the desiccator unit: water vapor

The material balance of water in the gas phase contained by the chamber of the desiccator unit (see Figure 2.4.2-3) is determined by the water leakage coming from all the petri dishes and the adsorption rate to the silica gel as stated in Equation 5

$$\frac{dn_{W}^{CG}}{dt} = \underbrace{N^{P}S^{LEAK}J_{LEAK}}_{leakage}\underbrace{-S^{ADS}J_{ADS}}_{adsorption} \qquad (5)$$

$$@\ t = 0, \qquad n_{W}^{CG} = n_{W}^{0,CG}$$

where water flows are modelled as a flux multiplied to the corresponding cross-sectional surface, a usual. In Equation 5, N^P is the number of petri dishes placed inside the desiccator unit and $S^{LEAK}J_{LEAK}$ represents the water flow coming from a single petri dish. S^{ADS} represents the total surface of the adsorbent beads of silica gel. The leakage rate is always a positive term for the chamber of the desiccator unit (i.e. $J_{LEAK} \geq 0$), whereas the adsorption rate is negative (i.e. $J_{ADS} \geq 0$).

2.4.2.7 Adsorbent solid phase: water vapor adsorbed in silica gel

The material balance of water in the solid adsorbing phase is reported in Equation 6

$$\frac{dn_W^{ADS}}{dt} = \underbrace{S^{ADS}J_{ADS}}_{adsorption} \qquad (6)$$
$$@\ t = 0, \qquad n_W^{ADS} = n_W^{0,ADS}$$

where adsorption rate is always a positive term (i.e. $J_{ADS} \geq 0$).

2.4.2.8 Intracellular liquid phase: water in cytoplasm

The material balance of water in a single cell is determined only by osmosis. In fact, trehalose is assumed to be impermeant to cell membrane and only water can be exchanged with the suspending solution during the air-drying process. Therefore, the intracellular content of trehalose is assumed to be reached somehow through osmotic equilibration with the suspending solution before the air-drying process begins. Moreover, intracellular crystal formation is neglected since during the air-drying process cells shrink thus reaching a volume which is assumed to be too small for nucleation according to the classic nucleation theory (see Equation 20). Thus, the following balance of water content inside any single cell may be written

$$\frac{dV_W^{CELL}}{dt} = \underbrace{-S^{CELL}J_{OSM}\tilde{v}_W}_{osmosis} \qquad (7)$$
$$@\ t = 0, \qquad V_W^{CELL} = V_W^{0,CELL}$$

where $\tilde{v}_W$ represents the molecular volume of water and S^{CELL} is the surface area of a cell membrane (i.e. assuming a spherical shape for cells $S^{CELL} = (4\pi)^{\frac{1}{3}}(3\,V^{CELL})^{\frac{2}{3}}$). Water exchanged via osmosis between liquid phase and cytoplasm may be a positive or negative term (i.e. $J_{OSM} \gtreqless 0$) when cells shrink or swell, respectively, depending on the osmolality gradient between intra- and extracellular compartments.

2.4.3 Mass transport: diffusion fluxes

In this section, the material flux through the contact surface between two facing phases is modelled according to the classic two-film theory, by defining a driving force and the corresponding material transport resistance on the basis of the phase equilibrium attained at the contact surface.

2.4.3.1 Evaporation in the Petri dish

According to the compartmental modelling approach, all the phases accounted for are assumed to be perfectly mixed so that concentration gradients are confined to a pseudo-stationary diffusive layer of thickness δ. As a consequence, according to the two-film theory the evaporative flux coming from the liquid is equal to that one entering the gas phase as stated below

$$J_{EVAP} = \frac{\mathfrak{D}_W^L}{\delta^L}\left(C_W^L - C_W^{L,*}\right) = \frac{\mathfrak{D}_W^G}{\delta^G}\left(C_W^{PG,*} - C_W^{PG}\right) \quad (8)$$

where $\mathfrak{D}_w$ represents the diffusivity of water in a phase, C_W and δ are the corresponding water concentration in the bulk of the phase and thickness of the diffusive layer, respectively, while C_W^* is the corresponding concentration at the contact surface. $C_W^{PG,*}$ and $C_W^{L,*}$ are determined by means of the Vapor-Liquid equilibrium relationship (i.e. $C_W^{PG,*} = f(C_W^{L,*})$). In analogy with electric circuit analysis, $\frac{\mathfrak{D}_W^L}{\delta^L}$ and $\frac{\mathfrak{D}_W^G}{\delta^G}$ represent the liquid and gas conductances of water evaporation rate, respectively.

According to the classic two-film theory, a material flux may be determined through the definition of a global transport coefficient in relation to a global driving force. For water evaporation from the liquid sample to the gas phase inside any Petri dish, a gaseous global driving force is defined by means of $C_W^{L\to G}$ which represents the water concentration in the gas phase at equilibrium with the water concentration in the bulk of the liquid phase, i.e. $C_W^{L\to G} = f(C_W^L)$. This way evaporation flux can be written as it follows

$$J_{EVAP} = K_{EVAP}^G\left(C_W^{L\to G} - C_W^{PG}\right) \quad (9)$$

where K_{EVAP}^G is the global transport coefficient in gas phase, obtained as the reciprocal of the sum of all the mass transport resistances as shown in Equation 10.

$$\frac{1}{K_{EVAP}^G} = \left(\overbrace{\frac{1}{\left(\frac{\mathfrak{D}_W^G}{\delta^G}\right)}}^{gas} + \overbrace{\frac{1}{\left(\frac{\mathfrak{D}_W^L}{\delta^L}\right)}\frac{C_W^{L\to G} - C_W^{PG,*}}{C_W^L - C_W^{L,*}}}^{liquid}\right) \quad (10)$$

If we divide the resistance in gas phase $\left(\frac{\mathfrak{D}_W^G}{\delta^G}\right)^{-1}$ by the total resistance shown in Equation 10, the percentage of gas phase resistance to global (gas + liquid) resistance for water evaporation is obtained as it follows:

$$R_{EVAP}^G\% = 100\%\left(1 + \frac{\mathfrak{D}_W^G\delta^L}{\mathfrak{D}_W^L\delta^G}\frac{C_W^{L\to G} - C_W^{PG,*}}{C_W^L - C_W^{L,*}}\right)^{-1} \quad (11)$$

When $R_{EVAP}^G\%$ is equal to zero the resistance to water evaporation is confined in the diffusional layer of the liquid phase and no concentration gradient in the gas phase is obtained, whereas when $R_{EVAP}^G\%$ is equal to 100 % transport resistance is only on the gas side and a flat concentration profile results in the liquid layer.

2.4.3.2 Adsorption in the silica gel

Similarly to evaporation, water adsorption from the chamber in the desiccator unit and the porous beads of silica gel is modelled as a diffusive flux between two facing phases across the corresponding diffusive layers, by following the Linear Driving Force approximation typically used to model adsorptive system:

$$J_{ADS} = \frac{\mathfrak{D}_W^G}{\delta^{ADS}}\frac{\varepsilon}{\tau}\ (\bar{q}_W^* - \bar{q}_W)\frac{\rho_{ADS}}{PM_W} = \frac{\mathfrak{D}_W^G}{\delta^{ADS}}\left(C_W^{CG} - C_W^{CG,*}\right) \tag{12}$$

In particular, an effective diffusion in porous medium is accounted for by means of porosity ε a tortuosity τ in the adsorbent particles. $\frac{\rho^{ADS}}{PM_W}\bar{q}_W$ and C_W^{CG} are the water concentration in the bulk of the contacting phases, i.e. the solid adsorbent and the gas in the chamber of the desiccator unit, respectively. In fact, concentration inside adsorbing medium are typically measured in terms of mass fraction of adsorbing species with respect to the mass of adsorbent medium (i.e. $\bar{q}_W$). As usual, $\frac{\rho^{ADS}}{PM_W}\bar{q}_W^*$ and $C_W^{CG,*}$ are the molar concentration of water at equilibrium in the interface between solid and gas phases ruled by the Vapor-Solid equilibrium relationship, i.e. $\bar{q}_W^* = f\left(C_W^{CG,*}\right)$. In analogy with electric circuit analysis, $\frac{\mathfrak{D}_W^G}{\delta^{ADS}}$ and $\frac{\mathfrak{D}_W^G}{\delta^{ADS}}\frac{\varepsilon}{\tau}$ represent the gas and solid conductances of water adsorption rate, respectively.

Following the same procedure adopted for evaporation, a global transport coefficient in solid phase is defined for water adsorption flux by the definition of $\bar{q}_W^{G\to S}$ which represents the water concentration in the solid phase at equilibrium with the water concentration in the bulk of the gas phase in the chamber of the desiccator unit, i.e. $\bar{q}_W^{G\to S} = f\left(C_W^{CG}\right)$. This way adsorption flux can be written as it follows

$$J_{ADS} = K_{ADS}^G\left(\bar{q}_W^{G\to S} - \bar{q}_W\right) \tag{13}$$

Where K_{ADS}^G is the global transport coefficient in solid phase, obtained as the reciprocal of the sum of all the mass transport resistances

$$\frac{1}{K_{ADS}^G} = \left(\overbrace{\frac{1}{\left(\frac{\mathfrak{D}_W^G}{\delta^{ADS}}\right)}\frac{(\bar{q}_W^{G\to S} - \bar{q}_W^*)}{\left(C_W^{CG} - C_W^{CG,*}\right)}}^{gas} + \overbrace{\frac{1}{\frac{\rho_{ADS}}{PM_W}\left(\frac{\mathfrak{D}_W^G}{\delta^{ADS}}\frac{\varepsilon}{\tau}\right)}}^{solid}\right) \tag{14}$$

Again, the percentage of gas phase resistance to global (gas + solid) resistance for water adsorption is obtained as it follows:

$$R_{ADS}^G\% = 100\%\left(1 + \frac{C_W^{CG} - C_W^{CG,*}}{\frac{\rho_{ADS}}{PM_W}\frac{\varepsilon}{\tau}(\bar{q}_W^{G\to S} - \bar{q}_W^*)}\right)^{-1} \tag{15}$$

When $R_{ADS}^G\%$ is equal to zero the resistance to water adsorption is confined in the diffusional layer of the solid phase and no concentration gradient in the gas phase is obtained, whereas when $R_{ADS}^G\%$ is equal to 100% transport resistance is only on the gas side and a flat concentration profile results in the solid layer inside the adsorbing particle of silica gel.

2.4.3.3 Leakage from a single petri dish to the chamber of the desiccator unit

Assuming that water flow from the petri dishes to the chamber is due to diffusion and convection may be neglected, the leakage transport is modelled as a gaseous flux across the annular surface between the outer petri wall and the lid with the diffusion path δ^{LEAK} shown in Figure 2.4.2, and it can be expressed as

$$J_{LEAK} = \frac{\mathfrak{D}_W^G}{\delta^{LEAK}}\left(C_W^{PG} - C_W^{CG}\right) \tag{16}$$

In analogy with electric circuit analysis, $\frac{\mathfrak{D}_W^G}{\delta^{LEAK}}$ represents the conductance of leakage rate.

2.4.3.4 Cell osmosis

According to the two-parameter formalism typically adopted to describe cell osmosis, the water exchange rate between a cell and suspending solution is determined through Equation 17,

$$J_{OSM} = \frac{L_P RT}{\tilde{v}_W}\left(M_{TRE}^{L} - M_{TRE}^{CELL}\right) \tag{17}$$

where the driving force is given in terms solute osmolality in the intra- and extracellular compartments, i.e. M_{TRE}^{CELL} and M_{TRE}^{L} respectively. In particular, L_P represents water permeability to cell membrane and is characterized by an Arrhenius-like dependence on temperature as shown in Equation 18, while $\tilde{v}_W$ is the molecular volume of water.

$$L_P = L_P^0 \exp\left(-\frac{E_{a,P}}{RT}\right) \tag{18}$$

2.4.4 Crystal formation: Population Balance Equation (PBE)

In this work crystal formation in the liquid solution contained in any single petri dish is described on the basis of the Classical Nucleation Theory (CNT). In particular, since a perfectly mixed liquid phase is assumed according to the compartmental modelling approach adopted in this work, a Population Balance Equation (PBE) is used to describe the dynamics of formation from nucleation to growth of dihydrate trehalose crystals inside the liquid solution [17]. According to the PBE approach, a size distribution in the number population of dihydrate trehalose crystals is developed, from the smallest ones (i.e. nucleus) to the larger ones (i.e. grown crystals). Thus, $n_{TREh}^S(r,t)\,dr$ represents the number of dihydrate trehalose sugar crystals with a radius between r and $r + dr$ at time t, and the following PBE may be derived with the corresponding initial and boundary conditions:

$$\begin{aligned}
&\frac{\partial n_{TREh}^S(r,t)}{\partial t} + \frac{\partial}{\partial r}\left[G_{TREh}(r,t)\cdot n_{TREh}^S(r,t)\right] = B_0(r^C,t)\,\delta[r-r^C] \\
&n_{TREh}^S = 0, \qquad @\ t = 0, \qquad \forall r \in [0,+\infty), \qquad I.C. \\
&G_{TREh} n_{TREh}^S = 0, \qquad @\ r = 0, \qquad \forall t > 0, \qquad B.C. \\
&G_{TREh} n_{TREh}^S = 0, \qquad @\ r \to \infty, \qquad \forall t > 0, \qquad B.C.
\end{aligned} \tag{19}$$

where, $B_0(r^C, t)$ represents the nucleation rate and G_{TREh} the growth rate of the crystal radius r. In particular, the adopted initial condition corresponds to the initial absence of any dihydrate trehalose crystal in the liquid solution, while the meaning of the boundary conditions is that crystals with nonsensical sizes cannot grow. Moreover, r^C represents the size of the smallest crystal, i.e. the nucleus, and the term in the right side of Equation 19 contains the delta Dirac function $\delta[r - r^C]$ centered in r^C. This means that, nucleation rate $B_0(r^C, t)$ is accounted for in Equation 19 only at $r = r^C$, so that the positive term on the right side of the PBE is equal to zero at any other radius $r \neq r^C$.

2.4.4.1 Nucleation rate

The nucleation rate is obtained as the product of the specific nucleation rate $J_{TREh}(r^C, t)$ with the volume of liquid solution V^L.

$$B_0(r^C, t) = J_{TREh}(r^C, t)\, V^L \tag{20}$$

This way, a nucleation rate increasing with the liquid volume is obtained. According to CNT the specific nucleation rate is driven by diffusion as described by the following equation

$$J_{TREh}(r^C, t) = J^0_{TREh} \mathfrak{D}^L_{TRE}\, exp\left(-\frac{E^S_{a,TREh}}{k_B T}\right) \tag{21}$$

where activation energy $E^S_{a,TREh}$ depends on the dihydrate trehalose surface tension γ_{TREh} and the radius r^C of a thermodynamically stable embryo of a crystal as it follows

$$E^S_{a,TREh} = \frac{4}{3}\pi\gamma_{TREh}(r^C)^2 \tag{22}$$

r^C is related to trehalose super-saturation $\frac{x^L_{TRE}}{x^{solubility}_{TRE}}$ as expressed by the following equation

$$r^C = \frac{2\gamma_{TREh}\tilde{v}_{TREh}}{RT \ln\left(\frac{x^L_{TREh}}{x^{solubility}_{TREh}}\right)} \tag{23}$$

Since r^C may take only positive values, nucleation rate $B_0(r^C, t)$ is different from zero only when $x^L_{TRE} > x^{solubility}_{TRE}$, i.e. when $\omega^L_W < \omega^{solubility}_W$ in the phase diagram used in this work. This means that nucleation occurs only when the composition of the liquid phase overcomes the solubility curve shown in Figure 2.4.1.

It is worth noting that, $E^S_{a,TREh}$ appearing in Equation 22 increases with r^C, which in turn increases at low super-saturation (i.e. when $\frac{x^L_{TRE}}{x^{solubility}_{TRE}} \cong 1$). This means that, at low super-saturation levels a slow nucleation rate results. On the other hand, at large super-saturation levels $\mathfrak{D}^L_{TRE}$ appearing in Equation 21 decreases, since a critically high viscosity η^L is reached when the trehalose content in the parent liquid solution increases.

2.4.4.2 Crystal growth rate

The growth rate of a crystal is determined by means of the following equation

$$G_{TREh}(r,t) = \mathfrak{D}_{TRE}^{L}\frac{\Omega}{r} \tag{24}$$

where Ω represents the driving force evaluated as

$$\Omega = \frac{x_{TRE}^{L} - x_{TRE}^{solubility}}{x_{TRE}^{solidus} - x_{TRE}^{solubility}} \tag{25}$$

As a consequence, similarly to the nucleation rate a reduced crystal growth rate results at low super-saturation (when $x_{TRE}^{L} \cong x_{TRE}^{solubility}$) as well as when trehalose content increases and $\mathfrak{D}_{TRE}^{L}$ decreases. Moreover, crystal growth in Equation 24 is inversely proportional to crystal radius, which means that smaller crystals grow in size much faster than larger ones.

2.4.4.3 Numerical solution of (PBE): the method of moments

In this work the PBE is not directly solved to determine the time-varying size distribution of the crystal population $n_{TREh}^{S}(r,t)$. Only the moments of this size distribution are actually determined [18]. The moments of the distribution are defined as:

$$\mu_n(t) = \int_0^{+\infty} (r)^n \, n_{TREh}^{S}(r,t)\, dr = \langle (r)^n \rangle \tag{26}$$

In particular, by assuming that crystals have a spherical shape some of the first moments have a special meaning: for instance, the zero-th moment $\mu_0(t)$ represents the total number of crystals in the population, while $\mu_2(t)$ and $\mu_3(t)$ are proportional to the total surface and volume of precipitated crystals. Moreover, the ratio $\frac{\frac{4}{3}\pi\mu_3(t)}{4\pi\,\mu_2}$ represents an average radius of the crystal size distribution, the so-called Sauter-mean radius, which increases or decreases if crystal growth rate is larger or smaller than nucleation rate, correspondingly. The higher the number (n) of the moments accounted for, the more precise is the method of moments to adequately represent the underneath size distribution $n_{TREh}^{S}(r,t)$.

The temporal variation of the n-th moment is obtained through the analytical integration of Equation 19

$$\frac{d\mu_n}{dt} = n\langle (r)^{n-1} G_{TREh}(r,t) \rangle + (r^C)^n B_0(r^C,t) \tag{27}$$

which reduces to

$$\frac{d\mu_n}{dt} = n\mathfrak{D}_{TRE}^{L}\Omega\mu_{n-2} + (r^C)^n B_0(r^C,t) \tag{28}$$

once $G_{TREh}(r,t)$ is expressed by Equation 24.

In summary, the PBE is a partial differential-integral equation whose solution is transformed in the solution of the system of ordinary differential equations representing the temporal variation of the moment of the crystal size distribution. If one account for the first 4 moments, the following equations are obtained

$$\frac{d\mu_3}{dt} = 3\mathfrak{D}_{TRE}^{L}\Omega\mu_1 + (r^C)^3 B_0(r^C,t) \tag{29}$$

$$\frac{d\mu_2}{dt} = 2\mathfrak{D}_{TRE}^{L}\Omega\mu_0 + (r^C)^2 B_0(r^C,t) \tag{30}$$

$$\frac{d\mu_1}{dt} = \mathfrak{D}_{TRE}^{L}\Omega\mu_{-1} + r^{C}B_0(r^{C},t) \tag{31}$$

$$\frac{d\mu_0}{dt} = B_0(r^{C},t) \tag{32}$$

It is worth noting that, according to the method of the moments the rate of crystal formation $R_{CRYSTAL}$ appearing in Equations 2-3 is obtained as

$$R_{CRYSTAL} = \frac{1}{\tilde{v}_{TREh}}\frac{dV_{TRE}^{S}}{dt} = \frac{4\pi}{3\tilde{v}_{TREh}}\frac{d\mu_3}{dt} \tag{33}$$

2.4.4.4 Quadrature Method of Moments

Due to the adopted crystal growth rate inversely proportional to the crystal radius r (see Equation 24), the moment μ_{-1} appears in Equation 31 without an ordinary differential equation representing its temporal variation. In the corresponding scientific literature this well-known problem of the method of moments is referred to as the closure of the system of the ordinary differential equations 29-32. In this work, the problem of the mathematical closure is solved by means of the Quadrature Method of Moments (QMOM) [18], solved at a pre-set order $N_q = 2$ which corresponds to account for $2N_q$ moments (i.e. from μ_0 to μ_3). This method is based on the following quadrature approximation for the calculation of the moments

$$\mu_n(t) = \int_0^{+\infty} (r)^n n_{TREh}^{S}(r,t)dr \cong \sum_{i=1}^{N_q} w_i(t)\cdot\left(r_i(t)\right)^n \tag{34}$$

where the weights $w_i(t)$ and abscissass $r_i(t)$ are determined through the Product-Difference (PD) Algorithm. According to the PD algorithm, first the *P* matrix $[(2N_q+1)\ x\ (2N_q+1)]$ needs to be determined. With *j* and *k* representing the indexes of rows and columns in the *P* matrix, respectively, the elements of the first column are calculated as

$$P_{j,1} = \begin{cases} 1 & if\ j = k \\ 0 & if\ j \neq k \end{cases} \tag{35}$$

with $k = 1$ and $j \in (1, \dots, 2N_q + 1)$. Then, the elements of the second column are determined as

$$P_{j,2} = (-1)^{j-1}\mu_{j-1} \tag{36}$$

$$P_{2N_q+1,2} = 0 \tag{37}$$

with $k = 2$ and $j \in (1, \dots, 2N_q)$.

Finally, the elements of the all the other columns in the P matrix are calculated as

$$P_{j,k} \coloneqq \begin{cases} P_{1,k-1}P_{j+1,k-2} - P_{1,k-2}P_{j+1,k-1}, & j \in 1, \dots, 2N_q + 2 - k \\ 0, & j \in 2N_q + 3 - k, \dots, 2N_q + 1 \end{cases} \tag{38}$$

for $k \in (3, \dots, 2N_q + 1)$.

Once the P matrix is determined, the Coefficients of the continued fraction α_l are calculated: the first $\alpha_1 = 0$ while all the others are evaluated as

$$\alpha_l = \frac{P_{1,l+1}}{P_{1,l}P_{1,l-1}} \qquad l \in 2, \dots, 2N_q \tag{39}$$

Then the elements of a tridiagonal Jacobi matrix are determined according to

$$a_i = \alpha_{2i} + \alpha_{2i-1}, \qquad i \in 1, \dots, N_q \tag{40}$$

$$b_i = \sqrt{\alpha_{2i+1} \cdot \alpha_{2i}}, \qquad i \in 1, \dots, N_q - 1 \tag{41}$$

where a_i and b_i are the diagonal and the codiagonal elements of the Jacobi matrix, respectively. Once the tridiagonal matrix is determined, abscissas $r_i(t)$ and weights $w_i(t)$ in Equation 34 are calculated as the eigenvalues and eigenvectors of the Jacobi matrix, respectively. In particular, the weights are calculated as $w_i = \mu_0 v_{i,1}^2$, where $v_{i,1}$ is the first component of the i-th eigenvector $\boldsymbol{v_i}$. This way, the undefined moment μ_{-1} can be determined as

$$\mu_{-1}(t) = \sum_{i=1}^{N_q} w_i(t) \cdot \big(r_i(t)\big)^{-1} \tag{42}$$

and the problem of the closure is solved.

It is worth noting that, according to QMOM the goodness of approximation of the underneath crystal size distribution by the number of moments accounted for may be checked by comparing $\mu_3(t)$ calculated by Equation 29 with the following one

$$\mu_3(t) = \sum_{i=1}^{N_q} w_i(t) \cdot \big(r_i(t)\big)^{3} \tag{43}$$

2.4.5 Results and discussion

The numerical solution of the model equations is achieved by means of a homemade program written in FORTRAN language. In particular, the ordinary differential equations are integrated through the Livermore Solver for Ordinary Differential Equations (LSODE) [19], i.e. a marching procedure for initial value problems, while IMTQL2 (EISPACK) [20] is used to calculate the eigenvalues and eigenvectors in the QMOM to solve the PBE representing crystal formation.

In this work, the results of the model simulations corresponding to a seven days air-drying process of hMSCs suspended in a water + trehalose liquid solutions are analyzed and discussed by means of a parametric sensitivity analysis, given the absence of valuable data on the system investigated. In particular, first a base case is chosen and analyzed. Then the results obtained by systematically changing some key parameters related to system sizes, geometries and operating conditions are compared to the base case and discussed. In fact, the values adopted in the simulations for some model parameters (for instance the values assigned to the thickness of the diffusion layers in the gas and liquid phase δ^G e δ^L, or to J^0_{TREh} and γ_{TREh} used for the nucleation rate of the crystal size distribution) are characterized by a high level of uncertainty. However, we deliberately choose to analyze system behavior by varying some key variables like system sizes, geometries, and operating conditions, those who are chosen and set by the operator working on the desiccator unit.

2.4.5.1 Parametric sensitivity analysis: Base case

The parameter values of the proposed model used in the parametric sensitivity analysis for the base case are reported in Table 2.4.1 and 2.4.2.

Table 2.4.1: Constant model parameters for the parametric sensitivity analysis.

Parameter	***Value***	***Units***	***Reference***
$E_{a,P}$	51840	$[J/mol]$	[20]
J^0_{TREh}	$1.78 \cdot 10^{24}$	$[1/m^5]$	[17]
k_B	$1.3806488 \cdot 10^{-23}$	$[J/\ K]$	[22]
L^0_P	154.5	$[\mu m/Pa \cdot s\ ]$	[20]
$\mathcal{N}_A$	$6.022 \cdot 10^{23}$	$[\#/mol]$	[22]
PM_{TRE}	$3.42296 \cdot 10^{-1}$	$[kg/mol]$	[22]
PM_w	$1.80153 \cdot 10^{-2}$	$[kg/mol]$	[22]
R	8.314472	$[J/mol\ K]$	[22]
$V^{ISO,CELL}$	$1.8 \cdot 10^{-15}$	$[m^3]$	[20]
γ_{TREh}	$1.043 \cdot 10^{-3}$	$[J/m^2]$	[17]
δ^G	$1.022874 \cdot 10^{-3}$	$[m]$	This work
δ^L	$1 \cdot 10^{-9}$	$[m]$	This work
ν_B	0.2	$[-]$	[20]
$\tilde{v}_{TRE}$	$2.11 \cdot 10^{-4}$	$[m^3/mol]$	[23]
$\tilde{v}_{TREh}$	$2.470306 \cdot 10^{-4}$	$[m^3/mol]$	This work
$\tilde{v}_W$	$1.80153 \cdot 10^{-5}$	$[m^3/mol]$	[22]

In particular, J^0_{TREh} and γ_{TREh} are taken from literature and are actually related to water and crystal ice formation. δ^G and δ^L are estimated from literature sources where the system investigated does not refer specifically to the one addressed in this work.

Other parameters such as system sizes and geometries are evaluated on the basis of the real desiccator unit used by the Japanese partner of the Drynet project, shown in Figure 2.4.2. On the other hand, the osmotic parameters such as the isotonic cell volume $V^{ISO,CELL}$, its inactive fraction ν_B, and the water permeability through cell membrane with its Arrhenius-like dependence on temperature $L_P(T)$ are specifically those of hMSCs from UCB.

The simulation results of the base case at varying times of the air-drying process are shown in the phase diagram reported in Figure 2.4.4: the red points represent the liquid phase composition during the process.

The initial water mass fraction is equal to 0.83 which is typically assumed to be sufficient for the stabilization of the cells in the long-term preservation via desiccation [14].

Table 2.4.2: System sizes, geometries, and operating conditions for the base case of the parametric sensitivity analysis.

Parameter	***Value***	***Units***	***Reference***
C^{CELL}	10^{14}	$[\#/m^3]$	[15]
M^0_{TRE}	600	$[mol/m^3]$	[15]
N^P	20	$[\#]$	[15]
P_{TOT}	101325	$[Pa]$	[15]
$\bar{q}^0_w$	0	$[kg_w/kg_{ADS}\,]$	[15]
r^{ADS}	$2 \cdot 10^{-3}$	$[m]$	This work
RH^0	0.5	$[-]$	[15]
S^{LEAK}	$9.83723 \cdot 10^{-5}$	$[m^2]$	This work
S^L	$6.3617 \cdot 10^{-5}$	$[m^2]$	This work
T	298.15	$[K]$	[15]
$V^{0,SAMPLE}$	$4 \cdot 10^{-8}$	$[m^3]$	[15]
V^C	$1.5625 \cdot 10^{-2}$	$[m^3]$	This work
V^P	$9.62 \cdot 10^{-6}$	$[m^3]$	This work
W^{ADS}	1	$[kg_{ADS}]$	This work
δ^{LEAK}	$5.27 \cdot 10^{-3}$	$[m]$	This work
ε	0.4	$[-]$	This work
ρ^{ADS}	700	$[kg/m^3]$	This work

It is apparent that, in the base case a relatively rapid evaporation is obtained, and liquid composition quickly approaches the glass transition curve despite of entering the biphasic zone (SOL+LIQ). In particular, Figure 2.4.5 shows the corresponding temporal profile of water content in the extracellular liquid phase: due to evaporation, the number of water moles decreases in time, initially quickly up to about 1.2 hours, then much more slowly.

This profile is actually the result between the rates of evaporation and cell osmosis, with the first one acting as a sink and the second one as a source for the water content in the extracellular liquid phase, according to Equation 2.

After about 1.2 hours from the start of the process, the slope changes abruptly and the decrease of water content continuous only at very slow rate until the percentage of the residual water content in the sample eventually reaches a value equal to 1.4% with respect to the initial one. Basically, in the first two hours 98 % of the initial water in the phase is removed, while it takes up to 7 days to remove another 1 % of water.

To explain the cause of this abrupt change in the rate of dehydration of the sample, the corresponding temporal profiles of the water percentage mass fraction and diffusivity in the liquid phase are reported in Figure 2.4.6.

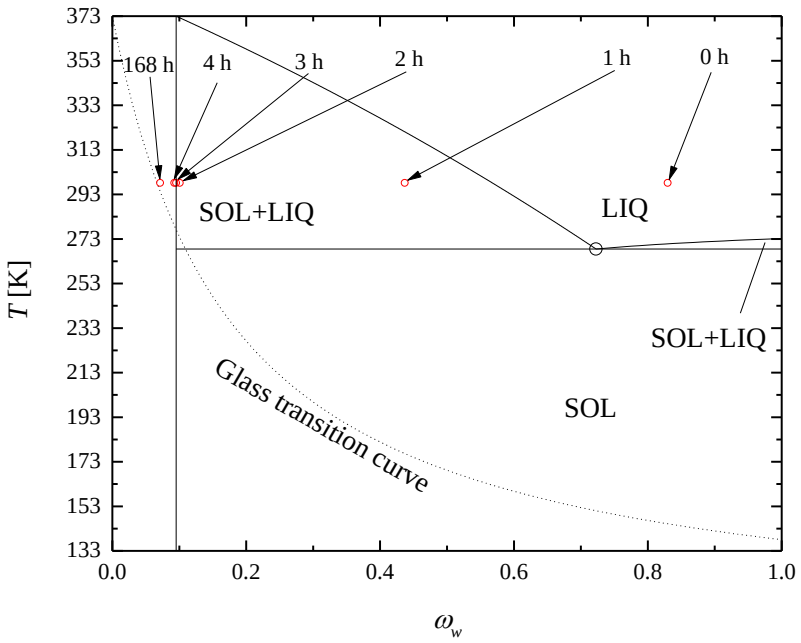

Figure 2.4.4: Temperature - composition phase diagram of the binary solution water + trehalose: change in liquid phase composition during the air-drying process (Base case)

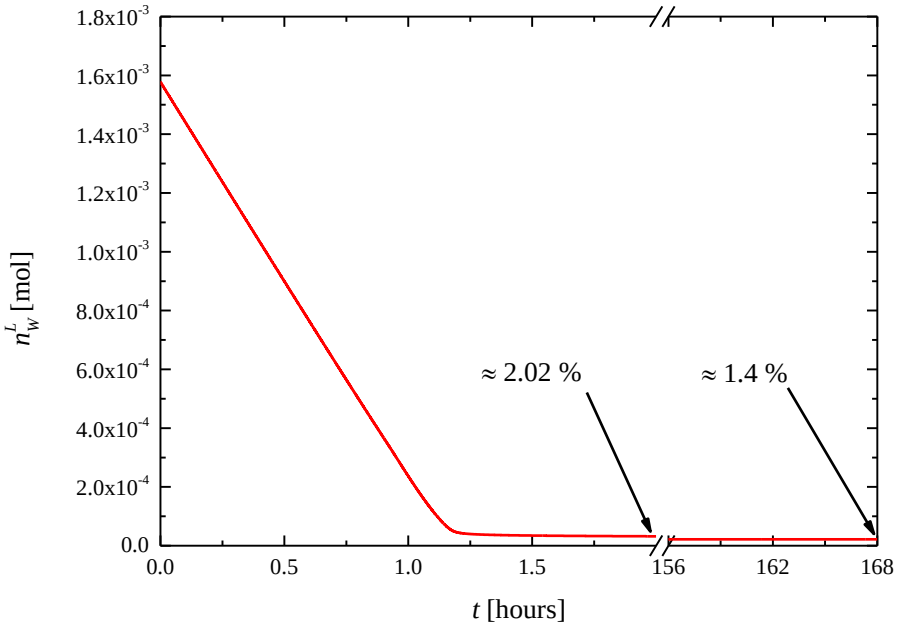

Figure 2.4.5: Temporal profile of water moles in the extracellular liquid phase. Residual water indicated as percentage of the initial content. (Base case).

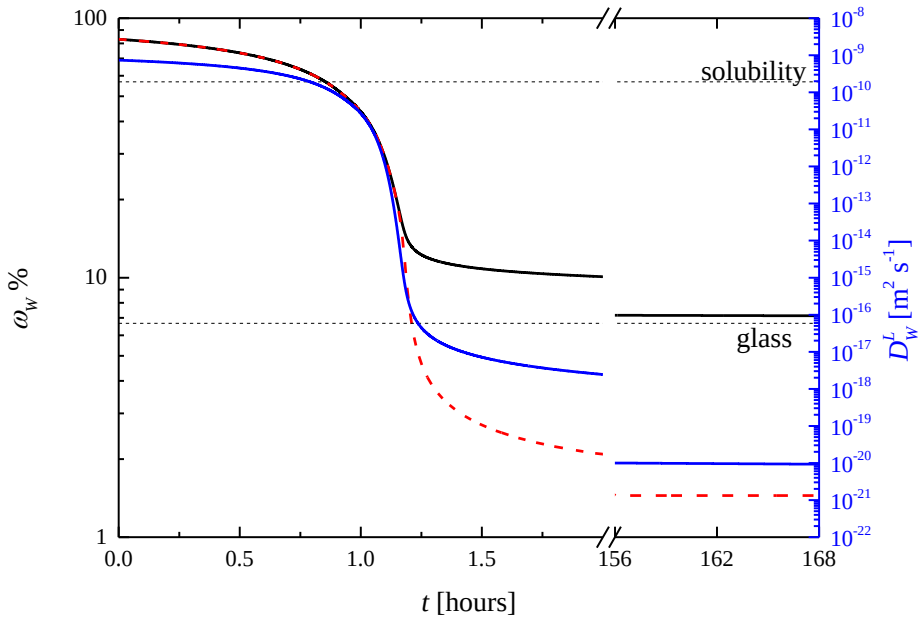

Figure 2.4.6: Temporal profiles of the water percentage mass fraction ω_W^L ——— and diffusivity $\mathfrak{D}_w^L$ ——— in the extracellular liquid phase. The profile of the water percentage mass fraction at the liquid interface (equilibrium) $\omega_W^{L,*}$ - - - - is shown as well. (Base case).

Here, the water percentage mass fraction at the evaporating interface (i.e. equilibrium) between gas and liquid phase as well as the solubility limit for crystal formation, and the composition at glass transition are also reported for the sake of comparison.

Due to an evaporation initially faster than the other phenomena, in less than 1 hour the decreasing mass fraction of water reaches the solubility curve, which means that crystal formation may now take place (cf. Figure 2.4.4). Water diffusivity in the liquid phase decreases as well. Initially, when water fraction is still relatively large, a negligible difference between the compositions in the bulk of the liquid phase and at the interface with the gas is obtained, meaning that water diffusion in the liquid phase is not limiting evaporation. Then, after about 1.2 hours when the system has already entered the biphasic (S+L) zone, the difference between these two compositions in the diffusion layer of the liquid phase increases considerably, while water diffusivity drops to very low values. This means that from now on evaporation rate is limited by water diffusion in the liquid phase. Later, water mass fraction keeps on decreasing in time, but at a slower rate until approaching glass transition. Even though a large super-saturation is established, crystal formation does not occur. This means that crystal formation is favored by thermodynamics but is heavily hindered by kinetics.

In Figure 2.4.7, the temporal profile of the percentage resistance to evaporation rate due to the gas phase is plotted along with the evaporation flux.

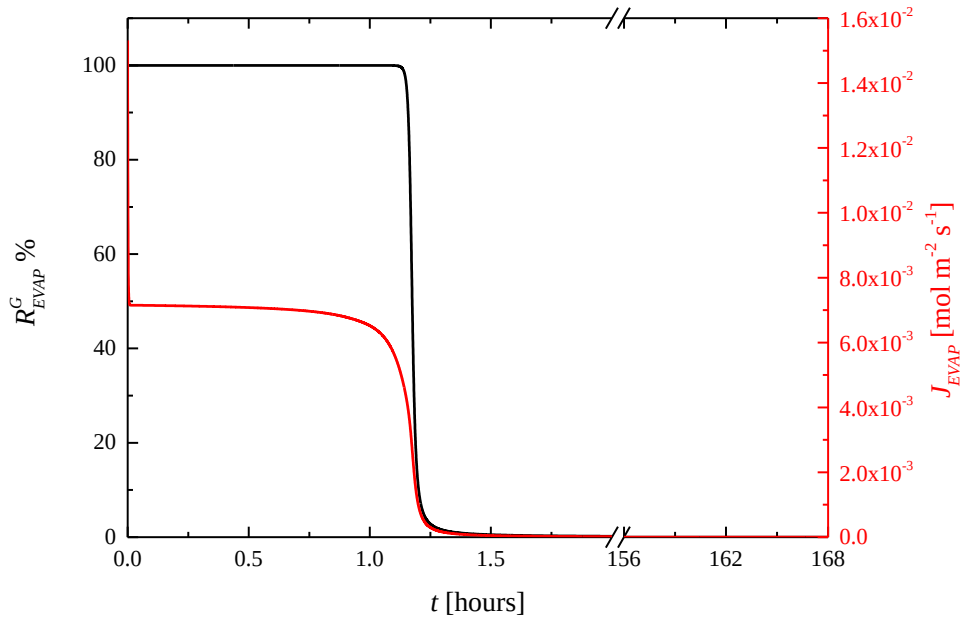

Figure 2.4.7: Temporal profiles of the percentage resistance to evaporation rate due to the gas phase and evaporation flux. (Base case).

It is apparent, that according to the two-film theory at about 1.2 hours the step limiting to evaporation rate abruptly changes from water diffusion across the gas layer to water diffusion across the liquid layer. Besides, after an initial instantaneous decrease related to the formation of a gradient composition in the gas phase, the evaporation flux decreases rapidly towards very low values, when water diffusion in the liquid layer becomes the controlling phenomenon. However, even if the composition in the bulk of the liquid phase approaches the glass transition at the end of the process as shown in Figures 2.4.4 and 2.4.6, a very slow evaporation begins after 1.2 hours: thus water removal from the liquid sample proceeds very slowly and a very long air-drying process results.

The temporal profiles of intra- and extracellular osmolalities of trehalose along with the percentage of intracellular water volume (i.e. cell humidity content) are shown in Figure 2.4.8 to analyze the osmotic response of the cells.

It is apparent that cell osmosis is a relatively fast phenomenon since intra- and extracellular compositions (i.e. the driving force for osmosis in Equation 17) show a negligible difference: both decrease in time since cell shrink in response to the increasing concentration of trehalose in the suspending liquid phase due to water evaporation. A humidity content of 1.6 % inside the cells is eventually reached. This value is slightly larger (i.e. 0.2 %) than the one reached in the suspending liquid phase (cf. Figure 2.4.5). This small difference on humidity content between intra- and extracellular compartments is due to the limited formation of dihydrate trehalose crystals in the extracellular liquid phase that consumes a small quantity of water according to the stoichiometry shown in Equation 1.

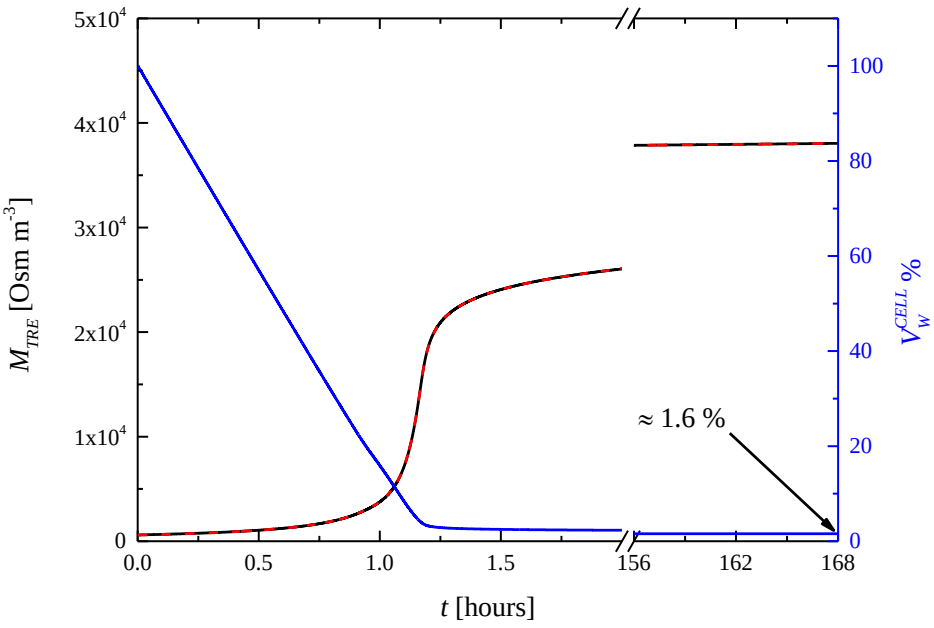

Figure 2.4.8: Temporal profiles of trehalose osmolalities in the intracellular M_{TRE}^{L} ——— and extracellular M_{TRE}^{CELL} – – – liquid phases, and percentage of intracellular water volume $V_W^{CELL}\%$ ———. (Base case).

This is confirmed by the temporal profile of the trehalose contained in the extracellular liquid phase shown in Figure 2.4.9 as the percentage of the initial content: only a 12.2% decrease is eventually obtained, besides within the first 1.2 hours of air-drying process time, i.e. when the system just entered the biphasic (S+L) zone in the phase diagram (cf. Figure 2.4.1) and the driving force of crystal formation is relatively small in comparison to the final one.

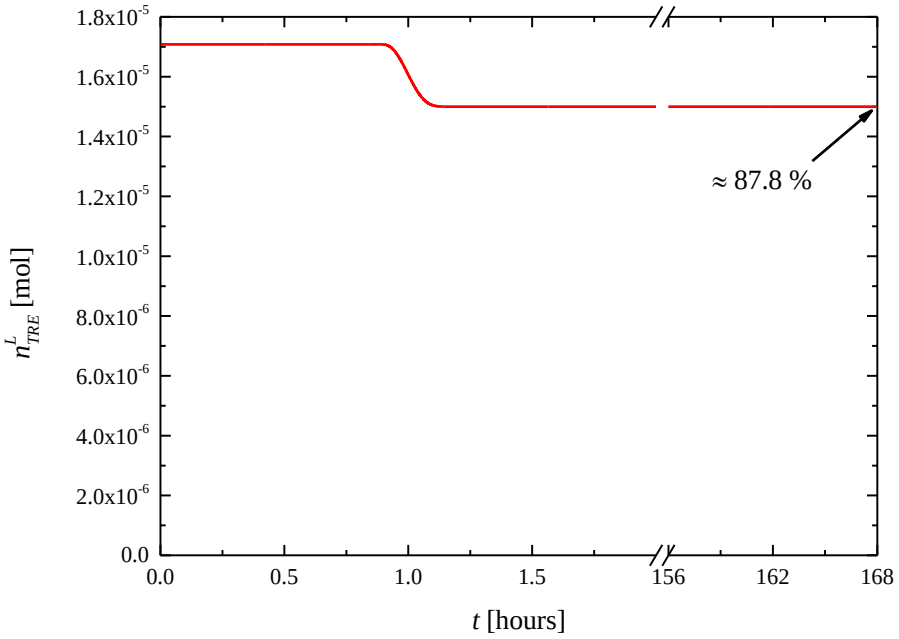

Figure 2.4.9: Temporal profile of the percentage trehalose content dissolved in the extracellular liquid phase. (Base case).

The temporal profile of the Sauter-mean radius of the evolving dihydrate trehalose crystal size distribution is shown in Figure 2.4.10: after 0.857 hours from the beginning of the process (more precisely, 25 s after the system enters the biphasic (S+L) zone in the phase diagram reported in Figure 2.4.4), the first crystal nuclei are formed and start to grow. Shortly after, the mean radius decreases rapidly to a lower value, indicating that new nuclei are formed at a rate faster than the growth rate of older crystals previously born. This means that the final crystal size distribution in the liquid extracellular phase is mainly constituted of many tiny crystals instead of few larger ones, which may play a relevant role on determining the final cell viability of the air-drying process.

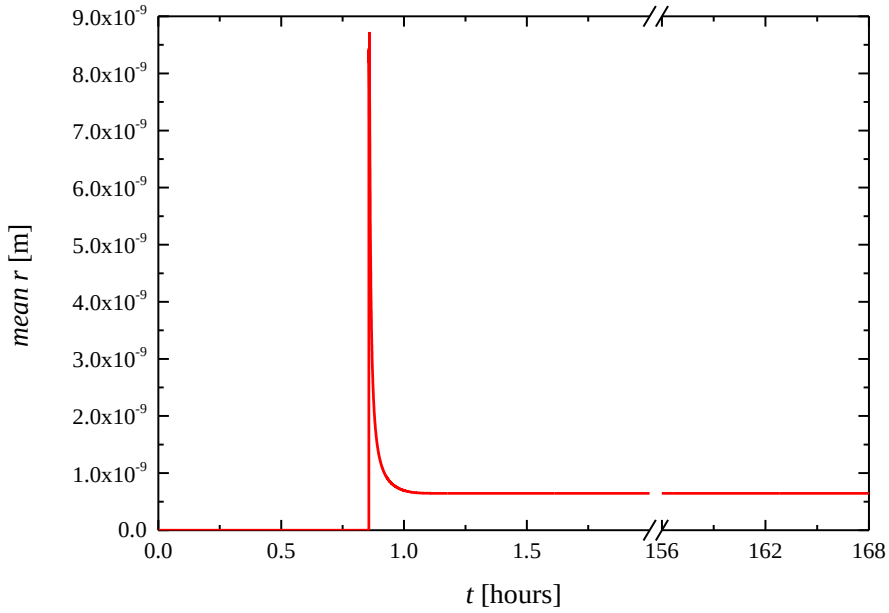

Figure 2.4.10: Temporal profile of the Sauter-mean radius of the trehalose dihydrate crystal size distribution. (Base case).

Turning our attention to the other possible resistances to water removal rate from the liquid sample to silica gel in the desiccator unit, the temporal profiles of the relative humidity in the gas phase inside any petri dish and in the chamber of the desiccator unit (i.e. $RH = \frac{C_W^{PG} \text{ or } C_W^{CG}}{P_{SW}(T)/RT}$) are shown in Figure 2.4.11 along with the leakage flux between the two compartments across the free space left by the unsealed lid.

An abrupt initial increase from the starting value of 50 % is obtained for the RH inside the petri dishes due to the initial evaporation from the liquid sample. Then a stationary value up to 1.2 hours is attained before a rapid decrease towards the RH in the chamber. This latter one is shown to increase slowly, since water vapor in the chamber is effectively adsorbed by the silica gel. Thus, it is not surprising that leakage flux basically follows the profile of RH inside the petri dishes (i.e. its driving force, according to Equation 16). Besides, the leakage flux maintains a positive value during the entire process, which means that the flow of water vapor through the unsealed lid is always going from the petri dishes to the chamber and never changes its direction, thanks to the adsorbing capacity of the silica gel.

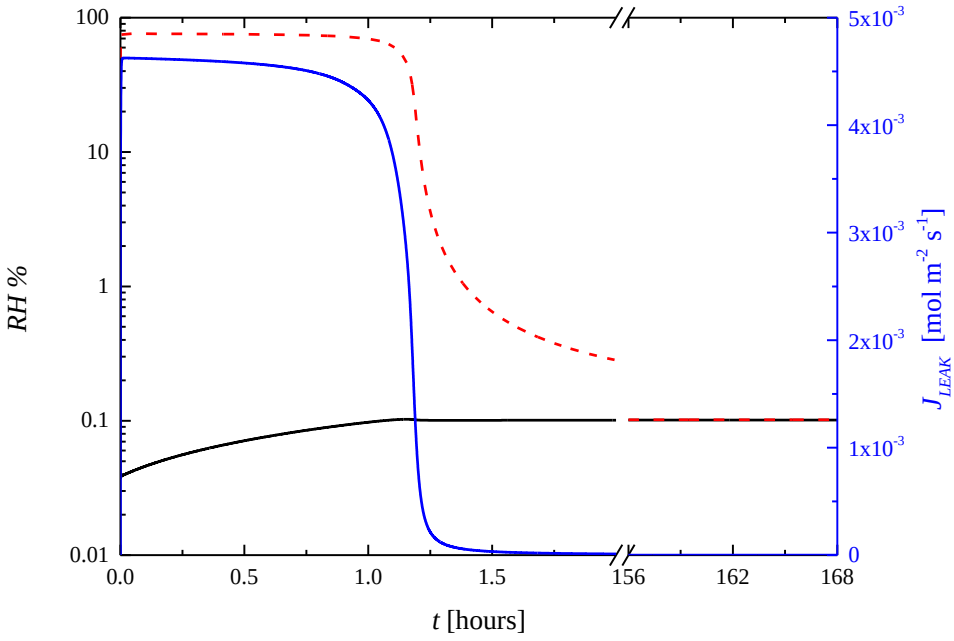

Figure 2.4.11: Temporal profiles of the relative humidity RH% in the gas phase of the petri dishes – – – and in the chamber of the desiccator unit ——, and the leakage flux from the unsealed petri dishes J_{LEAK} ——. (Base case).

It is worth noting that, this behavior basically depends on the used quantity of silica gel (i.e. 1 kg in this simulation) and a different result would be obtained if a lower amount of adsorbent beads was placed inside the desiccator unit. Moreover, the difference between the RH in the gas phase inside any petri dish and in the chamber of the desiccator unit shown in Figure 2.4.11 is maintained for a long time. This means that leakage is a controlling phenomenon in the sequence of steps for water removal from the liquid sample to the silica gel. Finally, the temporal profile of the adsorbed water in the silica gel along with the final adsorbed percentage with respect to the maximum absorbable (i.e. 17.8563 mol) are shown in Figure 2.4.12. As can be seen in Figure 2.4.12, the driving force of adsorption is negligible (i.e. the difference between n_W^{ADS} and $n_W^{ADS,*}$ is equal to zero throughout the entire process), thus adsorption in silica gel never represents a limiting phenomenon for water removal from the samples. Again, after 1.2 hours adsorption rate decreases to a much lower value, but continues throughout the entire drying process. Besides, according to the two-film theory the resistance to water flow due to adsorption in the silica gel is always confined in the gas side as shown in Figure 2.4.13.

In summary, according to the model simulations of the base case, during the air-drying process of hMSCs, regardless of the resistance to water removal by the lead of the unsealed petri dish, evaporation rate is still relatively fast in comparison with crystal formation. As a consequence, glass formation is eventually reached in the residual liquid sample along with an extended dehydration of the suspended cells assuring a long-term lyo-protection. However, after an initial rapid change, system variation becomes very slow and a very long air-drying process results. This is due to the decrease towards critical values of water diffusivity in the liquid phase, as water evaporates and trehalose concentration increases. When this happens the whole process slows down, with an evaporative resistance to water flow inside the petri dish moving from the gas to the liquid side,

which represents the rate limiting step in the sequence osmosis, evaporation, leakage, and adsorption followed to dehydrate the cells.

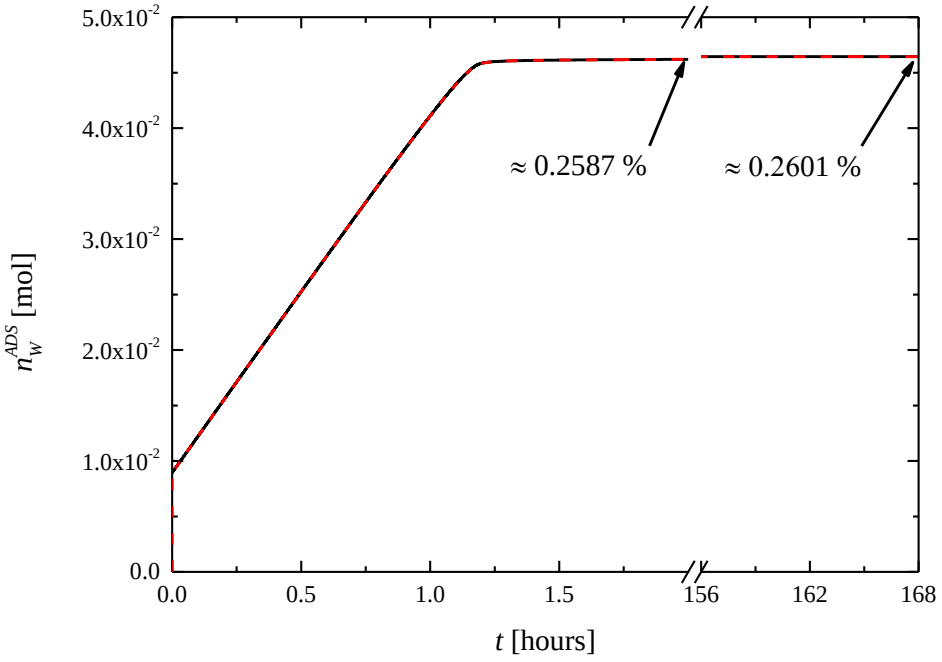

Figure 2.4.12: Temporal profile of water moles adsorbed in silica gel n_W^{ADS} – – –, and final adsorbed percentage. $n_W^{ADS,*}$ ——— at the solid interface (equilibrium) is shown as well. (Base case).

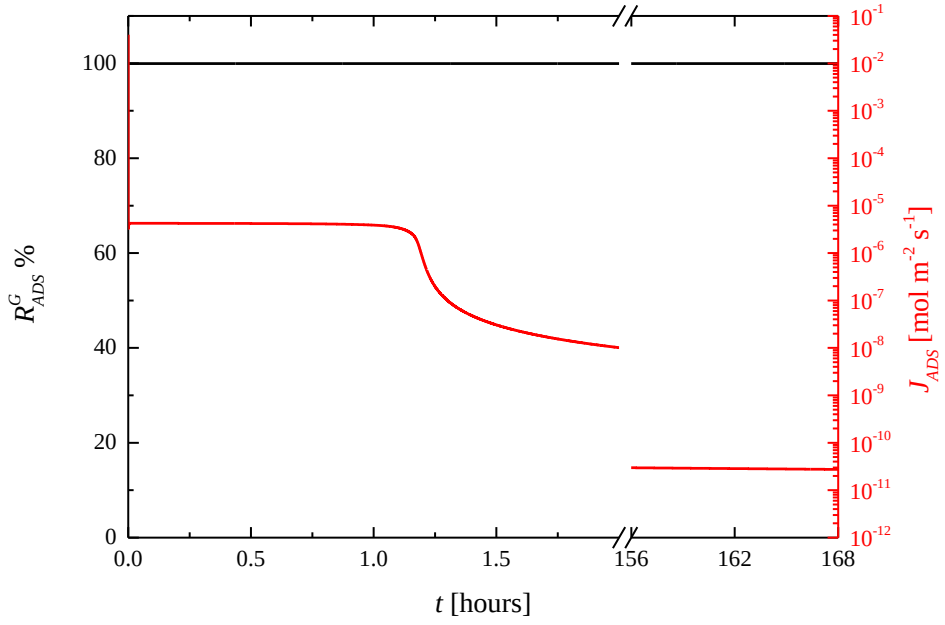

Figure 2.4.13: Temporal profiles of the percentage resistance to adsorption rate due to the gas phase and adsorption flux. (Base case).

2.4.5.2 Parametric sensitivity analysis: glass formation

In this section, the results of a series of model simulations where glass instead of crystal formation is favored are shown and discussed. The different model simulations are obtained through a *one factor at time* analysis of parametric sensitivity, i.e. by varying individually relevant system sizes, geometries and operating conditions. For the sake of brevity, only the figures showing the simulation results necessary to highlight the differences of system behavior with respect to the base case are reported.

2.4.5.2.1 Case 1. Increasing the evaporative surface area

In this case, the gas-liquid interface area where evaporation takes place inside any single petri dish is increased with respect to the base case by keeping constant the initial volume of the liquid sample. This corresponds to the choice made by the operator during the experimental run in the desiccator unit to use a slimmer silicone insulator placed at the bottom surface of the petri dish where the liquid sample is actually contained (see Figure 2.4.2). In particular, the liquid sample now considered is a cylinder 10 times shorter with a 10 times larger surface (i.e. $S^L = 6.3617 \cdot 10^{-4}\ m^2$) than the one used for the base case.

The corresponding system behavior followed in the phase diagram is shown in Figure 2.4.14. The comparison with the analogous Figure 2.4.4 of the base case, shows that the air-drying process is more rapid in this case, with the composition of the liquid phase approaching the glass transition in about 1 hour instead of 2. This is expected since a larger surface area for evaporation corresponds to an increased evaporation rate ($S^L J_{EVAP}$) as stated in Equations 2 and 4.

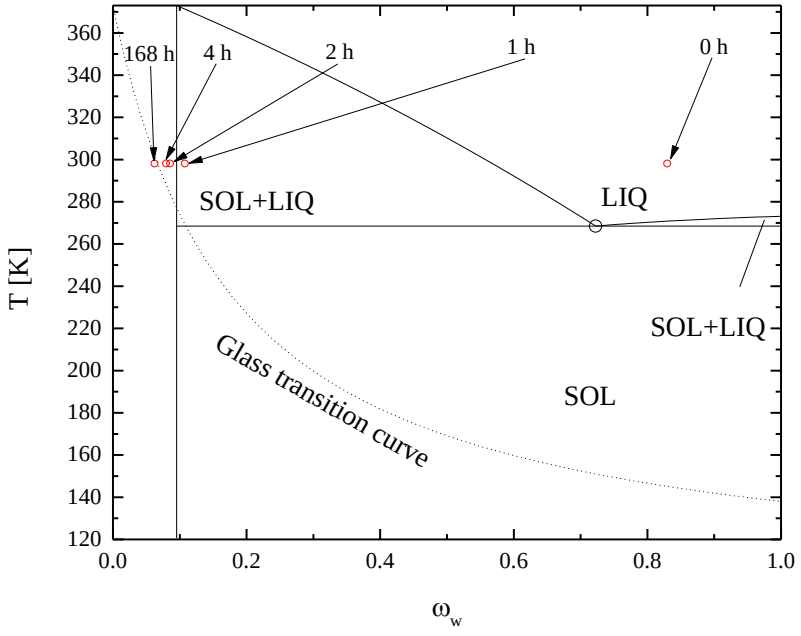

Figure 2.4.14: Temperature - composition phase diagram of the binary solution water + trehalose: change in liquid phase composition during the air-drying process (Case 1, increasing the evaporation surface area)

However, once a low water content inside the liquid sample is reached the process again slows down considerably, thus showing a behavior similar to the base case. This means that the variation of water diffusivity in the liquid sample still plays a relevant role, and water evaporation still represents the rate limiting step in the sequence osmosis, evaporation, leakage, and adsorption followed to dehydrate the cells. The humidity content in the liquid sample and inside the cells eventually reached at the end of the process are equal to 1.26% and 1.36%, respectively, i.e. lower than those obtained in the base case (1.4% and 1.6%, respectively) due to a faster evaporation. Besides, the difference in humidity content between the liquid phase and inside the cells is decreased in comparison with the base case, which means that less crystals are now formed. In fact, only 7.3% of the trehalose initially present in the liquid sample is precipitated in comparison with the 12.2% formed in the base case: crystal formation is hindered in comparison with the base case, due to a more rapid increase of the viscosity in the liquid sample caused by the enhanced evaporation rate. In this case nucleation rate is so fast in comparison with crystal growth that a population of even smaller crystals is eventually formed. Moreover, as a consequence of a faster evaporation, an increased amount of water is finally adsorbed in the silica gel after 7 days.

2.4.5.2.2 Case 2. Increasing the cross-sectional area surface for the leakage from the Petri dish

In this case, the cross-sectional area for the leakage flux S^{LEAK} of water vapour from any petri dish to the chamber of the desiccator unit through the unsealed lid is increased. This corresponds to the choice made by the operator during the experimental run in the desiccator unit to cover any single petri dish with a larger slid (see Figure 2.4.2). In particular, the annular area now considered is 10 times larger (i.e. $S^{LEAK} = 9.83723 \cdot 10^{-4}\ m^2$) than the one used for the base case. According to Equations 4-5 this corresponds to increase the leakage flow rate ($S^{LEAK} J_{LEAK}$). Of course, the same result would be obtained by decreasing δ^{LEAK}, i.e. by increasing the conductance of the leakage flux defined in Equation 16. The corresponding system behavior followed in the phase diagram is shown in Figure 2.4.15.

A very similar behavior to the previous case is obtained: a more rapid air-drying process with respect to the base case is simulated, with the composition of the liquid phase quickly reaching the glass transition. This is expected, since in the base case leakage was found to be limiting for water removal from the liquid sample. Therefore, when increasing leakage flow a faster evaporation results. Of course, the same result would be obtained by reducing the diffusion path in the leakage flux δ^{LEAK} which corresponds to the choice made by the operator during the experimental run in the desiccator unit to use a shorter lid (see Figure 2.4.2).

On the other hand, after an initial rapid change, once again system response slows down considerably, due to the water diffusivity in the residual liquid phase reduced to critical levels as trehalose concentration increases. However, the humidity content in the liquid sample and inside the cells eventually reached at the end of the process are now equal to 1.57% and 1.6%, respectively, i.e. larger than those obtained in the previous case as well as in the base case. This means that a lower dehydration of cells is now reached, which may be dangerous for the long-term preservation.

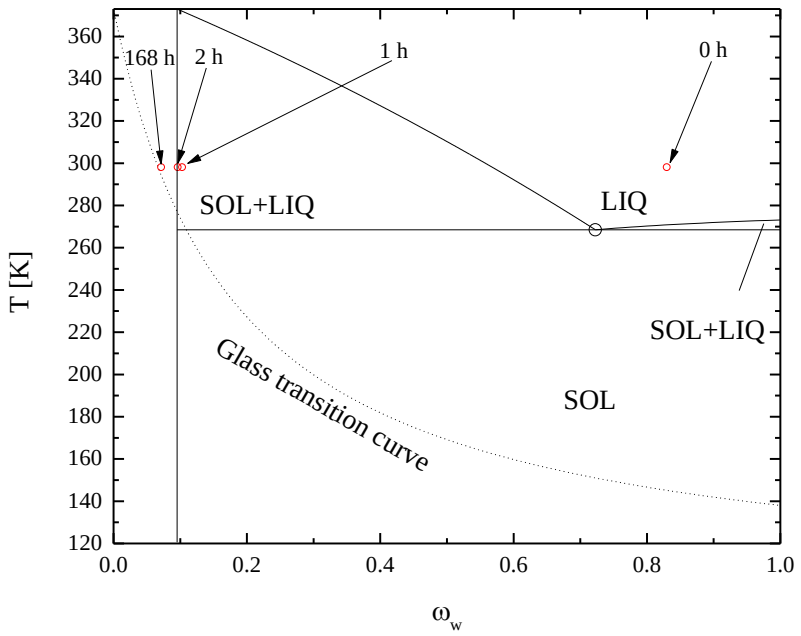

Figure 2.4.15: Temperature - composition phase diagram of the binary solution water + trehalose: change in liquid phase composition during the air-drying process (Case 2, increasing the leakage surface area).

This result explains why evaporation rate needs to be limited by covering the petri dishes: as pointed out by [14] an extremely quick evaporation may lead to the formation of a thin glassy skin over the liquid sample, a crust that basically stops evaporation and prevents the complete dehydration of the cells, which is a necessary condition for long-term preservation.

2.4.5.2.3 Case 3. Reducing the sample height (volume)

If sample height is reduced 10 times with respect to the base case, a smaller liquid volume results (i.e. $V^{SAMPLE} = 4 \cdot 10^{-9}\ m^3$). It is worth noting that this means that a lower amount of water is actually present initially in the liquid sample to be transferred to silica gel, and less trehalose is potentially available for crystal formation. As such, the system moves more quickly towards glass formation than in the base case, as shown in Figure 2.4.16.

The humidity content the liquid sample and inside the cells eventually reached at the end of the process are both equal to 1.36%, i.e. lower than those obtained in the base case, with a very limited crystal formation since only 0.11% of the trehalose now precipitates.

Since the initial volume of the liquid sample is 10% of that used in the base case, a 90% reduction of adsorbed water in the silica gel is expected with respect to the base case at the end of the process. However, this is not the case since the amount of water eventually adsorbed turns out to be only 70 % less than that obtained in the base case. The explanation of this unexpected result is that, when such a small liquid sample volume is considered, the amount of water vapor initially present in the gas phase of the chamber of the desiccator unit

is not negligible and a relevant fraction of adsorbed water onto silica gel come from the vapor initially contained in the chamber instead of from the sample.

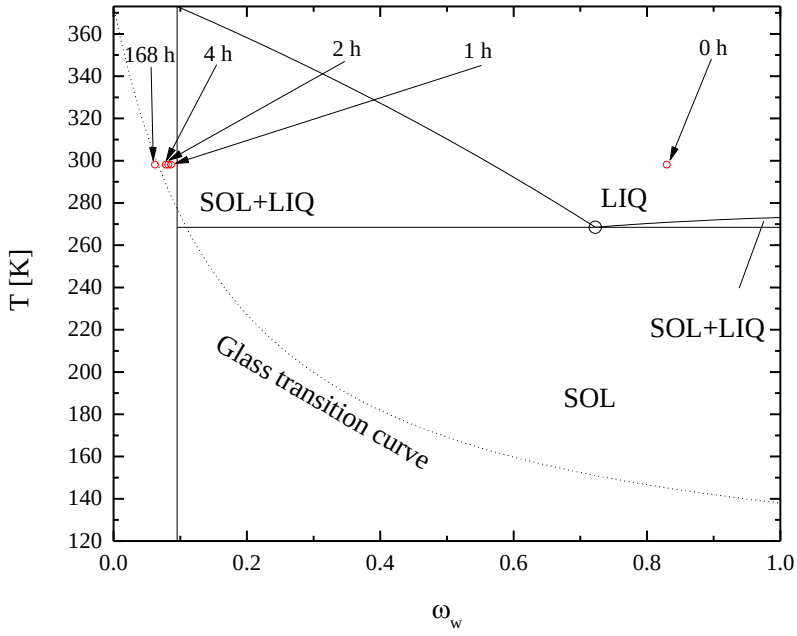

Figure 2.4.16: Temperature - composition phase diagram of the binary solution water + trehalose: change in liquid phase composition during the air- drying process (Case 3, decreasing the sample height (volume))

2.4.5.2.4 Case 4. Reducing the trehalose osmolality

When the initial trehalose osmolality is reduced 10 times in comparison with base case (i.e. $M^0_{TRE} = 150\ Osm/m^3$), a larger amount of water is present inside the liquid sample with respect to the base case. For this reason, in the phase diagram shown in Figure 2.4.17 the decrease due to evaporation of the water mass fraction in the liquid phase starts from a point positioned more to the right with respect to the cases analyzed so far. Despite this, after two hours from the beginning of the air-drying process the water mass fraction is reduced more than in the base case (cf. Figure 2.4.4), indicating that a faster evaporation is actually taking place at least initially. In fact, from the initial slope of the curve shown in Figure 2.4.18 a flow rate equal to 1.6 mol/h for the water leaving the liquid sample is calculated in comparison with the 1.32 mol/h of the base case determined from Figure 2.4.2, i.e. almost 6% faster. Once again, the relevant role played by water diffusivity in the liquid phase and its non-linear dependence on composition is highlighted. Of course, at the fastest water evaporation corresponds the lowest crystal formation among the different cases analyzed so far: only 0.82% of trehalose precipitates. In this case the final humidity content reached in the liquid phase and inside the cells are both equal to 0.36%, i.e. the smallest ones. Actually, the extension of cell shrinkage in comparison with the other cases is due to the larger water volume initially contained inside the cells: if the same final composition (i.e. glass transition) is reached, more water has to exit the cells for osmotic equilibration with the liquid sample, and an extended cell dehydration is eventually reached.

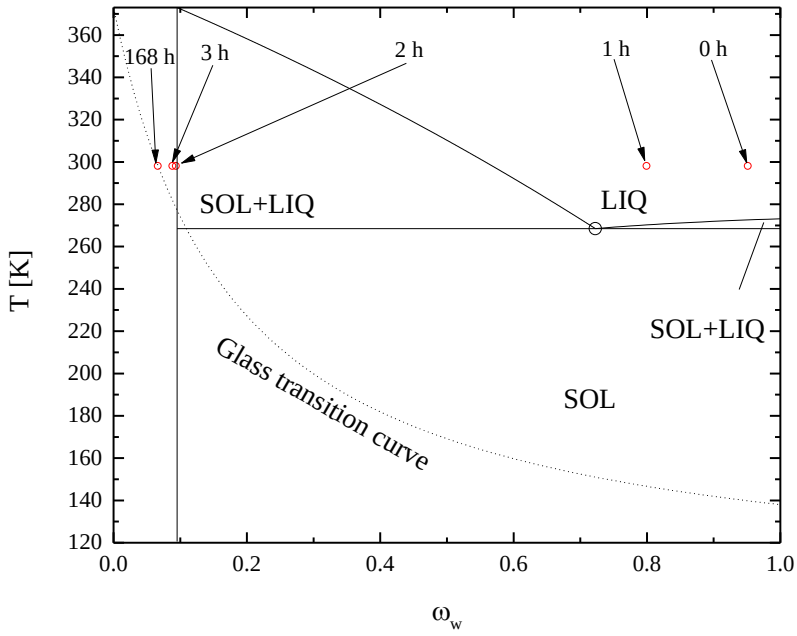

Figure 2.4.17: Temperature - composition phase diagram of the binary solution water + trehalose: change in liquid phase composition during the air-drying process (Case 4, decreasing trehalose osmolality)

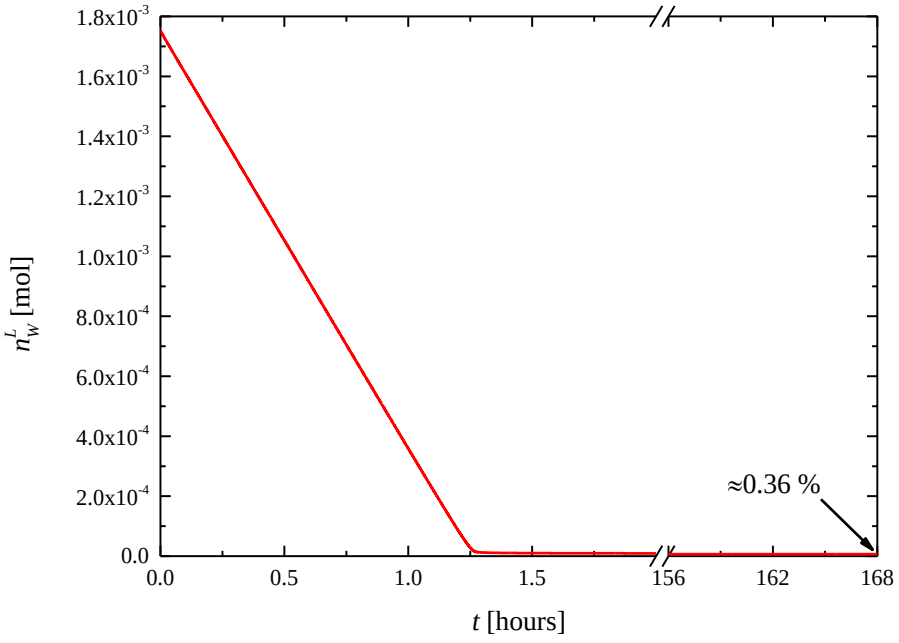

Figure 2.4.18: Temporal profile of water moles in the extracellular liquid phase. Residual water indicated as percentage of the initial content. (Case 4, reducing the trehalose osmolality)

In summary, a 10 times increase of the surface area of the sample with respect to the base case enhances even more evaporation rate in comparison with crystal formation during the air-drying process of hMSCs; after an initial rapid variation, the residual liquid solution is slowly transformed into sugar glass, with an extended dehydration of the suspended cells. The same effect is obtained with a 10 times decrease with respect to the base case of the resistance to water diffusion through the lid of the unsealed petri dishes, or by using a 10 times smaller sample volume, or starting with a trehalose osmolality 4 times lower. In the water flow from the sample to the silica gel a non-negligible resistance is always represented by the leakage flux due to the lid covering the unsealed petri dishes, while cell osmosis and adsorption are relatively fast and do not represent a limiting step.

2.4.5.3 Parametric sensitivity analysis: crystal formation

In this section, the results of a series of model simulations where crystal instead of glass formation is favored and eventually reached are shown and discussed, in comparison with the cases discussed so far.

2.4.5.3.1 Case 5. Reducing the evaporative surface area

In this case, the gas-liquid interface area where evaporation takes place inside any single petri dish is reduced by keeping constant the initial volume of the liquid sample. In particular, the liquid sample now considered is a cylinder 10 times taller with a 10 times smaller surface (i.e. $S^L = 6.3617 \cdot 10^{-6}\ m^2$) than the one used for the base case: from this point of view, this case is just the opposite of the case 1 previously discussed. The corresponding system behavior followed in the phase diagram is shown in Figure 2.4.19.

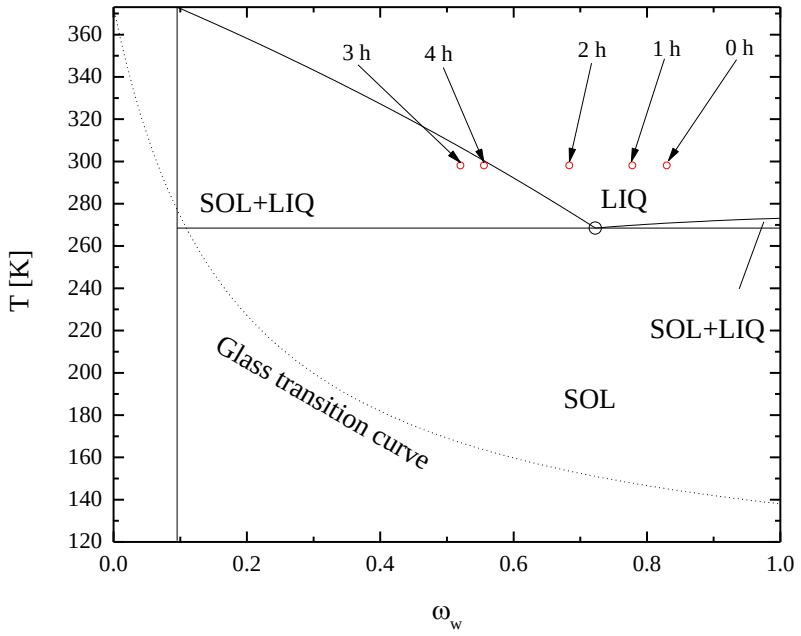

Figure 2.4.19: Temperature - composition phase diagram of the binary solution water + trehalose: change in the composition during the air-drying process (Case 5, reducing the evaporative surface area of the sample).

It is worth noting that, in this case the simulation results of the model are reported only up to 5 hours since a stationary behavior is reached by the system, when the liquid sample is completely consumed.

It is apparent that now system behavior is completely changed: due to a reduced evaporative surface area, evaporation rate ($S^L J_{EVAP}$ in Equations 2 and 4) decreases so much that crystals instead of glass are formed inside the sample. In particular, once the liquid phase enters the biphasic zone (S+L), crystal formation is fast enough to bring back the composition of the residual liquid solution towards the solubility curve as clearly shown in Figure 2.4.19.

Moreover, a complete water removal from the liquid sample is reached in only 3.5 hours as shown in Figure 2.4.20: thus, unexpectedly when evaporation rate is slowed down a much faster air-drying process results.

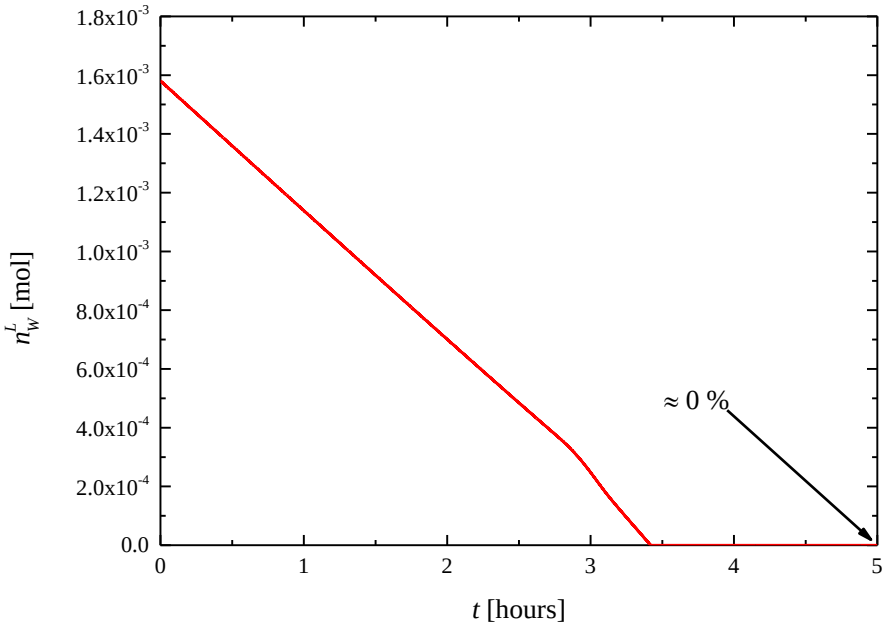

Figure 2.4.20: Temporal profile of water moles in the extracellular liquid phase. Residual water indicated as percentage of the initial content (Case 5, reducing the evaporative surface area of the sample).

More specifically, in this case the decrease of water content in the liquid sample shown in Figure 2.4.20 starts initially slower in comparison with the base case (cf. Figure 2.4.5), due to a reduced evaporation rate. However, after about 3 hours water removal accelerates as shown by the increasing slope in Figure 2.4.20, while it considerably slows down after 1.2 hours in Figure 2.4.5. This acceleration is due to crystal formation of dihydrate trehalose which now consumes liquid water according to the reaction scheme of Equation 1 once the system enters the biphasic zone.

To explain this unexpected behavior, the corresponding temporal profiles of the water percentage mass fraction and water diffusivity in the liquid phase are reported in Figure 2.4.21 to be compared with the corresponding one of the base case reported in Figure 2.4.6. Here, the water percentage mass fraction at the liquid interface (equilibrium) and the corresponding values on the solubility curve and on the glass transition curve are shown as well, for the sake of comparison.

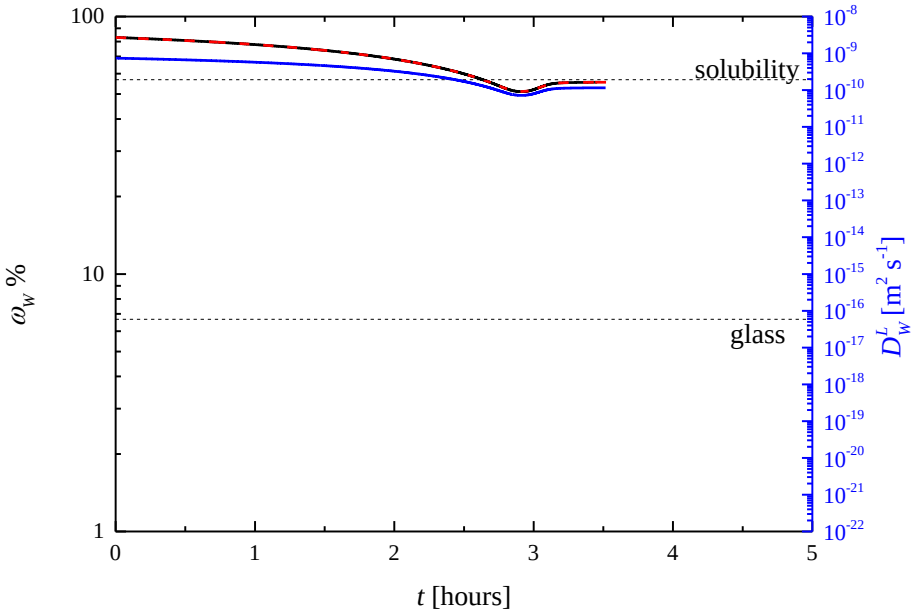

Figure 2.4.21: Temporal profiles of the water percentage mass fraction ω_W^L ——— and diffusivity $\mathfrak{D}_w^L$ ——— in the extracellular liquid phase. The profile of the water percentage mass fraction at the liquid interface (equilibrium) $\omega_W^{L,*}$ – – – is shown as well. (Case 5, reducing the evaporative surface area of the sample).

In this case, after about 2.5 hours, the mass fraction of water reaches the solubility curve due to evaporation, which means that crystal formation may now start. However, in contrast with the system behavior shown in Figure 2.4.6, now crystal formation is faster than evaporation and is capable to bring the liquid composition back to the solubility limit until the liquid phase is completely consumed at about 3.5 hours from the beginning of the process. As a consequence, the temporal variations of the liquid phase composition are limited in comparison with those shown in Figure 2.4.6 for the base case; now the composition of the liquid phase remains almost constantly close the solubility curve, i.e. with a relatively high content of water, and does not arrive up to glass transition where a relevant trehalose content is present. Accordingly, water diffusivity in the liquid phase does not decrease abruptly like in the base case, but it is maintained at relatively large values as shown in Figure 2.4.21 in comparison with Figure 2.4.6.

Once again, the determining role in the air-drying process played by water diffusion in the liquid phase emerges: when crystal formation is faster than evaporation, the liquid composition remains at the solubility limit, i.e. with a relatively large water content; for this reason, diffusion in the liquid phase remains relatively high during the whole process, without the abrupt decrease shown in the base case; as a consequence a slow but constant evaporation rate leads to a faster air-drying process.

Besides, as shown in Figure 2.4.22 in this case the resistance to evaporation rate according to the two-film theory is constantly confined in the diffusion layer of the gas phase, from the beginning of the process until a complete removal of the liquid phase is eventually achieved: no shift of the controlling step in the evaporation flux from the gas to the liquid side is now taking place, contrarily to the base case (cf. Figure 2.4.7).

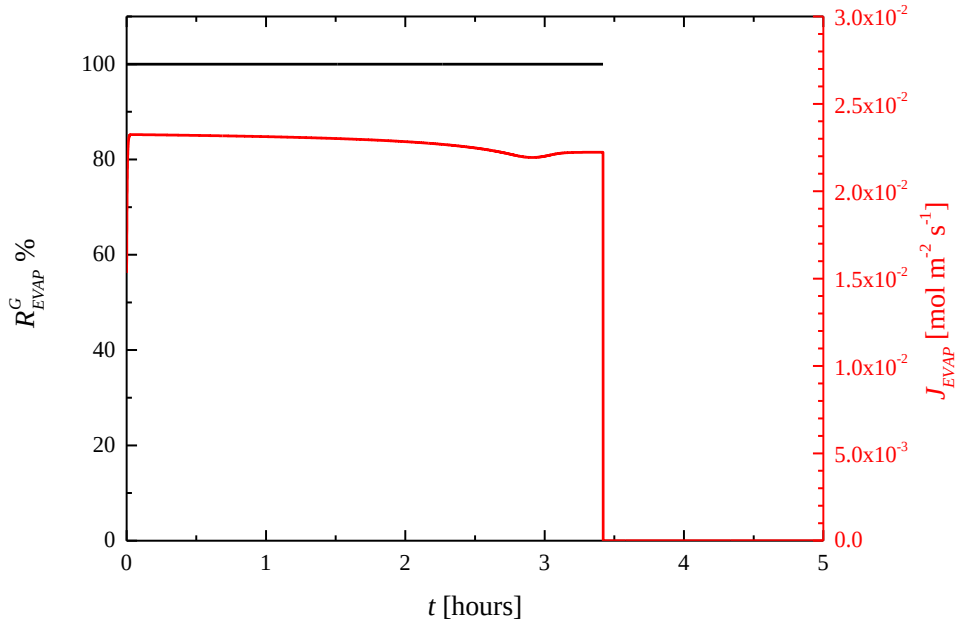

Figure 2.4.22: Temporal profiles of the percentage resistance to evaporation rate due to the gas phase and evaporation flux. (Case 5, reducing the evaporative surface area of the sample).

As a consequence, since generally speaking gas diffusion is faster than liquid diffusion, the evaporative flux in this case is always larger than in the base case (i.e. 10^{-2} [mol/m^2 s] vs 10^{-3} [mol/m^2 s] by comparing Figures 2.4.22 and 2.4.7), even if a lower evaporation rate results due to a reduced evaporative surface area.

Cells osmosis is still a relatively fast phenomenon, since the negligible difference of trehalose osmolalities between intra- and extracellular compartments reported in Figure 2.4.8 for the base case is simulated also in this case shown in Figure 2.4.23.

However, in this case when crystal formation brings the liquid composition back to the solubility curve, cells stop shrinking and start swelling so that the temporal profile of intracellular water volume percentage actually goes through a minimum as shown in Figure 2.4.23. For this reason, inside the cells a very high humidity content equal to 25.67 % eventually remains at the end of the process, which means that an effective long-term preservation by air-drying is not possible under these conditions.

The temporal profiles reported in Figures 2.4.24-25 show that basically 100% of the initially dissolved trehalose is removed from the sample by crystal formation by generating a population of many but small trehalose dihydrate crystals.

Turning our attention to the other possible resistances to water removal rate from the liquid sample to silica gel in the desiccator unit, the temporal profiles of the relative humidity in the gas phase inside any petri dish and in the chamber of the desiccator unit are shown in Figure 2.4.26 along with the leakage flux between the two compartments across the free space left by the unsealed lid.

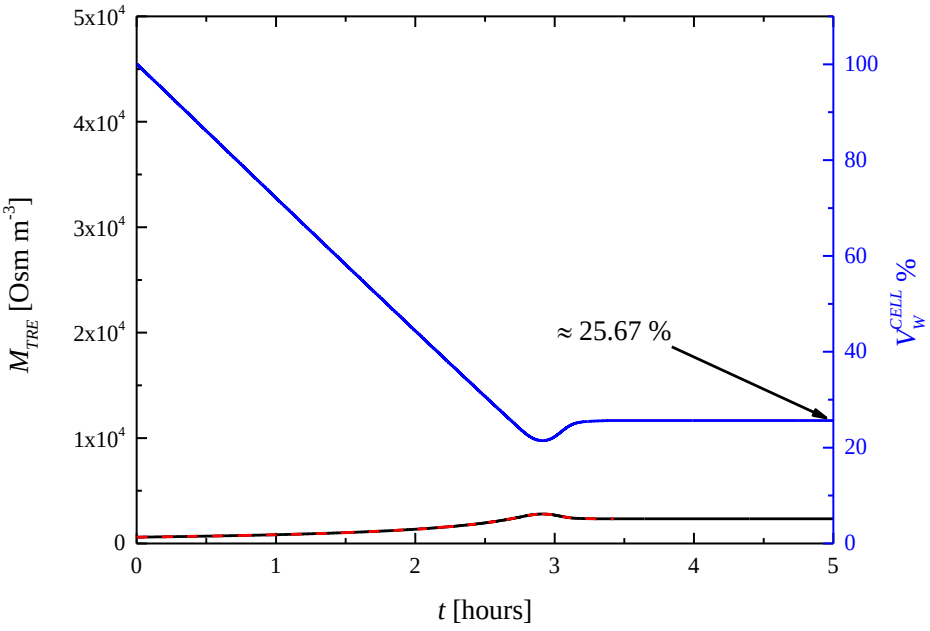

Figure 2.4.23: Temporal profiles of trehalose osmolality in the intracellular M_{TRE}^{L} ——— and extracellular M_{TRE}^{CELL} – – – liquid phases, and percentage of intracellular water volume $V_W^{CELL}\%$ ———. (Case 5, reducing the evaporative surface area of the sample).

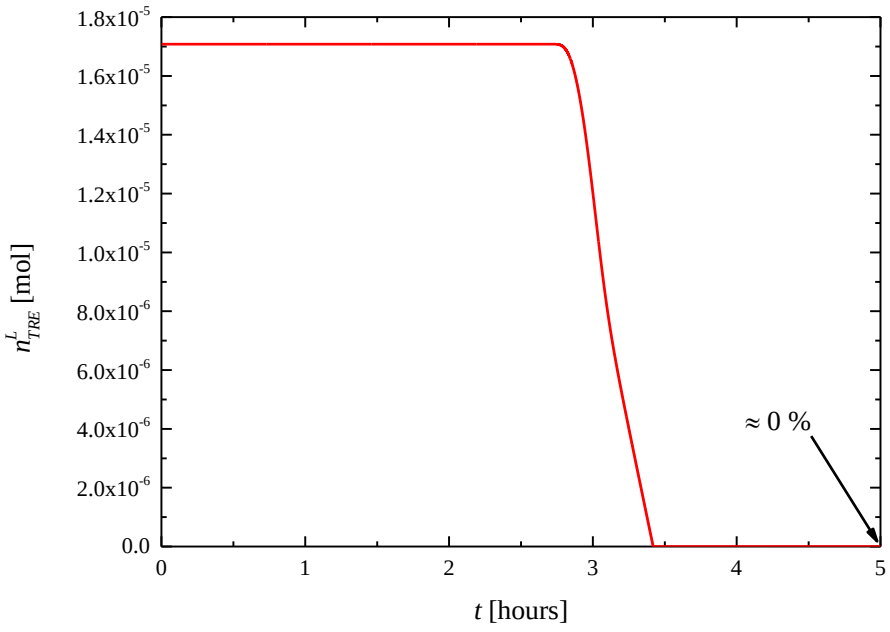

Figure 2.4.24: Temporal profile of the percentage trehalose content dissolved in the extracellular liquid phase. (Case 5, reducing the evaporative surface area of the sample).

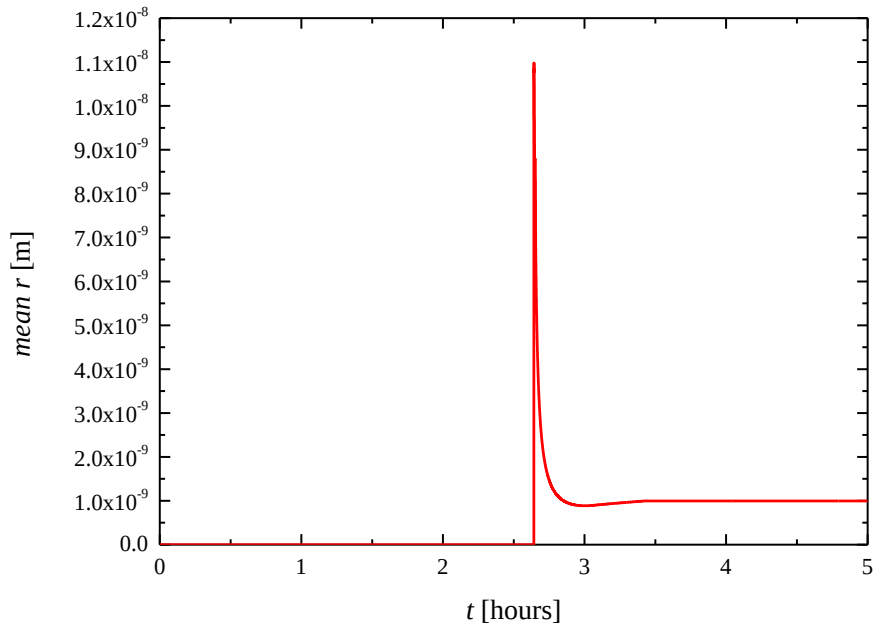

Figure 2.4.25: Temporal profile of the Sauter mean radius of the trehalose dihydrate crystal size distribution. (Case 5, reducing the evaporative surface area of the sample).

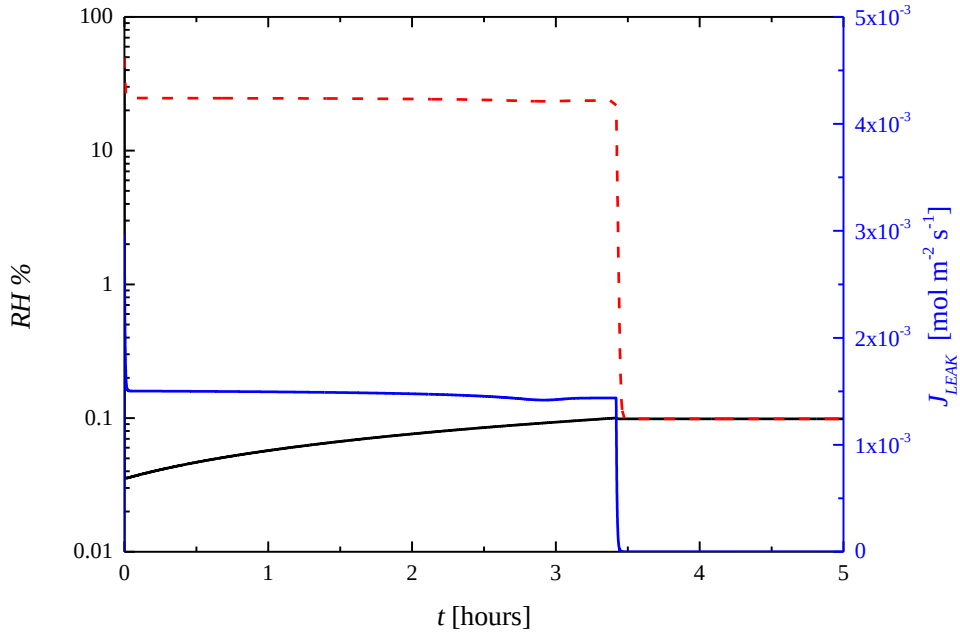

Figure 2.4.26: Temporal profiles of the relative humidity RH% in the gas phase of the petri dishes – – – and in the chamber of the desiccator unit ——, and the leakage flux from the unsealed petri dishes J_{LEAK} ——. (Case 5, reducing the evaporative surface area of the sample).

An abrupt initial decrease from the starting value of 50 % is obtained for the RH inside the petri dishes due to the combination of a slow evaporation and a fast leakage, whose rate remains relatively high due to the quick adsorption onto the silica gel in the chamber. Later, RH inside the petri dishes attains an almost constant value until the liquid sample is completely consumed, i.e. up to 3.5 hours when evaporation stops and RH in the petri abruptly decreases to become equal to the RH in the chamber of the desiccator. The latter one, on the other hand, increases slowly since water vapor in the chamber is effectively adsorbed by the silica gel. Therefore, the leakage flux basically follows the profile of RH inside the petri dishes as it was for the base case, with an abrupt decrease at 3.5 hours when the liquid sample is completely consumed.

Just like it was for the base case shown in Figure 2.4.11, a visible difference between the RH in the gas phase inside any petri dish and in the chamber of the desiccator unit is maintained throughout the process, at least until the liquid sample is completely consumed. This means that also in this case the water flow across the unsealed lid (i.e. leakage) is a controlling phenomenon in the sequential steps of water removal from the liquid sample to the silica gel.

Finally, the temporal profile of the adsorbed water in the silica gel along with the final adsorbed percentage with respect to the maximum absorbable are shown in Figure 2.4.27.

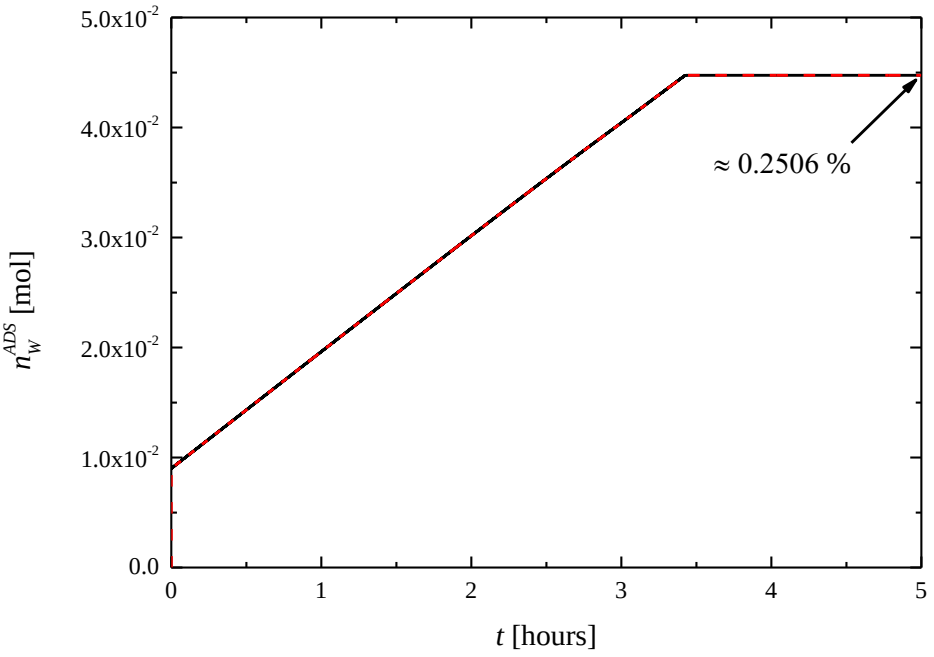

Figure 2.4.27: Temporal profile of water moles adsorbed in silica gel n_W^{ADS} – – –, and final adsorbed percentage. $n_W^{ADS,*}$ ——— at the solid interface (equilibrium) is shown as well. (Case 5, reducing the evaporative surface area of the sample).

By comparing with the results of the base case reported in Figure 2.4.12, a slightly lower water percentage is eventually adsorbed in this case, since some of the water initially contained in the liquid sample is consumed by crystal formation according to the stoichiometry of Equation 1.

Again, as can be seen in Figure 2.4.27, the driving force of adsorption is negligible (i.e. the difference between n_W^{ADS} and $n_W^{ADS,*}$ is equal to zero throughout the entire process), thus adsorption in silica gel never represents a limiting phenomenon for water removal from the samples.

After 3.5 hours the adsorption rate stops since the liquid sample is completely consumed, and evaporation as well as leakage do not take place any longer. Besides, according to the two-film theory the resistance to water flow due to adsorption in the silica gel is always confined in the gas side, just like it was for the base case (cf. Figure 2.4.28).

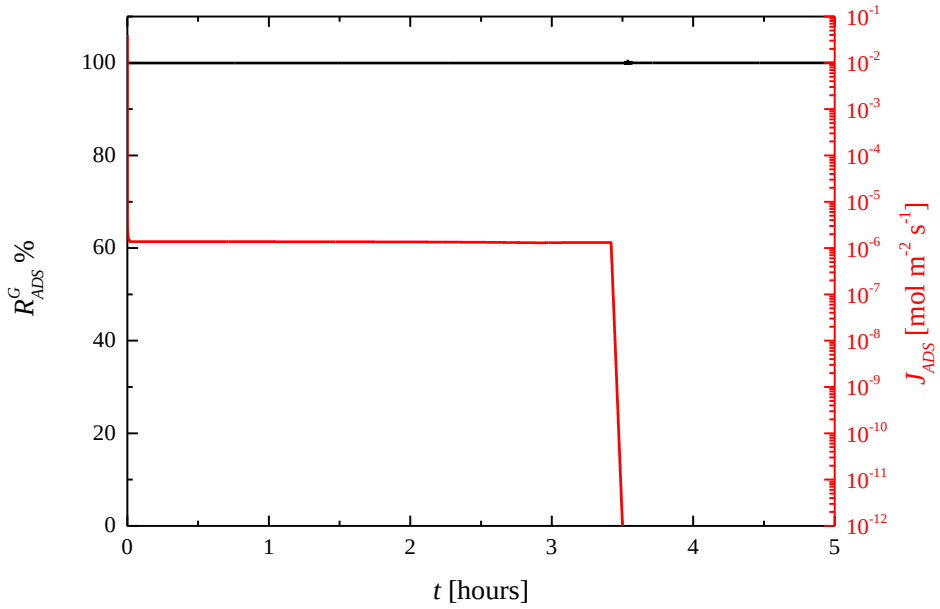

Figure 2.4.28: Temporal profiles of the percentage resistance to adsorption rate due to the gas phase and adsorption flux. (Case 5, reducing the evaporative surface area of the sample).

In summary, with a 10 times decrease of the surface area of the sample with respect to the base case, evaporation rate slows down and crystal instead of glass formation actually takes place in the sample. A much faster air-drying process results since a constant evaporation rate is maintained throughout the process until the liquid sample is completely consumed. This is due to a constant water diffusivity in the liquid sample, where trehalose concentration does not increase too much being constrained at the solubility limit by crystal formation. However, a limited cell dehydration is eventually reached. This, in combination with the absence of the lyo-protectant sugar glass, does not allow to guarantee an effective long-term preservation for the cells. As in the base case, cell osmosis and adsorption are relatively fast, while the leakage flux across the lid of the petri dishes still represents a limiting step of the air-drying process.

2.4.5.3.2 Case 6. Decreasing the cross-sectional area surface for the leakage from the Petri dish

In this case, the cross-sectional area for the leakage flux S^{LEAK} of water vapour from any petri dish to the chamber of the desiccator unit through the unsealed lid is decreased. This corresponds to the choice made by

the operator during the experimental run in the desiccator unit to cover any single petri dish with a tighter slid (see Figure 2.4.2). In particular, the annular area now considered is 10 times smaller (i.e. $S^{LEAK} = 9.83723 \cdot 10^{-6}\ m^2$) than the one used for the base case: from this point of view, this case is just the opposite of the case 2 previously discussed. According to Equations 4-5 this corresponds to decrease the leakage flow rate. Of course, the same result would be obtained by increasing δ^{LEAK}, i.e. by decreasing the conductance of the leakage flux defined in Equation 12.

The corresponding system behavior followed in the phase diagram is shown in Figure 2.4.29, where crystal instead of glass formation is still taking place like for the case 5.

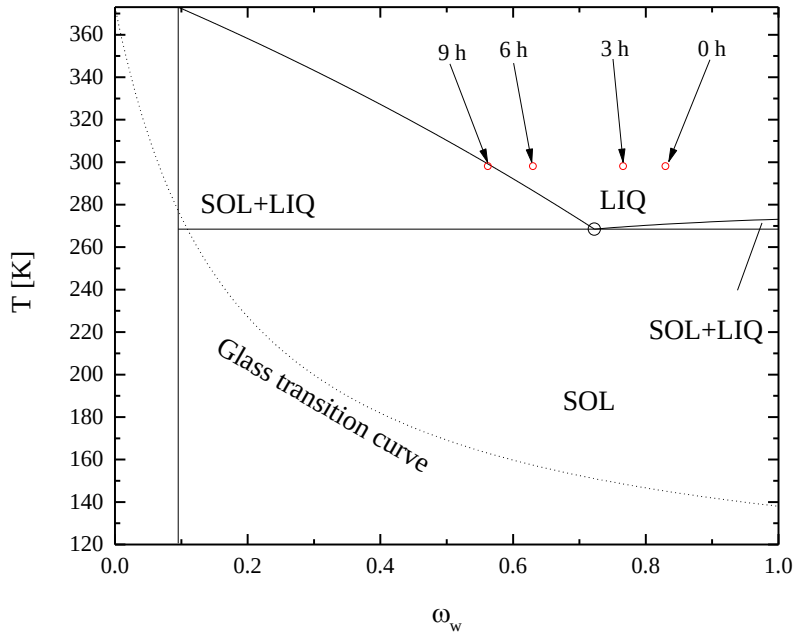

Figure 2.4.29: Temperature - composition phase diagram of the binary solution water + trehalose: change in liquid phase composition during the air-drying process (Case 6, decreasing the leakage surface area).

By decreasing the leakage rate a slower air-drying process is obtained with respect to case 5 (cf. Figures 2.4.19 and 2.4.29): now it takes about 9 hours to completely consume the liquid sample with a final humidity content inside the cells equal to 26%. 100% of the trehalose initially present in the sample is still consumed by crystal formation with the generation of slightly larger crystals. In addition, more water vapor accumulates in the petri dish so that RH reaches saturation in the gas phase inside the petri dishes, and cell osmosis as well adsorption do not represent a limiting step in the dehydration process. Therefore, by decreasing the conductance of the leakage flow the obtained results are similar to those of case 5 in general, but system response is slower, indicating that a more relevant role is played by the leakage in the process, as expected.

2.4.5.3.3 Case 7. Increasing sample volume

Now the opposite to case 3 previously discussed is addressed. More specifically, the sample height is increased 10 times with respect to the base case and a larger liquid volume is considered (i.e. $V^{SAMPLE} = 4 \cdot 10^{-7}\ m^3$).

Of course, this means that a larger amount of water is present in the liquid sample to be transferred to silica gel, and more trehalose is available for crystal formation. As such, the system moves more slowly towards crystal formation than case 5, as shown in Figure 2.4.30 (cf. Figure 2.4.19).

Besides it is worth noting that, on the basis of CNT the nucleation rate B_0 expressed in Equation 20 increases with sample volume thus enhancing the rate of crystal formation with respect to evaporation rate. That's the reason why glass formation does not occur as shown in Figure 2.4.30. Basically, in this case a very similar system behavior to case 6 is obtained.

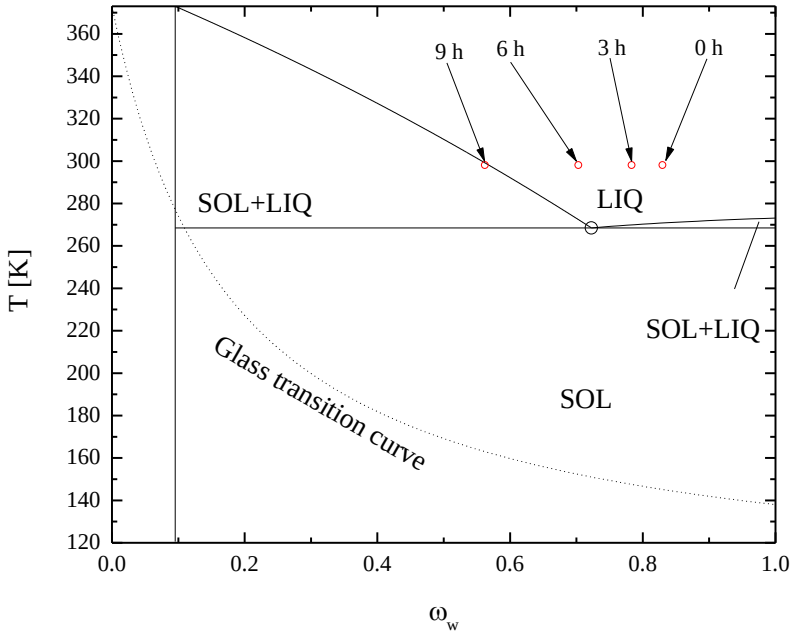

Figure 2.4.30: Temperature - composition phase diagram of the binary solution water + trehalose: change in liquid phase composition during the air- drying process. (Case 7, increasing the sample height (volume))

2.4.5.3.4 Case 8. Increasing the trehalose osmolality

If a 10 times increase with respect to base case is considered for the initial trehalose osmolality (i.e. $M^0_{TRE} = 2200\ Osm/m^3$) this means that a smaller amount of water is actually present inside the liquid sample. Thus, in the phase diagram shown in Figure 2.4.31 the decrease due to evaporation of the water mass fraction in the liquid phase starts from a point positioned more to the left with respect to the cases analyzed so far, closer to the solubility curve.

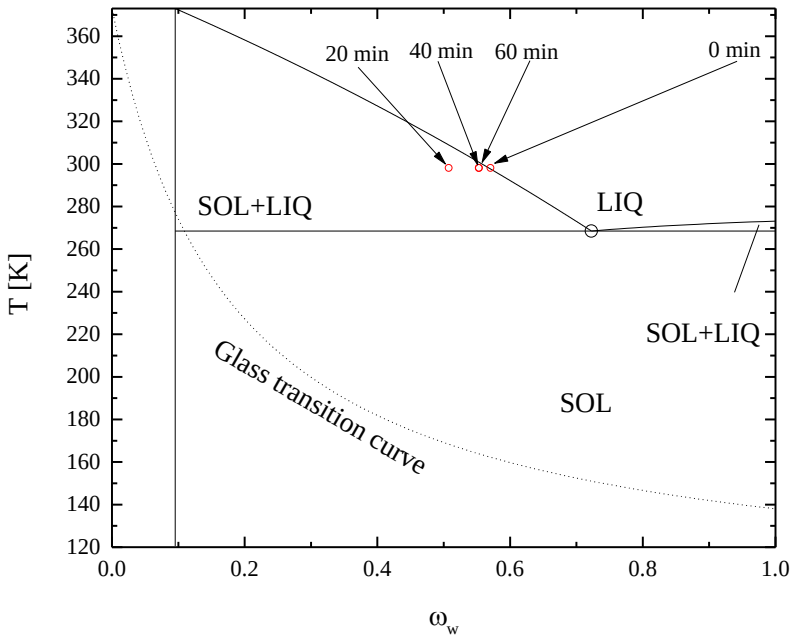

Figure 2.4.31: Temperature - composition phase diagram of the binary solution water + trehalose: change in liquid phase composition during the air- drying process. (Case 8, increasing the trehalose osmolality)

As clearly shown in Figure 2.4.31, even in this case crystals instead of glass are formed, and the liquid composition goes back and forth around the solubility curve once entered the biphasic zone.

Unexpectedly, the air-drying process of the case 8 is the fastest among all the others simulated in this work. This is due to the small amount of water present in the liquid phase which is quickly removed by evaporation and by the formation of dihydrate trehalose crystals. This latter one, in fact, starts right after the beginning of the process almost simultaneously with evaporation, since liquid composition is already close to the solubility limit. However, an unacceptably large humidity content is eventually left inside the cells (i.e. 93.18%) meaning that no effective cell dehydration is achieved: this is the worst scenario for long-term preservation, with cells maintaining almost all the initial intracellular water without sugar glass protection. Besides, nucleation and growth rates are now comparable which lead to the formation of a lower number of larger crystals, which are potentially harmful for the cells. On the other hand, leakage is still a limiting step to water transfer while cell osmosis and adsorption onto silica gel are relatively fast.

2.4.6 Conclusions

In this work, a mathematical model for the description of the air-drying process (at room temperature and atmospheric pressure) of hMSCs with trehalose is developed by referring to a specific desiccator unit where silica gel is used as water trap. The ultimate goal is to provide a deterministic model to support and guide the optimization of a long-term preservation process for these precious cells in alternative to the classic cryopreservation carried out in liquid nitrogen at -196 °C. To this aim, all the physico-chemical phenomena that may occur in the process (i.e. evaporation, cell osmosis, crystal formation or glass transition, leakage

through the lids of the petri dishes, and adsorption) are accounted for by means of a compartmental model: driving forces are defined as deviations from the corresponding thermodynamics equilibria, while the two-film theory is adopted to describe the material exchange at the contacting interfaces between two communicating phases/compartments.

First, the thermodynamics equilibria of the system are determined on the basis of an extensive and careful analysis of the fragmentary scientific literature on the topic, where contradictory data are reported. Later, transport parameters for the model simulations are chosen: given that for the system investigated in this work no valuable data is found in the literature, the adopted parameter values are taken form the literature even if referred to different systems.

Based on these uncertainties, in this work a parametric sensitivity analysis is performed by varying some key system sizes, geometries and operating conditions. This way it is shown that, depending on the specific choices made by the operator running the desiccator unit, two possible outcomes may be eventually reached. In fact, according to the proposed model the competition between evaporation and crystal formation in the sample is responsible of the system behavior and determines the cell fate at the end of the process. More specifically, by varying the surface area or the volume of the sample to be dried as well as the trehalose content or the tightening of the lids covering the petri dishes, it is shown that evaporation may be made faster or slower than crystal formation. In the first case, sugar glass is formed in the sample and an extended dehydration of the cells is eventually achieved. Thus, an effective lyo-protection for the cells may be realized but only with a very long air-drying process, due to the increasing trehalose concentration in the liquid sample that progressively slows down evaporation (i.e. in the sample diffusivity decreases and viscosity increases to critical values). On the other hand, when evaporation is slower than crystallization, a limited cell dehydration is eventually achieved and sugar crystals instead of glass are formed in the sample containing the cells. In this case, a shorter air-drying process results but an effective lyo-protection cannot be achieved. In conclusion, by varying system sizes and geometries as well as the operating conditions, the evaporation rate need to be optimized in order to reach an acceptable final cell viability (by favoring glass formation with a large cell dehydration) while reducing the duration of the air-drying process.

2.4.A1 Appendix - Thermodynamic parameters

The phase diagram for the binary system water + trehalose is used to define the driving forces of the different physico-chemical phenomena involved in the drying process, including Solid-Liquid (crystal formation) and Vapor-Liquid (Evaporation) equilibria. Actually, by taking into account the glass transition temperature, a so-called extended phase diagram is adopted in this work where the formation of a metastable phase is considered. Regarding this, actually the kinetics of glass formation is not modelled in this work, and an abrupt transformation from the residual liquid phase to glass is assumed to take place. An adsorption isotherm is used for the Vapor-Solid equilibrium of water onto silica gel.

2.4.A1.1 Solid-liquid equilibria

Contradictory references are available in the scientific literature regarding the binary phase diagram of the trehalose + water system. In particular, for the water solubility in trehalose several references may be found where the reported experimental data do not perfectly match.
The origin of this contradiction is that two stable crystal sugar forms are actually present in the system. For this reason, a comparison among the different literature sources is here presented to explain the selection necessarily made to perform the simulations of the proposed model. The crystal sugar form most commonly used in desiccation studies is trehalose dihydrate which precipitates at room temperature, while the other one (i.e. anhydrous trehalose) is obtained by removing water via a thermal process. The curve of water solubility in trehalose dihydrate ranges from the eutectic point at the intersection with the freezing curve to a water mass fraction equal to 0.1, while water solubility in anhydrous trehalose is confined in the interval [0;0.1] of the water mass fraction.
The phase diagram provided by [24] where data measured by different authors is shown in Figure 2.4.A1.1. Here, the freezing curve and the curve of water solubility in trehalose dihydrate are shown along with the glass transition curve. It is apparent that two series of data for water solubility in trehalose dihydrate are actually available, testifying the great uncertainty among different references in the literature on this topic. In particular, in Figure 2.4.A1.1 no data was provided for anhydrous trehalose, that is completely neglected.

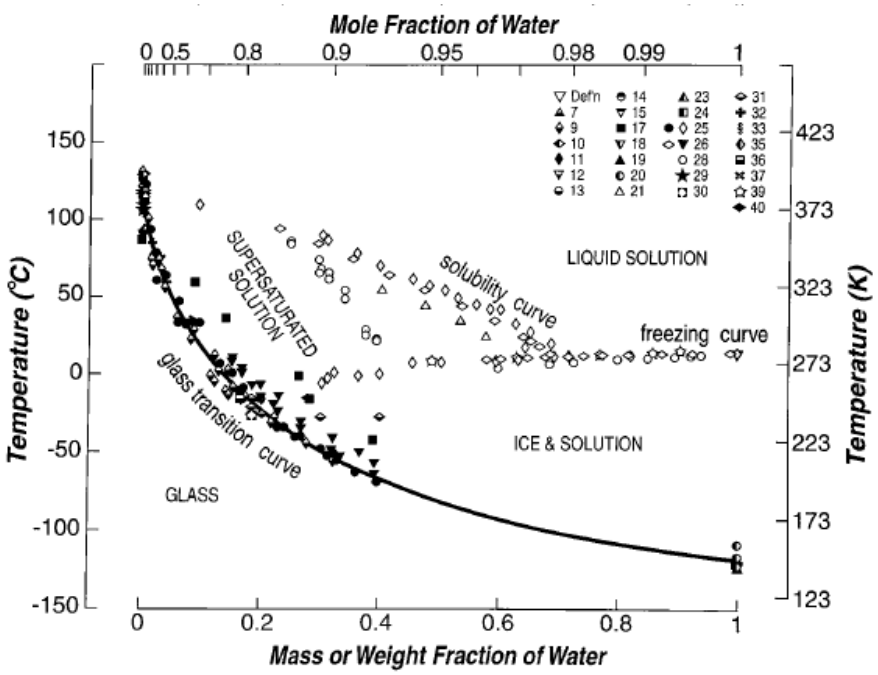

Figure 2.4.A1.1: Phase diagram for water + trehalose system [24]

For this reason, in this work measured data are fitted with the following two equations:

$$T_{solubility}\,[K] = 373 + 210.13831(exp(0.05839170944) - exp(0.61312\omega_W)) \quad \text{(A1.1)}$$

$$T_{freezing}\,[K] = 273 + 78.31051(exp(-2.74601) - exp(-2.74601\omega_W)) \quad \text{(A1.2)}$$

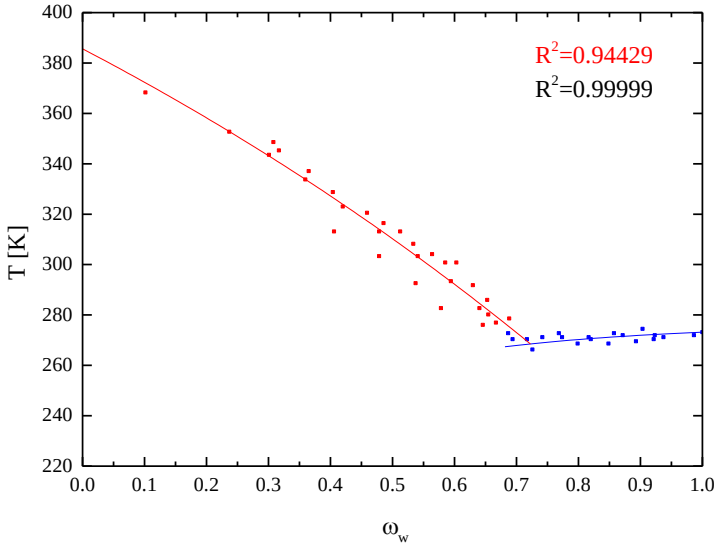

Figure 2.4.A1.2: Data (Chen T. et al., 2000) T vs ω_wa P: 1 atm. – Freezing curve (This work), – Solubility curve (This work).

From this phase diagram, the equilibrium composition on the solubility curve necessary to define the driving force of the crystal formation of dihydrate trehalose at 25 °C is readily calculated : $\omega_W^{solubility} = 0.568516367$, or $x_W^{solubility} = 0.961589433$.

2.4.A1.2 Vapor-liquid equilibrium

A limited number of references is available in the literature on the Vapor-liquid equilibrium for the binary system water + trehalose. Typically, the equilibrium between the liquid and gas phase is considered dependent only on water activity as reported by [25]. In particular, vapor pressure at equilibrium may be calculated by means of Equation 19

$$P_W^{sat} = x_W^L\,\gamma_W(x_W^L, T)\,P_{SW}(T) \quad \text{(A1.3)}$$

where $P_{SW}(T)$ represents the vapor pressure of pure water and $\gamma_W(x_W^L, T)$ is the coefficient of water activity in the liquid solution with trehalose.

2.4.A1.2.1 Vapor pressure of pure water

As reported in [26], the following empirical equations (i.e. Wagner equation) may be used to determine vapor pressure of pure water in a relatively large temperature and pressure ranges, i.e. 273 K ≤ T ≤ 647.3 K and 0.01 bar ≤ $P_{SW}(T)$ ≤ 221 bar:

$$ln(P_R) = \frac{1}{T_R} + [a(1-T_R) + b(1-T_R)^{1.5} + c(1-T_R)^3 + d(1-T_R)^6] \quad \text{(A1.4)}$$

$$P_R = \frac{P_{SW}(T)}{P_C\ 10^5\ \left[\frac{Pa}{bar}\right]} \quad \text{(A1.5)}$$

$$T_R = \frac{T}{T_C} \tag{A1.6}$$

whose parameters are reported in Table 2.4.A1.1.

Table 2.4.A1.1: Wagner equation parameters for pure water [26].

Parameter	***Value***	***Units***
a	-7.77224	$[-]$
b	1.45684	$[-]$
c	-2.71942	$[-]$
d	-1.41336	$[-]$
P_C	220.64	$[bar]$
T_C	647.14	$[K]$

2.4.A1.2.2 The coefficient of activity for water in the binary liquid system water + trehalose.

Sato and colleagues [27-28] proposed the following empirical equation which was obtained through a non-linear regression of experimental data at 25 °C:

$$\gamma_W = exp[-8.775(1 - x_W)^2], \qquad @\, T = 25°C \tag{A1.7}$$

Clearly, this equation does not allow to represent Vapor-liquid equilibrium in the phase diagram at varying temperature.

The comparison of model predictions obtained through the empirical Equation 24 and measured data on the coefficient of activity for water in a liquid solution with trehalose is shown in Figure 2.4.A1.3. The data is available only at low concentrations of trehalose, where the match with the empirical equation (black line) is satisfactory.

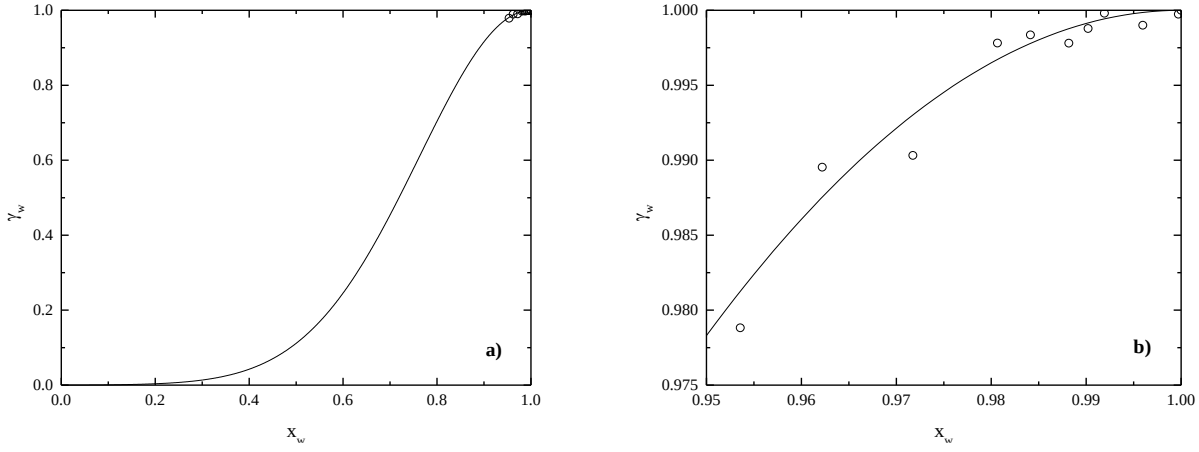

Figure 2.4.A1.3: Comparison of measured data and model results: a) – Prediction by the empirical Equation 24 [27-28]; b) Zooming in.

2.4.A1.3 Vapor-solid equilibrium

The Vapor-solid equilibrium $\bar{q}_W^* = f(P_w)$ for water onto silica gel needs to be determined for the simulations of the proposed model. Regarding this, the scientific literature reporting adsorption isotherms is vast, and a variety of mathematical expressions is actually available. In this work Dubinin-Radushkevich's adsorption

isotherm [29] is compared by means of a non-linear regression of the experimental data reported by [30] which are related to a Grade 03 commercial silica gel.
The Dubinin-Radushkevich's adsorption isotherm [29] is shown in equation A1.8

$$\bar{q}_W^* = W_{0,1}\, exp\left[-\left(\frac{\bar{A}_W^*}{E_{0,1}}\right)^2\right] + W_{0,2}\, exp\left[-\left(\frac{\bar{A}_W^*}{E_{0,2}}\right)^2\right] \quad \text{(A1.8)}$$

where $\bar{A}_W^*$ represents the adsorption potential of water at the interface with the solid phase and is related to water vapour pressure P_w through Equation A1.9,

$$\bar{A}_W^* = -RTln\left(\frac{P_w}{P_{SW}(T)}\right) \quad \text{(A1.9)}$$

In this adsorption isotherm 4 adjustable parameters are introduced, namely $E_{0,1}$, $E_{0,2}$, $W_{0,1}$, $W_{0,2}$, whose values is determined by a best-fitting procedure ($R^2 = 0.99885$). The values of the adjustable parameters are reported in Table 2.4.A1.2.

Table 2.4.A1.2: Parameter values for the Dubinin-Radushkevich s isotherm.

Parameter	***Value***	***Units***
$E_{0,1}$	7869.43	$[J/mol]$
$E_{0,2}$	2995.35	$[J/mol]$
$W_{0,1}$	0.0936156	$[kg_w/kg_{ads}]$
$W_{0,2}$	0.228071	$[kg_w/kg_{ads}]$

2.4.A1.4 Glass transition curve

One of the simplest mathematical expression of the glass transition curve is the Gordon-Taylor's equation [24]. Here, the glass transition temperature for the binary system water + trehalose is considered as a function of water and trehalose mass fractions.

$$T_g = \frac{\omega_{TRE} T_{g,TRE} + \omega_W k T_{g,W}}{\omega_{TRE} + \omega_W k} \quad \text{(A1.10)}$$

where $T_{g,TRE}$ e $T_{g,W}$ are reported in Table 2.4.A1.3 and represent the glass transition temperatures of pure trehalose and pure water.

Table 2.4.A1.3: Parameter values of the Gordon-Taylor's equation. [24]

Parameter	***Value***	***Units***
$T_{g,TRE}$	373	$[K]$
$T_{g,W}$	138	$[K]$

The parameter *k* depends on $T_{g,TRE}$ in °C as it follows

$$k = 0.0293 T_{g,TRE}[°C] + 3.61 \quad \text{(A1.11)}$$

According to the Gordon-Taylor's equation, at 25 °C a composition of glass transition equal to $\omega_{g,W} = 0.0667$ is readily calculated.

2.4.A2 Appendix – Material transport parameters

In this section the material transport parameters appearing in the proposed model are reported. First, the way the diffusivities in the liquid and gas phases are calculated as a function of temperature and composition is described, along with the way the thicknesses of the diffusional layers in both phases are chosen. Then, the adopted values for porosity and tortuosity of the silica gel adsorbent necessary to determine an effective diffusivity of the porous material are reported. Finally, the adopted value for water permeability to cell membrane is given.

2.4.A2.1 Diffusivity of water in the liquid phase.

According to [17] the diffusivity of water in the liquid phase may be calculated through the Stokes–Einstein equation reported below

$$\mathfrak{D}_w^L = \frac{k_B T}{6\,\pi\, a_w^0\, \eta^L} \tag{A2.1}$$

where η^L is the viscosity of the liquid solution, while a_w^0 is the apparent hydrodynamic radius of water which can be calculated as

$$a_W^0 = \left(\frac{3\tilde{v}_w}{4\pi \mathcal{N}_A}\right)^{\frac{1}{3}} \tag{A2.2}$$

The viscosity of the water + trehalose liquid solution appearing in Equation A2.3 may be determined by means of the following empirical equation (i.e. the so-called Mathlouthi and Génotelle equation) reported by [31]

$$log\left(\frac{\eta^L}{\eta^*}\right) = a_1 + a_2 x_{TRE}^L + \left(\frac{303 - T}{T - 182}\right)\left[b_1 + b_2 (x_{TRE}^L)^{n^*}\right] \tag{A2.3}$$

where $\eta^* = 10^{-3}\, Pa \cdot s$, is a constant reference value for viscosity, while x_{TRE}^L is molar fraction of the dissolved trehalose in the liquid phase, and T is system temperature in Kelvin. The other parameters of the Mathlouthi and Génotelle equation are reported in Table 2.4.A2.1.

Table 2.4.A2.1: Parameter values of the Mathlouthi and Génotelle equation [31].

Parameter	***Value***	***Units***
a_1	-0.159 ± 0.019	$[-]$
a_2	26.4 ± 0.35	$[-]$
b_1	1.31 ± 0.14	$[-]$
b_2	30.9 ± 8.1	$[-]$
n^*	1.20 ± 0.14	$[-]$

2.4.A2.2 Diffusivity of water in the gas phase.

During the air-drying process at 25 °C the maximum water vapor pressure due to evaporation attains a value equal to $\cong 10^{-2}$ atm. Since the process is carried out starting from atmospheric pressure, a simplifying assumption of the proposed model is that the gas phase inside any petri dish as well as in the chamber of the desiccator unit remain constantly at 1 atm. Therefore, it is implicitly assumed that the gas phase consists mainly in air at 25 °C and 1 atm. Thus, the diffusivity of water vapor in the gas phase is calculated as the water diffusivity in air by means of the following equation

$$\mathfrak{D}_w^G = 1.894775 \cdot 10^{-5} \frac{T^{2.072}}{P_{TOT}} \left[\frac{m^2}{s}\right] \quad \text{(A2.4)}$$

where P_{TOT} is the atmospheric pressure and T the system temperature Equation 58 is reported by [32] who specified its validity into the temperature range between 280 K and 450 K.

2.4.A2.3 Diffusional layer in the gas phase

Great uncertainty is found in the scientific literature concerning evaporation, and, in particular, to the value assigned to the thickness of the diffusional layer in the gas phase when the two-film theory is adopted to describe the evaporation rate. In fact, mass transport during the evaporation is generally found to be dependent on system sizes and operating conditions, which casts a doubt on the real possibility to simplify the mathematical description of the phenomenon by means of the two-film theory.
In a recent work [14] it is reported a value for the water mass transfer coefficient in the gaseous phase due to natural convection in air taken from [33] which corresponds to a thickness layer $\delta^G = 1.022874 \cdot 10^{-3}\ [m]$. This is the value used for the simulations of the proposed model reported in this work.

2.4.A2.4 Diffusional layer in the liquid phase

No references are found in the literature on the thickness of the diffusional layer in the liquid phase. In this work, the value $\delta^L = 10^{-9}\ [m] \cong 10^{-6} \cdot \delta^G$ is chosen by considering that the thickness of the liquid diffusion layer is expected to be quite smaller in comparison with the one of the gas phase during evaporation, at least initially.

2.4.A2.5 Properties of the adsorbent phase (silica gel)

The capacity to adsorb water vapor by the silica gel is strictly related to the size of the porous particles of the adsorbing material, along with its porosity and tortuosity. First, the radius of the silica gel particle is chosen $r_{ADS} = 2 \cdot 10^{-3}[m]$, according to the size reported in the literature [34]. Then, a typical value (i.e. $\varepsilon = 0.4$) is assigned to the porosity of the commercial Grade 03 silica gel considered in this work. Finally, tortuosity of the porous materials may be evaluated as a function of porosity by means of the expression reported in the literature [35]:

$$\tau = \varepsilon^{-\frac{2}{3}} \quad \text{(A2.5)}$$

where an increasing tortuosity with a decreasing porosity is typically described.

2.4.A3 Appendix - System variables

In order to easily understand the description of mass transport fluxes, a description of system variables, linked to the independent variables of the system of ODEs (Ordinary Differential Equations), is provided as follows. All the symbols are described in the Notation section.

2.4.A3.1 Volumes and constant values

$$N^{CELL} = C^{CELL} V^{0,SAMPLE} \quad \text{(A3.1)}$$

$$S^{ADS} = \frac{3\, V^{ADS}}{r^{ADS}} \quad \text{(A3.2)}$$

$$V^{ADS} = \frac{W^{ADS}}{\rho^{ADS}} \tag{A3.3}$$

$$\delta^{ADS} = \frac{r^{ADS}}{5} \tag{A3.4}$$

$$V^{CG} = V^{C} - N^{P}V^{P} - V^{ADS} \tag{A3.5}$$

$$V^{0,PG} = V^{P} - V^{0,SAMPLE} \tag{A3.6}$$

$$V^{0,CELL} = V^{ISO,CELL}[\nu_B + (1-\nu_B)(1+\tilde{v}_{TRE}M^0_{TRE})] \tag{A3.7}$$

$$V^{0,L}_W = \frac{V^{0,SAMPLE} - N^{CELL}V^{0,CELL}}{1+\tilde{v}_{TRE}M^0_{TRE}} \tag{A3.8}$$

$$P^0_W = RH^0P_{SW}(T) \tag{A3.9}$$

2.4.A3.2 Initial Conditions

$$n^{0,L}_W = \frac{V^{0,L}_W}{\tilde{v}_W} \tag{A3.10}$$

$$n^{0,L}_{TRE} = M^0_{TRE}V^{0,L}_W \tag{A3.11}$$

$$V^{0,CELL}_W = V^{ISO,CELL}(1-\nu_B) \tag{A3.12}$$

$$n^{0,PG}_W = \frac{P^0_W V^{0,PG}}{RT} \tag{A3.13}$$

$$n^{0,CG}_W = \frac{P^0_W V^{CG}}{RT} \tag{A3.14}$$

$$n^{0,ADS}_W = \frac{\bar{q}^0_W W^{ADS}}{PM_W} \tag{A3.15}$$

$$\mu_n = 0, \qquad \forall n \in [0,1,2,3] \tag{A3.16}$$

2.4.A3.3 Sample: liquid phase

$$V^{SAMPLE} = V^{L} + N^{CELL}V^{CELL} + V^{S}_{TRE} \tag{A3.17}$$

$$V^{L} = V^{L}_W + V^{L}_{TRE} \tag{A3.18}$$

$$V^{L}_W = \tilde{v}_W n^{L}_W \tag{A3.19}$$

$$V^{L}_{TRE} = \tilde{v}_{TRE} n^{L}_{TRE} \tag{A3.20}$$

$$C^{L}_W = \frac{n^{L}_W}{V^{L}} \tag{A3.21}$$

$$C^{L\to G}_W = \frac{x^{L}_W \gamma_w(x^{L}_W, T)P_{SW}(T)}{RT} \tag{A3.22}$$

$$x^{L}_W = \frac{n^{L}_W}{n^{L}_W + n^{L}_{TRE}} \tag{A3.23}$$

$$x_W^{L,*} = \frac{C_W^{L,*}}{C_W^{L,*} + \frac{n_{TRE}^L}{V^L}} \tag{A3.24}$$

$$x_{TRE}^L = 1 - x_W^L \tag{A3.25}$$

$$\omega_W^L = \frac{PM_W n_W^L}{PM_W n_W^L + PM_{TRE} n_{TRE}^L} \tag{A3.26}$$

$$\omega_W^{L,*} = \frac{PM_W C_W^{L,*}}{PM_W C_W^{L,*} + PM_{TRE} \frac{n_{TRE}^L}{V^L}} \tag{A3.27}$$

2.4.A3.4 Sample: cells and crystal sugar

$$V^{CELL} = V_W^{CELL} + V^{ISO,CELL}[\nu_B + (1 - \nu_B)\tilde{v}_{TRE} M_{TRE}^0] \tag{A3.28}$$

$$M_{TRE}^L = \frac{n_{TRE}^L}{V_W^L} \tag{A3.29}$$

$$M_{TRE}^{CELL} = M_{TRE}^0 \frac{V_W^{0,CELL}}{V_W^{CELL}} \tag{A3.30}$$

$$V_{TRE}^S = \frac{4\pi}{3}\mu_3 \tag{A3.31}$$

2.4.A3.5 Petri gas phase

$$V^{PG} = V^P - V^{SAMPLE} \tag{A3.32}$$

$$P_W^P = \frac{RTn_W^{PG}}{V^{PG}} \tag{A3.33}$$

$$C_W^{PG} = \frac{n_W^{PG}}{V^{PG}} \tag{A3.34}$$

2.4.A3.6 Chamber gas phase

$$P_W^C = \frac{RTn_W^{CG}}{V^{CG}} \tag{A3.35}$$

$$C_W^{CG} = \frac{n_W^{CG}}{V^{CG}} \tag{A3.36}$$

$$C_W^{PG,*} = \frac{x_W^{L,*}\gamma_w\left(x_W^{L,*}, T\right)P_{SW}(T)}{RT} \tag{A3.37}$$

2.4.A3.7 Solid phase: adsorbent

$$\bar{q}_W = \frac{n_W^{ADS} PM_W}{W^{ADS}} \tag{A3.38}$$

$$\bar{A}_W^* = -RTln\left(\frac{C_W^{CG,*}RT}{P_{SW}(T)}\right) \tag{A3.39}$$

$$\bar{A}_W^{G\to S} = -RTln\left(\frac{C_W^{CG}RT}{P_{SW}(T)}\right) \tag{A3.40}$$

$$\bar{q}_W^{G\to S} = W_{0,1}\,exp\left[-\left(\frac{\bar{A}_W^{G\to S}}{E_{0,1}}\right)^2\right] + W_{0,2}\,exp\left[-\left(\frac{\bar{A}_W^{G\to S}}{E_{0,2}}\right)^2\right] \tag{A3.41}$$

Notation of the Subchapter 2.4

Capital letters

$\bar{A}_W$	Adsorption potential in Dubinin-Radushkevich eq.	$[J\ mol^{-1}]$
B_0	Sugar crystal nucleation rate term	$[\#\ s^{-1}]$
C_i^k	Molar concentration of the i-th specie in the k-th phase	$[mol\ m^{-3}]$
C^{CELL}	Cell concentration in one sample	$[\#\ m^{-3}]$
$\mathfrak{D}_i^k$	Molecular diffusivity of the i-th specie in the k-th phase	$[m^2\ s^{-1}]$
$E_{a,P}$	Cell membrane water permeability activation energy	$[J\ mol^{-1}]$
$E_{a,TREh}^S$	Crystal sugar nucleation activation energy	$[J]$
$E_{0,1}$	Activation energy in Dubinin-Radushkevich eq.	$[J\ mol^{-1}]$
$E_{0,2}$	Activation energy in Dubinin-Radushkevich eq.	$[J\ mol^{-1}]$
G_{TREh}	Sugar crystal growth rate	$[m\ s^{-1}]$
J	Jacobi matrix	$[-]$
J_j	Molar flux referred to the j-th phenomenon	$[mol\ m^{-2}\ s^{-1}]$
J_{TREh}	Sugar crystal nucleation rate term	$[\#m^{-3}\ s^{-1}]$
J_{TREh}^0	Sugar crystal nucleation rate term parameter	$[m^{-5}]$
K_j^G	Global transport coefficient referred to the j-th phenomenon	$[m\ s^{-1}]$
L_P	Cell membrane water permeability	$[m\ Pa^{-1}\ s^{-1}]$
L_P^0	Cell membrane water permeability at $T \to \infty$	$[m\ Pa^{-1}\ s^{-1}]$
M_{TRE}^k	Trehalose osmolality in k-th phase	$[Osm\ m_W^{-3}]$
$\mathcal{N}_A$	Avogadro number	$[\#\ mol^{-1}]$
N^{CELL}	Number of cells contained in the sample	$[\#]$
N^P	Petri dishes number	$[\#]$
N_q	QMOM order	$[-]$
P	Pressure	$[Pa]$
P_{AIR}	Atmospheric air pressure	$[Pa]$
P_C	Critical pressure	$[bar]$
PM_i	Molar weight of the i-th specie	$[kg\ mol^{-1}]$
P_R	Reduced pressure	$[-]$
$P_{j,k}$	Coefficient of Product-difference Matrix QMOM	$[-]$
P_W^{sat}	Equilibrium water vapor pressure	$[Pa]$
P_{SW}	Vapor pressure of pure water	$[Pa]$
P_{TOT}	Total pressure	$[Pa]$
R	Gas constant	$[m^3\ Pa\ mol^{-1}\ K^{-1}]$
$R_{CRYSTAL}$	Molar crystal formation rate	$[mol\ s^{-1}]$
$R_{ADS}^G\%$	Percentage of the resistance to adsorption in gas phase	[%]
$R_{EVAP}^G\%$	Percentage of the resistance to evaporation in gas phase	[%]
RH^0	Initial Relative Humidity	$[-]$
S	Surface area	$[m^2]$
T	Temperature	$[K]$
T_C	Critic temperature	$[K]$
T_g	Glass transition temperature	$[K]$
T_R	Reduced temperature	$[-]$
V	Volume	$[m^3]$

W^{ADS}	Adsorbent mass	$[kg]$
$W_{0,1}$	Adsorption parameter in Dubinin-Radushkevich eq.	$[kg]$
$W_{0,2}$	Adsorption parameter in Dubinin-Radushkevich eq.	$[kg]$

Small letters

a	Wagner equation parameter	$[-]$
a_i^0	Apparent hydrodynamic radius of the i-th specie	$[m]$
a_1	Mathlouthi & Génotelle equation parameter	$[-]$
a_2	Mathlouthi & Génotelle equation parameter	$[-]$
a_i	Diagonal coefficients QMOM	$[-]$
b	Wagner equation parameter	$[-]$
b_1	Mathlouthi & Génotelle equation parameter	$[-]$
b_2	Mathlouthi & Génotelle equation parameter	$[-]$
b_i	Codiagonal coefficients QMOM	$[-]$
c	Wagner equation parameter	$[-]$
d	Wagner equation parameter	$[-]$
k	Gordon-Taylor parameter	$[-]$
k_B	Boltzmann constant	$[J\ K^{-1}]$
n^*	Mathlouthi & Génotelle equation parameter	$[-]$
n_i^k	Number of moles of the i-th specie in the k-th phase	$[mol]$
n_{TREh}^S	Solid trehalose dihydrate distribution function	$[\#\ m^{-1}]$
$\bar{q}_W$	Adsorbed water vapor fraction	$[kg_W\ kg_{ADS}^{-1}]$
r	Crystal radius	$[m]$
r^{ADS}	Adsorbent particle radius	$[m]$
r^C	Critical crystal embryo radius	$[m]$
r_i	Abscissas (discrete) QMOM	$[m]$
t	Time	$[s]$
x_i	Molar fraction of the i-th specie	$[-]$
w_i	Weight function (discrete) QMOM	$[-]$

Greek letters

α_l	Coefficients of the continued fraction QMOM	$[-]$
γ_i	Activity coefficient of the i-th specie	$[-]$
γ_{TREh}	Trehalose dihydrate surface energy	$[J\ m^{-2}]$
δ	Dirac delta function	$[-]$
δ^{LEAK}	Leakage length	$[m]$
δ^k	Thickness of the diffusive layer in the k-th phase	$[m]$
ε	Porosity	$[-]$
η	Viscosity	$[Pa\ s]$
η^*	Reference viscosity	$[Pa\ s]$
μ_n	QMOM n-th moment	$[m^n]$
$\boldsymbol{v_i}$	i-th Eigenvector	$[-]$
$v_{i,1}$	First component of the i-th Eigenvector	$[-]$
v_B	Inactive osmotic volume fraction	$[-]$
ρ_{ADS}	Adsorbent mass density	$[kg\ m^{-3}]$
τ	Tortuosity of porous material	$[-]$
$\tilde{v}_i$	Molar volume of the i-th specie	$[m^3\ mol^{-1}]$
Ω	Crystal growth driving force	$[-]$

ω_i	Mass fraction of the i-th specie	$[-]$

Superscripts

ADS	Adsorbent
C	Chamber
CG	Gas phase in Chamber
$CELL$	Cell
G	Gaseous phase
ISO	Isotonic
L	Liquid phase
$LEAK$	Leakage
P	Petri
PG	Gas phase in Petri
S	Solid phase
$SAMPLE$	Sample
$solidus$	Composition of solid trehalose dihydrate
$solubility$	Saturation condition of trehalose-water solution
0	Referred to initial condition
*	Referred to the interface between two phases at equilibrium
→	Referred to the hypothetical equilibrium between two phases

Subscripts

ADS	Adsorption
AIR	Air
g	Glass
$EVAP$	Evaporation
$freezing$	Referred to the freezing curve
$LEAK$	Leakage
OSM	Osmosis
$solubility$	Referred to the solubility curve
TRE	Trehalose
$TREh$	Trehalose Dihydrate
TOT	Total
W	Water

References of the Subchapter 2.4

1. Meryman, H.T., (2007) Cryopreservation of living cells: Principles and practice. *Transfusion*, 47, pp. 935-945. https://doi.org/10.1111/j.1537-2995.2007.01212.x
2. Ferreira, L.M.R., Mostajo-Radji, M.A., (2013). How induced pluripotent stem cells are redefining personalized medicine. *Gene*, 520(1), pp. 1-6. https://doi.org/10.1016/j.gene.2013.02.037
3. Lin, C., Yu, C., Ding, S., (2013) Toward directed reprogramming through exogenous factors. *Curr Opin Genet Dev*, 23, pp. 519-525. https://doi.org/10.1016/j.gde.2013.06.002
4. Shevde, L.A., Riker, A.I., (2009). Current concepts in biobanking: Development and implementation of a tissue repository. *Front Biosci* (Schol Ed) 1, pp. 188-193. https://doi.org/10.2741/s18
5. Fountain, D., Ralston, M., Higins, N., Gorlin, J.B., Uhl, L., Wheeler, C., Antin, J.H., Churchill, W.H., Benjamin, R.J., (1997). Liquid nitrogen freezers: a potential source of microbial contamination o hematopoietic stem cell components. *Transfusion*, 37, pp. 585-591. https://doi.org/10.1046/j.1537-2995.1997.37697335152.x
6. Hand, S.C., Menze, M.A., Toner, M., Boswell, L., Moore, D., (2011). LEA proteins during water stress: Not just for plants anymore. *Annu Rev Physiol*, 73, pp. 115-134. https://doi.org/10.1146/annurev-physiol-012110-142203
7. Crowe J.H., Carpenter J.F., Crowe L.M.,(1998). The role of vitrification in anhydrobiosis, *Annu Rev Physiol*, 60, pp. 73-103. https://doi.org/10.1146/annurev.physiol.60.1.73
8. Green, J. L., Angell, C. A., (1989). Phase Relations and Vitrification in Saccharide-Water Solutions and the Trehalose Anomaly, *J Phys Chem*, 93(8), pp. 2880–2882. https://doi.org/10.1021/j100345a006
9. Roberts C.J., Franks F., (1996). Crystalline and amorphous phases in the binary system water–*β*,*β*-trehalose**,** *J Chem Soc, Faraday Trans*, 92 (8), pp. 1337-1343. https://doi.org/10.1039/FT9969201337
10. Mehl, P.M., (1997). Solubility and glass transition in the system α-*D*-trehalose/water. *J Therm Anal*, 49, pp. 817–822. https://doi.org/10.1007/BF01996765
11. Miller, D.P., de Pablo, J.J., Corti, H., (1997). Thermophysical Properties of Trehalose and Its Concentrated Aqueous Solutions. *Pharm Res*, 14, pp. 578–590. https://doi.org/10.1023/A:1012192725996
12. Aksan, A., Toner, M., (2004). Isothermal Desiccation and Vitrification Kinetics of Trehalose−Dextran Solutions. *Langmuir*, 20(13), pp. 5521-5529. https://doi.org/10.1021/la0355186
13. Aksan, A., Irimia, D., He, X., Toner, M., (2006). Desiccation kinetics of biopreservation solutions in microchannels. *J Appl Phys*, 99(6), ID 2181280. https://doi.org/10.1063/1.2181280
14. He, X., Fowler, A., Menze, M., Hand, S., Toner, M., (2008). Desiccation Kinetics and Biothermodynamics of Glass Forming Trehalose Solutions in Thin Films. *Ann Biomed Eng*, 36, pp. 1428–1439. https://doi.org/10.1007/s10439-008-9518-8
15. Watanabe, K., Imanishi, S., Akiduki, G., Cornette, R., Okuda, T. (2016). Air-dried cells from the anhydrobiotic insect, Polypedilum vanderplanki, can survive long term preservation at room temperature and retain proliferation potential after rehydration, *Cryobiology*, 73, pp. 93-98. https://doi.org/10.1016/j.cryobiol.2016.05.006
16. Kikuta, S., Watanabe, S.J., Sato, R., Gusev, O., Nesmelov, A., Sogame, Y., Cornette, R., Kikawada, T., (2017). Towards water-free biobanks: long-term dry-preservation at room temperature of desiccation-sensitive enzyme luciferase in air-dried insect cells. *Sci Rep*, 7, ID 6540. https://doi.org/10.1038/s41598-017-06945-y
17. Fadda, S., Briesen, H., Cincotti, A., (2011). The effect of EIF dynamics on the cryopreservation process of a size distributed cell population. *Cryobiology*, 62, pp. 218-231. https://doi.org/10.1016/j.cryobiol.2011.03.006
18. Marchisio, D., Fox, R., (2013). *Computational Models for Polydisperse Particulate and Multiphase Systems* (Cambridge Series in Chemical Engineering). Cambridge: Cambridge University Press. https://doi.org/10.1017/CBO9781139016599
19. Radhakrishnam, K., Hindmarsh, A.C., (1993). Description and Use of LSODE, the Livermore Solver for Ordinary Differential Equations. NASA Reference Publication 1327. Lawrence Livermore National Laboratory Report UCRL-ID-113855.
20. Press, W.H., Teukolsky, S.A., Vetterling, W.T., Flannery, B.P., (1996). *Numerical Recipes in Fortran 77: the Art of Scientific Computing*. Second Edition", vol. 1.

21. Casula, E., Asuni, G.P., Sogos, V., Fadda, S., Delogu, F., Cincotti, A., (2017). Osmotic behaviour of human mesenchymal stem cells: Implications for cryopreservation. *PLoS ONE*, 12(9), ID e0184180. https://doi.org/10.1371/journal.pone.0184180
22. Lide D. R. *CRC Handbook of Chemistry and Physics*, 84th Edition (2003-2004).
23. Shirakashi, R., Takano, K., (2018). Recrystallization and Water Absorption Properties of Vitrified Trehalose Near Room Temperature, *Pharm Res* (2018) 35: 139. https://doi.org/10.1007/s11095-018-2420-7
24. Chen T., Fowler, A., Toner, M., (2000). Literature Review: Supplemented Phase Diagram of the Trehalose–Water Binary Mixture, *Cryobiology*, Volume 40, Issue 3, Pages 277-282, ISSN 0011-2240, https://doi.org/10.1006/cryo.2000.2244
25. Gaïda, L.B., Dussap, C.G., Gros, J.B., (2006). Variable hydration of small carbohydrates for predicting equilibrium properties in diluted and concentrated solutions. *Food Chemistry*, 96 (3), 387-401, ISSN 0308-8146, https://doi.org/10.1016/j.foodchem.2005.02.053
26. Poling, B.E., Prausnitz, J.M., O'Connel, J.P., (2001). *The Properties of Gases and Liquids*, 5th Edition. McGraw-Hill: New York. ISBN 0-07-011682-2.
27. Sato, Y., Kawabuchi, S., Irimoto, Y., Miyawaki, O., (2004). Effect of water activity and solvent-ordering on intermolecular interaction of high-methoxyl pectins in various sugar solutions. *Food Hydrocolloids*. 18. 527-534. https://doi.org/10.1016/j.foodhyd.2003.09.001
28. Sato, Y., Miyawaki, O., (2016). Analysis of hydration parameter for sugars determined from viscosity and its relationship with solution parameters, *Food Chemistry*, Volume 190, Pages 594-598, ISSN 0308-8146, https://doi.org/10.1016/j.foodchem.2015.05.119
29. Van Den Bulck, E., (1990). Isotherm correlation for water vapor on regular-density silica gel, *Chemical Engineering Science*, Vol. 45, No. 5, pp. 1425-1429, 1990
30. Nastaj, J., Aleksandrzak, T., (2013). Adsorption Isotherms of Water, Propan-2-ol, and Methylbenzene Vapors on Grade 03 Silica Gel, Sorbonorit 4 Activated Carbon, and HiSiv 3000 Zeolite. *J Chem Eng Data*, 58, 2629−2641. https://doi.org/10.1021/je400517c
31. Longinotti, M.P., Corti, H.R., (2008). Viscosity of concentrated sucrose and trehalose aqueous solutions including the supercooled regime, *J Phys Chem Ref Data*, 37, ID 1503. https://doi.org/10.1063/1.2932114
32. Sharafian, A., Bahrami, M., (2013). Adsorbate uptake and mass diffusivity of working pairs in adsorption cooling systems, *Int J Heat Mass Transfer*, 59, pp. 262–271. https://doi.org/10.1016/j.ijheatmasstransfer.2012.12.019
33. Alsoy, S., Duda, J.L., (1999). Modeling of multicomponent drying of polymer films. *AIChE J*. 45, pp. 896–905. https://doi.org/10.1002/aic.690450420
34. Pesaran, A., Mills, A.F., (1987). Moisture transport in silica gel packed beds—II. Experimental study. *Int J Heat Mass Transfer*, 30(6), pp. 1051-1060. https://doi.org/10.1016/0017-9310(87)90035-4
35. Matyka, M., Khalili, A., Koza, Z., (2008). Tortuosity-porosity relation in porous media flow, *Phys Rev E*, 78, ID 026306. https://doi.org/10.1103/PhysRevE.78.026306

Chapter 3. Mechanical processing of powders by Ball Milling

3.1 Milling dynamics and propagation of mechanically activated self-sustaining reactions

3.1.1 Introduction

Mechanical processing by ball milling (BM) is a powder metallurgy methodology that uses collisions between milling tools to induce physical and chemical changes in granular bodies confined inside a reactor [1,2]. When the milling tools collide, their surfaces trap a small fraction of the powder charge, thus subjecting it to mechanical loading [3,4]. Non-hydrostatic mechanical stresses arise across the network of contacts between the powder particles, giving rise to a disordered network of mechanical forces acting on the level of individual particles [4]. Local particle configurations influence the way local stresses distribute. Thus, individual particles can experience loading conditions differing in nature, rate and intensity. Correspondingly, the loaded material can exhibit different local physical and chemical responses. Frictional heat production, cold-welding, fracturing, plastic deformation, work-hardening processes that take place on the macroscopic scale [1,3,5] can be accompanied, on the microscopic one, by the forced mixing of chemical species and the activation of physical and chemical transformations [6-16].

Although such transformations typically have gradual kinetics, often extending over long processing times [1,2,17-19], highly exothermic systems can undergo self-sustaining high-temperature reactions [1,2,17,20]. These are characterized by a two-stage kinetics, with the initial microstructural refinement promoted by BM suddenly replaced by a chemical transformation able to proceed autonomously without any further input of mechanical energy due the fast liberation of the reaction heat [20]. Ignition marks the discontinuity between the two stages, and makes mechanically activated self-sustaining high-temperature reactions (MSRs) a special case of self-propagating high-temperature synthesis [21-25].

Ignition represents a crucial aspect of MSRs and, thus, significant attention has been paid to its study [20,26-35]. In particular, systematic experimental investigation aimed at measuring the activation time preceding the ignition of the MSR, commonly referred to as the ignition time, which has been shown to depends on several factors including chemical composition, impact energy, amount of reactants and temperature [20,26-35].

In contrast, much less attention has been devoted to the mechanisms governing the MSR propagation inside the mechanochemical reactor under operational conditions. In principle, it is quite reasonable to expect that the dynamics of milling tools and powder particles can affect the degree of chemical conversion and the nature of final products. Nevertheless, the direct experimental investigation of the propagation process raises considerable difficulties due to the rapid motion of the reactor, the violent stirring of the powder charge, the scarcely predictable ignition time and the high rate of chemical conversion. Overall, such factors translate into

fragmentary and contradictory empirical evidence simply suggesting that MRS do not result necessarily in the complete conversion of reactants to products and that the variation of BM conditions can even determine the suppression of MRSs [20,26-35]. Nevertheless, detailed information on the way milling dynamics can affect MSRs is highly desirable in view of a reliable exploitation of MRSs in materials manufacturing contexts.
Based on the considerations above, the present study aims at throwing light on the way MSRs propagate across the powder charge under operational conditions. To this aim, we use numerical simulations to investigate the dynamics of a granular body inside the reactor of a SPEX Mixer/Mill 8000 ball mill in the presence of a single milling ball. The reactor swing gives rise to a granular flow with internal dynamics determined by the milling frequency. Ignition is simply modelled by activating the chemical conversion in a single powder particle and describing the reaction propagation to other particles via a phenomenological set of rules. We show that different propagation modes can exist depending on the milling frequency and the propagation rate.
Details of numerical methods are given in the following.

3.1.2 Numerical methods

Numerical simulations take advantage of the mathematical description of the reactor motion in a SPEX Mixer/Mill 8000. Manufactured by SPEX SamplePrep LLC, the ball mill is equipped with a 230 V - 50 Hz motor that rotates at 1425 rpm and activates an eccentric fulcrum through a pulley system. The fulcrum is rigidly connected with a mechanical arm that has a clamp assembly to secure the reactor at the end. A recall spring moderates the arm swing. The reactor consists of a cylindrical container with inner height and diameter equal to about 5.8 and 3.8 cm respectively. Once the reactor is clamped to the mechanical arm, its geometrical center lies on the axis of the mechanical arm at about 10 cm from the fulcrum axis. The reactor undergoes an angular harmonic displacement on the vertical plane and a synchronous rotation around the axis of the mechanical arm at a frequency. The angular swings on the vertical and on the horizontal planes have amplitude, respectively θ_0 and α_0, equal to 15°. Full details can be found elsewhere [36,37].
An inertial Cartesian reference frame centered on the eccentric fulcrum can be used to describe the trajectory of any point of the reactor [36,37]. The dynamics of balls and powder particle inside the reactor can be conveniently described with reference to a non-inertial Cartesian frame moving with the reactor and with the origin at its center of [36,37]. The inertial and non-inertial Cartesian reference frames are shown in Figure 3.1.1 for illustrative purpose. Since acceleration components along inertial Cartesian axes take values about 20 times larger than gravity, we neglect it. Calculations were performed considering a cylindrical reactor approximately 5.8 cm in height and 1.9 cm in radius. The reactor contained 5000 spherical particles with mass of 0.7 mg and diameter of 0.3 mm. Stainless steels jar and balls were used. A single milling ball with mass and diameter equal to 8 g and 1.24 cm respectively was considered. Powder particles and milling ball occupy, approximatively, the 0.11% and 1.52% of the reactor volume respectively. The ball-to-powder mass ratio is equal to about 2.28. This value is well within the range of ball-to-powder mass ratios typically utilized in milling experiments, which can usually be as small as 0.5 and as large as 24 [1,2,17].

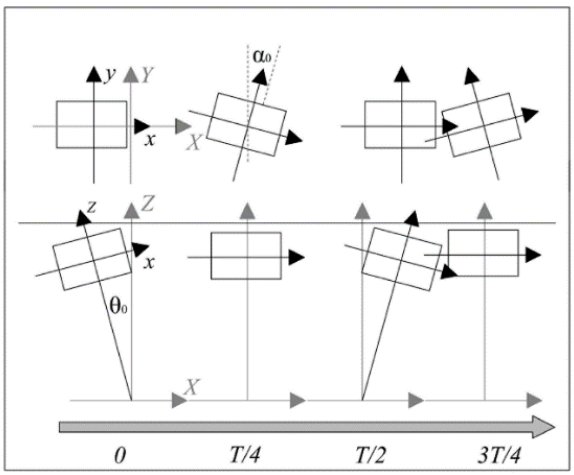

Figure 3.1.1: Inertial and non-inertial Cartesian reference frames used to describe the reactor swing and the dynamics of ball and powder particles inside the reactor.

In the absence of contacts with each other or with the reactor wall and bases, ball and powder particles undergo uniform rectilinear motion. Contacts between balls, powder particles and reactor walls are described using the discrete element method [38,39]. Accordingly, the effects of normal and tangential forces on the colliding bodies are evaluated using a combination of springs and dashpots [38,39]. Since accurate calculations indicate that tangential forces typically are much smaller than normal ones, in this study they have been neglected. Normal forces are expressed as

$$N = -\kappa\, \varepsilon - \gamma\, \frac{d\varepsilon}{dt}. \qquad (1)$$

This equation describes the force of a damped harmonic oscillator with repulsion and dissipation terms that allow modelling partially elastic collisions. Thus, κ is the Hooke's constant, γ is a damping coefficient, ε is the deformation undergone by the colliding surfaces and t is time [38,39]. Force parameters are 4.14×10^{6} kg s^{-2} and 5.5452×10^{1} kg s^{-1} for collisions with the reactor wall, and 3.622×10^{2} kg s^{-2} and 4.85×10^{-3} kg s^{-1} for collisions among particles and milling ball. Equations of motion were integrated using the Verlet algorithm with a time step of 5 μs [39,40]. The milling frequency, ν, was varied in the interval between 11.6 and 21.6 Hz.

For convenience, the initial configuration of powder particles and ball consisted of an ordered array not in contact with reactor wall and bases. Order is lost very quickly once ball and powder particles collide with each other and with the reactor wall and bases. Ball and powder particle dynamics has fully relaxed after two complete reactor swings and the resulting disordered dynamics is no longer affected by initial conditions.

Once the dynamics has suitably relaxed, a powder particle randomly selected among those compressed by the ball against one of the reactor bases during an impact is ignited. Accordingly, its conversion degree the reaction in individual particles is given a phenomenological description using the Johnson-Mehl-Avrami kinetics [39]. Accordingly, the conversion degree is related to time by the expression

$$\alpha = 1 - exp(-k\, t^{n}) \qquad (2)$$

where k is the rate constant, t is time and n the Avrami exponent. Based on available literature [41], n was given the value of 1.649.

Reaction propagation from a given particle to a neighboring one is modelled by two simple phenomenological rules that must be satisfied simultaneously. First, a non-reacting particle can be ignited by a reacting one if it is distant from the latter less than a selected distance, d_{ig}. Second, a reacting particle can ignite a non-reacting particle only if its conversion degree α is between two suitably chosen set values α_{min} and α_{max}. For convenience, α_{max} was set equal to $1 - \alpha_{min}$.

These rules undeniably provide only an oversimplified description of the reaction propagation. At the same time, however, they make the simulation of the ignition and propagation processes affordable. In this regard, it is worth noting that a rigorous description of the mechanically activated ignition, and of the subsequent propagation, is not only out of the scope of the present work, but, presently, also out of reach of routine scientific computation. The physics and chemistry involved render the problem highly complex. On the one hand, simulations have to properly describe the mechanics of impacts and the associated dissipation of mechanical energy of ball and powder particles. On the other, they have to account for the thermodynamics and kinetics of a rapid chemical transformation taking place out of equilibrium in an ever-changing environment. The chemical transformation involves individual particles, which are also the primary heat sources due to the liberation of the latent heat of reaction. Any given particle is a world of its own that exchanges heat with a turbulent gaseous atmosphere and, during impacts, with other particles by direct contact. It is not easy to combine the discrete dynamics of individual particles with the continuum of atmosphere while describing the underlying heat transfer processes. However, it is not difficult to identify the most important factors determining the ignition and the propagation of the chemical reaction. First, the higher the chemical transformation rate, the higher the rate of temperature increase in individual particles, which results in a more efficient heat transfer. Second, the shorter the distance between two particles, the more intense and the easier the heat exchange between them.

It is precisely from these two considerations that the phenomenological rules used in simulations derive. The choice of a minimum distance to allow ignition reminds to the description of an effective heat transport inside a granular flow. The choice of a conversion degree interval relates to the description of the heat generation rate. This latter typically involves a maximum, being limited by a low temperature initially and by the progressive depletion of reactants subsequently. Using these two criteria allows avoiding the rigorous approach based on the combination of heat generation rate inside each particle with the thermal conduction and radiation between particles, reactor walls, and milling ball. Simultaneously, it allows capturing the fundamental features of the heat transfer processes, making simulations feasible.

Simulations were performed varying the frequency of the reactor swing, ν, the reaction constant k, the ignition distance, d_{ig}, and the lower threshold of conversion degree, α_{min}. Parameter values were combined as summarized in Table 3.1.1 to explore the effect of BM conditions on the reaction propagation.

In particular, the reactor swing frequency ν was varied between 11.6 and 21.6 Hz, the rate constant k between 6.845×10^{-2} and 6.845×10^{2} s^{-1}, and the ignition distance d_{ig} between 7×10^{-5} and 7×10^{-4} m. Similarly, α_{min} was varied between 0.05 and 0.30.

Table 3.1.1: Parameter values utilized to carry out numerical simulations. Data refer to variable parameters, namely the frequency ν (Hz) of the reactor swing, the rate constant k (s-1) of the Johnson-Mehl-Avrami kinetic law, the ignition distance d_{ig} (m) and the lower ignition threshold of conversion degree α_{min}.

Simulation run	ν	k	d_{ig}	α_{min}
1	14.6	6.845×10^{2}	7×10^{-4}	0.3
2	21.6	6.845×10^{2}	7×10^{-4}	0.3
3	21.6	6.845×10^{2}	7×10^{-5}	0.3
4	14.6	6.845×10^{2}	7×10^{-5}	0.3
5	14.6	6.845×10^{1}	7×10^{-4}	0.3
6	14.6	6.845×10^{1}	7×10^{-5}	0.3
7	21.6	6.845×10^{1}	7×10^{-4}	0.3
8	21.6	6.845×10^{1}	7×10^{-5}	0.3
9	14.6	6.845×10^{0}	7×10^{-4}	0.3
10	14.6	6.845×10^{0}	7×10^{-5}	0.3
11	21.6	6.845×10^{0}	7×10^{-4}	0.3
12	21.6	6.845×10^{0}	7×10^{-5}	0.3
13	14.6	6.845×10^{-1}	7×10^{-5}	0.3
14	14.6	6.845×10^{-2}	7×10^{-5}	0.3
15	14.6	6.845×10^{-2}	7×10^{-5}	0.05
16	11.6	6.845×10^{2}	7×10^{-4}	0.3

3.1.3 Results and discussion

The initial configuration used to start simulations has been suitably chosen to make relaxation as faster as possible. The positions of ball and powder particles inside the reactor are shown in Figure 3.1.2a.

The reactor is at the inversion point of its swing. While ball and powder particles are at rest, the reactor base accelerates toward ball and powder particles. The first contacts between the reactor base and cylindrical wall, on the one hand, and the ball and powder particles, on the other, trigger the disordered dynamics of the granular system. This is entirely involved within a quarter of the reactor swing period. Information about starting conditions is lost within two cycles of the reactor swing, almost independent of the milling frequency. Once relaxed, the system reaches a steady state dynamics characterized by the displacement of ball and powder particles between the opposite reactor bases. The simple visualization of the system evolution in time allows capturing the crucial features of granular flow (see Supplementary Information – video_propagation.avi). A suitably chosen system configuration is shown in Figure 3.1.2b for illustrative purposes. It can be seen that

powder particles do not scatter throughout all the available reactor volume, but rather occupy a relatively small portion of it. The continuous energy exchange within the granular flow and between powder particles and milling tools make the dynamics strongly dissipative. Accordingly, it never results in particle configurations spreading across the entire reactor volume. Although individual powder particles undergo an intrinsically disordered dynamics, the granular body keeps quite compact in its whole. Accelerations due to the synchronous reactor rotations and oscillations tend to push the powder particles against the reactor walls. At any time, only a few powder particles can be found moving freely across the reactor volume along trajectories diverging from the mass of the granular body, mostly caused by energetic rebounds within the granular flow. The vast majority of powder particles simply remain in contact with the reactor walls or quite close to them.

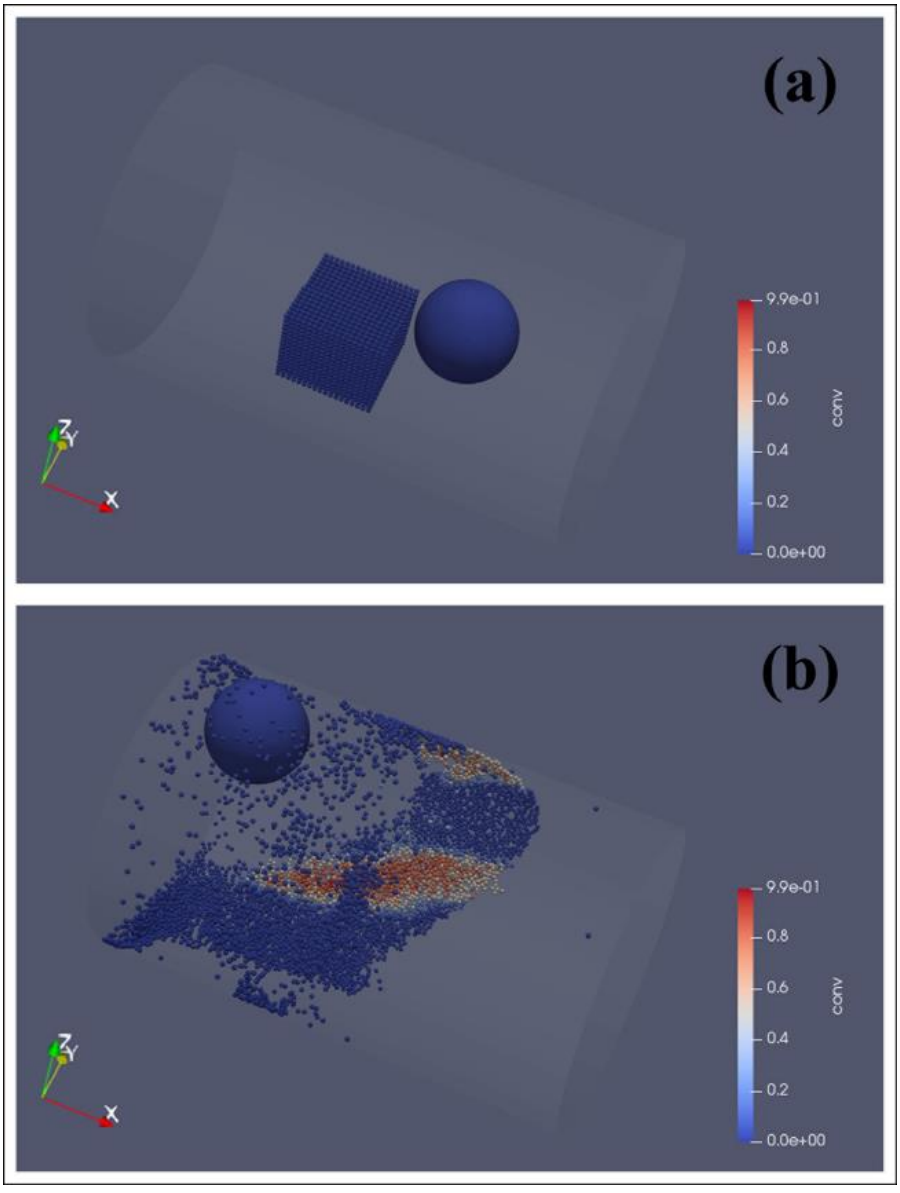

Figure 3.1.2: (a) Initial and (b) relaxed configurations of ball and powder particles. Data refer to the case of a reactor swung at 14.6 Hz. Inside the reactor, a MSR is propagating. The color of individual powder particles measures the degree of chemical conversion (blue – low conversion degrees; red – high conversion degrees).

Consequent to the dissipative dynamics experienced by the powder particles, the granular flow couples its dynamics with the reactor movement. Accordingly, the displacement of the granular body in its whole between the opposite reactor bases is definitely periodic. This clearly emerges from the numerical analysis of the granular flow with reference to the non-inertial Cartesian frame, which has the *x* axis coincident with the main axis of the cylindrical reactor. The quantity that allows a suitable insight into the dynamics of individual powder particles is their *x* coordinate. Its variation in time provides a reliable description of the main displacements undergone by each particle. In turn, the statistical distribution of the *x* coordinate of powder particles gives a relatively clear idea of the movement undergone by the granular body.

The statistical distributions of the *x* coordinate obtained at different points along the reactor cycle are shown in Figure 3.1.3.

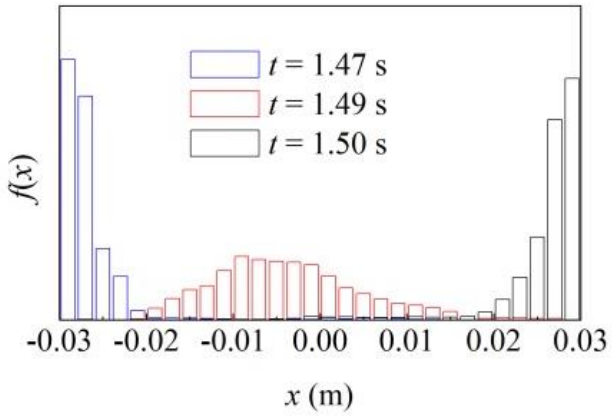

Figure 3.1.3: Distributions $\boldsymbol{f(x)}$ of the *x* coordinates of powder particles. Data refer to three different times during a simulation run investigating the ball and powder particle dynamics inside a reactor swung at 14.6 Hz. The bin size is equal to 0.002 m.

Distribution curves are quite different from each other and suggest the occurrence of contractions and expansions of the granular body in response to the mechanical forces acting during the reactor cycle. At the lowest time considered, the reactor has just passed the point of maximum velocity in the inertial Cartesian frame. As it decelerates, powder particles start detaching from the reactor base and begin traveling across the reactor from one base to the other. Correspondingly, the granular body undergoes the first expansion stages along the main axis of the cylindrical reactor. While powder particles move towards the opposite base, mostly close to the cylindrical wall, the reactor keeps decelerating. At the intermediate time considered, the reactor is between the point of maximum velocity and the inversion point of its motion. The granular body has fully expanded under the effect of accelerations due to oscillations and rotations and the corresponding distribution curve of x coordinate appears quite broad. Shortly after the reactor has started moving in the opposite direction, the first powder particles come into contact with the reactor base and the granular body progressively undergoes a contraction. Reactor and granular body have opposite movement and the powder particles regroup on the reactor base. A new expansion stage of the granular body takes place when the reactor reaches the point of maximum velocity. The cycle is repeated and the granular flow exhibits periodicity synchronous to the reactor swing.

The ball has a disordering effect on the dissipative dynamics of the granular body. Due to its significantly larger mass and size, it easily pushes away any powder particle that comes into contact with it. Therefore, at least on the average, contacts between ball and granular body result in the scattering of powder particles along different directions. Vice versa, powder particles have an ordering effect on the ball dynamics. At any given close approach between ball and reactor wall and bases, a certain number of powder particles are trapped. Compressed between the surfaces of ball and reactor, they absorb part of the mechanical energy of the impact, thus softening the collision elasticity. A certain amount of the ball energy at impact is dissipated in the deformation work of powder particles and another amount is spent in the scattering of powder particles away from the impact point. It follows that the ball undergoes partially elastic impacts that can be approximately described by a restitution coefficient of about 0.5. On the average, the ball undergoes two main impacts with the reactor bases per cycle of the reactor swing. Therefore, ball impact frequency is twice the frequency of the reactor swing, in agreement with previous studies [36,37].

Since the compression of powder particles and the consequent deformation processes are accompanied by local temperature rises [1,2,17,20], the MSR was initiated during impacts. In particular, one of the powder particles undergoing compression was randomly selected and its chemical conversion was allowed to change, from that moment, according to Eq. 2.

Once ignited, the reaction proceeds in individual particles at a rate determined by the selected Johnson-Mehl-Avrami kinetics. For sake of illustration, let us consider three powder particles close to each other in the initial ordered configuration. These powder particles ignite at different times during the simulation run with the first parameters listed in Table 3.1.1. Their degrees of chemical conversion, α, are shown in Figure 3.1.4a as a function of time, t.

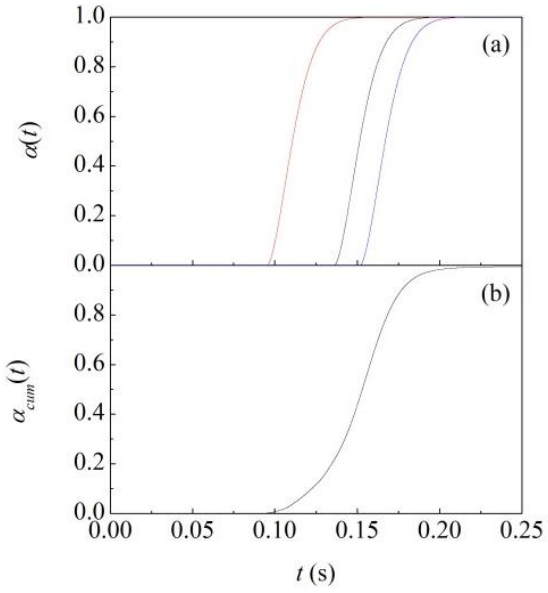

Figure 3.1.4: (a) The degree of chemical conversion, $\alpha(t)$, for three particles that are nearest neighbours in the initial configuration and (b) the cumulative degree of chemical conversion, $\alpha_{cum}(t)$, as a function of time, t. Data refer to the first simulation described in Table 3.1.1.

First, it can be seen that the reaction takes place on a time scale comparable with the period of the reactor swing, reaching completion in about 6×10^{-2} s. Second, although the powder particles were initially nearest neighbors, their ignition times are different. This is a clear result of the effective disordering dynamics governing ball and granular body inside the moving reactor.

Whereas the reaction rate in individual particles is determined exclusively by the Johnson-Mehl-Avrami kinetics and is, thus, independent of external factors, reaction propagation from one particle to the other can be expected to depend on the dynamics of the granular body. In this regard, it is useful to refer to the cumulative chemical conversion degree

$$\alpha_{cum}(t) = \frac{1}{N_p} \sum_{i=1}^{N_{ig}(t)} \alpha_i(t) \tag{3}$$

which represents the overall conversion degree averaged over the total number of powder particles, N_p. In particular, the cumulative conversion degree $\alpha_{cum}(t)$ at time t is obtained by summing the conversion degrees $\alpha_i(t)$ at time t of every reacting particle. Of course, the number of reacting particles, $N_{ig}(t)$, varies with time t. It follows that $\alpha_{cum}(t)$ equals 1 only when all of the N_p powder particles forming the granular body have reacted completely.

The cumulative conversion degree $\alpha_{cum}(t)$ for the simulation run with the first parameters listed in Table 3.1.1 is shown in Figure 3.1.4b as a function of time t. The curve exhibits sigmoidal shape. Although apparently smooth, it presents several slope variations that appear as small irregularities and shoulders. This clearly suggests that the reaction does not propagate steadily across the granular body. Rather, we can expect that it is affected by the granular flow dynamics.

The irregular progress of the MSR can be suitably pointed out taking into due account the ignition time, t_{ig}, of individual powder particles. Ignition times, indeed, reveal when individual particles get involved in the reaction. The cumulative distribution of t_{ig} over the entire set of powder particles are shown in Figure 3.1.5.

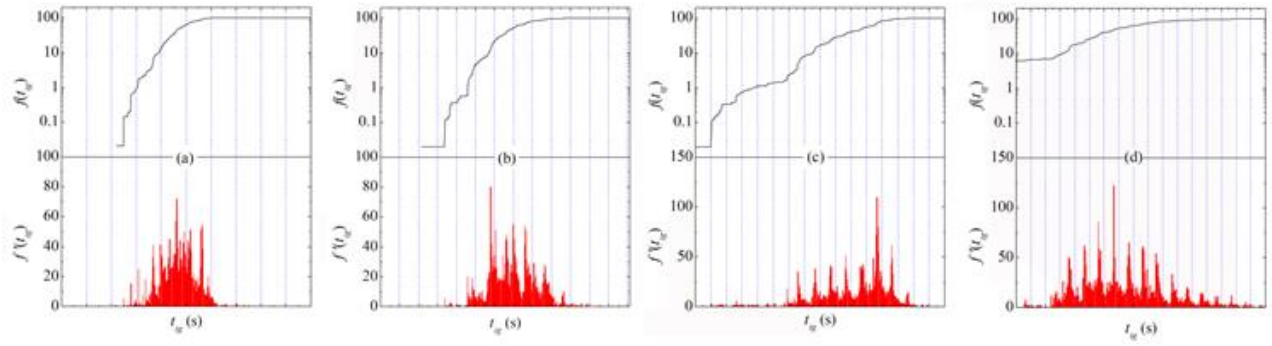

Figure 3.1.5: Cumulative distributions of ignition times (upper panel) and their first derivative (lower panel) over the whole set of powder particles for the fourth (a), sixth (b), tenth (c) and thirteenth (d) simulations described in Table 3.1.1. Vertical dashed lines correspond to the inversion points of the reactor swing. The bin size varies from 3.5×10^{-4} to 1.4×10^{-3} s.

Their first derivatives are also shown to highlight irregularities. Data refer to four representative case studies that differ from each other for the value of the rate constant k of the Johnson-Mehl-Avrami reaction kinetics. Specifically, we reduced the k value from 6.845×10^{2} to 6.845×10^{-1} s^{-1}, the other parameters being the same. According to general expectations, reaction propagation undergoes a corresponding deceleration. In all the cases, cumulative distributions clearly reveal irregular propagation processes characterized by sudden rises in the number of reacting particles followed by shoulders and even plateaus extending over time intervals of variable length. The first derivative of cumulative distributions shows that the number of reacting particles changes discontinuously. In particular, data show that a significant number of new particles are ignited in correspondence of the inversion points of the reactor swing, marked by the vertical dotted lines in Figure 3.1.5, or close to them. Accordingly, we can readily infer that ignition of individual particles takes place in bursts, mostly related to the contractions that the granular body undergoes periodically as a result of the reactor swing. It is during contraction stages that powder particles come into closer contact, thus fulfilling the ignition condition governed by ignition distance d_{ig}. The comparison between plots in Figure 3.1.5 indicates that the smaller the rate constant k, the more evident the above-mentioned behavior. The first derivative of the cumulative distribution of ignition times for the simulation run with the smaller k value exhibits distinct peaks of propagation in correspondence of the contractions of granular flow caused by the impingement of powder particles on the reactor base. Further reduction of the k value can be expected to make the effect even more evident on longer simulation times.

The variation of simulation parameters affects reaction propagation and, then, cumulative conversion degree $\alpha_{cum}(t)$ as shown in Figure 3.1.6.

Most evident effects stem from the variation of the rate constant k accounting for the reaction rate in individual powder particles. Data in Figure 3.1.6a show that reaction propagation significantly accelerates as k increases. This can be ascribed to the rapid attainment in reacting powder particles of conversion degrees higher than the minimum threshold α_{min} required to activate the reaction in non-reacting powder particles distant less than d_{ig}. Once that a certain number of powder particles start reacting, reaction propagation to non-reacting particles during contractions of the granular body can be very fast. In most favorable cases, even a single contraction can be sufficient to obtain complete conversion within a single reactor swing.

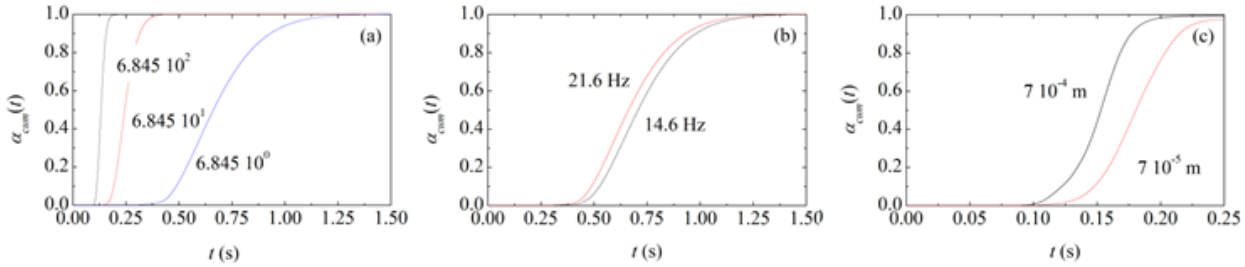

Figure 3.1.6: The cumulative degree of chemical conversion, $\boldsymbol{\alpha_{cum}(t)}$, as a function of time, $\boldsymbol{t}$, obtained from simulation runs with different values of (a) rate constant of the Johnson-Mehl-Avrami kinetics, (b) frequency of the reactor swing and (c) ignition distance. Parameter values are shown.

The frequency of the reactor swing, ν, and the ignition distance, d_{ig}, are much less influential than than the minimum threshold for individual particle ignition, α_{min}. It can be seen from Figures 3.1.6b and 3.1.6c that reaction propagation accelerates only slightly as ν and d_{ig} increase. In the former case, acceleration is ascribable to the direct relationship existing between the frequency of the reactor swing and the frequency of contractions in the granular flow. Contractions favor the reaction propagation across the granular body as a consequence of the reduced distances between loose powder particles. Thus, any ν increase determines a corresponding increase of the reaction propagation once a sufficient number of particles have conversion degree higher than α_{min}. Similarly, an increase of the minimum distance required for a reacting particle to activate the reaction in a neighbouring, non-reacting particle favours reaction propagation. In particular, the longer d_{ig}, the higher the probability of propagating the MSR in the granular body when its contraction is not maximum.

3.1.4 Conclusions

Numerical findings indicate that the propagation of MSRs in a SPEX Mixer/Mill 8000 ball mill depends on factors related to the reactor swing and to the intrinsic reaction rate in individual powder particles. The numerical model takes advantage of the accurate description of the ball and powder particle dynamics inside the moving reactor, based, in turn, on a reliable reconstruction of contact dynamics. Numerical simulations clearly show that powder particles form a granular body governed by a strongly dissipative dynamics. The fast energy redistribution among powder particles allows the granular flow to exhibit a periodic behavior. Despite the disordered trajectories of individual powder particles, the granular body undergoes quite regular displacements between the two opposite reactor bases. Overall, the granular flow is characterized by alternating contraction and expansion stages. Contractions take place when the granular body moving in a certain direction impacts on the reactor base moving in the opposite direction, whereas expansion starts when the reactor has reached the point of maximum velocity. Two contraction and two expansion stages occur per cycle of the reactor swing.

The granular flow is disordered by the ball. Much bigger than powder particles, the ball is able to push them away. Accordingly, the powder particles are scattered across the reactor volume. Every time the ball impacts on the reactor wall or bases, it compresses a relatively small number of powder particles. This results in a significant dissipation of the ball mechanical energy during the impact, which allows the establishment of a partially inelastic impact regime. As a consequence, the ball undergoes two main impacts per cycle of the reactor swing within the whole range of reactor swing frequency explored. Thus, the results obtained satisfactorily agree with experimental and numerical evidence from previous studies.

We have used the numerical reconstruction of ball and powder particles trajectories to investigate the relationship between the granular flow dynamics and the propagation of MSRs inside a moving reactor. To this aim, we have chosen to describe the reaction of a single powder particle according to a Johnson-Mehl-Avrami kinetics. Although phenomenological, this description is sufficient to enable the evaluation of factors

potentially affecting the MSR propagation. Reaction was first ignited in a single particle randomly chosen among those compressed by the ball during an impact with the reactor base. We observe that the propagation strongly depends on the rate constant of the phenomenological kinetic law. In particular, propagation is favored by large values of the rate constant. Less influential factors are the distance at which a reacting particle can ignite the MSR in a non-reacting particle and the frequency of the reactor swing. In any case, numerical findings clearly show that the MSR proceeds via an irregular, discontinuous propagation process. Specifically, bursts in the reaction ignition in individual powder particles occur approximately in correspondence of the contractions undergone by the granular flow as a result of the intrinsic dynamics of the granular body.

Our results allow deeper insight into the dynamics governing the motion of ball and powder particles inside a moving reactor of the SPEX Mixer/Mill 8000 and helps clarifying the conditions under which MSRs propagate. Further work is needed to perform a systematic exploration of the parameter space.

References of the Subchapter 3.1

1. Sopicka-Lizer, M., editor. (2010). *High-Energy Ball Milling. Mechanochemical Processing of Nanopowders*, Cambridge (UK), Woodhead Publishing. ISBN-10: 1845695313
2. Delogu, F., Mulas G., editors. (2010). *Experimental and Theoretical Studies in Modern Mechanochemistry*. Kerala (India), Transworld Research Network, 2. ISBN-10 : 8178954540
3. Courtney, T.H., (1995). Process Modeling of Mechanical Alloying, *Mater. Trans. JIM*, 36, pp. 110–122. https://doi.org/10.2320/matertrans1989.36.110
4. Delogu, F., (2012). Are processing conditions similar in ball milling and high-pressure torsion? The case of the tetragonal-to-monoclinic phase transition in ZrO2 powders. *Scr Mater*, 67, pp. 340–343. https://doi.org/10.1016/j.scriptamat.2012.05.031
5. Maurice, D.R, Courtney, T.H., (1990). The physics of mechanical alloying: A first report. *Metall Trans A*, 21, pp. 289–303. https://doi.org/10.1007/BF02782409
6. Fu, X.Y., Falk, M.L., Rigney, D.A., (2001). Sliding behavior of metallic glass: Part II. Computer simulations, *Wear*, 250, pp. 420–430. https://doi.org/10.1016/S0043-1648(01)00607-X
7. Kadau, K., Germann, T.C., Lomdahl, P.S., Holian, B.L., (2002). Microscopic View of Structural Phase Transitions Induced by Shock Waves, *Science*, 296, pp. 1681–1684. https://doi.org/10.1126/science.1070375
8. Lund, A.C., Schuh, C.A., (2003). Atomistic simulation of strain-induced amorphization. *Appl Phys Lett*, 82, pp. 2017–2019. https://doi.org/10.1063/1.1563831
9. Odunuga, S., Li, Y., Krasnochtchekov, P., Bellon, P., Averback, R.S., (2005). Forced chemical mixing in alloys driven by plastic deformation, *Phys Rev Lett*, 95, pp. 93–96. https://doi.org/10.1103/PhysRevLett.95.045901
10. Delogu, F., Cocco, G., (2006). Numerical simulations of atomic-scale disordering processes at impact between two rough crystalline surfaces, *Phys Rev B*, 74, ID 35406. https://doi.org/10.1103/PhysRevB.74.035406
11. Delogu, F., (2008). Forced chemical mixing in model immiscible systems under plastic deformation, *J Appl Phys*, 104, ID 073533. https://doi.org/10.1063/1.2987476
12. Song, J., Srolovitz, D.J., (2008). Mechanism for material transfer in asperity contact, *J Appl Phys*, 104, ID 124312. https://doi.org/10.1063/1.3043582
13. Vo, N.Q., Odunga, S., Bellon, P., Averback, R.S., (2009). Forced chemical mixing in immiscible alloys during severe plastic deformation at elevated temperatures, *Acta Mater*, 57, pp. 3012–3019. https://doi.org/10.1016/j.actamat.2009.03.007
14. Delogu, F., (2010). Molecular dynamics of collisions between rough surfaces, *Phys Rev B – Condens Matter Mater Phys*, 82, pp. 1–9. https://doi.org/10.1103/PhysRevB.82.205415
15. Ashkenazy, Y., Vo, N.Q., Schwen, D., Averback, R.S., Bellon, P., (2012). Shear induced chemical mixing in heterogeneous systems, *Acta Mater*, 60, pp. 984–993. https://doi.org/10.1016/j.actamat.2011.11.014
16. Delogu, F., (2012). A possible alloying mechanism in idealized collisions between Cu and Sn crystals, *Chem Phys Lett*, 521, pp. 125–129. https://doi.org/10.1016/j.cplett.2011.11.071
17. Suryanarayana, C., (2001). Mechanical alloying and milling, *Prog Mater Sci*, 46, pp. 1–184. https://doi.org/10.1016/S0079-6425(99)00010-9
18. Delogu, F., (2008). A combined experimental and numerical approach to the kinetics of mechanically induced phase transformations, *Acta Mater*, 56, pp. 905–9012. https://doi.org/10.1016/j.actamat.2007.10.041
19. Benjamin, J.S., (1992). Fundamentals of Mechanical Alloying, *Mater Sci Forum*, 88–90, pp. 1–18. https://doi.org/10.4028/www.scientific.net/MSF.88-90.1
20. Takacs, L., (2002). Self-sustaining reactions induced by ball milling, *Prog Mater Sci*, 47, pp. 355–414. https://doi.org/10.1016/S0079-6425(01)00002-0
21. Merzhanov, A.G., Borovinskaya, I.P., (1974). A New Class of Combustion Processes, *Combust Sci Technol*, 10, pp. 195–201. https://doi.org/10.1080/00102207508946671
22. Munir, Z.A., Anselmi-Tamburini, U., (1989). Self-propagating exothermic reactions: The synthesis of high-temperature materials by combustion, *Mater Sci Reports*, 3, pp. 277–365. https://doi.org/10.1016/0920-2307(89)90001-7

23. Munir, Z.A., Holt, J.B., (1990). *Combustion and plasma synthesis of high-temperature materials*, Berlin, VCH Publisher. ISBN-10 : 3527278478
24. Moore, J.J., Feng, H.J., (1995). Combustion synthesis of advanced materials: Part I. Reaction parameters, *Prog Mater Sci*, 39, pp. 243–273. https://doi.org/10.1016/0079-6425(94)00011-5
25. Moore, J.J., Feng, H.J., (1995). Combustion synthesis of advanced materials: Part II. Classification, applications, and modelling, *Prog Mater Sci*, 39, pp. 275–316. https://doi.org/10.1016/0079-6425(94)00012-3
26. Tschakarov, C.G., Gospodinov, G.G., Bontschev, Z., (1982). Über den Mechanismus der mechanochemischen Synthese anorganischer Verbindungen, *J Solid State Chem*, 41, pp. 244–252. https://doi.org/10.1016/0022-4596(82)90142-6
27. Rusanov, V., Chakurov, C., (1989). On the development mechanism and kinetics of the explosive mechanochemical synthesis, *J Solid State Chem*, 79, pp. 181–188. https://doi.org/10.1016/0022-4596(89)90264-8
28. Schaffer, G.B., McCormick, P.G., (1991). Anomalous combustion effects during mechanical alloying, *Metall Trans A*, 22, pp. 3019-3024.
29. Schaffer, G.B., Forrester, J.S., (1997). The influence of collision energy and strain accumulation on the kinetics of mechanical alloying, *J Mater Sci*, 32, pp. 3157–3162. https://doi.org/10.1023/A:1018646616814
30. Takacs, L., Susol, M.A., (1996). Combustive mechanochemical reactions in off-stoichiometric powder mixtures, *Mater Sci Forum*, 225–227, pp. 559–562. https://doi.org/10.4028/www.scientific.net/MSF.225-227.559
31. Takacs, L., (1998). Combustion Phenomena Induced by Ball Milling, *Mater Sci Forum*, 269–272, pp. 513–522. https://doi.org/10.4028/www.scientific.net/MSF.269-272.513
32. Charlot, F., Gaffet, E., Zeghmati, B., Bernard, F., Niepce, J.C., (1999). Mechanically activated synthesis studied by X-ray diffraction in the Fe–Al system, *Mater Sci Eng A*, 262, pp. 279–288. https://doi.org/10.1016/S0921-5093(98)01017-X
33. Gras, C., Gaffet, E., Bernard, F., Niepce, J.C., (1999). Enhancement of self-sustaining reaction by mechanical activation: case of an Fe-Si system, *Mater Sci Eng A*, 264, pp. 94–107. https://doi.org/10.1016/S0921-5093(98)01108-3
34. Deidda, C., Delogu, F., Maglia, F., Anselmi-Tamburini, U., Cocco, G., (2004). Mechanical processing and self-sustaining high-temperature synthesis of TiC powders, *Mater Sci Eng A*, 375–377, pp. 800–803. https://doi.org/10.1016/j.msea.2003.10.025
35. Deidda, C., Delogu, F., Cocco, G., (2004). Changes in the Ta50C50 mechanochemical reactivity under different milling conditions, *J Metastable Nanocryst Mater*, 20-21, pp. 337–342.
36. Caravati, C., Delogu, F., Cocco, G., Rustici, M., (1999). Hyperchaotic qualities of the ball motion in a ball milling device, *Chaos*, 9, pp. 219–226. https://doi.org/10.1063/1.166393
37. Manai, G., Delogu, F., Rustici, M., (2002). Onset of chaotic dynamics in a ball mill: Attractors merging and crisis induced intermittency, *Chaos*, 12, pp. 601–609. https://doi.org/10.1063/1.1484016
38. Shäfer, J., Dippel, S., Wolf, D.E., (1996). Force Schemes in Simulations of Granular Materials, *J Phys I*, 6, pp. 5–20. https://doi.org/10.1051/jp1:1996129
39. Manai, G., Delogu, F., Schiffini, L., Cocco, G., (2004). Mechanically induced self-propagating combustions: Experimental findings and numerical simulation results, *J Mater Sci*, 39, pp. 5319–5324. https://doi.org/10.1023/B:JMSC.0000039237.93724.e9
40. Allen, M.P., Tildesley, D., (1987). *Computer Simulations of Liquids*, Oxford, Clarendon.
41. He, C., Stangle, G.C., (1998). A micromechanistic model of the combustion synthesis process: Mechanism of ignition, *J Mater Res*, 13, pp. 146–155. https://doi.org/10.1557/JMR.1998.0020

3.2 A mapping approach to pattern formation in the early stages of mechanical alloying

3.2.1 Introduction

Mixing processes lie at the basis of all the different forms of mechanochemistry. Widely recognized since long time as crucial for fabrication of alloys and composites by mechanical alloying (MA) [1], they are currently invoked to explain solventless organic synthesis by ball milling (BM) [2]. In both cases, powder blending via advective mixing in the reactor volume, plastic co-deformation of particles at individual impacts and forced chemical mixing at sheared interfaces combine into a far-from-equilibrium processing with unique effectiveness in inducing chemical reactions [3,4]. Yet, we still have an unsatisfactory understanding of the way mixing processes take place on the different scales and no mechanistic interpretation explicitly accounting for their occurrence during BM [1].

In this work, we propose a novel approach to the problem based on the combination of a kinetic model accounting for the discrete statistical nature of BM with an iterative description of microstructural evolution at individual impacts. While the model evaluates the relative amounts of powder subjected to a given number of plastic deformation events [4], a smooth, invertible mathematical transformation is used to reconstruct the configuration resulting from the material flow caused by plastic deformation in powder trapped at impacts. Aimed at showing the potential of the approach in the quantitative interpretation of experimental evidence, we apply it to the case of the lamellar structure formed during the early stages of MA of two ductile metals such as Ag and Cu. Specifically, we focus on the gradual refinement of the lamellar structure in composite Ag-Cu particles subjected to repeated co-deformation and describe the progressive interlamellar spacing reduction.

3.2.2 Methodologies

Experiments have been performed using commercial Ag and Cu powders with 99.99% purity. Powders were sieved to select particle size between 5 and 15 μm and used to prepare equiatomic Ag-Cu mixtures. Batches of 8 g were sealed under Ar atmosphere in a hardened steel reactor with a stainless-steel ball with mass and diameter equal to 12 g and 1.44 cm respectively and subjected to BM using a SPEX Mixer/Mill 8000 working at about 14.6 Hz. At selected time intervals, the reactor was emptied and refilled with a new batch.

Particle microstructure was investigated by scanning electron microscopy (SEM) in back-scattering mode using a Zeiss EVO LS15 SEM microscope. Observations were performed on samples prepared by embedding powders in epoxy resin and polishing with fine abrasives. Interlamellar spacing in composite particles was estimated by image analysis. At least 20 samples per case were analyzed.

Powder charge allows inelastic impact conditions characterized by an average collision frequency of about 29.2 Hz [5]. Since microstructure evolves under the effect of impacts, and not time, SEM observations were referred to the number of impacts.

Deterministic mapping was used to reproduce the stretching and folding processes that underlie MA. We selected a simple mapping procedure commonly utilized in the study of chaos and chaotic dynamics and proposed in previous work [6]. The non-linear shear transformation (NLST) consists of the unit operation described by the equations

$$x_{n+1} = x_n + 4\left(y_n - \frac{1}{2}\right)^2 \quad (1)$$

$$y_{n+1} = (x_{n+1} - 1)^2 + y_n \quad (2)$$

The mapping applies to a square $(x; y)$ domain with constant area and *x* and *y* coordinates between 0 and 1. The domain is described by a square matrix with 4096^2 elements and comprises two equal subdomains representing different chemical species. The NLST causes the deformation of the initial configuration according to advective relocations. These mimic the deformation processes that result in the formation of convoluted lamellar structures due to impacts. The interlamellar spacing was estimated using the same image analysis used for SEM micrographs.

Mapping was related to individual impacts via a kinetic model that takes into account the statistical nature of BM. Discussed in detail elsewhere [4], the model assumes that powders are randomly involved in individual impacts and that mechanical stresses give rise to critical loading conditions (CLCs) in a sub-volume V^* of the powder trapped at impact. Within such volume, plastic deformation activates the MA process. If V is the total volume of powder inside the reactor, $k = V^*/V$ is the volume fraction of powder affected by MA. It expresses the rate at which powders undergo CLCs. Based on BM stochasticity, the volume fractions $\chi_i(n)$ of powder subjected i times to CLCs after n impacts can be expressed as [4]

$$\chi_i(n) = \frac{(kn)^i}{i!} e^{-kn}, \quad (3)$$

which fulfils the condition $\sum_{i=0}^{\infty} \chi_i(n) = 1$. If we assume that powders exposed i times to CLCs exhibit interlamellar spacing l_i, the average interlamellar spacing can be calculated by the weighted sum over the volume fractions $\chi_i(n)$

$$l(n) = \sum_{i=0}^{\infty} \chi_i(n)\ l_i. \quad (4)$$

3.2.3 Results and discussion

A typical SEM micrograph of processed powder is shown in Figure 3.2.1a.

The sample consists of Ag and Cu particles not yet involved in the formation of composite particles and in composite particles formed by repeated co-deformation and cold-welding of initial reactants. Although pristine powders comprise particles with size from 5 to 15 μm, BM induces cold-welding and fracturing processes that affect significantly the particle size distribution. Along with the change of particle size, BM also induces the gradual increase of the number of composite particles and the evolution of their composition and microstructure.

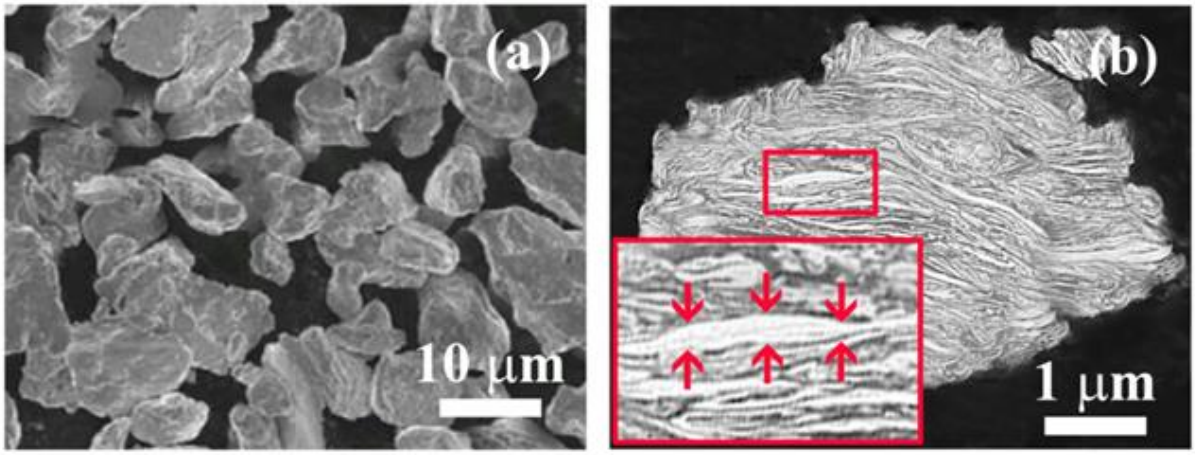

Figure 3.2.1: (a) SEM micrograph of Ag-Cu powders after about 2.0×10^4 impacts. (b) A composite particle. The inset shows an elemental domain and arrows measure its thickness.

To describe the formation and evolution of lamellar structure in composite particles, we identified approximately the major axis of each elemental metal domain and measured the domain thickness in different points of the major axis as shown in Figure 3.2.1b. Thickness was averaged over all the measurements performed per case. The obtained average interlamellar spacings, $l(n)$, are shown in Figure 3.2.2, where $ln\, l\,(n)$ is plotted as a function of the number of impacts, n.

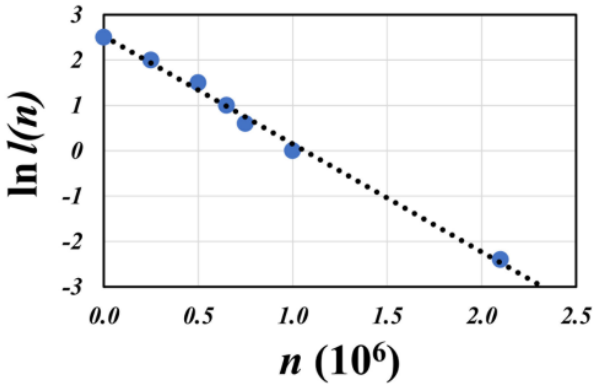

Figure 3.2.2: Semi-logarithmic plot of the average interlamellar spacing, $l(n)$, as a function of the number of collisions, n. The best-fitting curve is shown.

The semi-logarithmic plot gives rise to a seemingly linear arrangement of experimental points, which suggests, to a first approximation, the exponential variation of $l(n)$ with n.

According to Eq. 4, $l(n)$ values stem from the change of interlamellar spacings l_i with the number i of CLCs weighted by the corresponding mass fraction $\chi_i(n)$. Although possible in principle, the evaluation of the l_i spectrum is out of reach in conventional BM experiments. However, l_i estimates can be obtained if the effects of individual impacts on the lamellar structure are realistically described.

In this respect, the maps shown in Figure 3.2.3a indicate that NLST generates patterns quite similar to those associated with mechanical deformation of ductile metals [6] and advection cycles in fluids [7].

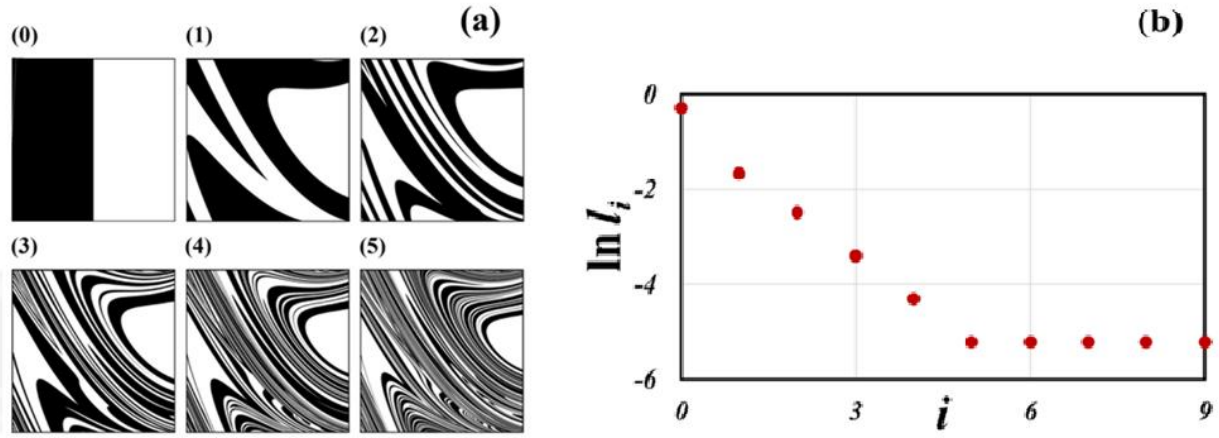

Figure 3.2.3: (a) Advection patterns generated by iteration of NLST. (b) The average thickness, t_i, of elemental domains as a function of map iterations, i.

A small number of iterations suffice to intimately mix the different domains into intricate configurations. Patterns clearly remind to the convoluted lamellar structure of composite particles formed during the early stages of MA and shown in Figure 3.2.1b. Thus, NLST seemingly provides a satisfactory description of experimental evidence.

Image analysis allowed evaluating the average thickness, t_i, of the different domains in the different maps. The obtained t_i values are shown in Figure 3.2.3b as a function of i. Advective mixing determines the rapid exponential t_i decrease. After 6 iterations, a plateau value is reached. Accordingly, new iterations fail to increase the mixing degree.

The t_i values can be regarded as modelling estimates of the interlamellar spacing l_i that characterizes lamellar structure in composite particles that have undergone i CLCs. If we assume that $t_i = \rho l_i$, where ρ is a proportionality constant, we establish a parallel between CLCs and map iterations. In other words, we use advection cycles described by the selected mapping procedure to describe the effects of CLCs on the microstructure of ductile Ag and Cu. Based on the proportionality between t_i and l_i, Eq. 4 can be re-written as

$$ln\, l\,(n) = ln\left[\sum_{i=0}^{\infty} \chi_i(n)\; t_i\right] - ln\,\rho \qquad (5)$$

We used Eq. 5 to best fit the experimental $l(n)$ points in Figure 3.2.2. The best-fitted curve almost overlaps the data, thus pointing out the remarkable capability of the modelling approach of capturing the essential features of the mixing process during the early stages of MA.

In this regard, further indication comes from the value of the best fitting parameter k, which is equal to about 5.1×10^{-6}. The k value obtained in the present work, which corresponds to the volume fraction of powder subjected to CLCs during individual impacts, is quite close to the one of about 2.7×10^{-6} obtained in previous

work on the MA of equiatomic Ag-Cu powder mixtures subjected to BM under similar processing conditions [8]. This supports the hypothesis that suitable mathematical modelling of mixing processes during the early stages of MA can significantly contribute to clarify the mechanistic features of transformations induced by BM.

3.2.4 Conclusions

In summary, we developed a modelling approach that captures the fundamental features of the lamellar structure refinement during the early stages of MA. A kinetic model able to describe the kinetics of processes activated by BM has been combined with a mathematical description of advection cycles induced by plastic deformation. The model curve satisfactorily best fits the experimental data obtained by suitably designed experiments. It follows that suitably chosen mapping procedures can be used to evaluate the spectrum of characteristic lengths that distinguish microstructure at the different refinement stages.

References of the Subchapter 3.2

1. Baláž, P., Achimovičová, M., Baláž, M., Billik, P., Cherkezova-Zheleva, Z., Criado, J.M., Delogu, F., Dutková, E., Gaffet, E., Gotor, F.J., Kumar, R., Mitov, I., Rojac, T., Senna, M., Streletskiikl A., Wieczorek-Ciurowa, K., (2013). Hallmarks of mechanochemistry: from nanoparticles to technology. *Chem Soc Rev*, 42, pp. 7571-7637. https://doi.org/10.1039/C3CS35468G
2. James, S.L., Adams, C.J., Bolm, C., Braga, D., Collier, P., Friščić, T., Grepioni, F., Harris, K.D.M., Hyett, G., Jones, W., Krebs, A., Mack, J., Maini, L., Orpen, A.G., Parkin, I.P., Shearouse, W.C., Steed, J.W., Waddell, D.C., (2012). Mechanochemistry: opportunities for new and cleaner synthesis, *Chem Soc Rev*, 41, pp. 413-447. https://doi.org/10.1039/C1CS15171A
3. Humphry-Baker, S.A., Garroni, S., Delogu, F., Schuh, C.A., (2016). Melt-driven mechanochemical phase transformations, *Nature Mater*, 15, pp. 1280-1286. https://doi.org/10.1038/nmat4732
4. Delogu, F., Takacs, L., (2018). Information on the Mechanism of Mechanochemical Reaction from Detailed Studies of the Reaction Kinetics, *J Mater Sci*, 53, pp. 13331-13342. https://doi.org/10.1007/s10853-018-2090-1
5. Cocco, G., Delogu, F., Schiffini, L., (2000). Toward a quantitative understanding of the mechanical alloying process, *J Mater Synth Proc*, 8, pp. 167-180. https://doi.org/10.1023/A:1011308025376
6. Shingu, P.H., Ishihara, K.N., Otsuki, A., (1995). Mechanical alloying and chaos, *Mater Sci Forum*, 179-181, pp. 5-10. https://doi.org/10.4028/www.scientific.net/MSF.179-181.5
7. Rothstein, D., Henry, E., Goltub, J.P., (1999). Persistent patterns in transient chaotic fluid mixing, *Nature*, 401, pp. 770-772. https://doi.org/10.1038/44529
8. Delogu, F., (2008). A mechanistic study of $Ag_{50}Cu_{50}$ solid solution formation by mechanical alloying, *Acta Mater*, 56, pp. 2344-2352. https://doi.org/10.1016/j.actamat.2008.01.024

3.3 Coupling of mixing and reaction in mechanochemical transformations

3.3.1 Introduction

Chemical reactions are processes in which one set of chemical substances is transformed into another set [1-3]. The chemical change is mediated by the rearrangement of electrons around the nuclei of elemental species and is commonly described in terms of breakage and formation of chemical bonds between atoms [1-3].

For chemical bonds to break and form, the chemical species have to come closer and closer. As they approach each other, chemical bonds become increasingly distorted and the overall potential energy increases [1-3]. At distances comparable with chemical bond lengths, reactants become partially bonded together by new chemical bonds that begin to form, possibly accompanied by the simultaneous weakening of other chemical bonds. The reactants gradually give rise to a collection of intermediate structures that persist while chemical bonds are forming and breaking near, or at, the saddle point of the potential energy surface [1-3]. The resulting activated complex exists for extremely short time periods and evolves with equal likelihood towards the initial reactants or new products [1-3].

These classical considerations make it clear that reactions involving two or more reactants can proceed only if the reactants are brought together on the molecular scale [4-6]. However, typically reactants are mixed only on the macroscopic, or mesoscopic, scales initially [4-6]. Therefore, the initial reactant mixture needs to be properly homogenized on the microscopic scale to overcome reactant segregation and enable, at least in principle, all the molecules to interact with each other [4-6].

This result can be achieved by physical mixing, which reduces the characteristic lengths associated with reactant segregation and, then, the differences in local concentration [7-10]. Whenever mixing is fast enough, the generation of new chemical species is governed by the intrinsic chemical kinetics [7-10]. Otherwise, the chemical species remain separated by diffuse or sharp reaction fronts. These fronts can assume very complex morphologies in the presence of external forcing able to induce heterogeneous flow, and phase stretching in particular [7-10]. Under these circumstances, the reaction rates can differ significantly from those observed under ideal mixing conditions.

If fluid phases are involved, diffusive mass transfer can take place at interfaces [11-15]. In this case, the rate of chemical reaction specifically depends on the Peclet number, i.e. the ratio of the characteristic time of diffusion to the characteristic time of shearing, and on the Damkohler number, equal to the ratio of the characteristic time of diffusion to the characteristic time of chemical reaction [11-15]. When diffusion can occur at relatively high rates, a diffuse interface forms and chemical species mix progressively.

The situation drastically changes when reactant molecules are in the solid state, which prevents any fast diffusion process [16-18]. Segregation is complete and the formation of products at the interface makes the reaction come to a complete arrest in a short time [16-18]. The only possible way to induce further chemical reaction is to generate new interface area to bring new reactant molecules into contact. Therefore, the reaction extent is entirely dependent on the scale of reactant segregation.

The forced mixing of reactants, and the consequent reaction progress through the constant generation of new interface area between reactants, is the characteristic feature of the mechanical processing of solids [19-22]. The method relies precisely upon the severe mechanical deformation of solid phases by the application of mechanical forces to continuously generate new interface area [19-22].

The mechanical processing of powders by ball milling is the most popular method in this regard [23-29]. The movement of the reactor, or of parts of it, makes milling balls collide with each other and with the reactor walls [23-29]. During each impact, a small fraction of the powder charge is trapped between the colliding surfaces and subjected to mechanical loading [23-29]. Loose powders experience dynamic compaction at relatively high strain rates and undergo mechanical deformation. Interfaces between reactants form and the repeated occurrence of impacts makes the microstructure evolve and the interface area increase.

The extent of reaction is determined by the mixing of reactants in combination with thermodynamic and kinetic factors [23-29]. This is especially true in mechanochemical reactions involving solid organic reactants [23-29], which are soft enough to severely deform under the effects of mechanical loading. Shear flow, in particular, can be expected to represent the primary phase deformation process. Organic solids can, thus, undergo repeated stretching and folding.

The importance of the rheological response of reactants in mechanochemical organic reactions has been already recognized and attention has been called on the related mixing effects [30]. Nevertheless, there is still a substantial lack of information on this issue and, as a consequence, a poor understanding of the mechanochemical reactivity itself. In addition, literature does not yet offer any practical indication about what experimentalists can expect from the combination of mixing and chemical processes during the mechanical activation and how experimental findings can be used to gain deeper insight into the chemistry activated by mechanical forces.

In this work, we aim precisely at providing information about the kinetics of mechanochemical reactions involving organic reactants. While a direct experimental study of the way local mixing processes can affect the reaction rate is presently out of reach, we believe that useful clues can be obtained by modelling. To this aim, we have developed a simplified numerical model that relates the overall reaction kinetics to the evolution of mixing fronts. We couple shear flows and chemical reactivity for mechanochemical transformations with initially segregated reactants separated by flat fronts.

Mixing effects during individual impacts are described by a discrete deformation map that mimics the deformation of soft phases under shearing conditions. The intrinsic reaction kinetics is accounted for by introducing a reaction probability between reactant molecules that face each other at the interface. The model takes into account the statistical nature of the mechanical processing by ball milling.

Taking advantage of such model, we carried out a systematic investigation of the apparent reaction kinetics varying the amount of powder effectively processed during individual impacts, the chemical composition of the reactant mixture and the reaction probability at the interface. We discuss how the statistical features and the interface area affect the reaction rate in combination with the reaction probability, showing the shape of

the resulting kinetic curves. Finally, we suggest how to use experimental data to extract information on the chemistry at work on the microscopic scale.

Notation is summarized at the end of the work.

3.3.2 Mechanical processing by ball milling

Ball milling is a discontinuous method that enables the mechanical processing of powder based on the occurrence of impacts [23-29]. As schematically shown in Figure 3.3.1, each impact involves only part of the processed powder, subjecting it to mechanical loading [23-29].

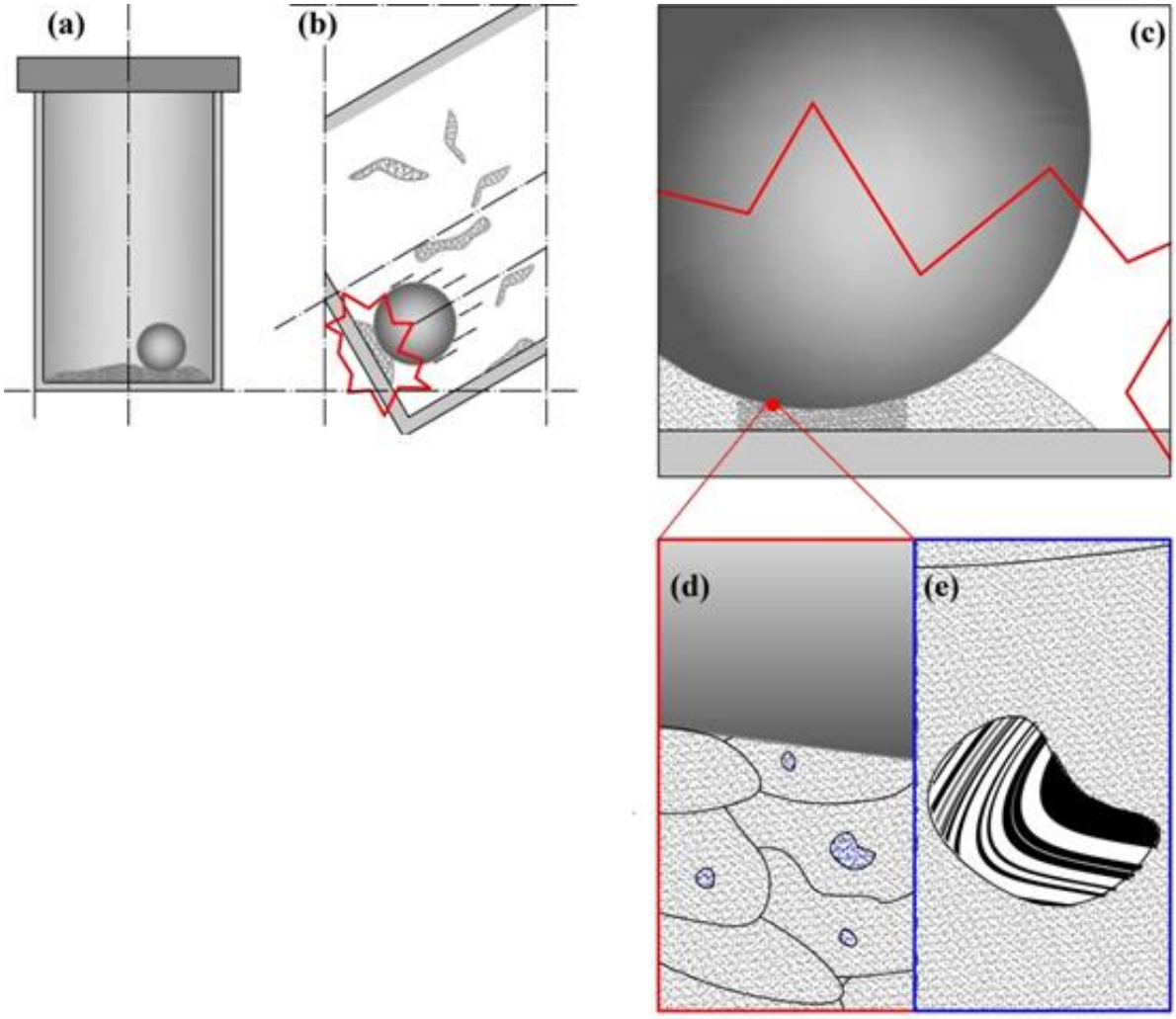

Figure 3.3.1: Schematic description of the mechanical processing of powder by ball milling. (a) The reactor contains ball and powder. (b) Due to the reactor motion, the ball impacts on the reactor wall, involving a small fraction of the powder charge. (c) Part of the powder involved in individual impacts undergoes effective dynamic compaction (darker region). (d) The powder particles affected by dynamic compaction undergo severe mechanical deformation and local mechanical stresses can become intense enough to impose CLCs in small volumes v^* located inside the particles or at their contact points (regions of variable shape). (e) The occurrence of CLCs gives rise to physical and chemical changes inside the volumes v^* (here represented as the mixing of a white *A* phase and a black *B* phase).

Mechanical forces apply to loose powders, thus inducing their dynamic compaction at relatively high strain rates [23-29]. As powder particles are compressed, their mobility is progressively reduced by contact forces, which eventually form inhomogeneous force chains percolating across interparticle contact points [23-29]. Under the effects of severe mechanical stresses, powder particles undergo plastic deformation and flow against each other or, in case of brittle materials, break into fragments [23-29]. Possibly, physical and chemical changes take place consequently [23-29].

Only a relatively small fraction of powder is involved in individual impacts and its involvement is inherently stochastic. Together with the continuous stirring of powders, this provides the mechanical processing by ball milling with an intrinsically discrete and statistical nature. These features affect any aspect of the powder processing and must be suitably taken into account in the kinetic description of mechanically induced reactions as well as in the analysis of experimental data.

To this aim, we have recently developed a kinetic model that can be utilized to relate the experimental evidence to the processes taking place on the microscopic scale during individual impacts [30]. The model is based on the following, few assumptions:

(i). consecutive impacts occur independent of each other;

(ii). chemical changes can only take place when the intensity of local mechanical stresses overcomes a threshold value, which identifies critical loading conditions (CLCs);

(iii). chemical changes take place in η small volumes v^* that are randomly distributed inside the powder volume trapped in individual impacts;

(iv). the involvement of volumes v^* in CLCs is stochastic;

(v). chemical changes involving volumes v^* take place on time scales shorter than impact duration, τ;

(vi). stirring keeps the powder charge uniform and homogeneous.

The repeated mechanical loading of powder particles in individual impacts implies that η volumes v^* can undergo CLCs 1, 2, … , i, … times depending on the total duration of the mechanical processing. The total volume of powder affected by CLCs during individual impacts, v, is equal to the product $\eta\, v^*$ and the ratio v/V between v and the total volume of powder, V, defines the volume fraction of powder that is subjected to CLCs per impact, κ. These considerations are schematically represented in Figure 3.3.1.

Simple statistical considerations suggest that the volume fraction of powder, $\chi_i(m)$, that has undergone CLCs i times after m impacts is [30]

$$\chi_i(m) = m!/[i!\ (m-i)!]\ \kappa^i\ (1-\kappa)^{m-i} \qquad (1)$$

In other words, any single m-th impact imposes CLCs only on a small fraction of the volume of powder trapped between the colliding surfaces, which, in turn, is a small fraction of the whole volume of powder inside the reactor. The milling dynamics inside the reactor is chaotic and the constant stirring of powders keeps the powder charge homogeneous. Thus, the powder trapped and the fraction of trapped powder affected by CLCs are effectively mixed with the rest of powder after any given impact.

The effective stirring and the fact that the powder is involved in impacts stochastically ensure that the fraction of powder involved in the m-th impact is not the same involved in the $m-1$-th impact and will not be the same involved in the m+1-th impact.

Once a certain number m of impacts have occurred, the volume fractions of powder affected 0, 1, 2, …, i, ... times by CLCs during individual impacts exhibit statistical distribution. When m is small, most of powder has never been affected by CLCs, and the statistical distribution is restricted to the lowest values of i. As ball milling proceeds, and the number m of impacts increases, distributions move towards larger values of i, since a larger volume fraction of powder has been involved in CLCs more times. In a single impact only the volume fraction of powder $\kappa = \eta \frac{v^*}{V}$ is affected by CLCs. Therefore, Eq. 1 represents the statistical distribution of the volume fractions of powder that, after a total number of m impacts, have experienced i CLCs.

Since volume v is much smaller than the total volume of powder, V, κ is much smaller than 1. Therefore, Eq. 1 can be re-written as

$$\chi_i(m) = \left[(\kappa\, m)^i / i!\right] exp(-\kappa\, m) \tag{2}$$

an expression that can be, sometimes, advantageous to use in mathematical modelling. Eqs. 1 and 2 fulfil the condition

$$\sum_{i=0}^{\infty} \chi_i(m) = 1 \tag{3}$$

Accordingly, at any given number m of impacts, the sum of the volumes of powders that have been affected by CLCs i times corresponds to the total volume of powder inside the reactor. Invariably, i is equal to m or smaller. Therefore, the sum in Eq. 3 can be restricted, in principle, to the first m terms. However, m is generally very large, and the limit to infinity is reasonable.

While Eqs. 1 and 2 account for the statistics underlying the involvement of volumes v^* in 1, 2, … , i, … CLCs, they provide no information about the physical and chemical changes that CLCs induce in volumes v^*. To this aim, the degree of physical and/or chemical transformation in individual volumes v^* must be related to the number of CLCs undergone by volumes v^* [30].

The simplest way to do that is to hypothesize that the volume fractions that have undergone CLCs different times, $\chi_i(m)$, exhibit different values of chemical conversion, α_i. Accordingly, the total degree of chemical conversion, $\alpha(m)$, can be expressed as

$$\alpha(m) = \sum_{i=1}^{\infty} \chi_i(m)\, \alpha_i \tag{4}$$

where $0 < \alpha_i < 1$.

Eq. 4 corresponds to the weighted average of the degrees of chemical conversion α_i over the volume fractions $\chi_i(m)$. It is the most general kinetic equation for mechanically activated transformations. Therefore, any analysis of experimental kinetics, or any description of mechanochemical kinetics, requires the independent estimation of the quantities $\chi_i(m)$ and α_i and the deconvolution of their contributions to Eq. 4.

In this regard, it is worth noting that difficulties are formidable. The deconvolution of statistical and chemical factors involves the independent measurement of $\chi_i(m)$ and α_i values. However, volumes v^* can be expected to be on the nanometer range and dispersed in a much larger volume of powder, which makes them out of reach for any systematic investigation based on the experimental methods currently available. Thus, the only way to gain insight, although indirect, on local processes is to analyze the available experimental data with the help of a suitably developed conceptual framework for the transformation kinetics.

In the following, we develop such a framework for the case study of organic reactants that give rise to interfacial reactions once effectively mixed. Specifically, we show how the occurrence of mixing processes and interfacial reactions in volumes v^* that have undergone i CLCs after m impacts can determine the spectrum of α_i values and, then, the shape of kinetic curves.

3.3.3 Interface area changes during impacts

The response of powder particles to local mechanical stresses is governed primarily by their mechanical properties. In turn, these are related to the chemical nature. In this regard, it is worth noting that molecular materials are generally about two orders of magnitude softer than ionic, covalent and metallic ones[9]. It is the weakness of intermolecular forces compared with chemical bonds to make the structure of molecular solids more prone to deformation than ionic, covalent and metallic solids, the applied mechanical forces being the same [31-34].

The application of directional mechanical stresses to molecular crystals with layered structure can easily induce shear deformation through the slippage of molecular planes [31-34]. Deformation mechanisms including slip deformation and twin deformation have been observed in molecular crystals characterized by strong in-plane interactions and weaker interlayer forces [31-34]. Molecular crystals characterized by anisotropic packing with strong and weak interaction patterns distributed along different crystalline directions can also exhibit significant bending [31-34]. In contrast, isotropic interactions in the three dimensions typically result in molecular crystals showing a brittle behavior [31-34]. Hardness, strain-rate sensitivity and granularity contribute determining the ability of molecular crystals to undergo plastic deformation and flow under the effects of severe mechanical stresses [31-34].

In this work, we focus on the chemical reaction between two initially segregated organic reactants. We assume that the organic solids have the same mechanical properties. Accordingly, they exhibit the same response to mechanical stresses and undergo the same deformation processes.

In this respect, we note that the intensity of mechanical forces typically experienced by trapped powders during individual impacts is remarkably higher than the yield stress of molecular materials [23-29,31-34]. Therefore, it can be reasonably expected that the organic reactants eventually undergo flow deformation under the effect of shear stresses.

Since ball milling, and, then, our kinetic model, are inherently discrete, we need a discrete description of the physical and chemical changes affecting the volume fractions of powder that have undergone CLCs different times. The first step in this direction is to describe the flow deformation undergone by the molecular solids

under shearing. To this aim, we take advantage of a mixing map that mimics the mechanical deformation of a material in the presence of shear stresses. Although various choices are possible [35-37], we selected the non-linear shear-transformation map that describes shear deformation based on the equations

$$x_{i+1} = x_i + 4\,(y_i + 1/2) \tag{5a}$$

$$y_{i+1} = y_i + (x_{i+1} - 1)^2 \tag{5b}$$

$$z_{i+1} = z_i \tag{5c}$$

where x, y and z are the Cartesian coordinates and i is the number of iterations.

Already used to describe the effects of shearing in binary alloys [38-39], the map applies to a three-dimensional cubic domain defined by Cartesian coordinates $0 \leq x \leq 1$, $0 \leq y \leq 1$ and $0 \leq z \leq 1$. The map operation relocates the points of the domain as shown in Figure 3.3.2.

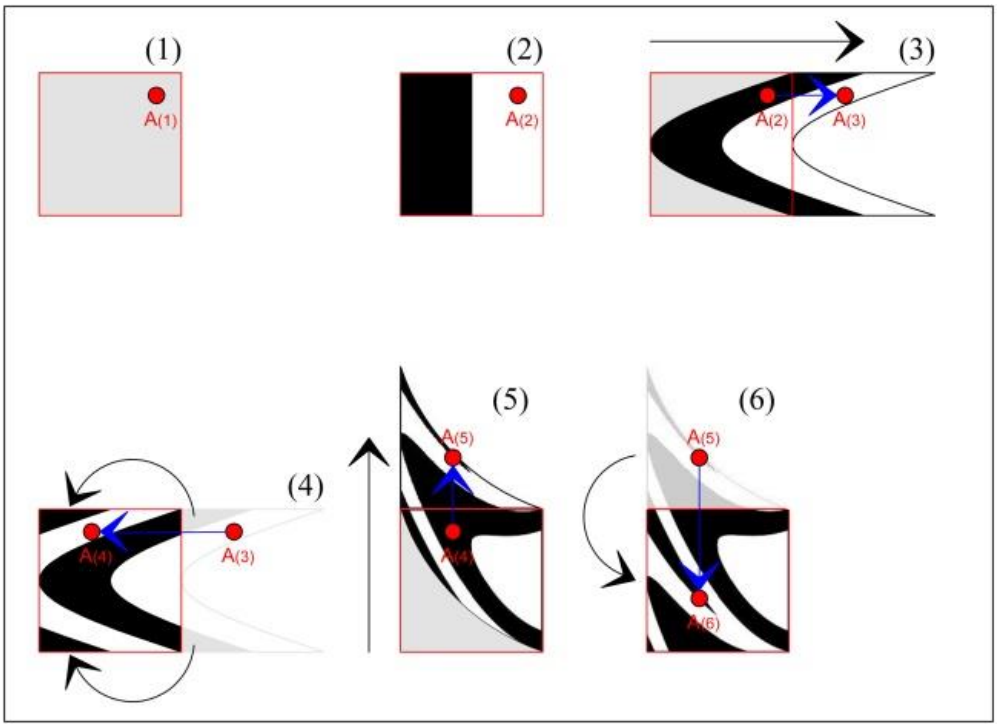

Figure 3.3.2: Schematic description of the mixing map operation. (1) Selection of the point A of coordinates $(x_i; y_i)$. (2) Identification of its chemical nature. (3) Evaluation of the new coordinate x_{i+1} from the initial one x_i. (4) Rescaling of the coordinate x_{i+1} to keep the point A within the domain. (5) Evaluation of the new coordinate y_{i+1} from the initial one y_i. (4) Rescaling of the coordinate y_{i+1} to keep the point A within the domain.

First, new x and y coordinates are generated. Then, the x and y coordinates of the points falling outside the initial cubic domain are suitably rescaled to fulfil the conditions $0 \leq x \leq 1$, $0 \leq y \leq 1$ and $0 \leq z \leq 1$. The volume remains constant.

When the cubic domain is divided in two, or more, sub-domains that correspond to different chemical substances *A* and *B*, the reiterated application of the map gives rise to mixing patterns. A few mixing patterns for the equimolar binary case can be seen in Figure 3.3.3.

As the number of iterations i increases, configurations become more and more intricate, reminding the mixing patterns obtained by advection during the flow deformation of fluids [35-37].

We use the non-linear shear-transformation map to describe the mixing processes occurring in the volumes v^* involved in CLCs 1, 2, … , i, … times. Specifically, the number of map iterations, i, is set equal to the number of CLCs undergone by volumes v^*. In this way, we univocally correlate mixing and CLCs.

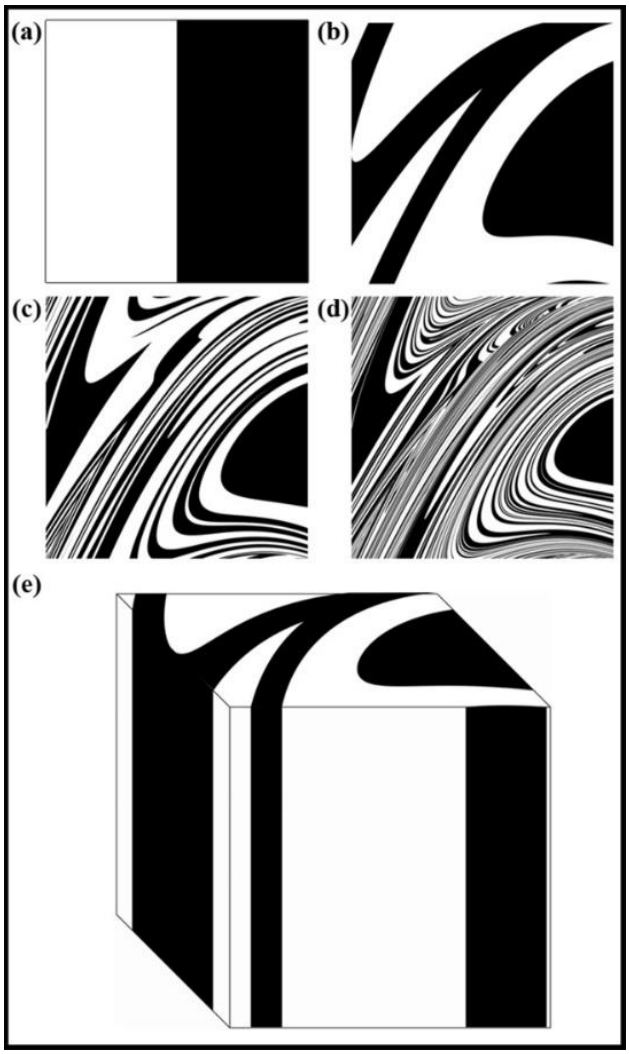

Figure 3.3.3: Mixing patterns generated by application of the mixing map to an equimolar binary mixture of chemical species *A* (white) and *B* (black). The initial configuration (a) is shown together with configurations obtained after 1 (b), 3 (c) and 5 (d) map iterations. (e) A three-dimensional view of the cubic element in panel (b).

We carried out calculations making any volume v^* correspond to a cubic domain including 4096×4096×4096 cubic units. We assume that these cubic units contain a single molecular unit each. For sake of illustration, let us consider chemical species *A* and *B* similar to glucose in size. Therefore, they have a molar volume of about 117 $cm^3\ mol^{-1}$, which means that molecular volume is around 1942 nm^3. It follows that the corresponding cubic units have side approximately equal to 12.5 nm. Thus, if we consider two sub-domains of *A* and *B* divided by a flat interface parallel to two faces of the cubic volume, the interface area separating the sub-domains is equal

to about 2.6×10^{9} nm^2. The whole domain has volume v^* equal to about 1.3×10^{14} nm^3, which corresponds to about 1.3×10^{-4} mm^3.

As the number of iterations i increases, configurations become more and more intricate, reminding the mixing patterns obtained by advection during the flow deformation of fluids [35-37].

We use the non-linear shear-transformation map to describe the mixing processes occurring in the volumes v^* involved in CLCs 1, 2, … , i, … times. Specifically, the number of map iterations, i, is set equal to the number of CLCs undergone by volumes v^*. In this way, we univocally correlate mixing and CLCs.

It is worth noting that the mechanical processing of organic compounds is commonly carried out using small amounts of powder ranging from a few grams to milligrams. For molecules similar to glucose, 3 mg corresponds approximately to a total volume V of 2 mm^3. We can expect that the volume fraction of powder subjected to CLCs during individual impacts, κ, is quite small. If we assume that it is equal to 1×10^{-3}, the total volume of powder involved in CLCs per impact, v, is equal to about 2×10^{-3} mm^3. Therefore, the number η of volumes v^* undergoing CLCs per impact is equal to about 15.

Starting from the considerations mentioned above, we can readily calculate the increase of interface area, S, due to the mixing of chemical species *A* and *B* during individual impacts. It can be expressed by an equation similar to Eq. 4, namely

$$S(m) = \sum_{i=1}^{\infty} \chi_i(m)\, S_i \tag{6}$$

In Eq. 6, $S(m)$ represents the total interface area generated as a function of the number of impacts, m, and S_i is the interface area associated with the volume fractions that have undergone CLCs i times, $\chi_i(m)$.

The different S_i values can be easily generated by iterating the mixing map described by Eqs. 5a, 5b and 5c. After each iteration, we simply evaluate the number of cubic units belonging to different chemical species *A* and *B* that are in contact with each other. Specifically, we consider two cubic units in contact when they have at least one face in common. Then, under the assumption that cubic units have sides 12.5 nm long, we calculate the pertinent S_i values.

The S_i values obtained for the equimolar mixture of chemical species *A* and *B* shown in Figure 3.3.3 are plotted in Figure 3.3.4a as a function of the number of CLCs, i. It can be seen that S_i increases smoothly with the number of CLCs. Starting from the initial value of about 2.6×10^{9} nm^2, the S_i estimates arrange according to a sigmoidal curve, reaching a plateau value around 1.1×10^{13} nm^2 after about 15 CLCs. Such plateau value is not far from the maximum interface area that can be obtained by a three-dimensional chessboard-like arrangement of alternating cubic units of chemical species *A* and *B*, which is equal to about 2.1×10^{13} nm^2. Therefore, we can draw the conclusion that mixing is effective.

Nevertheless, it is worth noting that the application of the non-linear shear-transformation map to a static domain does not exactly mirror the usual mechanical processing conditions met by powder during ball milling. These make the impacts occur stochastically and the powder can be expected to be trapped between colliding surfaces, and possibly undergo CLCs, with random orientation. For this reason, it is preferable to add a degree of freedom to our simulations, allowing the domain to randomly rotate by 90°, 180°, 270° or 360° around its

central axis between any two consecutive iterations of the mixing map. The S_i values obtained with the same initial configuration shown in Figure 3.3.2, but with the addition of random rotation, are also shown in Figure 3.3.4a.

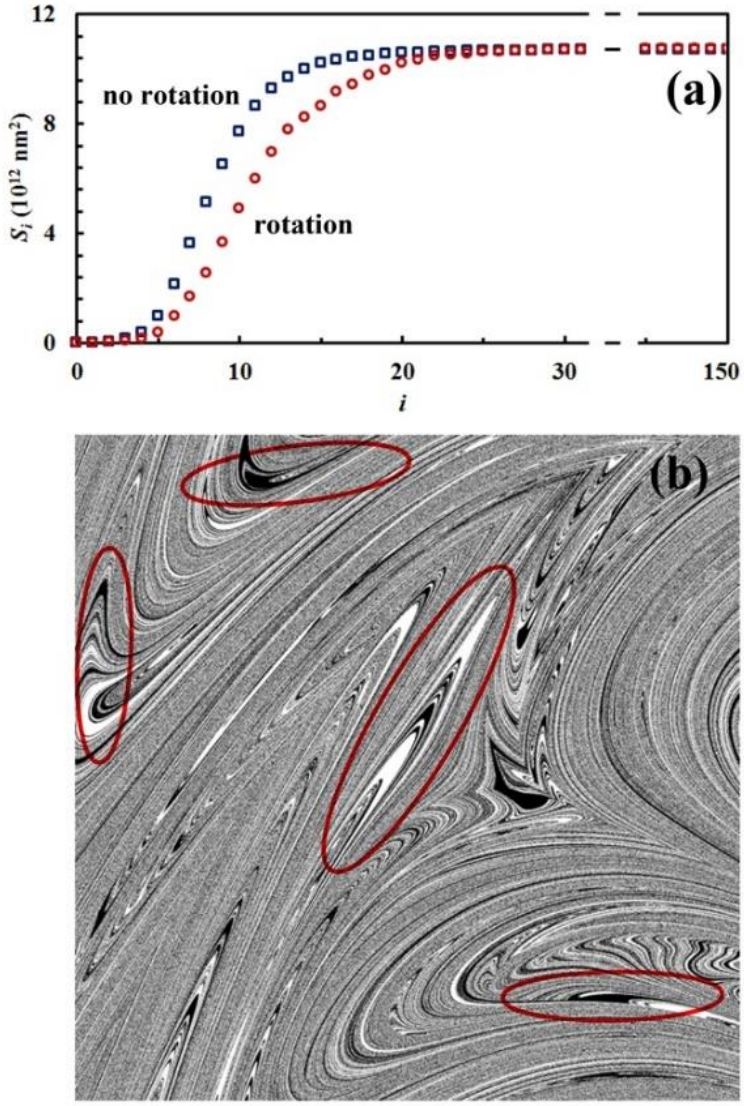

Figure 3.3.4: (a) The S_i values obtained as a function of the number of CLCs, i. Data refer to the equimolar mixture of chemical species A (white) and B (black). Datasets have been evaluated with and without random rotation. (b) Mixing pattern generated by application of the mixing map to an equimolar binary mixture of chemical species A and B in the presence of random rotation. The configuration has been obtained after 15 map iterations. Red ellipses are used to highlight vorticities.

Overall, differences between the S_i values obtained with and without random rotation are small. However, it can be easily seen that mixing is more effective in the absence of random rotation and that the mixing rate is correspondingly enhanced. We explain this apparent inconsistency with the fact that random rotation introduces unpredictable dynamics that eventually leads to the formation of vorticities. An example is shown in Figure 3.3.4b, where vortices are visible already after 15 map iterations. The regions involved in vorticity exhibit considerable persistence, with a marked reduction in the mixing rate of the cubic units that participate

in the collective motion. The observed persistence, and the associated slowing down of the mixing process, have immediate effects on the interface area generation, which takes place at a lower rate.

The mixture composition, i.e. the relative size of the sub-domains of the different chemical species *A* and *B*, affects the S_i plateau value, S_{fin}. Relevant data are plotted in Figure 3.3.5 as a function of the initial volume fraction of chemical species *A*, $\alpha_{0,A}$. It can be seen that S_{fin} increases starting from zero, reaches a maximum $S_{fin,max}$ for the equimolar mixture and, then, decreases to zero again.

Data can be best fitted by the equation

$$S_{fin} = 4\, S_{fin,max}\, \alpha_{0,A}\, \alpha_{0,B} \tag{7}$$

where 4 is the number of nearest neighbors for each cubic element in every slab identified by the *z* coordinate and $\alpha_{0,B} = 1 - \alpha_{0,A}$ is the initial volume fraction of the chemical species *B*.

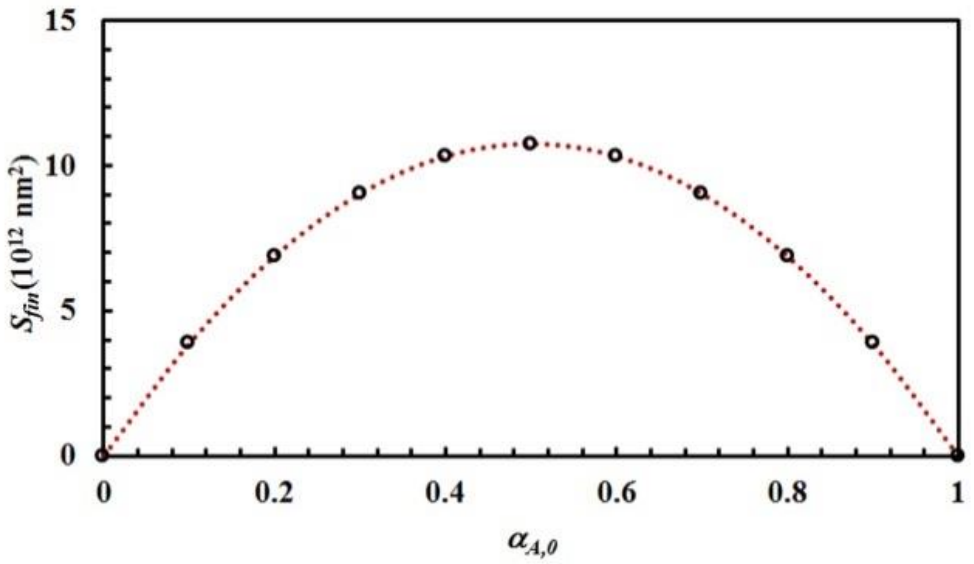

Figure 3.3.5: The S_i plateau value, S_{fin}, as a function of the initial volume fraction of chemical species *A*, $\alpha_{0,A}$. Best-fitted curve is also shown.

The observed dependence on chemical composition is the same expected for binary ideal solutions with a random mixing of chemical species *A* and *B*. We consider this similarity as an indication that the mixing map is able to give rise to effective mixing once a sufficiently large number of iterations have occurred.

3.3.4 Chemical changes during impacts

The occurrence of a chemical reaction at the interface between chemical species *A* and *B* significantly modifies the scenario discussed heretofore. New chemical products form at the interface and progressively reduce the interface area available to chemical reaction. Accordingly, the reaction rate also depends on the interplay between the generation of new interface area, due to the mixing process, and the generation of new chemical species, due to the chemical reaction at the interface.

We investigated this new scenario by assuming that any pair formed by cubic units of different chemical species *A* and *B* that have at least one face in common can react with a probability $0 \leq \Pi \leq 1$. When the chemical reaction occurs, both reactants *A* and *B* transform into product *C* as schematically shown in Figure 3.3.6. Therefore, the chemical equation can be written as

$$A + B \rightarrow 2C \tag{8}$$

In the initial stages, and as far as an interface is clearly distinguishable, the chemical reaction can be expected to remain confined to the interface separating the segregated chemical species. Then, once the chemical species have been intimately mixed as a result of the repeated flow deformation induced by CLCs, the chemical reaction can be expected to involve the whole volume affected by CLCs.

More complicated scenarios can emerge in the presence of three chemical species. In this respect, we chose focusing on the case study in which three reactants *A*, *B* and *C* are mixed together since the beginning. The chemical species *A* and *B* react, with probability $0 \leq \Pi_1 \leq 1$, to form the intermediate *D*.

In turn, the chemical species *C* reacts with *D* to form the final product *E* with a probability $0 \leq \Pi_2 \leq 1$. Thus, the overall reaction can be described as follows:

$$A + B \rightarrow 2D \tag{9a}$$

$$C + D \rightarrow 2E \tag{9b}$$

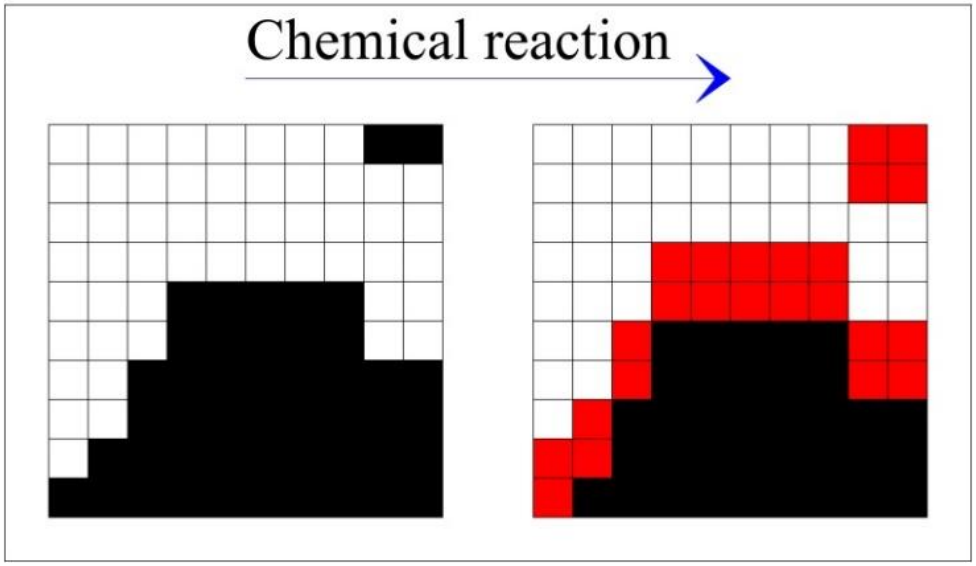

Figure 3.3.6: Schematic description of the transformation (from left to right) of reactants *A* (white) and *B* (black) that have come into contact at the interface into product *C* (red) as a consequence of map iterations.

Eqs. 9a and 9b describe a consecutive reaction kinetics that involves the chemical species *D* as an intermediate between reactants *A* and *B* and final product *E*. To our eyes, this reaction scheme is particularly interesting.

First, the additional reactant *C* can reduce the interface area available to the reaction between *A* and *B* and, then, reduce the reaction rate of the first reaction step. Second, the reaction probabilities Π_1 and Π_2, which can be reasonably expected to differ from each other, determine the persistence of the intermediate *D*. Finally, the

map operation disperses the chemical species *C* and *D* in the reaction volume, thus indicating how effectively dispersoids mix up with other chemical species.

All of these points have practical relevance. Numerous organic reactions involve, indeed, consecutive steps or the addition of catalytic amounts of liquid phases that have to be effectively dispersed into the reacting mixture. On the one hand, we show how the concentration of intermediate species evolves in the presence of effective mixing. On the other, we provide useful insight into the details of the mixing process and the way it affects the chemical behavior.

Simulations are performed according to the iterative scheme below:

1. initial configuration is generated, the chemical composition being determined by the relative number of cubic units belonging to different chemical species;
2. the configuration is rotated randomly based on a simple random number extraction;
3. the mixing map is applied and the cubic units relocated accordingly, thus generating a new configuration;
4. interface area is evaluated by counting the faces of cubic units belonging to different chemical species that are in contact with each other;
5. a fraction of the cubic units of different chemical species that are in contact with each other, numerically equal to the reaction probability considered, is transformed into a new chemical species based on a simple random number extraction;
6. steps 2 to 6 are reiterated.

In the following, we describe and discuss the chemical reaction in binary and ternary systems carrying out a systematic variation of chemical composition and reaction probabilities.

3.3.5 Reaction kinetics in binary systems

The initial configuration and the configuration after 15 impacts, the interface area between reactants *A* and *B*, $S(m)$, and the kinetic curves are shown in Figure 3.3.7 for the chemical composition identified by the $\alpha_{0,A}$ value equal to 0.1. Analogous data are shown in Figs. 3.3.8, 3.3.9, 3.3.10 and 3.3.11 for the $\alpha_{0,A}$ values equal to 0.2, 0.3, 0.4 and 0.5 respectively. Calculations have been carried out assuming that the reaction probability, Π, takes a value of 0.1.

It can be seen that 15 CLCs are always sufficient to induce a significant mixing of reactants *A* and *B* and product *C*. The formation of product *C* deeply affects the generation of the interface area between reactants *A* and *B*. Similar to the case in which no reaction occurs between *A* and *B*, described in Figure 3.3.4a, the interface area initially undergoes rapid growth. However, the gradual formation of *C* progressively reduces the interface area available to reaction, thus determining the attainment of a maximum and, subsequently, a significant decrease. This behavior has immediate consequences on the rate of the chemical reaction between *A* and *B*. The kinetic curve is invariably sigmoidal and the final plateau value depends on the chemical composition.

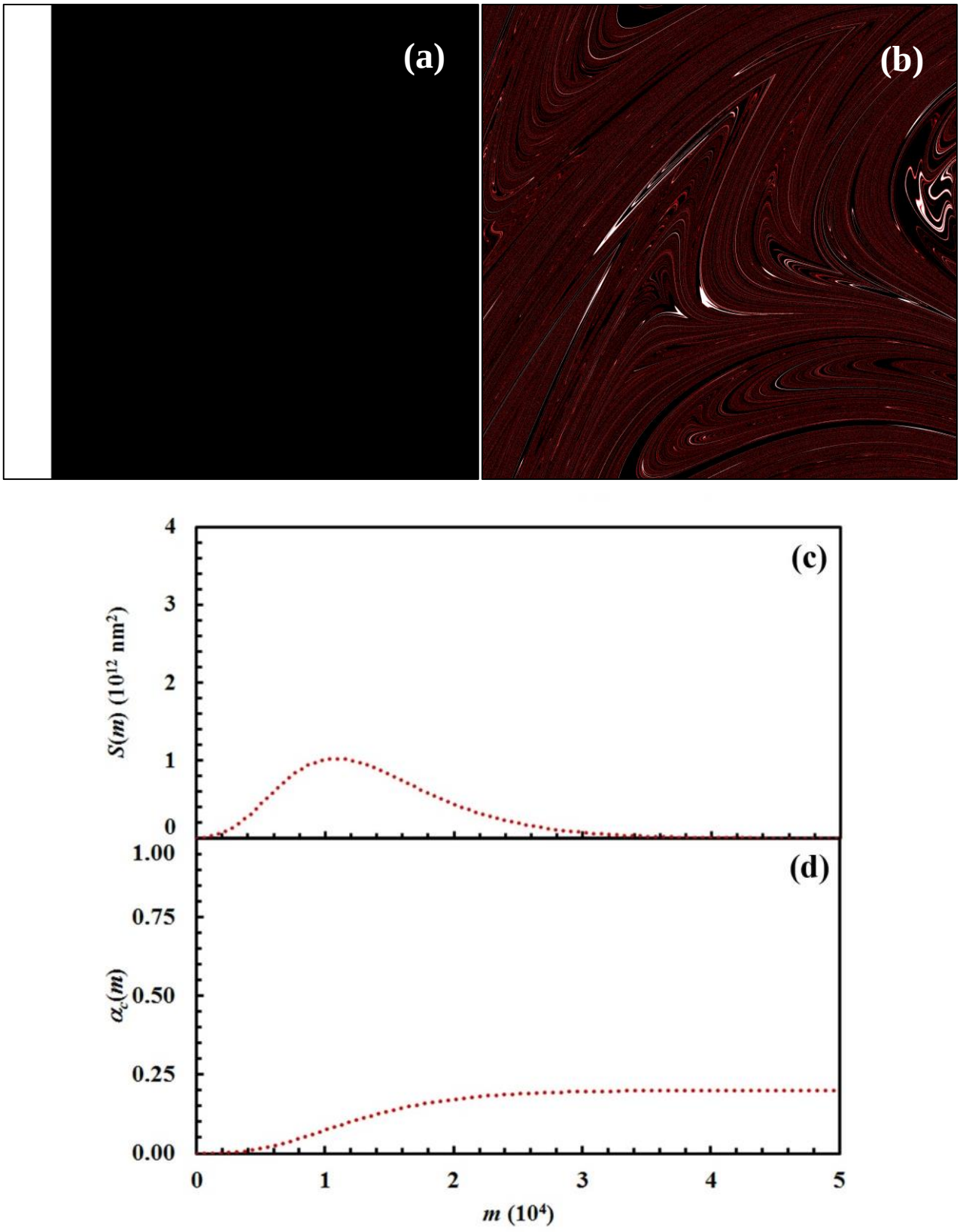

Figure 3.3.7: (a) Initial configuration (*A*, white; *B*, black) and (b) the configuration after 15 impacts (*C*, red). (c) Interface area between reactants *A* and *B*, $S(m)$, and (d) conversion degree of the product *C*, $\alpha_C(m)$, as a function of the number of impacts, m. Data refer to the chemical compositions identified by an $\alpha_{0,A}$ value equal to 0.1.

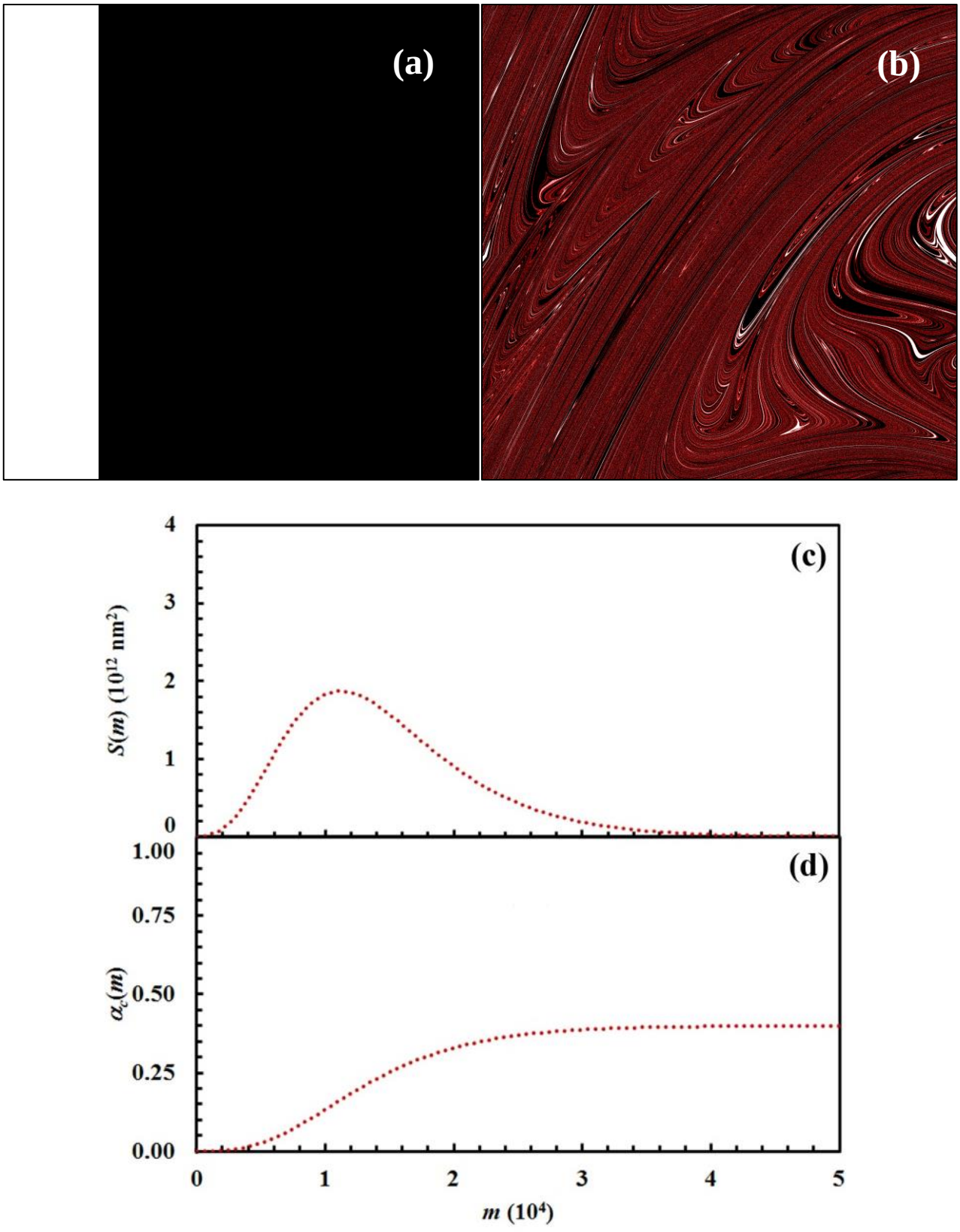

Figure 3.3.8: (a) Initial configuration (*A*, white; *B*, black) and (b) the configuration after 15 impacts (*C*, red). (c) Interface area between reactants *A* and *B*, $S(m)$, and (d) conversion degree of the product *C*, $\alpha_C(m)$, as a function of the number of impacts, m. Data refer to the chemical compositions identified by an $\alpha_{0,A}$ value equal to 0.2.

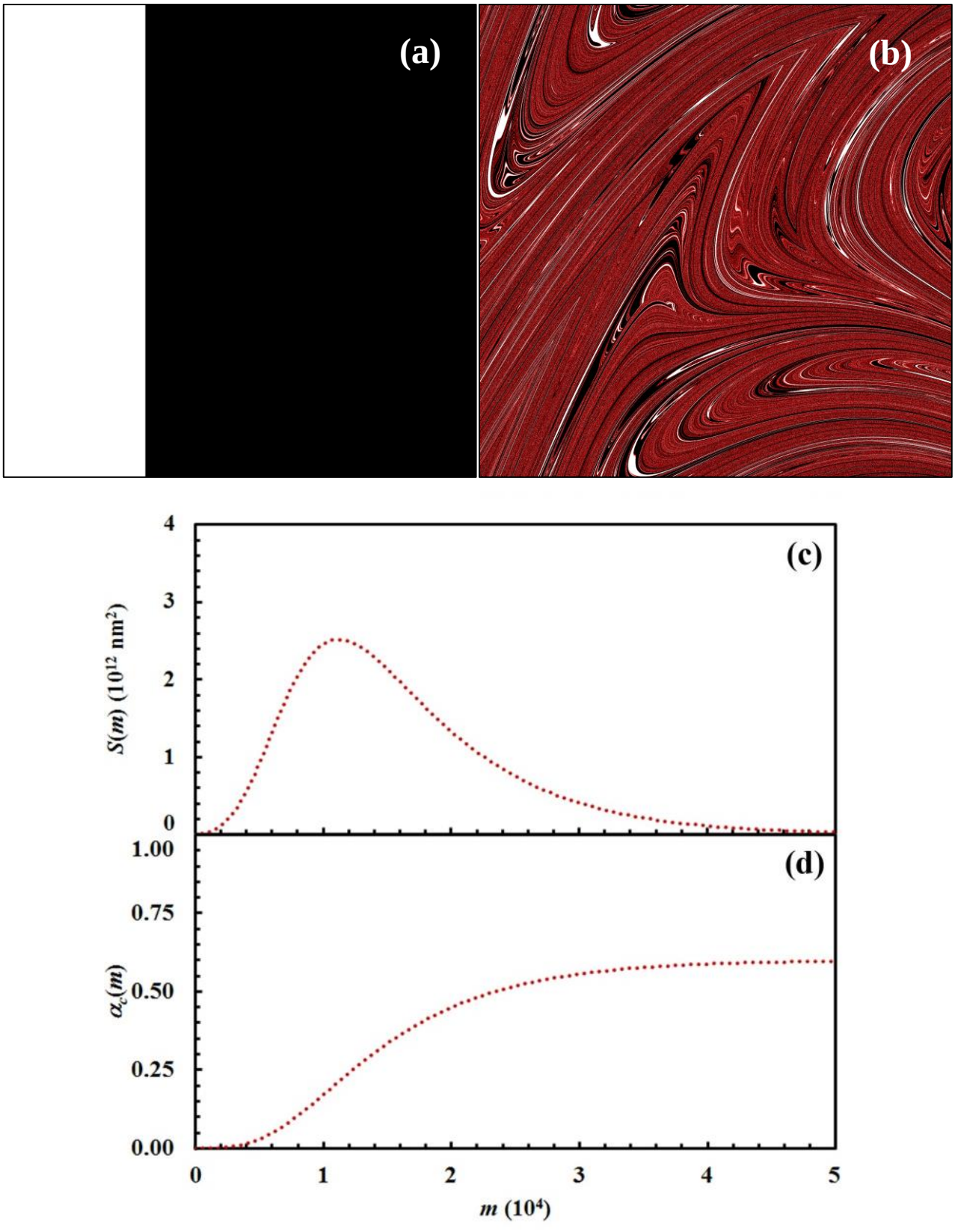

Figure 3.3.9: (a) Initial configuration (A, white; B, black) and (b) the configuration after 15 impacts (C, red). (c) Interface area between reactants A and B, $S(m)$, and (d) conversion degree of the product C, $\alpha_C(m)$, as a function of the number of impacts, m. Data refer to the chemical compositions identified by an $\alpha_{0,A}$ value equal to 0.3.

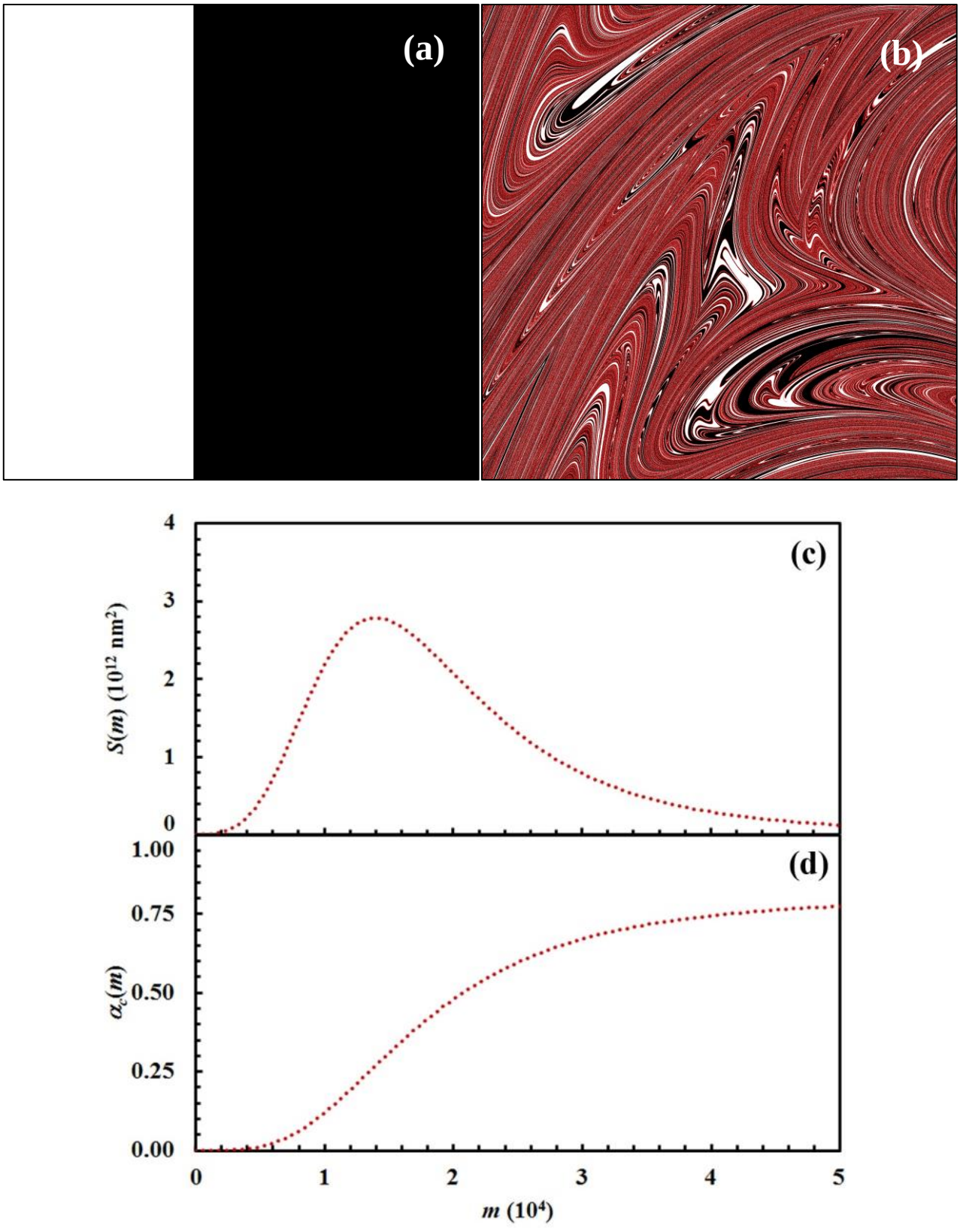

Figure 3.3.10: (a) Initial configuration (A, white; B, black) and (b) the configuration after 15 impacts (C, red). (c) Interface area between reactants A and B, $S(m)$, and (d) conversion degree of the product C, $\alpha_C(m)$, as a function of the number of impacts, m. Data refer to the chemical compositions identified by an $\alpha_{0,A}$ value equal to 0.4.

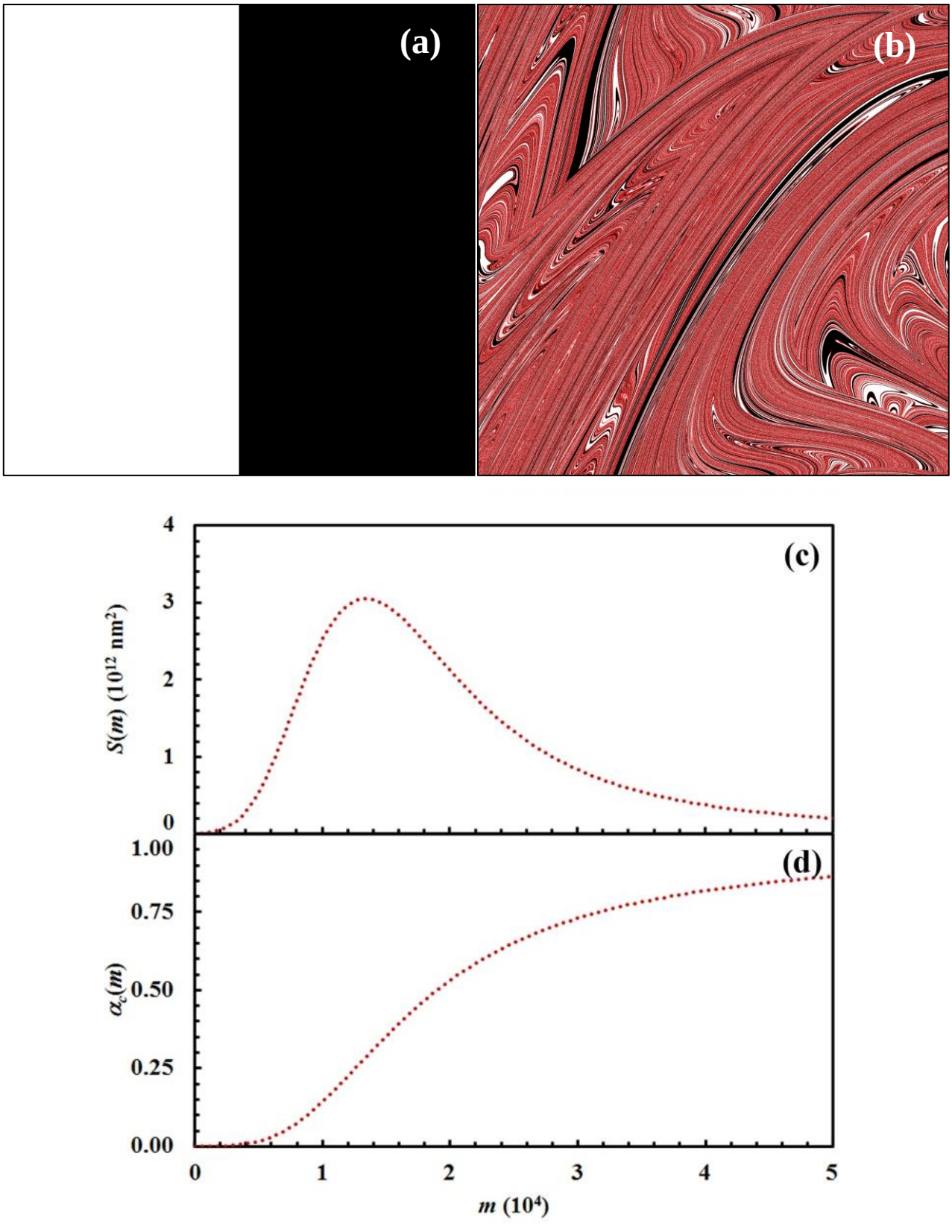

Figure 3.3.11: (a) Initial configuration (A, white; B, black) and (b) the configuration after 15 impacts (C, red). (c) Interface area between reactants A and B, $S(m)$, and (d) conversion degree of the product C, $\alpha_C(m)$, as a function of the number of impacts, m. Data refer to the chemical compositions identified by an $\alpha_{0,A}$ value equal to 0.5.

The deep link between interface area and reaction rate can be seen from Figure 3.3.12, where $S(m)$ and the first derivatives of the kinetic curve describing the formation of product *C*, $d\alpha_C(m)/dm$, are plotted as a function of the number of impacts, m. For brevity, we only show the curves referring to the mixtures with chemical compositions identified by the $\alpha_{0,A}$ values equal to 0.1, 0.3 and 0.5.

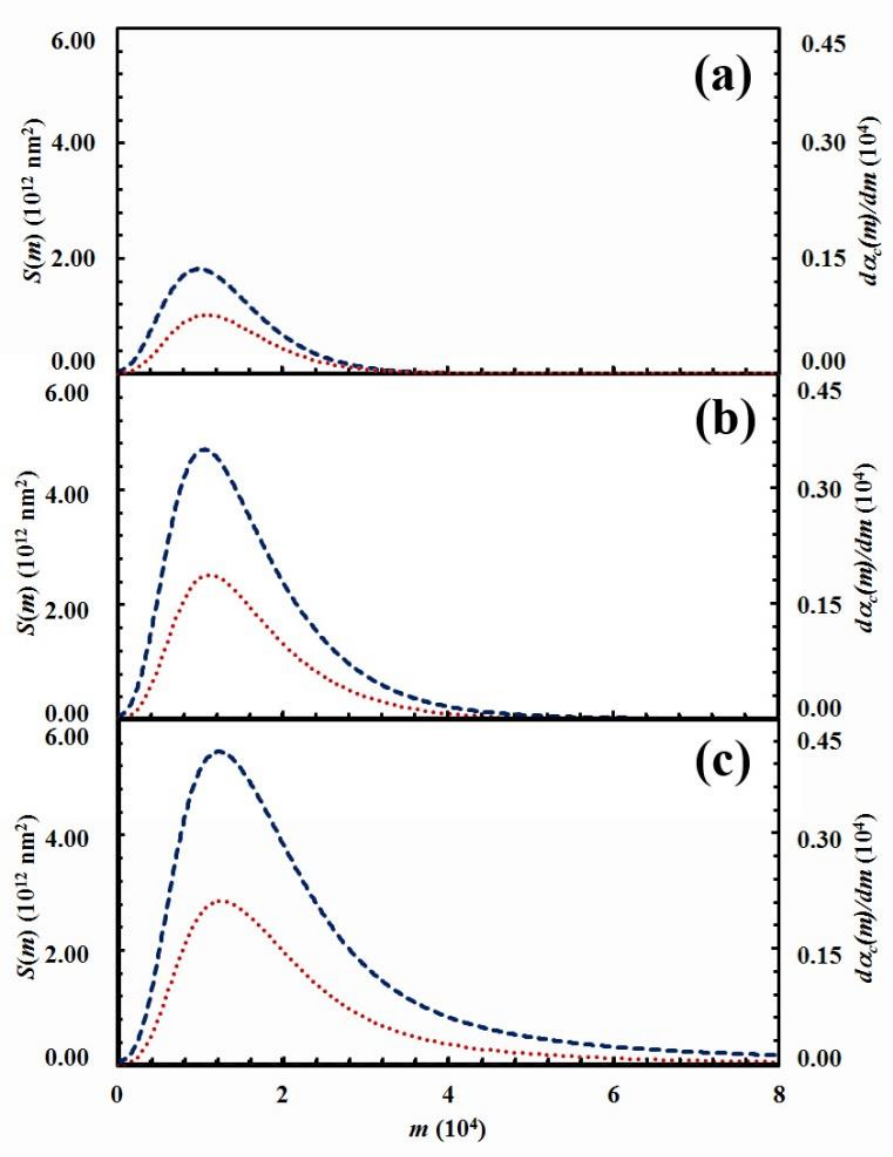

Figure 3.3.12: The interface area between reactants *A* and *B*, $S(m)$ (lower, red curve), and the first derivative of the kinetic curve describing the formation of product *C*, $d\alpha_C(m)/dm$ (upper, blue curve), as a function of the number of impacts, m. Data refer to the mixtures with chemical compositions identified by the $\alpha_{0,A}$ values equal to (a) 0.1, (b) 0.3 and (c) 0.5.

The $d\alpha_C(m)/dm$ curves have exactly the same shape as the $S(m)$ ones. As expected, both curves reach the maximum values after the same number of impacts have occurred. This means that the reaction rate is, somehow, proportional to the interface area available to reaction. This can be easily seen from Figure 3.3.13, where the first derivative of the kinetic curves is shown as a function of the total interface area between reactants *A* and *B*. In all cases, data give rise to a curve resembling a closed loop.

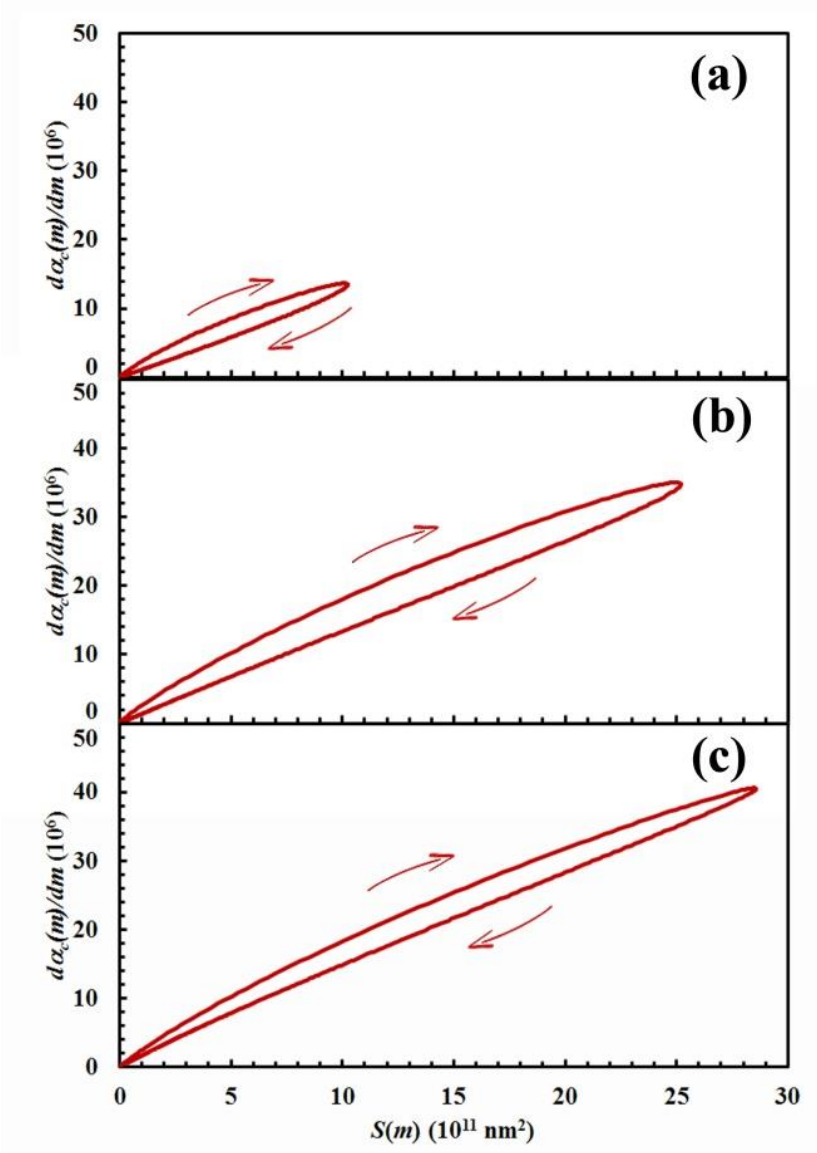

Figure 3.3.13: The first derivative of the kinetic curve describing the formation of product *C*, $d\alpha_C(m)/dm$, as a function of the interface area between reactants *A* and *B*, $S(m)$. Data refer to the mixtures with chemical compositions identified by the $\alpha_{0,A}$ values equal to (a) 0.1, (b) 0.3 and (c) 0.5. Arrows indicate the way the loop develops during the transformation.

In the very initial stages, the reaction rate is proportional to the interface area. In this regard, let us refer to Eq. 4. Taking into account Eq. 1, it can be rewritten as

$$\alpha(m) = \sum_{i=1}^{\infty} m!/[i!\ (m-i)!]\ \kappa^i\ (1-\kappa)^{m-i}\ \alpha_i \qquad (10)$$

After a single impact has taken place, m is equal to 1. The fraction of powder involved in CLCs once, $\chi_1(1)$, is equal to κ. The interface area between reactants *A* and *B* in the volume v involved in CLCs changes from its initial value, S_0, to the one determined by the first flow deformation process undergone by the powder and described by the first iteration of the mixing map, S_1. The amount of product *C* formed after reactants have

undergone CLCs once, α_1, is proportional to the product between the reaction probability, Π, and the interface area available to reaction, S_1. It follows that the degree of chemical conversion after the very first impact is

$$\alpha_C(1) \propto \kappa\, S_1 \Pi \tag{11}$$

Eq. 11 clearly shows that the initial slope of the curves in Figure 3.3.13 is proportional to the product κ Π. Immediately after the first impact, statistical factors affect the shape of the kinetic curve. In addition, mixing rapidly determines the generation of new interface area available to the reaction between *A* and *B*. In later stages, the formation of the product *C* and the consequent decrease of interface area between *A* and *B* depress the reaction rate. Therefore, the proportionality between $\alpha_C(m)$ and the κ, S_1 and Π quantities is partially lost. The effects of reaction probability, Π, on the chemical reaction can be inferred from the data shown in Figure 3.3.14. Data refer to the equimolar composition and have been obtained giving Π the values of 0.001, 0.01, 0.1, 0.5 and 1. We remark here that this latter Π value refers to the case in which reactants *A* and *B* react as soon as they come into contact at the interface.

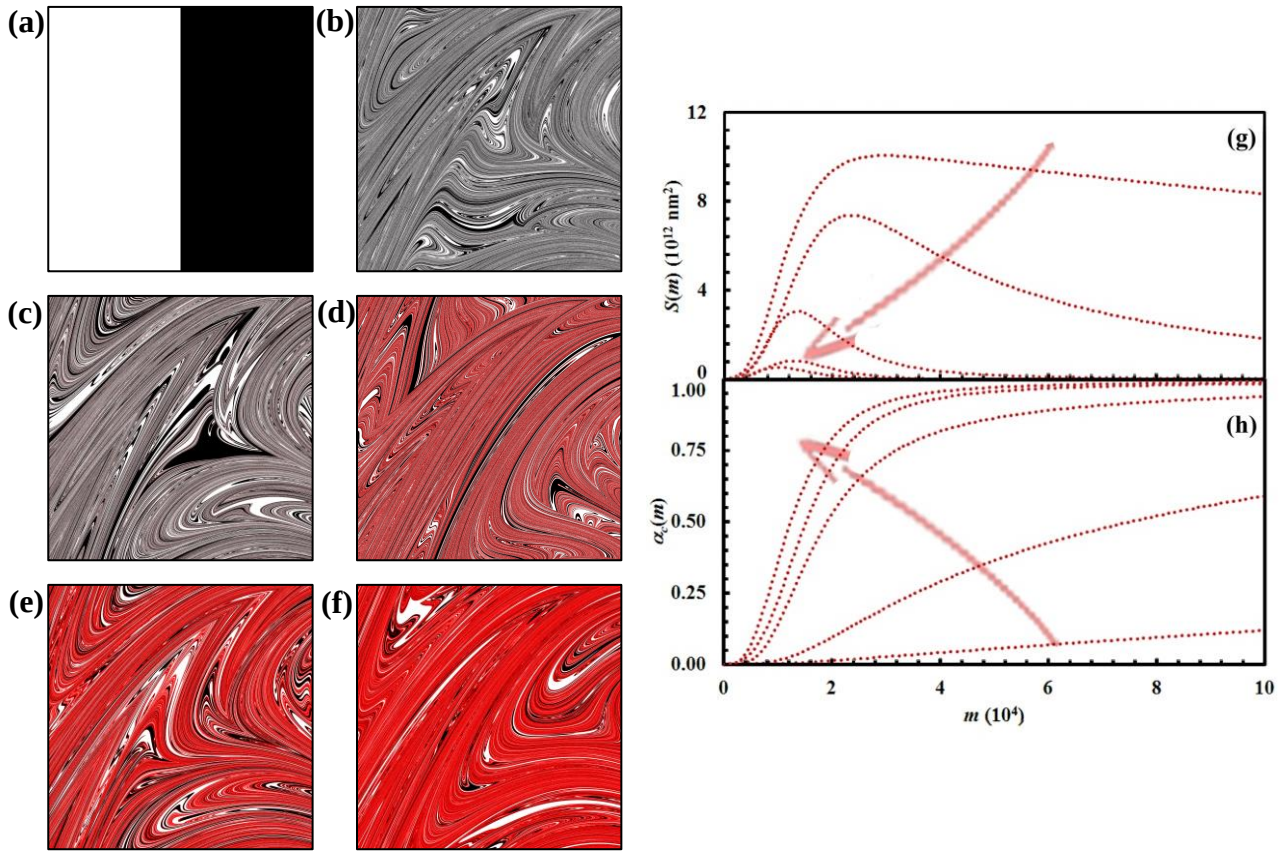

Figure 3.3.14: (a) Initial configuration (*A*, white; *B*, black). The configurations after 15 impacts (*C*, red) for the case studies in which the reaction probability, Π, was given a value equal to 0.001 (b), 0.01 (c), 0.1 (d), 0.5 and 1.0 (f). (g) Interface area between reactants *A* and *B*, $S(m)$, and (h) conversion degree of the product *C*, $\alpha_C(m)$, as a function of the number of impacts, m, for the different cases investigated. The reaction probability, Π, increases, as indicated by the arrows, from the upper to the lower curves in panel (g) and from the lower to the upper curves in panel (h).

According to general expectations, the reaction rate increases as the reaction probability Π increases. For the smallest Π values, the formation of the product *C* proceeds at very low rate. As a consequence, mixing takes over and the interface area $S(m)$ can reach values considerably larger than those observed in other cases. As Π increases, the maximum of the $S(m)$ curve becomes smaller and smaller and shifts toward a smaller number of impacts m. Correspondingly, the kinetic curve $\alpha_C(m)$ becomes steeper and steeper, thus indicating an increasingly faster chemical reaction.

Particularly noteworthy is the fact that the combination of mixing and chemical factors gives rise to marked differences in the kinetic curves. However, nothing has changed in terms of chemistry. The reaction takes place with the same mechanism. It is only the different conversion rate at the interface that makes the reaction kinetics apparently different.

3.3.6 Reaction kinetics in ternary systems

For brevity, calculations concerning the mixtures of three reactants have been restricted to three chemical compositions defined by the triplets of volume fractions $\alpha_{0,A}$, $\alpha_{0,B}$ and $\alpha_{0,C}$ of reactants *A*, *B* and *C*. The $\alpha_{0,A}$, $\alpha_{0,B}$ and $\alpha_{0,C}$ values have been suitably chosen to explore the chemical kinetics under sub-stoichiometric, stoichiometric and super-stoichiometric conditions. Accordingly, the first triplet of $\alpha_{0,A}$, $\alpha_{0,B}$ and $\alpha_{0,C}$ values is equal to 0.15, 0.15 and 0.70 respectively. The second and third triplets are, instead, equal to 0.25, 0.25 and 0.5, and to 0.35, 0.35 and 0.30 respectively. In all cases, the reaction probabilities between *A* and *B*, Π_1, and between *C* and *D*, Π_2, have been given the value of 0.1.

The first triplet defines a chemical composition with reactant *C* in large excess, so that it cannot be completely consumed by the reaction with the intermediate *D* generated by the chemical reaction between reactants *A* and *B*. Therefore, the surplus of unreacted *C* and the final product *E* are destined to coexist once *A*, *B* and *D* are totally consumed. The stoichiometric case is accounted for by the second triplet, and it involves the total consumption of *C* by reaction with *D* and the corresponding formation of *E*. This is the only chemical species that can be observed at the end of the consecutive reactions in this case. Under super-stoichiometric conditions, reactants *A* and *B* are in large excess. This allows the total consumption of *C*, while the surplus of unreacted *D* coexists with the final product *E* once the consecutive reactions are complete.

The results obtained for the three chemical compositions are shown in Figure 3.3.15. In the presence of reactant *C* in excess, the reaction between *A* and *B* at interface is significantly hindered.

The interface area $S(m)$ between the two reactants remains quite small. The intermediate *D* is rapidly consumed by *C* with formation of the final product *E*. The interface area $S(m)$ available to the chemical reaction between *A* and *B* becomes larger in the stoichiometric case. The amount of intermediate *D* formed is also larger. The reaction tends to completion, but the formation of the final product *E* is limited by mixing effects. Mixing effects are also evident in the super-stoichiometric case, where the amount of *D* generated by the chemical reaction between *A* and *B* exceeds the amount needed to consume *C* completely. In particular, it can be seen that the volume fraction of *D* keeps slowly increasing after most of *E* has been generated by

reaction with *C*. This is simply due to the hindrance that residual reactants *A* and *B* experience at the interface, with the amount of *D* in excess and the final product *E* reducing the total interface area available to the reaction.

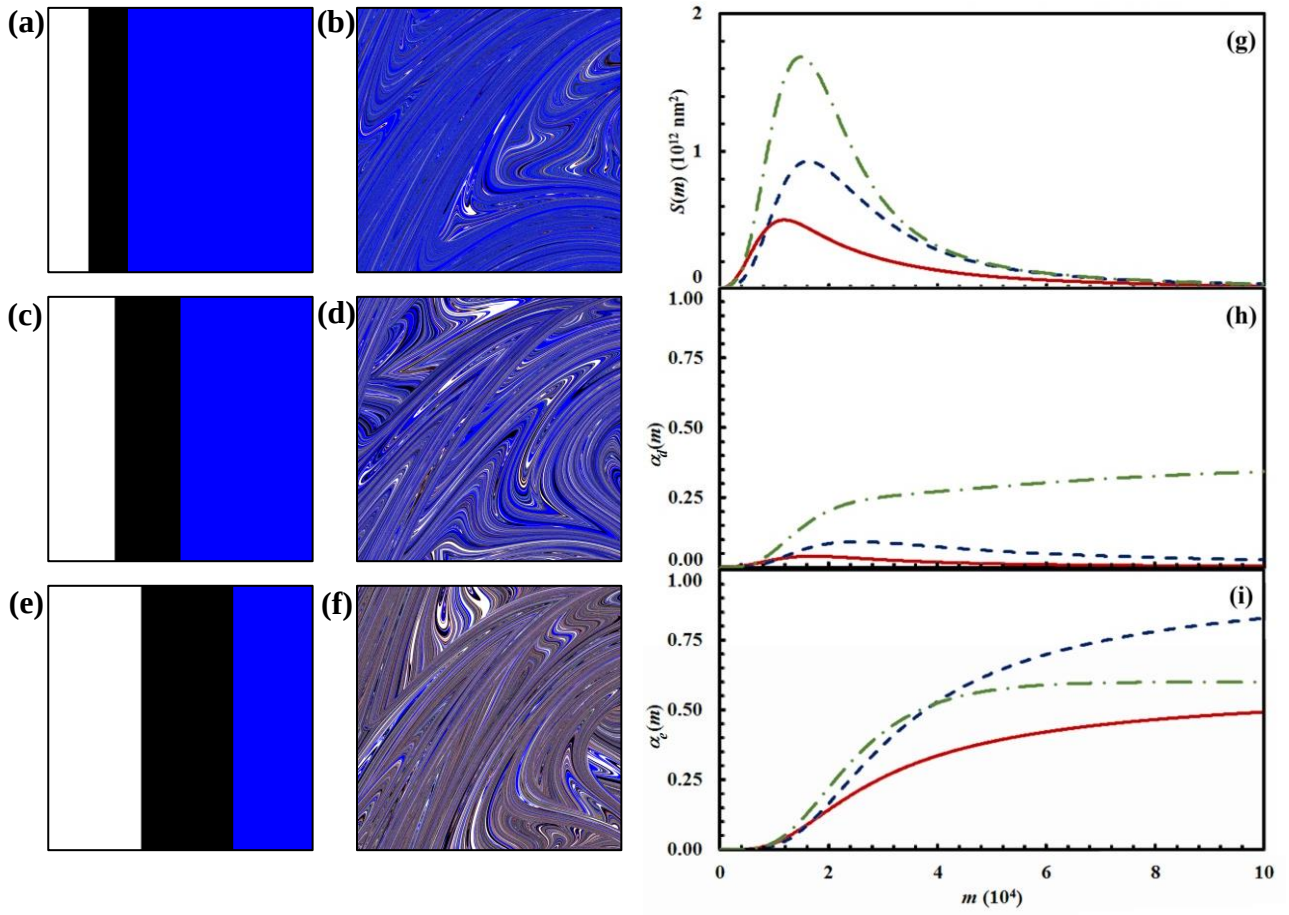

Figure 3.3.15: (a) Initial configuration (*A*, white; *B*, black; *C*, blue) and (b) the configuration after 15 impacts (*D*, red; *E*, green) for the chemical composition identified by $\alpha_{0,A}$, $\alpha_{0,B}$ and $\alpha_{0,C}$ values equal to 0.15, 0.15 and 0.70 respectively. (c) Initial configuration (*A*, white; *B*, black; *C*, blue) and (d) the configuration after 15 impacts (*D*, red; *E*, green) for the chemical composition identified by $\alpha_{0,A}$, $\alpha_{0,B}$ and $\alpha_{0,C}$ values equal to 0.25, 0.25 and 0.5 respectively. (e) Initial configuration (*A*, white; *B*, black; *C*, blue) and (b) the configuration after 15 impacts (*D*, red; *E*, green) for the chemical composition identified by $\alpha_{0,A}$, $\alpha_{0,B}$ and $\alpha_{0,C}$ values equal to 0.35, 0.35 and 0.30 respectively. (g) Interface area between reactants *A* and *B*, $S(m)$, (h) conversion degree of the intermediate *D*, $\alpha_D(m)$, and (i) conversion degree of the product *E*, $\alpha_E(m)$, as a function of the number of impacts, m, for the different cases investigated. Solid (red), dashed (blue), and dash dotted (green) lines refer to the sub-stoichiometric, stoichiometric and super-stoichiometric cases respectively.

Reaction probabilities Π_1 and Π_2 deeply affect the lifetime of intermediate *D*. We investigated their effect for the stoichiometric composition defined by the triplet of $\alpha_{0,A}$, $\alpha_{0,B}$ and $\alpha_{0,C}$ values equal to 0.25, 0.25 and 0.5 respectively. In particular, we varied systematically Π_2 between 0.001 and 1 while keeping Π_1 equal to 0.1. Pertinent data are shown in Figure 3.3.16. As expected, the lifetime of intermediate *D* decreases as Π_2 increases. For very small Π_2 values, the chemical reaction between *A* and *B* is almost complete before the intermediate *D* is sensibly consumed by the reaction with *C*. Under such circumstances, the two consecutive reactions proceed substantially independent of each other. Conversely, at relatively large Π_2 values, the

consumption of *D* by reaction with *C* is rapid enough to allow the final product *E* to reduce the interface area between *A* and *B* and affect their reaction rate.

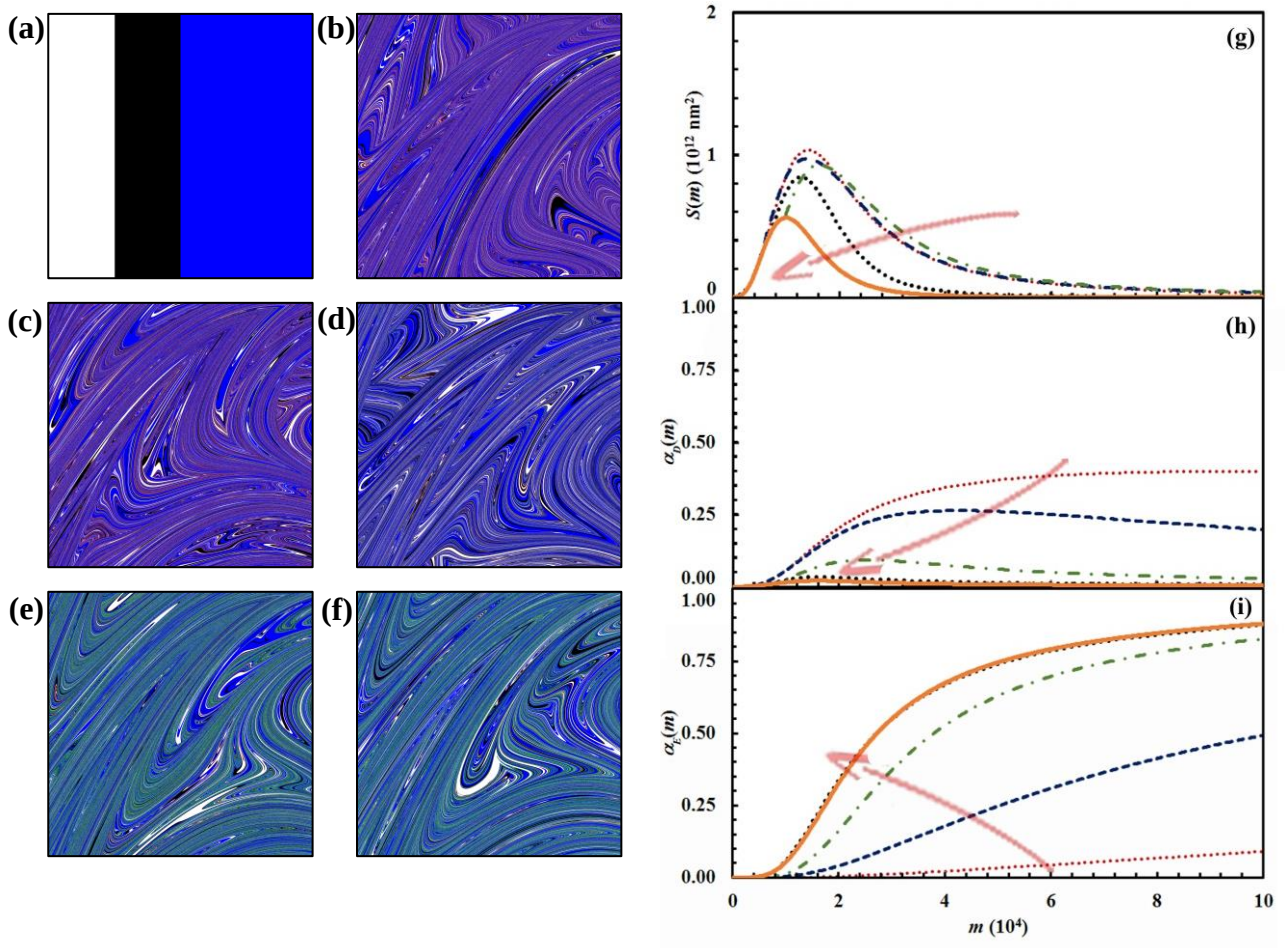

Figure 3.3.16: (a) Initial configuration (*A*, white; *B*, black; *C*, blue) and the configuration after 15 impacts (*D*, red; *E*, green) for the cases in which the reaction probability between *C* and *D*, Π_2, was given the value equal to (b) 0.001, (c) 0.01, (d) 0.1, (e) 0.5 and (f) 1.0. (g) Interface area between reactants *A* and *B*, $S(m)$, (h) conversion degree of the product *D*, $\alpha_D(m)$, and (i) conversion degree of the product *E*, $\alpha_E(m)$, as a function of the number of impacts, m. Data refer to the cases in which the reaction probability between *C* and *D*, Π_2, was given the value equal to 0.001, 0.01, 0.1, 0.5 and 1.0. The reaction probability between *C* and *D*, Π_2, increases, as indicated by the arrows, from the upper to the lower curves in panels (g) and (h), and from the lower to the upper curves in panel (i).

3.3.7 Discussion

The results presented heretofore outline the kinetic scenarios that can originate, during ball milling, from the interplay of mixing and chemical processes in powder mixtures consisting of molecular solids prone to flow deformation.

Being diffusion not allowed, interfaces remain sharp. Only shear deformation enables the constant increase and renewal of contacts between reactant species. This is what drives the chemical reaction to completion. The overall reaction rate depends on three independent factors. On the one hand, the rate at which the reaction

proceeds is related to the amount of powder subjected to CLCs during individual impacts and, then, to the statistical nature of the mechanical processing by ball milling. On the other hand, the conversion rate is unavoidably controlled by the rate at which reactant molecules react once they are in contact at the interface. Finally, the rate of the chemical transformation process is intrinsically dependent on the rate at which new interface area is generated by physical mixing. Concerning this latter factor, we remark that interface generation is intimately related to chemical composition.

The amount of powder that undergoes CLCs during individual impacts, measured by the volume fraction κ, has a predictable effect on the overall transformation rate. The latter increases as κ increases. This can be clearly seen from Figure 3.3.17, where a few representative kinetic curves are compared with each other.

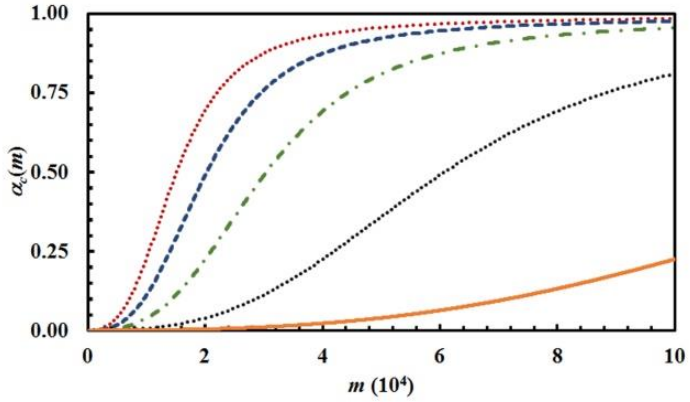

Figure 3.3.17: The conversion degree of the product C, $\alpha_C(m)$, as a function of the number of impacts, m. Data refer to the binary case with chemical composition identified by an $\alpha_{0,A}$ value equal to 0.5. The curves have been obtained using a reaction probability, Π, of 0.5 and the κ values of 1.0×10^{-4}, 2.5×10^{-4}, 5.0×10^{-4}, 7.5×10^{-4} and 1.0×10^{-3}. the volume fraction of powder that is subjected to CLCs per impact, κ, increases from the lower curve to the upper one.

The curves have been obtained using the same set of S_i values that refer to the equimolar mixture of chemical species A and B, while varying κ between 1×10^{-4} and 1×10^{-3}. The reaction probability between A and B molecules facing with each other at the interface, Π, was kept constant at 0.5.

While the variation of κ has a marked effect on the overall transformation rate, it does not affect the shape of the kinetic curves. Rather, the curves can perfectly overlap if the abscissae are properly re-scaled, i.e. if the number of impacts referred to a specific curve is multiplied by a suitable numerical factor (not shown for brevity). It follows that the shape of the kinetic curve is mostly determined by physical mixing and interface chemistry. More specifically, it is determined by the relative rates at which the mixing process and the chemical reaction at the interface proceed.

In this respect, we note that we have always used the same mixing map, which implies that the mixing process takes place always at the same rate. However, we have changed systematically the value of the reaction probability Π. Let us keep focused on the equimolar binary mixture. The numerical findings clearly suggest that mixing is the rate-limiting process when Π takes the highest values. In this case, the reaction at the interface is almost immediate and the chemical transformation needs new interface area to progress.

Conversely, mixing predominates for very small Π values. Under these circumstances, the reactants *A* and *B* reach very high degrees of mixing well before any significant chemical conversion.

This latter case immediately recalls the classical second-order kinetics of a chemical reaction between reactants *A* and *B* taking place in solution. The kinetic law can be simply expressed as [1-3]

$$\alpha_C(t) = K\,t\,(1 + K\,t)^{-1} \tag{12}$$

where $\alpha_C(t)$ is the conversion degree of the product *C*, *K* is the apparent rate constant and t is time. Eq. 12 can be readily obtained for the equimolar composition under the hypothesis that the chemical species *A* and *B* in solution are perfectly mixed [1-3].

We can expect that a similar kinetic law is valid for the mechanochemical reaction between *A* and *B* described by Eq. 8 provided that mixing is much faster than the chemical reaction. To test this hypothesis, we have generated a configuration with the reactants *A* and *B* well mixed starting from the initial configuration with equimolar composition having the chemical species segregated. To this aim, we have carried out 150 iterations of the mixing map. During these iterations, the reactants *A* and *B* were not allowed to react with each other to form the product *C*. The resulting configuration is shown in Figure 3.3.18a.

It can be seen that the chemical species *A* and *B* are dispersed over the whole volume of the cubic volume and well mixed with each other. We used this configuration as the starting configuration for the mechanochemical reaction between *A* and *B*. We evaluated the conversion degree of the product *C*, $\alpha_C(m)$, assuming that the volume fraction of powder affected by CLCs, κ, is equal to 1×10^{-3} and that the reaction probability at the interface, Π, is equal to 0.01. The obtained $\alpha_C(m)$ curve is shown in Figure 3.3.18b as a function of the number of impacts, m. The curve exhibits a smooth, monotonic increasing trend quite different from the sigmoidal one shown in Figure 3.3.11, which refers to the mechanochemical reaction between initially segregated reactants.

Data in Figure 3.3.18b can be best-fitted using a second-order kinetic law. To this aim, we have re-written Eq. 12 as

$$\alpha_i = k\,i\,(1 + k\,i)^{-1}\,, \tag{13}$$

where k is the apparent rate constant and time t has been replaced by the number of CLCs undergone by the powder, i. Then, we have substituted Eq. 13 in Eq. 4. The resulting equation satisfactorily best-fits the dataset in Figure 3.3.18b with a k value of 1.7×10^{-2}. It follows that the mechanochemical reaction between well-mixed chemical species can be actually compared to a solution reaction with second-order kinetics.

It is worth noting, however, that this is a highly idealized situation that can seldom occur in mechanochemical processes. Mixing in the solid state is always likely to occur on relatively long time scales, which implies, by default, that any chemical reaction at the interface starts well before mixing is complete.

The scenario changes drastically if the mechanical stresses, and the resulting shearing and mechanical energy deposition, induce the local melting of powder volumes. The formation of molten phases while shearing occurs, even for very short time intervals, can eventually give rise to much higher mixing degrees, typically not attainable by co-deformed solid phases. It follows that the chemical transformation processes can experience significant intensification. However, it is matter of debate whether or not the resulting chemistry has to be classified as a form of mechanochemistry.

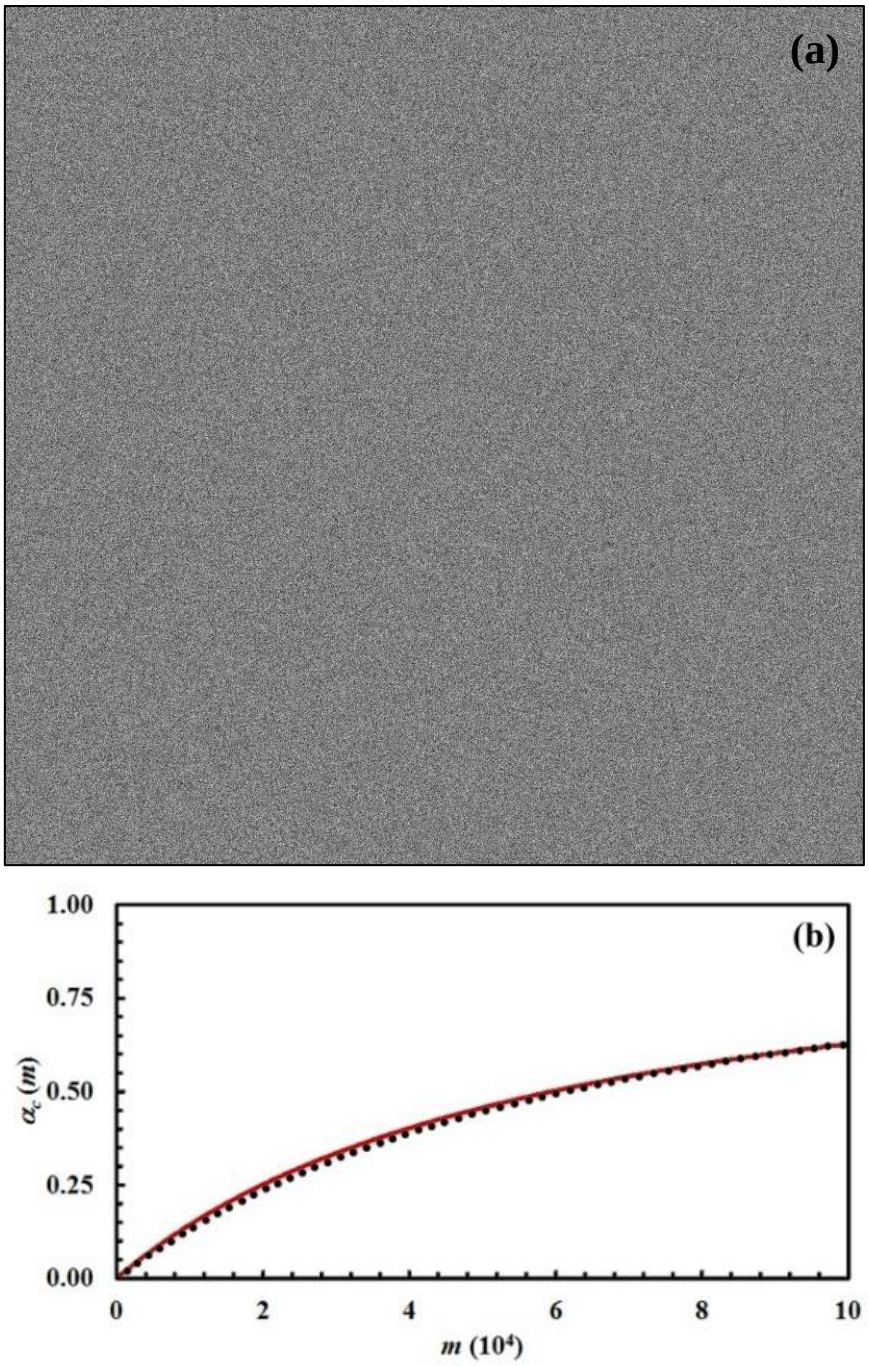

Figure 3.3.18: (a) Initial mixed configuration (*A*, white; *B*, black). (b) The conversion degree of the product *C*, $\alpha_C(m)$, as a function of the number of impacts, m. Data refer to the chemical composition identified by the $\alpha_{0,A}$ value equal to 0.5. Best-fitted curve is shown (solid, red line).

Now, turning our attention to experimental evidence in the field, we can say that our results compare, in principle, remarkably well with the experimental findings reported in the literature. Our simulations are seemingly able to reproduce most of the experimentally observed kinetic curves, thus providing a more fundamental interpretation.

Although a critical review and a detailed analysis of the experimental findings are out of the scope of the present work, it is worth focusing on their possible interpretation based on our kinetic model. Once more, for brevity and convenience we restrict our analysis to the binary case.

The first lesson to learn is that the experimental data stem from a combination of statistical and chemical factors as expressed by Eq. 4. Therefore, the two contributions must be suitably disentangled, which means that we have to separate the volume fractions of powder that have undergone i CLCs after m impacts, $\chi_i(m)$, from the associated concentration, α_i. Eq. 4 indicates that the concentration of product *C* after the very first impact is

$$\alpha_C(1) \cong \kappa\, \alpha_{1,C} \tag{14}$$

The quantity $\alpha_{1,C}$ can be expected to be very small. Therefore, the overall concentration of reactants, $\alpha_{1,A+B} = \alpha_{1,A} + \alpha_{1,B}$, can be expected to be approximately equal to 1. It follows that

$$\alpha_{A+B}(1) \cong (1-\kappa)\, \alpha_{1,A+B} \cong 1-\kappa \tag{15}$$

Thus, a first guess concerning the volume fraction of powder subjected to CLCs during individual impacts, κ, can be obtained by the initial slope of the kinetic curve describing the gradual decrease of reactants.

Once we have the first, rough κ estimate, a non-linear regression analysis of the experimental kinetic curves describing the variation of reactant (*A* and *B*) and product (*C*) concentrations $\alpha(m)$ can be carried out using Eq. 4. According to our model, once the mixing map describing physical mixing and the initial reactant configuration are chosen, the reaction kinetics depends only on the two quantities κ and Π. While the chemical kinetics expressed by the α_i values varies with the reaction probability Π, the volume fractions of powder subjected to i CLCs after m impacts, $\chi_i(m)$, are determined by the volume fraction affected by CLCs in individual impacts, κ. The κ and Π values can be obtained, in principle, by best fitting Eq. 4 to experimental data.

If the best fitting is not satisfactory, a new attempt can be made starting from the same rough κ estimate, but changing the initial reactant configuration, i.e. assuming a different volume distribution of sub-domains in volumes v^*. Along the same line, a different mixing map can be selected to improve the best fitting.

In all cases, the best fitting allows providing deeper insight into the experimental findings, moving from the macroscopic length scale to the one really involved in mechanochemical processes during individual impacts. Although simplistic, such analysis establishes a new, more reliable ground to compare the kinetics of different mechanochemical transformations or to relate the kinetics of a given mechanochemical reaction to the processing variables.

In this regard, we cannot help emphasizing that only the direct experimental evaluation of the different quantities involved in the mechanochemical transformation can really make the knowledge in the field advance. The characteristic size of the volumes involved in CLCs, v^*, the fraction of powder affected by CLCs during individual impacts, κ, the conversion degree associated with individual volumes v^*, α_i, and the related interface area, S_i, have to be estimated experimentally independent of each other. This is a tremendous challenge on the way to a full understanding of mechanochemistry, but it is also an exciting circumstance that can push researchers to struggle towards real progress in the field.

3.3.8 Conclusions

In this work, we addressed the kinetics of mechanochemical transformations involving molecular solids, one of the fundamental issues in the burgeoning field of mechanochemistry. Our investigation focused on the chemical behavior of molecular species that keep their structural integrity when subjected to mechanical stresses, but react with each other. We considered the case in which solid reactants are initially segregated and only the molecules that come into contact can form new chemical species. Thus, in addition to the propensity of molecules to react with each other, the chemical reaction rate depends on the interface area available to reactants. This, in turn, varies with the mixture composition and the degree of mixing between the solid phases, which increases as the molecular solids are repeatedly co-deformed.

Although the kinetic scenario can appear relatively simple, its description requires sophisticated theoretical and numerical methods. To this aim, we have developed a discrete kinetic model that combines the statistical nature inherent to the mechanical processing of powders by ball milling with a phenomenological description of physical mixing under the effects of shear stresses. The numerical calculation of discrete mixing maps allowed us to evaluate the interface area and monitor its gradual increase consequent to mechanical deformation. The assumption that the chemical reaction only involves, with a certain probability, reactant molecules in contact with each other finally enabled us to evaluate a chemical conversion degree.

We have carried out a systematic exploration of the transformation kinetics. Specifically, we have varied the amount of powder subjected to effective processing during individual impacts, the chemical composition of the powder mixtures and the reaction probability at the interface while using the same mixing map. In this way, we have evaluated the relative importance of the different factors involved in the mechanochemical reaction.

Unsurprisingly, we show that physical mixing plays a crucial role. Except for special cases, mixing represents the rate-limiting step of the mechanically activated chemical process. It is mixing that, to a large extent, determines the shape of the kinetic curve. Unless mixing is very effective and rapid, the combination of mixing and chemistry invariably results in a kinetic curve with sigmoidal shape. When mixing is much faster than the chemical reaction, however, the kinetics can approach the scenarios typical of classical solution chemistry.

Provided that accurate kinetic evidence is available, statistical and chemical factors can be disentangled, at least in principle. Under suitable assumptions, the kinetic analysis of experimental data can lead to the approximate, yet useful, evaluation of quantities on the mesoscopic and microscopic scales such as the interface area and the thickness of reacted layer. Displaying all of its potential in the presence of kinetic information systematically collected, our model can help filling the gap between macroscopic kinetic evidence and local processes taking place on the microscopic scale during individual impacts.

Notation of the Subchapter 3.3

A	reactant
B	reactant
C	product in binary systems - reactant in ternary systems
D	intermediate
E	product
h	thickness of the interface layer involved in the chemical reaction [m]
i	number of CLCs undergone by the powder
k	apparent rate constant for a mechanochemical second-order kinetics
K	apparent rate constant for a classical second-order kinetics [s^{-1}]
m	number of impacts
S	interface area between different chemical species [m^2]
$S_i(m)$	interface area for powder that has undergone CLCs i times after m impacts [m^2]
S_{fin}	plateau value of the interface area [m^2]
$S_{fin,max}$	maximum plateau value of the interface area [m^2]
t	time [s]
v	total volume of powder affected by CLCs per impact [m^3]
v^*	volume of powder affected by CLCs per impact [m^3]
V	total volume of processed powder [m^3]
x	Cartesian coordinate utilized in mixing map iterations
y	Cartesian coordinate utilized in mixing map iterations
z	Cartesian coordinate utilized in mixing map iterations
α	degree of chemical conversion
α_0	initial volume fraction of chemical species in the powder mixture
α_i	degree of chemical conversion of powder that has undergone CLCs i times after m impacts
η	number of volumes v^* affected by CLCs per impact
κ	volume fraction of powder that is subjected to CLCs per impact
Π	probability of reaction between two chemical species in contact
τ	impact duration [s]
χ	volume fraction of powder
$\chi_i(m)$	volume fraction of powder that has undergone CLCs i times after m impacts

References of the Subchapter 3.3

1. Connors, K.A., (1990). *Chemical Kinetics: The Study of Reaction Rates in Solution*, John Wiley and Sons, New York. ISBN: 978-0-471-72020-1
2. Levine, R.D., (2009). *Molecular reaction dynamics*, Cambridge University Press, Cambridge. https://doi.org/10.1017/CBO9780511614125
3. Houston, P.L., (2012). *Chemical Kinetics and Reaction Dynamics*, 3rd ed., McGraw-Hill, New York. ISBN: 9780486131696
4. Steinfeld, J.I., Francisco, J.S., Hase, W.L., (1999). *Chemical Kinetics and Dynamics*, Prentice-Hall PTR, Upper Saddle River. ISBN: 9780137371235
5. Levenspiel, O., (1999). *Chemical Reaction Engineering*, 3rd ed., John Wiley and Sons, New York. ISBN 9781601199218
6. Fogler, H.S., (2006). *Elements of Chemical Reaction Engineering*, 4th ed., Prentice-Hall PTR, Upper Saddle River. ISBN-13: 978-0130473943
7. Baldyga, J., Bourne, J.R., Hearn, S.J., (1997). Interaction between chemical reactions and mixing on various scales, *Chem Eng Sci*, 52(4), pp. 457-466. https://doi.org/10.1016/S0009-2509(96)00430-7
8. Clifford, M.J., Roberts, E.P.L., Cox, S.M., (1998). The influence of segregation on the yield for a series-parallel reaction, *Chem Eng Sci*, 53(10), pp. 1791-1801. https://doi.org/10.1016/S0009-2509(98)00054-2
9. Baldyga, J., Bourne, J.R., (1999). *Turbulent mixing and chemical reactions*, John Wiley and Sons, London. ISBN 9780471981718
10. Sturman, R., Ottino, J.M., Wiggins, S., (2006). *The mathematical foundations of mixing*, Cambridge University Press, Cambridge. ISBN 978-0-511-24354-7
11. Taitelbaum, H., Havlin, S., Kiefer, J.E., Trus, B., Weiss, G.H., (1991). Some properties of the a+b → C reaction-diffusion system with initially separated components, *J Stat Phys*, 65, pp. 873-891. https://doi.org/10.1007/BF01049587
12. Larralde, H., Araujo, M., Havlin, S., Stanley, H.E., (1992). Reaction front for A+B→C diffusion-reaction systems with initially separated reactants, *Phys Rev A*, 46, pp. 855-859. https://doi.org/10.1103/PhysRevA.46.855
13. Le Borgne, T., Ginn, T.R., Dentz, M., (2014). Impact of fluid deformation on mixing-induced chemical reactions in heterogeneous flows, *Geophys Res Lett*, 41, pp. 7898-7906. https://doi.org/10.1002/2014GL062038
14. Dentz, M., de Barros, F.P.J., (2015). Mixing-scale dependent dispersion for transport in heterogeneous flows, *J Fluid Mech*, 777, pp. 178-195. https://doi.org/10.1017/jfm.2015.351
15. Bandopadhyay, A., Le Borgne, T., Meheust, Y., Dentz, M. (2017). Enhanced reaction kinetics and reactive mixing scale dynamics in mixing fronts under shear flow for arbitrary Damköhler numbers, *Adv Water Res*, 100, pp. 78-95. https://doi.org/10.1016/j.advwatres.2016.12.008
16. Schmalzried, H., (1974). *Solid state reactions*, Verlag Chemie, Berlin. ISBN-13 : 978-0126258509
17. Ropp, R.C., (2003). *Solid state chemistry*, Elsevier Science, London. ISBN-13 : 978-0444514363
18. Toda, F., ed., (2005). *Organic solid state reactions*, Springer Verlag, Berlin. ISBN 978-3-540-22982-7
19. Butyagin, P. Y., (1971). Kinetics and Nature of Mechanochemical Reactions, *Usp Khim*, 40(11), pp. 1935-1959. https://doi.org/10.1070/RC1971v040n11ABEH001982
20. Heinicke, G., (1986). *Tribochemistry*, Akademie-Verlag, Berlin.
21. Suryanarayana, C., (2001). Mechanical alloying and milling, *Prog Mater Sci*, 46, pp. 1-184. https://doi.org/10.1016/S0079-6425(99)00010-9
22. Balaz, P., (2008). *Mechanochemistry in Nanoscience and Minerals Engineering*, Springer-Verlag Berlin Heidelberg, Berlin. https://doi.org/10.1007/978-3-540-74855-7
23. James, S.L., Adams, C.J., Bolm, C., Braga, D., Collier, P., Friscic, T., Grepioni, F., Harris, K.D.M., Hyett, G., Jones, W., Krebs, A., Mack, J., Maini, L. Orpen, A.G., Parkin, I.P., Shearouse, W.C., Steed, J.W., Waddell, D.C., (2012). Mechanochemistry: opportunities for new and cleaner synthesis, *Chem Soc Rev*, 41, pp. 413- 447. https://doi.org/10.1039/C1CS15171A
24. Friscic, T., (2012). Supramolecular concepts and new techniques in mechanochemistry: cocrystals, cages, rotaxanes, open metal–organic frameworks, *Chem Soc Rev*, 41, pp. 3493-3510. https://doi.org/10.1039/C2CS15332G

25. Sepelak, V., Düvel, A., Wilkening, M., Becker, K.-D., Heitjans, P., (2013). Mechanochemical reactions and syntheses of oxides, *Chem Soc Rev*, 42, pp. 7507- 7520. https://doi.org/10.1039/C2CS35462D
26. Balaz, P., Achimovicova, M., Balaz, M., Billik, P., Cherkezova-Zheleva, Z., Manuel Criado, J., Delogu, F., Dutkova, E., Gaffet, E., Gotor, F.J., Kumar, R., Mitov, I., Rojac, T., Senna, M., Streletskii, A., Wieczorek-Ciurowa, K., (2013). Hallmarks of mechanochemistry: from nanoparticles to technology, *Chem Soc Rev*, 42, pp. 7571- 7637. https://doi.org/10.1039/C3CS35468G
27. Takacs, L., (2013). The historical development of mechanochemistry, *Chem Soc Rev*, 42, pp. 7649-7659. https://doi.org/10.1039/C2CS35442J
28. Wang, G.-W., (2013). Mechanochemical organic synthesis, *Chem Soc Rev*, 42, pp. 7668-7700. https://doi.org/10.1039/C3CS35526H
29. Tan, D., García, F., (2019). Main group mechanochemistry: from curiosity to established protocols, *Chem Soc Rev*, 48, pp. 2274-2292. https://doi.org/10.1039/C7CS00813A
30. Carta, M., Colacino, E., Delogu, F., Porcheddu, A., (2020). Kinetics of mechanochemical transformations, *Phys Chem Chem Phys*, 22, 14489-14502. https://doi.org/10.1039/D0CP01658F
31. Reddy, C.M., Krishna, G.R., Ghosh, S., (2010). Mechanical properties of molecular crystals—applications to crystal engineering, *Cryst Eng Comm*, 12, pp. 2296-2314. https://doi.org/10.1039/C003466E
32. Mannepalli, S., Mangalampalli, K.S.R.N., (2017). Indentation Plasticity and Fracture Studies of Organic Crystals, *Crystals*, 7, ID 324. https://doi.org/10.3390/cryst7110324
33. Saha, S., Mishra, M.K., Reddy, C.M., Desiraju, G.R., (2018). From Molecules to Interactions to Crystal Engineering: Mechanical Properties of Organic Solids, *Acc Chem Res*, 51, pp. 2957-2967. https://doi.org/10.1021/acs.accounts.8b00425
34. Wang, C., Sun, C.C., (2020). The landscape of mechanical properties of molecular crystals, *Cryst Eng Comm*, 22, pp. 1149-1153. https://doi.org/10.1039/C9CE01874C
35. Ottino, J.M., (1989). *The kinematics of mixing: stretching, chaos and transport*, Cambridge University Press, Cambridge. ISBN-13 : 978-0521363358
36. Wiggins, S., Ottino, J.M., (2004). Foundations of chaotic mixing, *Phil Trans R Soc Lond A*, 362, pp. 937-970. https://doi.org/10.1098/rsta.2003.1356
37. Sturman, R., Ottino, J.M., Wiggins, S., (2010). *The Mathematical Foundations of Mixing. The Linked Twist Map as a Paradigm in Applications: Micro to Macro, Fluids to Solids*, Cambridge University Press, Cambridge. https://doi.org/10.1017/CBO9780511618116
38. Shingu, P.H., Ishihara, K.N., Otsuki, A., (1995). Mechanical Alloying and Chaos, *Mater Sci Forum*, 179-181, pp. 5-10. https://doi.org/10.4028/www.scientific.net/MSF.179-181.5
39. Pia, G., Traversari, G., Cincotti, A., Delogu, F., (2019). A mapping approach to pattern formation in the early stages of mechanical alloying, *Phil Mag Lett*, 99, pp. 192-198. https://doi.org/10.1080/09500839.2019.1653503

Chapter 4. Conclusions and future works

In this thesis, an analysis of two multiphase systems related to biomedical applications for regenerative medicine and materials science are analyzed: Chapter 2 is devoted to the study of long-term preservation of hMSCs from UCB, while the mechanical processing of powders by BM is addressed in Chapter 3.

In particular, the process known as cryopreservation, i.e. the long-term preservation of cells at -196 ° C in liquid nitrogen, is investigated for a suspension of hMSCs with DMSO. The latter one is used in cryopreservation as a permeant CPA to reduce ice formation in favor of glass during the freezing phase of the process. First, in this thesis a novel mathematical model capable to describe the non-perfect osmometer behavior of hMSCs is developed and proposed to optimize the cryopreservation protocol. These cells show a peculiar osmotic response which cannot be described by the classic two-parameter formalism typically adopted in the cryopreservation literature. In the new model called the SAR model, for the first time in cryopreservation literature osmosis is coupled to cell mechanics and cell membrane surface area regulation. This way, the trans-membrane permeation of ions/salt during any swelling phase where cell membrane is stretched is allowed through the temporary opening of mechanosensitive channels. For this reason. cells may now reach an equilibrium volume different from the initial isotonic one when isotonic conditions are re-established after osmotic excursions. The model, trained through data fitting for parameter estimation and validated through prediction of a new set of experimental runs, shows acceptable agreement with measured data.

Further validations need to be addressed given that the model predicts an elastic expansion of the cell membrane surface area (up to 30%) larger than what is reported in the literature for different cell lineages. For comparison, membrane expansion by 2-4 % has been reported for protoplasts, while excessive elastic membrane expansion could lead to cell lysis and may therefore be unrealistic. The dependence of the rate of membrane surface area variation upon tension can be revised in the future when experimental evidence and relevant measurements become available.

A relevant experiment would be to analyze the elastic response of this cell lineage through indentation or pulling tethers in order to check if the relatively large membrane surface area expansion is realistic, and to estimate the values of more specific elastic parameters (i.e. elastic modulus and resting tension). Moreover, the hypothesis of the coexistence of different sources of membrane reservoirs for exo- and endo-cytosis should be investigated. Indeed, a practically instantaneous release of more accessible membrane reservoirs, i.e. unfolding of the membrane, could be considered as an elastic expansion of the cell membrane surface. On the contrary, the release from endomembranes is considerably more sluggish in its contribution to an increase in the cell membrane surface area.

Finally, additional investigation should be performed to analyze the behavior of mechanosensitive ion channels in this specific cell lineage. The minimum opening tension could be measured through patch clamp analysis

and atomic force microscopy, and the variation of the amount of intracellular ionic solutes could be investigated by fluorescence analysis to validate the simplifications assumed in this work.

Later, in the second subchapter of this thesis, the proposed SAR model is deeply analyzed in comparison with the classic two-parameter model. First, an appropriate non-dimensional version of the model equations is derived to identify the relevant non-dimensional parameters. Then, a parametric sweep analysis is performed and discussed to highlight the features of the proposed model. It is shown that the SAR model progressively reduces to the two-parameter formalism when a negligible ion/salt exchange between intra- and extracellular compartments takes place, i.e. when ion/salt permeability is reduced below a critical value or CPA permeability is increased above a critical one. For the same reason, the SAR model with a cell membrane characterized by zero elasticity or infinite constant of relaxation rate is equivalent to the two-parameter model, given that at these extreme conditions MS channels cannot open.

It is found that, generally speaking in the SAR model cell volume and its composition at equilibrium depend on the position of the temporal window of MS channels opening, which is a complex function of model parameters and operating conditions: whereas at the end of any osmotic cycle a complete recovery of the initial, isotonic cell volume always results from the two-parameter model, in general a larger or lower cell volume is obtained with the new model, depending on the exact opening and closing time of MS channels during the osmotic excursions. This is not the case when the osmotic cycle with an impermeant solute like sucrose is used, where MS channels are open only during phase II when cells are suspended back in an isotonic solution. For this reason, with the SAR model only equilibrium equations after contact with impermeant sucrose may be analytically derived, albeit without the advantageous linearity of the Boyle Van't Hoff equation. This work demonstrates that the validity of these osmotic equilibrium equations with impermeant sucrose may be extended to any realistic set of model parameters, provided that enough time is allowed to the cell membrane for a complete relaxation. On the other hand, when a permeant CPA comes into play, a numerical integration of system dynamics, prolonged until steady state is eventually reached, is required to determine cell volume at equilibrium.

Moreover, a negligible hydrostatic pressure gradient across the cell membrane is found for osmosis rate if a realistic set of the model parameter values is adopted. While representing a justification to simplify the dynamic version of the SAR model for future use, this confirms that animal cells are well-known to possess a very fragile membrane made only of a double layer of phospholipid molecules. Despite this simplification of the SAR model, this paper shows that the mechanics of the cell membrane coupled with surface area regulation may be considered responsible for ion/salt exchange and the control of cell volume during cryopreservation without resorting to the complex pump and leak physiological model.

In the third subchapter of this thesis, the SAR model is adopted for a combined analysis of osmotic injury and cytotoxic effect when hMSCs from UCB are contacted with DMSO. This analysis is carried out from the experimental and theoretical perspectives. More specifically, a novel mathematical model is developed and proposed to interpret data, without the need to set in advance the cell Osmotic Tolerance Limits (OTLs), as traditionally done in cryopreservation literature. Comparisons between experimental data and theoretical

simulations are provided, first by performing a non-linear regression analysis to evaluate unknown model parameters, then by checking its reliability to predict system behavior measured at operating conditions different from those used during the best-fit procedure.

It is found that the cytotoxic effect of DMSO onto hMSCs is only mild and confined to the contact phase, while expansion lysis is fast and takes place only during the swelling in the removal phase. Thus, it is concluded that the cytotoxic effect on these cells may be limited considerably by adding DMSO in one step at low temperature and by strictly reducing the contact time to the one necessary for the osmotic equilibration. On the other hand, to limit the osmotic injury during the removal phase the excessive temporal increase of membrane stretching needs to be carefully avoided by adopting a properly designed multi-step strategy.

Since the production of liquid nitrogen, necessary for Cryopreservation, is of great impact on the environment, an alternative process of long-term conservation that mimics the protection mechanisms used in nature by special living beings to protect themselves from severe drought has been proposed and modeled. In the fourth subchapter a mathematical model for the description of the air-drying process at room temperature and atmospheric pressure of hMSCs with trehalose is developed by referring to a specific desiccator unit where silica gel is used as water trap. The ultimate goal is to provide a deterministic model to support and guide the optimization of a long-term preservation process for these precious cells in alternative to the classic cryopreservation carried out in liquid nitrogen at -196 °C. To this aim, all the physico-chemical phenomena that may occur in the process (i.e. evaporation, cell osmosis, crystal formation or glass transition, leakage through the lids of the petri dishes, and adsorption) are accounted for by means of a compartmental model: driving forces are defined as deviations from the corresponding thermodynamics equilibria, while the two film theory is adopted to describe the material exchange at the contacting interfaces between two communicating phases/compartments.

First, the thermodynamics equilibria of the system are determined on the basis of an extensive and careful analysis of the fragmentary scientific literature on the topic, where contradictory data are reported. Later, transport parameters for the model simulations are chosen: given that for the system investigated in this work no valuable data is found in the literature, the adopted parameter values are taken form the literature even if referred to different systems.

Based on these uncertainties, in this work a parametric sensitivity analysis is performed by varying some key system sizes, geometries and operating conditions. It is shown that, depending on the specific choices made by the operator running the desiccator unit, two possible outcomes may be eventually reached. In fact, according to the proposed model the competition between evaporation and crystal formation in the sample is responsible of the system behavior and determines the cell fate at the end of the process. More specifically, by varying the surface area or the volume of the sample to be dried as well as the trehalose content or the tightening of the lids covering the petri dishes, it is shown that the resulting evaporation may be faster or slower than crystal formation. In the first case, sugar glass is formed in the sample and an extended dehydration of the cells is eventually achieved. Thus, an effective lyo-protection for the cells may be realized but only with a very long air-drying process, due to the increasing trehalose concentration in the liquid sample that progressively slows

down evaporation (i.e. in the sample diffusivity decreases and viscosity increases to critical values). On the other hand, when evaporation is slower than crystallization, a limited cell dehydration is eventually achieved and sugar crystals instead of glass are formed in the sample containing the cells. In this case, a shorter air-drying process results but an effective lyo-protection cannot be actually achieved. In conclusion, by varying system sizes and geometries as well as the operating conditions, the evaporation rate need to be optimized in order to reach an acceptable final cell viability (by favoring glass formation with a large cell dehydration) while reducing the duration of the air-drying process.

In Chapter 3, the mechanical processing of powders by Ball Milling (BM) have been analyzed. The hypothesis is that, once the milling dynamics has been relatively clarified, so that the frequency and energy of impacts are known, the coupling with a relatively simple stochastic model can provide significant insight into the mechanochemical kinetics. More specifically the idea is that macroscopic kinetics can be related to local processes occurring on the microscopic scale based on a few assumptions concerning the volume of powder effectively processed during individual impacts and the stirring of powders during BM. To this ultimate goal, in the first subchapter, the propagation of MSRs in a SPEX Mixer/Mill 8000 ball mill depending on factors related to the reactor swing and to the intrinsic reaction rate in individual powder particles has been analyzed by numerical simulation. The numerical model takes advantage of the accurate description of the ball and powder particle dynamics inside the moving reactor, based, in turn, on a reliable reconstruction of contact dynamics. Numerical simulations clearly show that powder particles form a granular body governed by a strongly dissipative dynamics. The fast energy redistribution among powder particles allows the granular flow to exhibit a periodic behavior. Despite the disordered trajectories of individual powder particles, the granular body undergoes quite regular displacements between the two opposite reactor bases. Overall, the granular flow is characterized by alternating contraction and expansion stages. Contractions take place when the granular body moving in a certain direction impacts on the reactor base moving in the opposite direction, whereas expansion starts when the reactor has reached the point of maximum velocity. Two contraction and two expansion stages occur per cycle of the reactor swing.

The granular flow is disordered by the ball. Much bigger than powder particles, the ball is able to push them away. Accordingly, the powder particles are scattered across the reactor volume. Every time the ball impacts on the reactor wall or bases, it compresses a relatively small number of powder particles. This results in a significant dissipation of the ball mechanical energy during the impact, which allows the establishment of a partially inelastic impact regime. As a consequence, the ball undergoes two main impacts per cycle of the reactor swing within the whole range of reactor swing frequency explored. Thus, the results obtained satisfactorily agree with experimental and numerical evidence from previous studies.

We have used the numerical reconstruction of ball and powder particles trajectories to investigate the relationship between the granular flow dynamics and the propagation of MSRs inside a moving reactor. To this aim, we have chosen to describe the reaction of a single powder particle according to a Johnson-Mehl-Avrami kinetics. Although phenomenological, this description is sufficient to enable the evaluation of factors potentially affecting the MSR propagation. Reaction was first ignited in a single particle randomly chosen

among those compressed by the ball during an impact with the reactor base. We observe that the propagation strongly depends on the rate constant of the phenomenological kinetic law. In particular, propagation is favored by large values of the rate constant. Less influential factors are the distance at which a reacting particle can ignite the MSR in a non-reacting particle and the frequency of the reactor swing. In any case, numerical findings clearly show that the MSR proceeds via an irregular, discontinuous propagation process. Specifically, bursts in the reaction ignition in individual powder particles occur approximately in correspondence of the contractions undergone by the granular flow as a result of the intrinsic dynamics of the granular body.

Our results allow deeper insight into the dynamics governing the motion of ball and powder particles inside a moving reactor of the SPEX Mixer/Mill 8000 and helps clarifying the conditions under which MSRs propagate. Further work is needed to perform a systematic exploration of the parameter space.

In the second subchapter, a modelling approach that captures the fundamental features of the lamellar structure refinement during the early stages of MA has been developed. A kinetic model able to describe the kinetics of processes activated by BM has been combined with a mathematical description of advection cycles induced by plastic deformation. The model curve satisfactorily best fits the experimental data obtained by suitably designed experiments. It follows that suitably chosen mapping procedures can be used to evaluate the spectrum of characteristic lengths that distinguish microstructure at the different refinement stages.

In the third and final subchapter, the kinetics of mechanochemical transformations involving molecular solids, one of the fundamental issues in the burgeoning field of mechanochemistry, has been addressed. Our investigation focused on the chemical behavior of molecular species that keep their structural integrity when subjected to mechanical stresses, but react with each other. We considered the case in which solid reactants are initially segregated and only the molecules that come into contact can form new chemical species. Thus, in addition to the propensity of molecules to react with each other, the chemical reaction rate depends on the interface area available to reactants. This, in turn, varies with the mixture composition and the degree of mixing between the solid phases, which increases as the molecular solids are repeatedly co-deformed.

Although the kinetic scenario can appear relatively simple, its description requires sophisticated theoretical and numerical methods. To this aim, we have developed a discrete kinetic model that combines the statistical nature inherent to the mechanical processing of powders by ball milling with a phenomenological description of physical mixing under the effects of shear stresses. The numerical calculation of discrete mixing maps allowed us to evaluate the interface area and monitor its gradual increase consequent to mechanical deformation. The assumption that the chemical reaction only involves, with a certain probability, reactant molecules in contact with each other finally enabled us to evaluate a chemical conversion degree.

We have carried out a systematic exploration of the transformation kinetics. Specifically, we have varied the amount of powder subjected to effective processing during individual impacts, the chemical composition of the powder mixtures and the reaction probability at the interface while using the same mixing map. In this way, we have evaluated the relative importance of the different factors involved in the mechanochemical reaction.

Unsurprisingly, we show that physical mixing plays a crucial role. Except for special cases, mixing represents the rate-limiting step of the mechanically activated chemical process. It is mixing that, to a large extent,

determines the shape of the kinetic curve. Unless mixing is very effective and rapid, the combination of mixing and chemistry invariably results in a kinetic curve with sigmoidal shape. When mixing is much faster than the chemical reaction, however, the kinetics can approach the scenarios typical of classical solution chemistry.

Provided that accurate kinetic evidence is available, statistical and chemical factors can be disentangled, at least in principle. Under suitable assumptions, the kinetic analysis of experimental data can lead to the approximate, yet useful, evaluation of quantities on the mesoscopic and microscopic scales such as the interface area and the thickness of reacted layer. Displaying all of its potential in the presence of kinetic information systematically collected, our model can help filling the gap between macroscopic kinetic evidence and local processes taking place on the microscopic scale during individual impacts.